Modelling phosphate-based glasses for biomedical applications

Richard I. Ainsworth

Faculty of Mathematical & Physical Sciences
University College London

Thesis submitted for the degree of
Doctor of Philosophy of University College London.
Field of study: Chemical Physics.

October 2013

To Ania and Mum

I, Richard Ainsworth, confirm that the work presented in this thesis is my own. Where information has been derived from other sources, I confirm that this has been indicated in the thesis.

Richard Ainsworth
October 2013

Abstract

In this thesis, we present the application of theoretical methodologies to model several compositions of phosphate-based glasses (PBGs) for biomedicine. Quantum mechanical calculations of single crystal phosphorus pentoxide, P_2O_5, have been conducted using plane wave density functional theory. A rigorous structural, mechanical and electronic characterization of the two most stable phases, $o'(P_2O_5)_\infty$ and $o(P_2O_5)$, showed both to be highly elastically anisotropic due to structural features. Löwdin atomic charge and valence charge density analysis shows mixed ionic and covalent character in both phases.

A formal charge, shell-model force field, has been parameterized to reproduce the structural and mechanical properties of $o'(P_2O_5)_\infty$. This has been used to conduct classical molecular dynamics simulations of amorphous P_2O_5-CaO-Na_2O systems, via a melt-quench protocol. Dependent on composition, phosphorus atoms are primarily Q^1 and Q^2. Moreover, calcium ions coordinate to a significantly higher proportion of non-bonded oxygens than sodium.

Born-Oppenheimer and classical molecular dynamics simulations of amorphous P_2O_5-CaO-Na_2O-Ag_2O systems reveal a distorted octahedral / trigonal bi-pyramidal coordination environment for silver. An increase in the phosphorus to bonded oxygen bond disorder, and disproportionation in the medium-range structure, following the relation $2Q^2 \rightarrow Q^1 + Q^3$, is evidenced upon Ag-doping.

The influence of titanium on the structural, mechanical and electronic properties of PBG has been investigated via Born-Oppenheimer molecular dynamics and theoretical ^{31}P chemical shieldings calculations. Upon Ti-doping, a depolymerization of the phosphate network is offset by the formation of P-O-Ti and Ti-O-Ti linkages. The reconstructed theoretical ^{31}P NMR spectra compare well to experimental spectra, suggesting that the unimodal spectral peak comprises Q^{1-4} phosphorus. The bulk modulus rises from 38.96 GPa in PBG to 43.94 GPa for Ti-PBG, due to a more cross-linked glass network. Density of states calculations show a reduction in the band gap from ~ 3.3 eV to ~ 2.1 eV upon Ti-doping.

Publications

The work presented here has contributed to the following publications:

- Ainsworth, R. I., Christie, J. K., & de Leeuw, N. H. On the structure of biomedical silver-doped phosphate-based glasses from molecular dynamics simulations. Pending submission.

- Tommaso, D. D., Ainsworth, R. I., Tang, E., & de Leeuw, N. H. Modelling the structural evolution of ternary phosphate glasses from melts to solid amorphous materials. *Journal of Materials Chemistry B.* 1, 5054 (2013).

- Christie, J. K., Ainsworth, R. I. & de Leeuw, N. H. Nanoscale chains control the solubility of phosphate glasses for biomedical applications. *The Journal of Physical Chemistry B* 117, 10652 (2013).

- Ainsworth, R. I., Tommaso, D. D., Christie, J. K. & de Leeuw, N. H. Polarizable force field development and molecular dynamics study of phosphate-based glasses. *The Journal of Chemical Physics* 137, 234502 (2012).

- Ainsworth, R. I., Tommaso, D. D. & de Leeuw, N. H. A density functional theory study of structural, mechanical and electronic properties of crystalline phosphorus pentoxide. *The Journal of Chemical Physics* 135, 234513 (2011).

Acknowledgements

I would like to thank my supervisor Prof. Nora de Leeuw for her guidance and for giving me the freedom to pursue topics of interest. I would also like to express gratitude to my second supervisor Prof. Richard Catlow. I am grateful to Prof. Chris Pickard for his help and expertise in the calculation and analysis of theoretical NMR parameters. Thanks are due, to the post-doctoral researchers I have had the pleasure of collaborating with, Dr Devis Di Tommaso, Dr Jamieson Christie and Dr Thor Wikfeldt. Also thanks to Dr Umberto Terranova. I am also grateful to Prof. Tony Harker, whose door was always open and who helped broaden my knowledge of solid state physics over many years. Additionally, Dr Antonio Tilocca whose experience with simulations of amorphous systems was much valued. Thanks to my good friends Szymon Daraszewicz and Dr Zamaan Raza with whom many a beer and grumble were shared. Finally, the biggest thank you is reserved for my partner Ania, my Mum and my stepfather David, whose love and support over many years, has put me where I am today.

Table of Contents

7 Amorphous P_2O_5-CaO-Na_2O-Ag_2O systems 144

8 Amorphous P_2O_5-CaO-Na_2O-TiO_2 systems 162

9 Concluding remarks 184

List of Figures

List of Tables

Chapter 1

Introduction

1.1 Bioglass and phosphate-based glasses

The bioactive mechanism, by which living tissues attach to and integrate with an artificial implant through stable chemical bonds, is at the core of many current and propesctive applications of biomaterials. The first bioactive glass was invented by Larry Hench at the University of Florida in 1969. Professor Hench began by seeking to find a material that could bond to bone and survive the aggressive environment of the human body in response to the severe bone damage and amputations suffered by US soldiers serving in the Vietnam war. The main discovery was that of 45S5 Bioglass® of composition 46.1 mol% SiO_2, 26.9 mol% CaO, 24.4 mol% Na_2O, and 2.6 mol% P_2O_5, which formed a bond with bone so strong that it could not be removed without breaking the bone.[1] This was the first material that was found to form a chemical bond with bone, launching the field of bioactive ceramics, with many new materials and products being formed from variations on bioactive glasses,[2] glass-ceramics,[3] ceramics such as synthetic hydroxyapatite and other calcium phosphates.[4]

Such glasses have shown great success in many clinical applications especially in the dental and orthopaedic fields. However, the SiO_2 component is rarely absorbed, it inhibits the rate of resorption,[5, 6] and the long-term reaction locally and systemically is not yet fully understood, raising concerns over its long-term use *in vivo*.[7, 8] Derivative materials such as phosphate-based glasses (PBG) in the system P_2O_5-CaO-Na_2O have unique properties, the most interesting of which from a biomedical point of view, is the ability to completely dissolve in aqueous media. Furthermore, this solubility behaviour can be compositionally modified such that dissolution rates can vary over orders of magnitude.

1.2 Rationale and scope

The study of PBG is inherantly a multiscale endeavour as electronic and atomistic properties give rise to bulk-structural characteristics and in turn macroscopic properties, including biocompatibility and the materials interaction characteristics with living tissue. Significant experimental work has been undertaken to elucidate the structures, dissolution characteristics and interactions with biological systems of PBG along with the roles of dopants.[9–12] There is however a dearth of literature pertaining to applied theoretical approaches. The latter help gain a fundamental understanding of the atomic level structure and how glasses interact with and dissolve in an aqueous medium. In particular, classical simulations, based on empirical potentials, and *ab initio* techniques, based on an explicit description of the electronic structure, can provide atomistic level information (often only indirectly attainable from experiment) to help provide a more complete picture of many physical properties and their compositional dependencies. The extensive research into phosphosilicate glasses using computational approaches[13, 14] was matched by a single *ab initio* molecular dynamics study of PBG by Tang *et al.*[15] at the start of this work, providing strong motivation for the work presented here. The overriding theme of the thesis is a thorough investigation of the compositional dependence of bulk-structure for a host of biomedically applicative PBGs and doped-PBGs (d-PBGs). To this end, the thesis outlines the computational modelling of various compositions of PBGs and d-PBGs using bulk periodic calculations. The work has a strong focus towards the application of theoretical methodologies for the calculation of various physical properties, but is also methodological, in the sense that it seeks to set up robust simulation protocols.

1.3 Outline of thesis

The current Chapter 1 introduces and contextualises PBG and seeks to motivate the work to follow. Chapter 2 introduces the three main synthesis routes for PBG namely, melt-quench, sol-gel and the unique method of drawing PBG into fibres. Furthermore, an extensive review of the current and potential applications with a focus on the physio-chemical and biological studies, *in vitro* and *in vivo*, that have been conducted. This chapter is intended to give the reader an appreciation of the medical uses of PBG, and highlight how cellular response and other biologically relevant properties may be linked to compositionally dependent dissolution and ion release rates. Chapters 3 and 4 introduce important theoretical concepts that form the basis of the work presented in this thesis. Chapter 3 highlights the origin of the complexity of the problem of quantum mechanical many-body systems, describing how the nuclear and electronic degrees of freedom may be separated and the power of variational methods for solving quantum mechanical equations. The theorems of Density Functional Theory (DFT) are presented allowing for a reformulation of the many-body problem in order to calculate the ground-state properties of the electronic system. The local density and generalized gradient approximations for exchange and correlation are outlined, along with the treatment of periodic systems and the pseudopotential approximation. Finally, solving the Kohn-Sham equations in plane-wave form is discussed, along with energy minimisation techniques and geometry optimisation. Chapter 4 deals with the molecular dynamics method for forces derived from both classical and *ab initio* techniques. Finite difference methods are introduced for the integration of the Newtonian equations of motion, along with a brief description of force fields techniques and the shell-model for polarisability. Finally, the field of statistical mechanics is introduced and the techniques used to calculate structural and theoretical properties using ensemble averaging.

The remainder of the thesis outlines original work that has been undertaken by the author and the results achieved. Each chapter begins with a brief introduction and review of the most relevant literature, in particular, any available experimental studies that have probed the structures of the simulated PBG from this work. Chapter 5 reports on a static DFT study of two phases of crystalline P_2O_5. An assessment is made of differing exchange-correlation and pseudopotential approximations for the most stable $o'(P_2O_5)_\infty$ phase, aswell as a structural comparison with the inclusion of the empirical dispersive correction. Structural parameters, mechanical and electronic properties are reported for both phases. Chapter 6 builds on the high level reference data calculated in the previous chapter and begins with a description of force field development based on the Born-ionic model. Phosphorus to oxygen Buckingham-type two-body and harmonic three-body potentials are fitted to reproduce the short-range structural and mechanical properties of $o'(P_2O_5)_\infty$ using a "brute-force" scanning approach over parametrical space. The final force field is then used to simulate three amorphous compositions in the system

P_2O_5-CaO-Na_2O using a classical melt-quench procedure. The final glasses are extensively structurally characterised and comparison is made to relevant experimental data.

Chapters 7 reports on Born-Oppenheimer (BOMD) and classical molecular dynamics simulations of amorphous P_2O_5-CaO-Na_2O-Ag_2O systems using full *ab initio* and classical melt-quench procedures respectively. Structural characterisations of the short- and medium-range are performed, for reference undoped and silver-doped compositons, and comparison made to neutron and x-ray diffraction data from experiment. Medium-range disproportionation and bond disorder are analysed, as a function of the presence of Ag, from the relevant Q^n distributions and radial distribution functions respectively. Atomic charges are analysed from BOMD trajectories.

Chapter 8 reports on BOMD simulations of amorphous P_2O_5-CaO-Na_2O-TiO_2 systems. Full *ab initio* melt-quenches are conducted for a reference PBG and Ti-PBG followed by full structural characterisations to assess the influence of Ti atoms. Theoretical ^{31}P NMR parameters calculated using the gauge projector augmented method are reported and relevant bonding environment dependencies analysed. Theoretical 1-D ^{31}P NMR spectra have been reconstructed and comparison made to experimental data. Further to this, results from mechanical and electronic properties are presented.

The final Chapter 9 summarises the broad research objectives that have been fulfilled and describes the specific findings of each piece of work. Finally, future avenues of potential research are discussed drawing comparison to theoretical modelling of amorphous phosphosilicates.

Chapter 2

Phosphate bioglass - a review

2.1 Overview

The following review of published scientific literature is intended to frame and contextualise the work reported in this thesis. From this perspective, the aim is to give an overview of the medical applications, as well as a discussion of the biological, chemical and materials science literature covering unique properties of phosphate-based glass (PBG). The literature is primarily categorized by composition, since this thesis is heavily based on the investigation of composition-dependent properties. Most of the review focuses on physiochemical data pertaining to dissolution with other *in vitro* studies. Reference is made to relevant *in vivo* literature but this does not form the focus of this review. The literature related to structural, electronic, atomistic, mechanical and other physical properties (from experiment and theory) will be thoroughly discussed elsewhere, specifically as part of each chapter where comparison is made to the reported computational work. The compositional nomenclature used henceforth for amorphous systems is, P = P_2O_5, C = CaO, N = Na_2O, followed by the percentage molar composition for each component.

2.2 Melt-quenched bulk glasses

Bulk glasses are typically synthesised via a melt-quench procedure in which a mixture of oxide precursors, such as NaH_2PO_4, $CaCO_3$ and P_2O_5, are melted in a furnace at temperatures of over 1270 K. Once a homogeneous melt has been achieved, the glass is formed by casting into different shapes. The melts are cooled quickly ("quenched") through the glass transition temperature (T_g) and then subsequently cooled very slowly in an annealing step to remove any residual stress.

Materials properties can be compositionally tuned and the inclusion of dopants can produce materials for specific medical applications. Discussion here is primarily focused on the doping of ternary PBG to make quaternary compositions. Synergistic approaches also exist where two or more dopants are introduced into the ternary P_2O_5-CaO-Na_2O system to form quinternary+ compositions.[16]

2.2.1 Undoped

Undoped PBGs are classified as those compositions in the P_2O_5-CaO-Na_2O system. Unlike SiO_2-based bioglasses, PBG have the unique property of completely dissolving in aqueous solution, where the dissolution rates can be compositionally tuned over orders of magnitude.[17] Figure 2.1 shows the inverse exponential relationship between solubility ($g.cm^{-2}.h^{-1}$) and increasing CaO mol% for compositions in the range $(P_2O_5)_{0.45}(CaO)_x(Na_2O)_{0.55-x}$ (x = 0.16, 0.20,..., 0.40). A surface plot of individual data points is given in Figure 2.2 (data taken from [17]), to show how weight loss per unit area varies as a function of time as well as composition[9]. Inspection of the Figure inset shows how the gradient of weight loss per unit area vs. time (i.e. solubility) decreases after approximately 20 h in aqueous media for compositions x = 0.32-0.40. This non-linearity in solubility (dissolution rate) with increased CaO mol% may be linked to a two-stage dissolution process.

Ahmed *et al.*[18] have studied the effect of composition on the solubility of PBG in distilled water. Their findings show that solubility decreases with increasing CaO mol%, approaching a linear relation in the case of P50C30N20 over the first 200 h in solution. pH levels were noted to decrease over time, attributed to the release of Ca^{2+} and Na^+ ions. It is significant to note that the higher P_2O_5 containing compositions, P50 and P55, decreased the pH of solution to pH 3.5-4 and pH 2.5-3 respectively after 200 h, linked to the breakdown and subsequent release of PO_4^{3-} species. P45 compositions displayed increased biocompatibility, approaching neutral pH after 25 h in solution, which then decreased to pH 6.4 after 200 h.

The properties and cytotoxicity (toxicity to cells) of a wide range of compositions of PBG

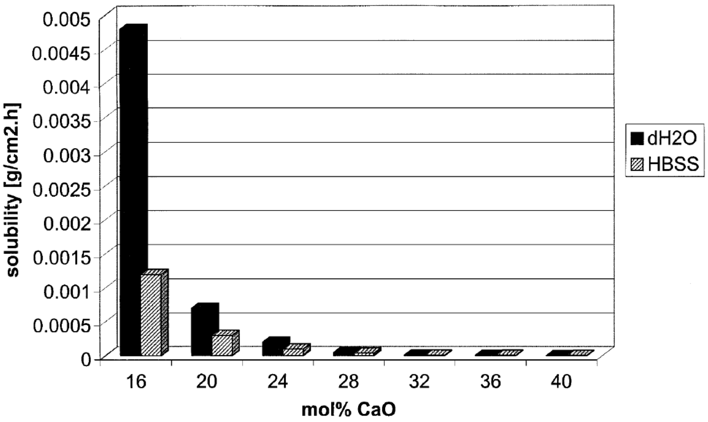

Figure 2.1: Solubility values plotted for the different P45 ternary glass compositions in distilled water (dH2O) and Hanks Buffered Saline Solution (HBSS) (Gibco BRL, Scotland).[17] Data obtained from the gradient of a linear fit to weight loss per unit area vs. time data.

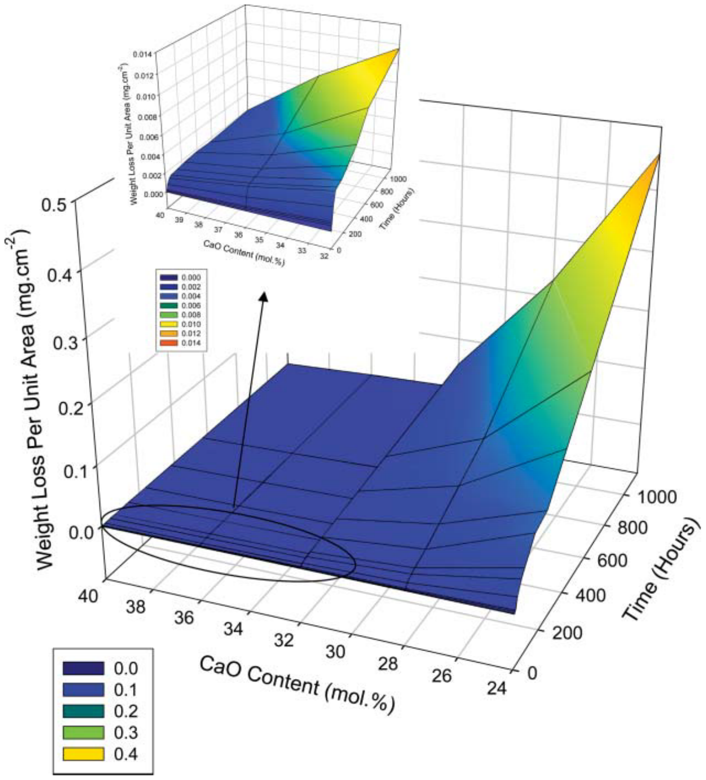

Figure 2.2: Weight loss per unit area as a function of composition and time in aqueous media.[9] Data taken from Franks *et al.*[17] for compositions $(P_2O_5)_{0.45}(CaO)_x(Na_2O)_{0.55-x}$ (x = 0.24, 0.28,..., 0.40).

have been studied by Uo *et al.*,[19] in order to assess biocompatibility. Human pulp cells were cultured in the α-minimum essential medium (α-MEM) and incubated for 24 h with the sample glass powders. Post-incubation, the pH of the medium was measured and the cytotoxicity estimated by the Alamar Blue assay. P50 compositions displayed relatively low toxicity, which increased with P_2O_5 content with a corresponding decrease in pH from ~7.5 for P50 to pH 1.4-5.6 (dependent on CaO/Na_2O ratio and hence dissolution rate) for P60 compositions. For P60/70/80 compositions, the cytotoxicity was considered to be primarily dependent on the change in pH. For the neutral P50 compositions, in which ion concentration in the media was still affected, cytotoxicity was low with the exception of the Ca-free P50N50 composition. The latter, despite having pH 7.2, displayed high cell toxicity due to "extremely fast" dissolution. The authors conclude that cytotoxicity decreases with increasing CaO content and decreasing P_2O_5 content,[1] which could be explained by the change in pH and ion strength in the medium.

Salih *et al.*[20] investigated the biological response of two human osteoblast cell lines MG63 and HOS(TE85) *in vitro*, in the presence of increasing concentrations of extracts of glasses P45C8N47, P45C16N39, P45C28N27 and P45C40N15. MTT assays demonstrated that cell proliferation was unaffected by the least soluble glasses (P45C28N27 and P45C40N15) but was markedly reduced for P45C8N47 and P45C16N39 compositions. ELISA assay results also showed the two, low CaO and highly soluble compositions, down-regulate the expression of bone sialoprotein, osteonectin and fibronectin proteins, which have a major role in bone metabolism and integrity. It was found that the highest CaO mol% and lowest solubility composition, P45C40N15, up-regulated all three antigens. The differential influence of ion species released from the glasses into the culture media and material-induced pH differences between the extracts are thought to be key factors. The high solubility of P45C8N47 and P45C16N39 results in increased pH, compared to P45C28N27 and P45C40N15, due to increased release of Na^+ and PO_4^{3-} species into solution. This increase in pH is likely detrimental to optimal osteoblast metabolism. The antigenic up-regulation for P45C40N15 is thought to be linked to Ca^{2+} release[2] which is, despite the composition's low solubility, the highest of all the glasses studied.[17]

It has been suggested that the use of MG63 and HOS(TE85) cell lines[20, 23] to model osteoblast proliferative behaviour is inappropriate.[24] Skelton *et al.*[25] investigated the effect of PBG on osteoblast and osteoblast-like proliferation, differentiation and death *in vitro*, using human bone marrow derived cells (hBMSCs) and human fetal osteoblast-like 1.19 cells (HFOBs). Exposure in culture to the compositions studied, $(P_2O_5)_{0.50}(CaO)_{0.50-x}(Na_2O)_x$ (x

---

[1] Under the caviat that this holds for the compositions studied.

[2] Divalent cations play key roles in cell activation mechanisms, thereby controlling many growth-associated processes and functional activities of cells.[21, 22]

= 0.02, 0.04,..., 0.10), inhibited cell adhesion and proliferation along with increasing cell death for both hBMSCs and HFOBs. The reductions in pH of the culture medium after 4 weeks in the presence of PBG extracts were linked to cell death. It was stated that this correlation does not indicate cause and it was postulated that the medium ion concentrations of sodium and phosphate are likely to have a deleterious effect. It was concluded that PBG effects could be mediated through several factors, such as PBG surface integrity during dissolution, the effect of PBG dissolution products on molecules associated with cell function or the effect of pH change on cell metabolism. Finally, it was noted that the composition P50C48N2 did support some osteogenic proliferation and early differentiation.

Navarro *et al.*[26] prepared glasses $(P_2O_5)_{0.445}(CaO)_{0.445}(Na_2O)_{0.110-x}(TiO_2)_x$ (x = 0.000 and 0.050) (Ti-doped PBG discussed in Section 2.2.3) to evaluate cellular response *in vitro*. It was found that the undoped composition did not elicit a toxic response from WST assay results but, a toxic response was found when the cells were cultured directly on the glass surface. It is stated that these results are in contrast to *in vivo* rabbit models,[27] which show good biocompatibility with osteoconductive properties for the same undoped composition. It is suggested that the *in vitro*/*in vivo* contradiction may result from *in vivo* local chemical changes being buffered by the physiological environment, in which the continuous circulation of body fluids helps to smooth local conditions. Moreover, cellular degradation mechanisms can modify the biological performance of a material *in vivo*.

2.2.2 Silver, Copper & Gallium - antimicrobial effects

The doping of ternary PBG with species that have known biocidal effects, such as silver (Ag^+) and copper (Cu^{2+}) ions, offers a potential alternative to current methods for the treatment of infection. The ions can be incorporated into the glass matrix, providing a controlled, site-specific delivery system predicated on the degradation characteristics of the bulk glass.

Silver ions are used to control urinary tract infections in long-term indwelling catheters. Gilchrist *et al.*[28] showed that using the silver-releasing device SilverLine^{TM}in conjunction with silver-doped PBG, a safe non-toxic, non-corrosive sustained release of silver ions was achievable within the catheter. This prevented bacterial proliferation and blocked organisms from tracking up the line from the collecting bag. The authors state that clinical experience from short-stay patients has demonstrated a “marked reduction in the infection rate of acute catheterized patients". Avent *et al.*[29] have fabricated cast tubes of silver-doped PBG and characterized the bulk structure using ^{31}P MAS NMR. Silver ion release rates in distilled water and simulated inorganic/organic urine were analysed along with identification of dissolution speciation. Their findings show that the concentration of silver from a dissolving silver-doped PBG exceeds the solubility product of compacted silver chloride, proving advantageous for use in catheter applications.

PBGs in the compositional range $(P_2O_5)_{0.50}(CaO)_{0.30}(Na_2O)_{0.20-x}(Ag)_x$ $(x = 0 - 0.15)$ are capable of a broad spectrum of bactericidal activity.[30] In disk diffusion assays, the compositions demonstrate microbistatic effects against organisms including *Staphylococcus aureus*, *Escherichia coli*, *Bacillus cereus*, *Pseudomonas aeruginosa*, methicillin-resistant *Staphylococcus aureus* and *Candida albicans*. The viability of *S. aureus* and *E. coli* is reduced by a $3 - 4$ order of magnitude compared to controls at 3 and 5 mol% Ag. The dissolution rates are noted to decrease with increasing Ag content and "low silver-containing PBG gave a more potent effect against the pathogens investigated, as compared to the higher silver containing PBG compositions".[30] It was noted that silver appeared to affect the respiratory chain in Gram-positve *S. aureus* and Gram-negative *E. coli*, with importance placed on the mechanisms of surface binding and damage to membrane function in the bactericidal effect.

Organisms such as *S. aureus* commonly form biofilms. These are sessile communities of cells attached to a substratum and embedded in a matrix of extracellular polymeric substances produced by the cells themselves. Diseases, such as endocarditus and osteomylitis, are caused by such biofilms whose bacteria often show decreased susceptibilities to antibiotics and the body's immune defence system. Valappil *et al.*[31] have studied the effect of silver content on the structure and antibacterial activity of silver-doped PBG noting it to be an effective bactericidal agent against *S. aureus* biofilms. The bactericidal effect was found to be dependent on the silver ion release rate, $0.42 - 1.22\ \mu g.mm^{-2}.h^{-1}$ for compositions $(P_2O_5)_{0.50}(CaO)_{0.30}(Na_2O)_{0.20-x}(Ag)_x$ $(x = 0.10, 0.15$ and $0.20)$. The highest release rate and bacterial activity was found for the 10 mol% Ag composition. It is noted that a significant reduction in the biofilm growth occurs in 24h, after which the silver ions released from the glass did not prevent the re-emergence of viable bacteria from the biofilms. It is postulated that the formation of a dead bacterial layer at the interface with the PBG, along with silver diffusion characteristics, may be key factors here. Finally, it is stated that although high concentrations of silver ions are of importance for bactericidal action against biofilms, it is key that cyto/biocompatibilty is not sacrificed as a result. The 10, 15 and 20 mol% Ag glasses released silver concentrations of 0.083, 0.055 and 0.064 ppm.h^{-1} respectively, well below the minimum cyclotoxic concentration of 1.6 ppm for human cells.

Another study by Mulligan and co-workers[32] reports the effects of copper-doped PBGs on biofilms of *Staphylococcus sanguis*, one of the predominant bacteria found in dental plaque. It was noted that the inclusion of copper leads to changes in the rate of solubility, hence the Ca^{2+}/Na^{+} ratio was adjusted such that the solubility was nominally the same (0.3062 ±0.07 mg.cm^{-2}.h^{-1}) *in vitro* for all the compositions studied. The viability of *S. sanguis* biofilms grown on hydroxyapatite, PBG and coppper-doped PBG discs (see Figure 2.3) in artificial saliva, was assessed at specific time intervals.

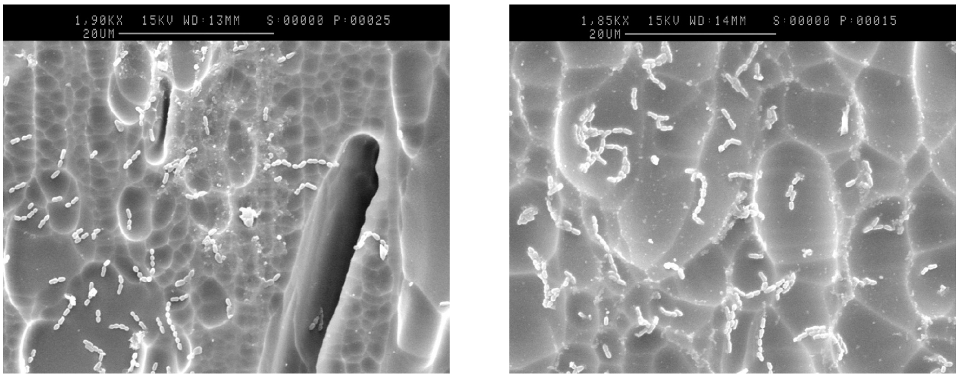

Figure 2.3: SEM images of *S. sanguis* on a P45C22N33 disc (left-hand panel) and P45C20N30Cu5 disc (right-hand panel) after 6 h. (From Mulligan *et al.*[32])

At 24h the biofilms grown on 5 and 10 mol% Cu PBGs displayed 0.8-0.9 and 1.0-1.3 log reductions in viability respectively. Viability of *S. sanguis* returned to levels similar to those of the controls after 24h, suggested to reflect the fact that dead cells form a barrier to the diffusion of antibacterial ions.

In order to circumvent the toxic effects of antibiotics/antiseptics and the development of resistant bacterial strains, the incorporation of doped PBG in wound dressings is proposed as an alternative. Sheridan *et al.*[33] have studied the potential toxic effects of silver- and copper-doped PBGs, along with two conventional antiseptic agents, on mammalian cells *in vitro*, in order to assess their viability for this application. A standard MTT assay was used to evaluate the cytotoxicity or activity of cultured mouse fibroblasts.

Infecting bacteria require iron for growth and the functioning of key enzymes, such as those involved in DNA synthesis, electron transport and oxidative stress defences. The gallium ion Ga^{3+} has an ionic radius nearly identical to that of Fe^{3+} and can function as a “Trojan horse” since many biological systems are unable to distinguish these two ions. The sequential oxidation and reduction of Fe^{3+} is critical for many of its biological functions, however Ga^{3+} cannot be reduced under the same conditions which is a key factor in its antibacterial effectiveness. $(P_2O_5)_{0.45}(CaO)_{0.16}(Na_2O)_{0.39-x}(Ga_2O_3)_x$ (x = 0.00, 0.01, 0.03 and 0.05) have been synthesized by Valappil *et al.*[34] using the conventional melt quenching technique. Antibacterial effects were observed, in disk diffusion assays, against *Pseudomonas aeruginosa*, *Staphylococcus aureus* and *Escherichia coli*, along with a small effect against methicillin-resistant *Staphylococcus aureus* and *Clostridium difficile.* It was found that 1 mol% Ga_2O_3 was sufficient to mount a potent antibacterial effect against the test organisms and, since dissolution and subsequent ion release rates were found to decrease with increased Ga_2O_3 content, excellent long-term release of Ga^{3+} ions into the medium was obtained. ^{31}P MAS NMR data revealed the glass networks to be comprised of 72 - 75 % Q^2 and 25 - 28 % Q^1,[3] with no significant compositional-dependent trends. Thermal analysis showed that the glass transition temperature (T_g) increased from 614.84 K in P45C16N39 to 643.14 K in P45C16N34G5, in line with the fact that Ga_2O_3 is known to be a refractory material. ^{71}Ga NMR measurements showed gallium ions to occupy an octahedral coordination, whilst FTIR spectroscopy provided evidence for the presence of a small proportion of tetrahedral gallium. Pickup *et al.*[35] confirmed the presence of GaO_6 octahedra by x-ray methods for the same compositions. The authors state that the strengthening of the network under substitution of Na_2O by Ga_2O_3, is due, in part, to the presence of these octahedra inhibiting the migration of Na^+ ions. The effect of substituting Na_2O for CaO on structure, properties and antibacterial activity, has been studied for compositions containing a fixed 3 mol% Ga_2O_3.[36] It was shown that increasing the CaO content for compositions containing 14, 15 and 16 mol% CaO, caused a decrease in degradation rate from 17.6 to 13.4 to 7.3 $\mu g.mm^{-2}.h^{-1}$ respectively. Ga^{3+} release rate and antimicrobial activity against *Pseudomonas aeruginosa* were also reduced with increasing CaO content. The composition P45C14N38G3 was further analysed for its biocidal effect on *Pseudomonas aeruginosa* biofilms and found to have maximum effect after 48 h. Due to the antibacterial mechanism, it is proposed that high-

---

[3] Q^n terminology, where n is the number of oxygens bound to a phosphorus atom, that in turn bond to another phosphorus atom.

level Ga^{3+} resistance is unlikely to develop in subjected bacteria and due to reduced levels of Fe^{3+} in human tissues, enhanced effects are likely under physiological conditions. In conjunction with the fact that Ga^{3+} is approved by the US FDA for intravenous administration, it is stated that gallium-doped PBGs are a potentially highly promising new therapeutic agent against *Pseudomonas aeruginosa.* Granular forms could be used for the prevention of bacterial infections in bone and could, for example, be used as coating on fracture fixation pins, either subcutaneuosly or transcutaneously.

2.2.3 Titanium - hard tissue engineering

Doping the ternary PBG system with TiO_2 leads to increased chemical durability and mechanical strength,[37–39] lending such materials to hard tissue engineering applications. Moreover TiO_2 is known to induce calcium phosphate surface nucleation in CaO-P_2O_5 based systems.[40] Navarro *et al.*[26] studied the effects of solubility and *in vitro* cell response of human skin fibroblasts by means of toxicity (WST assay), adhesion and proliferation tests. Their results showed that the substitution of 5 mol% CaO for TiO_2 led to a reduction in dissolution rates by a factor of 10 (weight loss after 100 days in SBF decreased from 3 % to 0.25 % upon Ti-doping). Based on the cells that were cultured directly on the surfaces of each glass composition, it was shown that cellular response was improved for the TiO_2-containing composition. This was attributed to the reduction in solubility and more a controlled release of ions into solution, which was postulated may lead to a more stable local pH.

Navarro and co-workers have studied the physiochemical, morphologic and structural evolution of Ti-PBG, containing up to 8 mol% TiO_2, in SBF at 310 K.[38] It was found that the glass dissolution rate decreased from 3.10×10^{-6} g.cm^{-2}.h^{-1} $\pm7.02 \times 10^{-7}$, for undoped PBG, to 3.25×10^{-7} g.cm^{-2}.h^{-1} $\pm8.63 \times 10^{-8}$ for 8 mol% % TiO_2 PBG in SBF. Glass surface degradation was analysed using environmental scanning electron microscopy (ESEM), revealing important differences between the 0, 3, 5 and 8 mol% TiO_2 compositions. After 4 weeks of dissolution, the undoped composition showed numerous pits and the formation of a possible hydrated layer partially separated from the surface, whereas the 3, 5 and 8 mol% TiO_2 compositions were scarcely degraded. However, an incipient exfoliation process was noted on the surface of the 3 mol% TiO_2 composition. After 7 weeks in SBF, a more marked degradation of the materials was noted. A disruption of the theorized hydrated surface layer and etch pits were observed for 3 and 5 mol% TiO_2 compositions, whereas the 8 mol% glass surface only presented the formation of deeper polish lines and numerous furrows. At the end of the 16 week test, all compositions studied displayed the formation of numerous holes and grooves created by the decomposition of the surface layer. Their results conclusively demonstrated that the inclusion of TiO_2 enhanced the chemical durability of the glasses.

Neel and Knowles[41] have synthesised PBG $(P_2O_5)_{0.50}(CaO)_{0.30}(Na_2O)_{0.20-x}(TiO_2)_x$ (x = 0.00, 0.01, 0.03 and 0.05). *In vitro* cyto-biocompatibility was assessed through MG63 human osteosarcoma cell attachment and viability, using scanning electron microscopy and confocal microscopy, respectively. There was an observed relative reduction in cell attachment for x = 0.01, compared to the compositions x = 0.03 and 0.05. This was linked to the relatively higher degradation rate with a rapid reduction in the surrounding pH to acidic level. It is concluded that PBGs incorporating 3 mol% and 5 mol% TiO_2 could be a successful substrate for bone tissue engineering applications.

2.2.4 Strontium - hard tissue regeneration and cancer therapy

Strontium is routinely administered as a treatment for osteoporosis in the form of strontium ranelate and is indicated for use in post-menopausal women. It has been shown that strontium strengthens bone, increases bone mass/density and lessens the possibility of vertebral and hip fracture in elderly women. This has been attributed to the fact that the human body absorbs strontium as if it were calcium and the higher atomic weight of Sr^{2+}, compared to Ca^{2+}, accounts for the increase in bone density. The radioactive isotopes ^{89}Sr and ^{85}Sr are used to treat scattered painful bone metastases that affect two thirds of patients with advanced and metastatic cancers.[42] Despite studies on amorphous ternary systems, such as SrO-H_2O-P_2O_5[43] and Na_2O-SrO-P_2O_5,[44] there exists only one study for P_2O_5-CaO-Na_2O-SrO systems.[45] Abou Neel *et al.*[45] synthesized d-PBG in the systems $(P_2O_5)_{0.50}(CaO)_{0.30}(Na_2O)_{0.20-x}(SrO)_x$ (x = 0.00, 0.01, 0.03 and 0.05) to evaluate the materials for potential use in bone tissue regeneration. Characterisation via ^{31}P MAS NMR revealed that, as the Sr^{2+} content is increased, there is a slight disproportionation of Q^2 phosphorus environments into Q^1 and Q^3. It was also noted that density, T_g and degradation rate all rise with increasing SrO mol%. Cell viability was assessed using HOS, to obtain a preliminary estimate of biological compatibility, with live-dead staining and confocal laser scanning microscopy. It was found that incorporation of

Sr^{2+} produced glasses with better cellular response than Sr^{2+} -free glasses, but relatively lower response than the positive control. It is suggested that this feature may be due to the degradation nature of the glasses and not due to the presence of strontium, since the P50C30N20 composition had lower degradation but the worst cellular response. It is stated that further compositional tailoring is required to improve biocompatibility.

2.2.5 Aluminium - hard tissue engineering

Along with silica, alumina (Al_2O_3) is the most widely utilized ceramic for dental and bone implants. High mechanical strength and chemical stability are advantageous for high load-bearing applications, such as partial and total hip replacement surgery. PBG in the systems $(P_2O_5)_{0.445}(CaO)_{0.445}(Na_2O)_{0.110-x}(Al_2O_3)_x$ (x = 0.000, 0.030, 0.050 and 0.080) have been developed and assessed for biomedical applications.[46] The physicochemical and structural evolution was analyzed during *in vitro* degradation in SBF (simulated body fluid) and it was found that weight loss in SBF was greatly reduced upon Al_2O_3 inclusion. The undoped PBG displayed the greatest changes in pH, with an initial rise to pH 7.3 after 100 h in SBF, due to increased release of Na^+ ions into solution. The increased SBF pH leads to a more rapid glass degradation and the release of HPO_4^{2-} and PO_4^{3-}, with an accompanying decrease in pH to pH 6.9 after 500 h. Higher concentrations of Al_2O_3 show flatter pH profiles. Ionic concentration results support this analysis confirming that the addition of Al_2O_3 reduces aqueous attack and stabilises the network from chemical attack. The formation of surface apatite layers on PBG is a key aspect for hard tissue engineering and a reliable metric of a composition's bioactivity. To investigate the formation of surface calcium phosphate, a fourier transform infrared (FTIR) spectrum of the surface was taken after 30 days of immersion in SBF. Compositions x = 0.000 and x = 0.030 both display the presence of surface calcium phosphate with crystallization apparent for the undoped composition. For $Al_2O_3 \geq 5$ mol% surface calcium orthophosphate was not detected within the first 30 days due to decreased solubility.

Smith *et al.* have further studied the atomic-scale structure of the afore mentioned compositions using neutron diffraction and solid state ^{27}Al MAS NMR.[47] They found that density is dependent upon composition, with an initial increase in density with increasing Al_2O_3 content but beyond 3 mol% Al_2O_3, a decrease. The NMR data revealed that aluminium is present in 4, 5 and 6-fold coordination. The authors have postulated that the density changes may be explained in terms of an increase in the relative concentration of 4-coordinated aluminium at the expense of 6-fold aluminium, as the Al_2O_3 content is increased beyond 3 mol%. Using coordination numbers obtained from the simulation of neutron diffraction data, it is concluded that phosphorus is present as both -PO_2- link groups and -PO_3 chain-terminating end groups. The proportion of -PO_3 increases with Al_2O_3 content, indicative of a more fragmented network. It is inferred that since P-O-P bonds are readily hydrolysed in water, a more condensed network dissolves at an increased rate[4] and the increased fragmentation upon increased doping results in reduced dissolution rates and concomitant lower bioactivity. Moreover, the substitution of Na^+ for the higher field strength Al^{3+} ion, is cited as a further mechanism to explain the dissolution rate trends.

2.2.6 Cobalt, Copper, Selenium & Zinc - veterinary applications

Trace element deficiencies are common in many countries and affect animal health, productivity and welfare. PBG doped with a range of trace elements, such as cobalt,[48] copper, selenium and zinc (e.g. Tracerglass, Cosecure® and Zincosel®), can be used as an intra-ruminal soluble bolus. This method has significant advantages over others, such as injections, supplementation of the water, incorporation into compound feeds and free-access feed blocks, in extensive grazing situations (recently reviewed by Grace and Knowles[49]).

Rumen-boluses, based on the systems P_2O_5-CaO-Na_2O-MgO-CuO, have been developed and administered to sheep,[50] confirming that, for CuO 10 mol% compositions, boluses placed in the rumen release the trace element into the intestinal tract. Furthermore, significant increases in plasma caeruloplasmin activity, erythrocyte superoxide dismutase and blood packed cell volume are noted, indicating increased copper absorption.

Telfer *et al.*[51] carried out a trial in cattle that were put out to graze on a pasture known to produce both copper and selenium deficiency in the animals. Two groups of cows were selected and one group given two pellets of Tracerglass-C (administered via the balling-gun method to the recticulorumen), while the other group were left as untreated controls. Blood samples were taken at the time of administration (Day 0) and subsequently at days 69, 152, 188 and 288. These were analysed for plasma copper, caeruloplasmin and glutathione peroxidase.

---

[4] In contrast to much literature stating that higher network connectivity leads to a decrease in dissolution rate.

Their results showed that Tracerglass-C treatment prevented the occurence of copper and selenium deficiencies. A second trial, conducted on Swaledale ewes over 345 days concluded that, Tracerglass-S cured a copper deficiency at Day 0 and prevented the later occurence of a cobalt deficiency and marginal selenium deficiency (Days 287 and 345). The study illustrated that, for a single treatment (reducing the handling of the animals), the bolus is effective for up to a year's duration and is not toxic to the animal.

Givens *et al.*[52] investigated the use of copper-containing PBG bolus to provide a supplement of copper for suckled calves. Their findings showed that the copper contained in the soluble glass boluses appeared to prevent hypocupraemia in calves as effectively as regular copper injections. Kendall *et al.*[53] studied the effects of Cosecure® (a PBG doped with 0.5 wt% cobalt, 0.15 wt% selenium and 13.2 wt% copper) and Zincosel® (a PBG doped with 15.2 wt% zinc, 0.5 wt% cobalt and 0.15 wt% selenium) on the trace element status of extensively grazed sheep over winter. Two trials were conducted, the first making comparison between two groups of 300, 8-month-old ewe lambs, one of which was administered Zincosel® and the other untreated as a control. The second trial used three groups of 105 8-month-old ewe lambs, which were administered Zincosel® and Cosecure® respectively, with the third acting as the control. In order to test for the status of each trace element, blood was taken prior to bolus administration and again after 4 months. Zincosel® was shown to consistently increase the status of all three trace elements, zinc, cobalt and selenium, over at least 100 days. The increases in cobalt and selenium status were similar to those achieved using Cosecure®, which also increased the copper status of the sheep. Further assessments of Cosecure® on blood mineral status have been undertaken by Hayashida and co-workers,[54] proving the bolus to be beneficial for does fed under backyard farming conditions.

Recent work by Kendall *et al.*[55] has studied the trace element and humoral immune response of lambs post-bolus administration. A prototype Zincosel® derivative bolus, containing 15.1 wt% zinc, 0.52 wt% cobalt and 0.15 wt% selenium, was used in the study. Trace element status was analysed on days 0, 20, 42 and 63 post administration with test subjects that had received bolus displaying higher plasma zinc concentrations than that of the controls on days 42 ($p < 0.05$) and 63 ($p < 0.01$). Immunisation with keyhole limpet haemacyanin (KLH) antigen on day 34 was followed by an assessment of IgG response by direct ELISA on days 20, 42, 49 and 63. The humoral response was enhanced, with the bolused lambs having significantly greater anti-KLH IgG levels on day 42 ($p < 0.05$) and day 63 ($p < 0.01$). The authors conclude that administration of bolus resulted in an increased antibody response and fulfilled the daily requirements for cobalt, selenium and zinc, with an elevated status of these elements compared to unsupplemented controls grazing the same pasture.

2.3 Melt-quenched glass fibres

Phosphate-based glass fibres (PGF) have potential applications in the engineering of soft tissues, such as muscles and ligament due to the afore mentioned biocompatibility and specifically, a morphology that can mimic the fibrous nature of these tissue types. Cell transplantation, using muscle precursor cells, has been suggested for a number of myopathies (muscle diseases) such as Duchenne muscular dystrophy.[56] However the failure of clinical trials based on myoblast (muscle cell) transplantation therapy was due to rapid and massive death of donor myoblasts soon after myoblast injection.[57, 58] PGF have the potential to be used as cell delivery vehicles,[59] attaching and growing muscle precursor cells *ex vivo*, which could then be implanted.

Synthesis typically involves the fibres being drawn onto a rotating collecting drum from a re-molten glass. The diameter of the fibre is dependent upon the drum speed, with a higher speed corresponding to a smaller diameter.[60] PGF diameter is of critical importance for cell orientation,[61] with the latter taking place along the axis of a fibre (see Figure 2.4) as opposed to around its circumference for fibre diameters (fd) $\sim$ size of cell body (cb). For fd $<$ cb cells tend to wrap around the fibre and for fd $>$ cb cells can orientate either parallel or perpendicular to the long axis of the fibre. In light of this sensitivity, it has been proposed that PGF can act as a contact guide for nerve regeneration, since neuronal cells may be guided from either end of an injured nerve.

2.3.1 Aluminium & Zinc - soft tissue engineering

Much work relating to PGF has centred on the synthesis and *in vitro* evaluation of three-dimensional scaffolds/composites that offer an alternative for current surgical procedures. An exemplar case is the surgical replacement of craniofacial muscle via the transfer of local or free flaps. Donor site morbidity and tissue rejection are common problems in such proced-

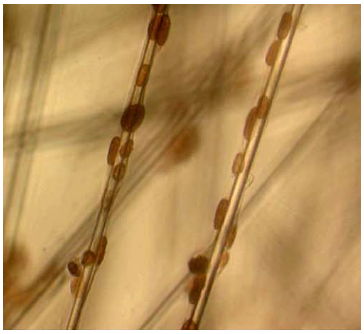

Figure 2.4: Muscle cells preferentially aligning along the axis of iron-PGF, leading to the formation of multinucleate mytotubes (developing skeletal muscle fibres).[59]

ures and a proposed alternative is to engineer autologous skeletal muscle *in vitro*, which can then be re-implanted into the patient. Shah *et al.*[62] assessed three differing configurations of glass fibres scaffolds distinguished by the spatial distribution and orientation of $(P_2O_5)_{0.629}(Al_2O_3)_{0.219}(ZnO)_{0.152}$ PGF in collagen I (found in abundance in the interstitial extracellular matrix of skeletal muscle) and collagen IV/laminin substrates. The configurations are termed “bundle” (parallel orientation), “spread” (low density with no overlap or preferred orientation) and “mesh” (high density overlapping fibres with no preferred orientation). The scaffolds supported the growth and differentiation of human masseter muscle-derived cell cultures. Furthermore, it was shown that a three-dimensional “mesh” arrangement of PGF was best suited to stimulate cell attachment and proliferation. The formation of prototypic muscle fibres was enhanced using high density seeded cells with Matrigel and insulin-like growth factor. The authors conclude PGF scaffolds can support the *in vitro* engineering of human craniofacial muscle.

2.3.2 Iron & Magnesium - hard tissue engineering, cell delivery vehicles & neural repair

Ahmed *et al.*[60] have fabricated PGF from P50 and P55 compositions. Fibre diameters in the range 8μm - 40μm were produced with similar composition-dependent solubility trends to bulk glasses.[18] For smaller diameters, increased solubility was noted and linked to a higher surface area to volume ratio. For P45 compositions, a low melt viscosity and high fluidity lead to an inability to draw fibres, linked to lower network connectivity and phosphate chain lengths. Of the undoped compositions studied,[60] those that can be drawn into fibres (i.e. P50 and P55) have poor biocompatibility since they are too soluble for cell attachment and proliferation. Ahmed *et al.*[59] have subsequently doped the PGF with a quaternary component, Fe_2O_3, between 1 - 5 mol%. A decrease in solubility was noted for increasing CaO and Fe_2O_3 mol%. Biocompatibility was assessed using a conditionally immortal muscle precursor cell line derived from the H-2Kb-tsA58 immortomouse. Compositions containing 4 - 5 mol% were found to support cell attachment and differentiation (attributed to enhanced chemical durability).

Quaternary glasses in the compositional range $(P_2O_5)_{0.50}(CaO)_{0.46}(Na_2O)_{0.04-x}(Fe_2O_3)_x$ (x = 0.00, 0.01, 0.02 and 0.03) have been evaluated *in vitro*, as three-dimensional scaffolds for tissue engineering of the bone-ligament interface.[63] Assessment of degradation rates in tissue culture growth medium show that the iron-PGF, of mean diameter 30 μm, display a composition dependent behaviour, with slower degradation for increased Fe_2O_3 mol% (see Figure 2.5). Figure 2.6 shows human craniofacial osteoblast (HOB) proliferation patterns on differing fibres after 1, 7 and 14 days in culture. It shows that for compositions x = 0.00 and x = 0.01, survival of cells beyond 7 days in culture was not sustained, whereas substantial growth took place on the least soluble fibres (x = 0.03). The study also investigated the potential for attaching a secondary cell type, human oral fibroblasts (HOF) and maintaining the phenotype specific to each cell. It was found that the scaffolds accommodated the separate seeding of both cell populations in co-culture and could potentially lead to the *in vitro* simulation of the anatomical structure of a bone-ligament tissue interface.

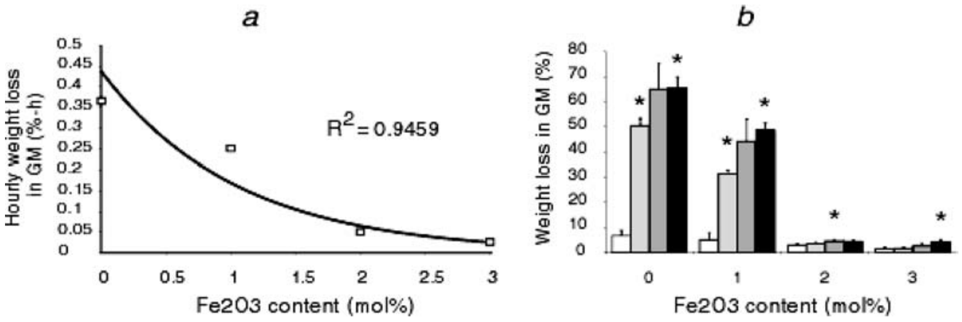

Figure 2.5: (a) Hourly weight loss in tissue culture growth medium (GM) vs. PGF Fe_2O_3 mol%. (b) Weight loss values at days 1 (white bars), 4 (light grey bars), 7 (dark grey bars) and 10 (black bars) in GM. Error bars ± s.d..[63]

The segregation of differing cell types in co-cultures in order to regenerate interface structures, such as the hard-soft tissue enthesis, has been a proposed application for multilayered PGF collagen scaffolds.[64] A common problem with tissue engineering scaffolds is the main-

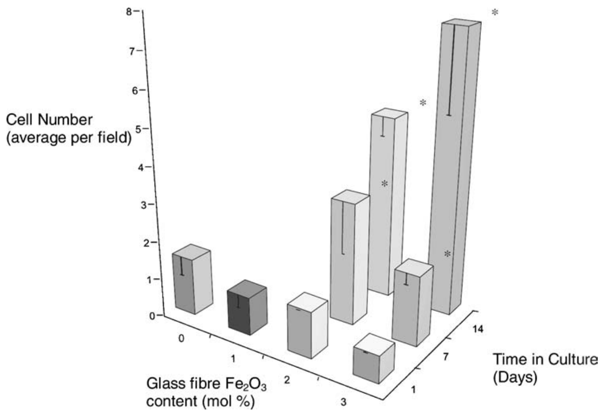

Figure 2.6: Craniofacial osteoblast (HOB) proliferation patterns on PGF of 0, 1, 2 and 3 mol% Fe_2O_3 after 1, 7 and 14 days in culture. Error bars ± s.d..[63]

tenance of seeded cell viability and function due to limitations of oxygen and nutrient transfer. The incorporation of microchanneling, using unidirectionally aligned PGF in dense collagen scaffolds, has been morphologically and mechanically characterized.[64] PGF of 30 - 40 μm diameter were prepared and pre-aligned before being placed on a glass slide forming the base of the mould. Collagen setting and compaction was applied using a combination of compression and capillary action to form sheets. The compressed sheets (50 μm thick) were then rolled along their short axis (parallel to the long axis of the PGF) to give a spirally assembled scaffold as shown in Figure 2.7.[5] There was a significant increase in strength and modulus with the incorporation of P50C30N17F3 PGF and a significantly lower elongation to break, when compared to control collagen-only scaffolds. Cell viability analysis was carried out using human oral fibroblasts (HOF). It was found that cell viability increased to ∼100% for compacted collagen sheets, with and without PGF, compared to the non-compressed collagen

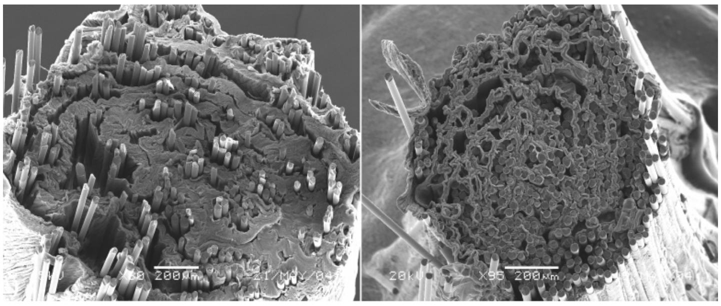

Figure 2.7: Morphological characterizations of PGF-collagen scaffolds. (a) SEM of cross-sectional PGF-collagen spiral constructs with PGF generated at 25 Hz SMF and (b) with PGF generated at 12.5 Hz SMF with increased PGF density.[64]

---

[5] Drum speed and stepper motor frequency (SMF) control fibre diameter, fibre to fibre spacing and PGF number in the scaffold.

control at ~86%. Viability reduced to ~80% for the spiral constructs and cell mortality was localised near PGF, due to high stiffness and compressive/shear forces during the production of the scaffolds. Perfusion limitations were cited as a possible contributing factor and it was suggested that the degradation of PGF may help overcome this by providing channelling for oxygen, nutrients and waste products. Figure 2.8 shows channel formation via the degradation of P50C25N25 PGF to form microchannels. Ultrasound imaging, through the movement of coated microbubble agents, was used to characterize the channelling, confirming its continuous nature diameter and size to be 30-40μm. The authors state that such channel sizes are ideally suited for mammalian tissue models and could play an important role in improving hypoxia/perfusion limitations, along with transportation of cells, nutrients and potentially blood vessels through dense implants.

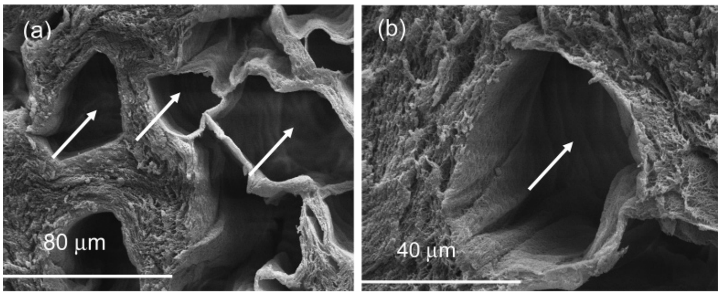

Figure 2.8: Channel formation via the degradation of PGF in PGF-collagen spirals. (a) SEM image of a cross-section through the collagen scaffold, leaving a cluster of channels post-PGF degradation. (b) SEM image of a channel close-up.[64]

The generation of channels in dense collagen constructs has been further investigated by Alekseeva *et al.*,[65] with the aim to control the rate and direction of tissue ingrowth, in order to regulate vascularization and innervations of the implant by the host. Their study used P50C25N25 PGF, vertically fixed onto a carrier ring and immersed in phosphate buffered saline, to undergo partial dissolution. The level of the buffer was decreased stepwise over 6 h creating a conically shaped, tapering fibre cross-section. Of the fibres synthesised, a specimen was 19.5 mm in length, ranging from 36 μm to 25.8 μm diameter across its length. These tapered PGF were then incorporated into collagen constructs. It is proposed that such conical forms will produce a time-dependent channel opening *in vivo*, which is of particular importance for vascular and nerve tissue engineering, as well as the maintenance and survival of thicker implants. Furthermore, bridging the glial scar around spinal cord injuries is a major clinical problem which could be solved by time- and direction-controlled channel formation, as proposed with PGF constructs such as these.

The preferential mechanical properties of Fe/Mg-doped compositions have sparked interest in quinternary PGF as candidate for high-modulus degradable substitutes for metals, in biomedical applications. Polylactide matrices reinforced with P40M24C16N16F4 PGF have been fabricated to achieve flexural properties in the range 30 GPa modulus and 350 MPa strength.[66] Using these PGF compositions, novel bioresorbable screws have been developed[67] for potential use in the fixation of bone fractures resulting from trauma. Maximum flexural and push-out properties for composite screws, based on PGF-reinforced polylactic acid (PLA), increased by ∼100% compared to PLA screws. Maximum shear load and stiffness also increased by ∼30% and ∼40% respectively, for composite screws in comparison to PLA. These early studies are encouraging and it is stated that further investigations are required to assess the degradation and mechanical retention properties *in vitro* and *in vivo*.

The effectiveness of P50C40N5F5 PGF as spatial cues for axonal growth, following nerve injury, has been assessed *in vivo*.[68] Cylindrical PGF-collagen scaffolds were developed and implanted into the gap between the proximal and distal stumps, following complete transection of rat spinal cords at T9. Figure 2.9B shows the PGF distributed on a collagen sheet, which was tightly rolled to form a scaffold of 1.8 mm diameter. Post-drying, the scaffold was then cut into 3 mm lengths ready for implantation (Figure 2.9C). The parallel alignment PGF was intended to provide physical guidance cues to regenerating axons. Implantation was carried out for control (PGF-free collagen scaffolds) and experimental (PGF-collagen scaffolds) groups as illustrated in Figures 2.9D-H.

Post-implantation, axonal outgrowth and concomitant restoration of locomotor and bladder functions were investigated. The Basso, Beattie and Bresnahan (BBB) open-field locomotor scale was used to evaluate behavioural recovery of hindlimb locomotion, once per week from 1 week after implantation until sacrifice at 12 weeks. The BBB scale is graded from 0 (“no observable hindlimb movement”) to 21 (“normal hindlimb movement”). BBB scores for the control and experimental groups increased at the same rate for the first 6 weeks post-injury, from ∼0 (week 1) to ∼3.5 (week 6). From week 6 onwards, BBB scores continued to rise for the experimental group to $\mathrm{BBB}^{\mathrm{12weeks}}_{\mathrm{expt.}} = 6.2 \pm 1.6$. The control group scores continued to rise but at a slower rate after six weeks with $\mathrm{BBB}^{\mathrm{12weeks}}_{\mathrm{control}} = 4.4 \pm 1.0$. No statistical differences in bladder control tests (urinary frequency and bladder pressure) were noted between the control

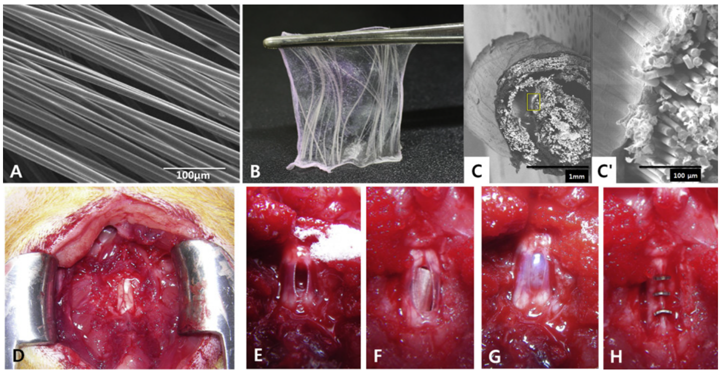

Figure 2.9: (A) Fabrication of PGF. (B) PGF-collagen gel complex after dehydration. (C) Three-dimensional PGF-collagen scaffold (C′ magnified image of the yellow box in C). (D-H) Procedure for implantation of three-dimensional scaffolds into completely transected rat spinal cords. (D) Exposure of dura mater at T8-9 of adult rat spinal cord. (E) Complete transection and gap formation. (F) Implantation of PGF-collagen scaffold in the experimental group. (G) Implantation of collagen scaffold in the control group. (H) Closure of the dura mater with microstaples.[68]

and experimental groups. It was noted however, that one of the five subjects receiving PGF-collagen scaffold returned to normal bladder function, implying the reconnection of autonomic pathways between the proximal and distal stumps.

Analysis of inflammatory cell infiltration is one indicator of biocompatibility. Figure 2.10A-D shows ED-1 positive cells (associated with inflammatory response) gathered at the borders of the scaffold and the proximal and distal stumps in both groups at 1 and 4 weeks post-implantation. As can be seen from Figure 2.10E, the numbers of ED1-positive cells did not differ between the control and experimental groups 1 (acute-stage) and 4 (subacute-stage) weeks after implantation; nor did they differ between these periods within each group. Astrocyte glial cells, stained red (GFAP), also gathered at the borders of the scaffold and spine stumps, but rarely migrated into the tranplants in both groups. These results show there to be no significant adverse inflammatory response of experimental groups when compared to the control.

Immunohistochemistry results showed that, for the experimental group, some axons in the proximal and distal stumps were extended into the scaffold at 12 weeks. Further to this, axons that grew along PGF were noted in the transverse section of the PGF-collagen scaffold after 4 weeks. Neither of these features were noted in the control group. The authors conclude that PGF may have a beneficial effect on functional recovery following complete transection of the thoracic spinal cord in rats.

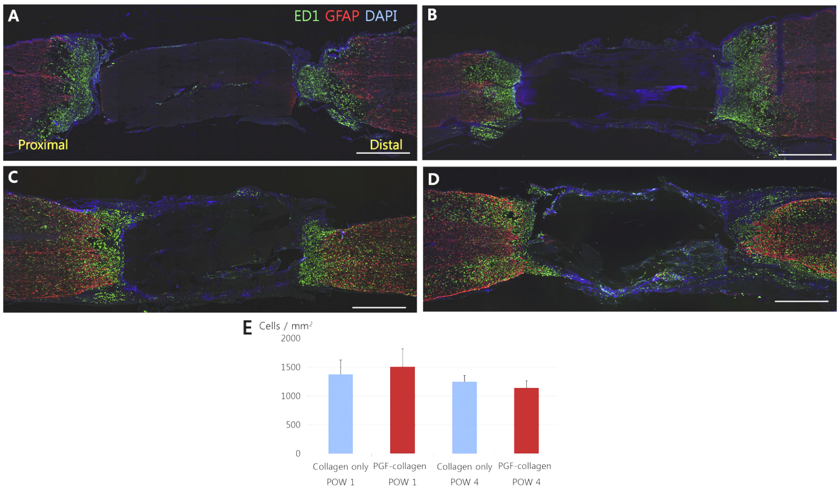

Figure 2.10: Distribution of macrophages in sagittal sections of injured spinal cords (A,B) 1 week and (C,D) 4 weeks after implantation of collagen scaffolds (A,C) and PGF-collagen scaffolds (B,D). (E) Numbers of ED1-positive (cellular marker for activated macrophages) cells at each assessment period in control and experimental groups. Scale bar = 1 mm. Glial fibrillary acidic protein (GFAP) and DAPI nuclear and chromosome counterstain (emits blue fluorescence upon binding to AT regions of DNA).

2.3.3 Synergistic (Silicon, Magnesium, Potassium & Titanium) - neural repair

$(P_2O_5)_{0.500}(CaO)_{0.300}(Na_2O)_{0.090}(SiO_2)_{0.030}(MgO)_{0.030}(K_2O)_{0.050-x}(TiO_2)_x$ (x = 0.000, 0.025 and 0.050) PGF have been synthesised/characterised[69] and subsequently studied for their potential application in the treatment of peripheral nerve injuries.[70] The authors found glass composition, initial PGF diameter and thermal treatment, to be the main factors influencing dissolution kinetics. Structural and compositional integrity was maintained during dissolution and cited as being key to biomedical suitably. It was shown that increased TiO_2 content leads to a decrease in solubility and PGF of smaller diameters experience increased weight loss percentage per unit time, due to a different specific surface area. Biological tests were carried out on aligned P50C30N9S3M3K2.5T2.5 PGF, using Neonatal Olfactory Bulb Ensheathing Cell Line (NOBEC) and Dorsal Root Ganglia (DRG) neurons. Figure 2.11 shows the different maturing processes that were observed for NOBEC cells incubated in the presence of PGF. NOBEC showed active proliferation and mitosis as shown in Figures 2.11a and b. Cell adhesion is one of the necessary conditions for cell migration across surfaces via adhesion, followed by contraction and movement, as a result of contractile forces. The migration of glial cells is fundamental in the nerve regeneration process. The NOBEC cells, in this study, adhered to the PGF surface, presenting cytoplasmatic processes extending toward the fibre surface (Figure 2.11c). Most of the S100-positive cells in contact with the PGF presented elongated shape and were well spread on the surface, enveloping the PGF (Figure 2.11d). The authors note that no PGF diameter dependence was observed for any of the afore mentioned cellular properties (PGF diameters used for biological tests were 25, 40 and 78 μm).

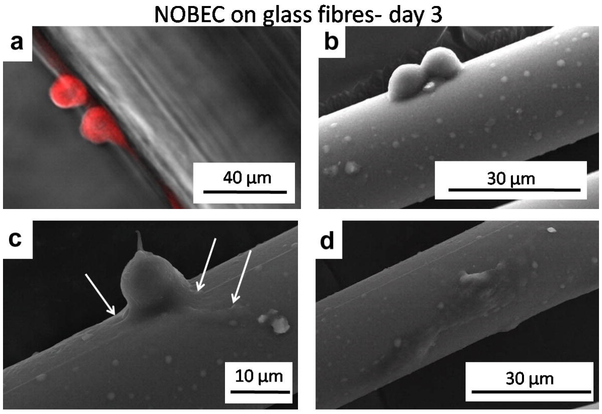

Figure 2.11: NOBEC cells after 3 days incubation in the presence of P50C30N9S3M3K2.5T2.5 PGF. NOBEC cells showing active proliferation and mitosis (a) on 78 μm diameter PGF (confocal microscope image) (for immunofluorescence reaction, primary antibody S100 and CY3 secondary antibody were used) and (b) on 25 μm diameter PGF (SEM image); (c) NOBEC cell adhering to the surface of 25 μm diameter PGF with cytoplasmatic processes extending from the cells to the fibre surfaces (indicated by arrows); (d) adhered NOBEC cell spread on the surface of 25 μm diameter PGF.[70]

Normal neuronal maturation of DRG neurons initiates with postmiotic neurons extending and retracting multiple short neuritic processes, which are comparable in length and growth rate in all directions. In neurons that elaborate an axon, one neurite outgrows the others. This first long B-tubulin-positive neurite continues to grow without tapering and becomes the single axon. The neuronal shape subsequently changes form multipolar to bipolar. These development stages were clearly noted on glass coverslips (used as a control in this study) between 0-3 days in culture. Cell attachment and neuronal integration (morphologically noted by slight cell elongation from an initial round shape as neurons extend out) was clearly identified on P50C30N9S3M3K2.5T2.5 glass slices (used as a secondary control), However, it was not possible to distinguish neurites due to furrows in the surface arising from the glass polishing process. All the neurons showed a biploar shape and presented one or two long growing B-tubulin-positive axons as shown in Figure 2.12. The long neurites observed for the neurons on the PGF were comparatively longer than those identified on the control glass coverslips. Thus, the presence of the fibres seemed to cause the polarization of neurons leading to one neurite, generally the longest, becoming the axon.

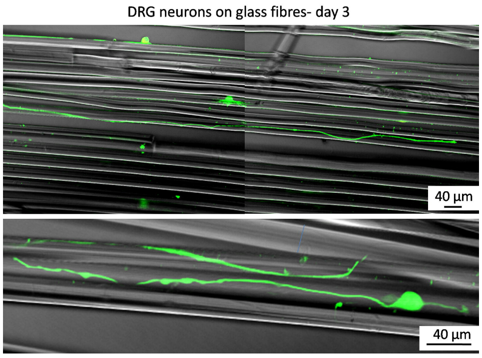

Figure 2.12: DRG neurons after 3 days incubation on 25 μm diameter P50C30N9S3M3K2.5T2.5 PGF, presenting long neurites extended along the fibre axis direction. For immunofluorescence reaction, primary beta-tubulin and ALEXA 488 a-mouse secondary antibody were used.

The ability of PGF to promote polarization and impart directionality suggests that they may be candidate materials for the directed growth of neurites, for the regeneration of peripheral and central nervous system tissue.

2.4 Sol-gel

The sol-gel process is a low temperature wet-chemical technique for the fabrication of oxide materials. It has several advantages over the high temperature melt-quench technique for the fabrication of phosphate glasses, namely, it does not lead to the high loss of volatile phosphorus during synthesis, as occurs with melt-quench. Moreover, bioactive molecules, such as proteins and antibiotics[6] can be successfully incorporated. The sol-gel process also offers increased versatility, since the precursor sol can be either deposited on a substrate to form a film, cast into a suitable container with the desired shape or used to synthesize ultra-fine powders.

Since the first preparation of silicate-based bioglasses in 1991 using sol-gel processing,[71] the literature pertaining to these systems has been prolific. By contrast, much less work exists on the sol-gel synthesis of phosphates,[7] with the first work on P_2O_5-CaO-Na_2O systems published in 2005[72] and subsequently a lower temperature route in 2007.[73]

Discussion is limited, as with the other sections of this review, to ternary PBG and d-PBG despite the existence of studies of biomedically applicative doped binary P_2O_5-CaO and P_2O_5-

---

[6] Which would otherwise decompose during the high temperature melt-quench process.

[7] Due to the demanding precursor chemistry, which is outlined in the review by Neel *et al.*.[10]

Na_2O systems, titanium-doped P_2O_5-CaO-TiO_2[74] and borate-doped P_2O_5-B_2O_3-Na_2O[75].

2.4.1 Undoped

$(P_2O_5)_{0.45}(CaO)_x(Na_2O)_{0.55-x}$ (x = 0.30, 0.35 and 0.40) PBG have been fabricated via sol-gel and melt-quench synthesis techniques.[76] A broad range of characterisation methods were used to investigate the short- and medium-range structure of the glasses. It is noted that the densities of the sol-gel glasses (2.1-2.4 $g.cm^{-3}$) are slightly lower than those of the melt-quench derived glasses ($\sim$2.6 $g.cm^{-3}$). It is suggested that a likely cause of this relates to the sol-gel synthesis, in which the glasses tend to have a higher closed porosity and hence a lower density. High energy X-ray diffraction and ^{31}P MAS NMR results suggest the sol-gel glasses have similar structures at the atomic scale, with similar Q^n distributions and atomic correlations. Similar dissolution properties and bioactive behaviour is therefore expected for sol-gel glasses in these compositions, compared to melt-quench glasses, with the added advantage of a low temperature synthesis route.

2.4.2 Cisplatin - chemotherapy

As stated previously, the sol-gel low-temperature synthesis allows for the incorporation of biologically active molecules, that could not survive the high temperatures necessary, in the preparation of glass biomaterials by melt-quenching methods. One such functional molecule is the chemotherapy agent cisplatin (*cis*-$[Pt(NH_3)_2(Cl)_2]$). Cisplatin is a widely used and effective cytotoxic agent in the treatment of malignancies of the lung, head and neck, and ovarian cancers.[77] Targeted delivery is expected to increase the drugs effectiveness in these applications. Pickup *et al.*[78] have prepared the sol-gel matrix P50C30N20 containing 1 wt% cisplatin. Their study used X-ray absorption spectroscopy to show that the chlorine ligands of cisplatin undergo exchange with oxygen during the synthesis, consistent with binding to the phosphate groups of the sol-gel and successful incorporation. UV-visible spectroscopy was used to reveal the subsequent release of cisplatin into an aqueous solution, the results of which showed a sustained *in vitro* release over a 4 day period. The authors state that, cisplatin-PBG microspheres could potentially be injected directly into a tumour, such that they become physically trapped within the smaller blood vessels (chemoembolization) and sustain the action of cisplatin through controlled release, thereby improving efficacy and reducing systemic toxicity. It is further proposed that co-dopants, such as gallium (known to inhibit tumour growth[79]), may be beneficially incorporated.

2.4.3 Gallium - antimicrobial

The gallium doped composition $(P_2O_5)_{0.50}(CaO)_{0.30}(Na_2O)_{0.17}(Ga_2O_3)_{0.03}$ has been prepared via a sol-gel synthesis and a structural comparison made to the undoped P50C30N20 composition.[80] Significant structural differences are noted over melt-quench derived PBG, especially with regard to the medium-range Q^n distribution. P50C30N20 from a melt-quench synthesis contains 95% Q^2,[73] whereas the sol-gel derived glass contains 40% Q^2.[80] The difference is accounted for by the presence of OH^- in the sol-gel glasses, which terminate the phosphate chains and reduce the connectivity. Analysis of ^{31}P MAS NMR spectra shows that incorporation of gallium into the sol-gel PBG leads to an increase in network connectivity. Antimicrobial activity was investigated using *S. aureus*, with the gallium-doped sol-gel glass and the undoped PBG as a negative control. It was shown that there is a net bactericidal effect against *S. aureus*, due to the presence of Ga^{3+} ions and that these materials have potential for use in antibacterial devices.

Chapter 3

Many-body Quantum Mechanics and Ground-State Density Functional Theory

"The underlying physical laws necessary for the mathematical theory of a large part of physics and the whole of chemistry are thus completely known, and the difficulty lies only in the fact that the exact application of these laws leads to equations much too complicated to be soluble"
- P. A. M. Dirac

In principle the properties of a non-relativistic system can be obtained by solving the many-electron Schrödinger equation (S.E.). In practice, this is an impossible task; indeed the resulting many-body problem has only been solved for systems with a handful of electrons. In this chapter, we will first show how the problem of finding the ground-state energy by solution of the many-electron S.E. can be circumvented by the use of the density functional theory (DFT). The Hohenberg-Kohn-Sham formulation of DFT is a reformulation of quantum mechanics, using the electron density as its fundamental parameter. It is possible to make a mapping from the system of interacting electrons to a fictitious system of non-interacting particles, which has the same ground-state density. Recasting the N-body problem as N single-body problems is a great simplification and one which facilitates its application for electronic structure calculations in extended systems.

3.1 Many-electron systems

We start with the time-independent Schrödinger equation (TISE),

$$\hat{H}\ \tilde{\Psi}(\{\vec{r_i}\},\{\vec{R_k}\}) = E\ \tilde{\Psi}(\{\vec{r_i}\},\{\vec{R_k}\}), \tag{3.1}$$

where $\tilde{\Psi}(\{\vec{r_i}\},\{\vec{R_k}\})$ derives from a separation of variables of the time-dependent state vector, as given in Equation 3.2.

$$\Psi(\{\vec{r_i}\},\{\vec{R_k}\},t) = \tilde{\Psi}(\{\vec{r_i}\},\{\vec{R_k}\})\Theta(t). \tag{3.2}$$

In the position-space representation (for a system containing M nuclei and N electrons), the non-relativistic Hamiltonian operator may be expressed as follows:

$$\begin{aligned}\hat{H} = &-\sum_{k=1}^{M}\frac{\hbar^2}{2m_k}\nabla^2_{\vec{R}_k} - \sum_{i=1}^{N}\frac{\hbar^2}{2m_e}\nabla^2_{\vec{r}_i} + \frac{1}{2}\sum_{k}^{M}\sum_{l\neq k}^{M}\frac{1}{4\Pi\epsilon_0}\frac{Z_k Z_l e^2}{|\vec{R}_k-\vec{R}_l|} \\ &+\frac{1}{2}\sum_{i}^{N}\sum_{j\neq i}^{N}\frac{1}{4\Pi\epsilon_0}\frac{e^2}{|\vec{r}_i-\vec{r}_j|} - \sum_{k=1}^{M}\sum_{i=1}^{N}\frac{1}{4\Pi\epsilon_0}\frac{Z_k e^2}{|\vec{R}_k-\vec{r}_i|},\end{aligned} \tag{3.3}$$

where $\vec{r_i}$ is the position of electron i and $\vec{r_j}$ is the position of electron j. $\vec{R_k}$ and $\vec{R_l}$ are the positions of nuclei k and l. m_k and m_e are the mass of nuclei k and an electron ($9.10938215(45)\times10^{-31}$kg), respectively. Z_l and Z_k are the atomic numbers of nuclei l and k, respectively. This expression consists of five terms: the kinetic energy operator for the nucleus, the kinetic energy operator for the electrons, the potential energy operator for nuclear-nuclear interactions, the potential energy operator for electron-electron interactions and the potential energy operator for nuclear-electron interactions.

For many electron systems there are no known analytic solutions since the electron-electron interaction becomes intractable (one mole contains $N{\sim}10^{28}$ electrons). Furthermore, the motions of the electrons are correlated via the Coulombic interaction. The electronic Schrödinger equation is therefore a complicated mathematical object of 3N variables, that incorporates the effects of correlation, thus preventing a separation of the electronic degrees of freedom into N single-body problems. The Hartree-Fock (HF) approach seeks to simplify this by introducing a mean field approximation, where an external field replaces the interaction of all the other electrons to an arbitrary particle. DFT also reduces the dimensionality of the problem to three, in which the many-body problem is effectively relocated into the definition of the exchange-correlation functional.

3.1.1 The Born-Oppenheimer approximation

The forces acting on both the electrons and nuclei, due to their electric charge, are of the same order of magnitude and so, the changes which occur in their momenta, as a result of these forces, must also be the same. Since nuclei are of the order of $\sim 10^3 - 10^5$ times more massive than electrons, they must have accordingly much smaller velocities. Thus, it is plausible that on the typical time-scale of the nuclear motion, the electrons will rapidly relax to the instantaneous ground-state configuration. In solving the TISE, resulting from the Hamiltonian operator in Equation 3.3, we can assume that the nuclei are stationary and solve for the electronic ground-state. Subsequently, we can calculate the energy of the system in that configuration and solve for the nuclear motion. The separation of electronic and nuclear motion is known as the Born-Oppenheimer (BO) or *adiabatic* approximation.[81]

We assume the following form of an eigenfunction for the Hamiltonian 3.3:

$$\tilde{\Psi}(\{\vec{r}_i\}, \{\vec{R}_k\}, t) = \Psi(\{\vec{r}_i\}; \{\vec{R}_k\})\Phi(\{\vec{R}_k\}) \tag{3.4}$$

and require that $\Psi(\{\vec{r}_i\}; \{\vec{R}_k\})$ (a wave-function that is dependent on electronic coordinates but only has a parametric dependence on nuclear coordinates), when applied to the electronic Hamiltonian ($\hat{H}_e$):

$$\hat{H}_e = -\sum_{i=1}^{N} \frac{\hbar^2}{2m_e} \nabla^2_{\vec{r}_i} + \frac{1}{2} \sum_{i}^{N} \sum_{j \neq i}^{N} \frac{1}{4\Pi\epsilon_0} \frac{e^2}{|\vec{r}_i - \vec{r}_j|} - \sum_{k=1}^{M} \sum_{i=1}^{N} \frac{1}{4\Pi\epsilon_0} \frac{Z_k e^2}{|\vec{R}_k - \vec{r}_i|}, \tag{3.5}$$

satisfies a new electronic TISE for the electrons in a static array of nuclei as given in

$$\begin{aligned} \left[-\sum_{i=1}^{N} \frac{\hbar^2}{2m_e} \nabla^2_{\vec{r}_i} + \frac{1}{2} \sum_{i}^{N} \sum_{j \neq i}^{N} \frac{1}{4\Pi\epsilon_0} \frac{e^2}{|\vec{r}_i - \vec{r}_j|} - \sum_{k=1}^{M} \sum_{i=1}^{N} \frac{1}{4\Pi\epsilon_0} \frac{Z_k e^2}{|\vec{R}_k - \vec{r}_i|} \right] \Psi(\{\vec{r}_i\}; \{\vec{R}_k\}) \\ = \mathcal{E}_e(\{\vec{R}_k\}) \Psi(\{\vec{r}_i\}; \{\vec{R}_k\}), \end{aligned} \tag{3.6}$$

where the dependence of the eigenvalues $\mathcal{E}_e$ on the nuclear positions is acknowledged. $\mathcal{E}_e(\{\vec{R}_k\})$ is known as the *adiabatic* contribution of the electrons to the energy of the system. The remaining non-adiabatic terms contribute very little to the energy, which can be demonstrated using time-independent perturbation theory (not presented here).

The adiabatic principle is crucial, allowing for the separation of nuclear and electronic motion (leaving a residual electron-phonon interaction). The assumption from this point forward is that the electrons respond instantaneously to the nuclear motion and always occupy the ground-state for the particular nuclear configuration. Varying the nuclear positions maps out a multi-dimensional ground-state potential energy surface and the motion of the nuclei in this potential can then be solved. For most problems, Newtonian mechanics generally suffices for this part of the problem and relaxation of the nuclear positions to the minimum-energy configuration (static) or molecular dynamics can be performed. For the remainder of this chapter, it is assumed that a system with a fixed nuclear configuration is to be treated, so that the electronic energy $\mathcal{E}_e$ is a constant and the electronic wave-function $\Psi(\{\vec{r}_i\})$ obeys the electronic TISE 3.6. The dependence of the electronic wave-function on the nuclear positions $\{\vec{R}_k\}$ is now suppressed. From this point forward, atomic units are used (unless otherwise stated), i.e. $\hbar = m_e = e = 4\pi\epsilon_0 = 1$.

3.1.2 The Rayleigh-Ritz variational method

We are interested in finding the electronic ground state $|\Psi_0\rangle$,[1] which is the eigenstate of the electronic Hamiltonian (see electronic TISE 3.6) with the lowest eigenvalue $\mathcal{E}_0$. Supposing we have a state close to the ground-state but with some small error. Since the eigenstates of the Hamiltonian form a complete set, the error can be expanded as a linear combination of the excited eigenstates. The whole state can thus be written as,

$$|\Psi\rangle = |\Psi_0\rangle + \sum_{n=1}^{\infty} c_n |\Psi_n\rangle , \tag{3.7}$$

where c_n are the appropriate complex coefficients, $\hat{H}|\Psi_n\rangle = \mathcal{E}_n |\Psi_n\rangle$ and $\langle\Psi_m|\Psi_n\rangle = \delta_{mn}$.[2] We now determine $\mathcal{E}_e$ (which is a functional of the wave-function) via the calculation of the expectation value of the Hamiltonian as follows:

---

[1] Use of Dirac notation. E.g. $\langle\Psi_m|\Psi_n\rangle = \int \Psi_m^* \Psi_n d\tau$, where * denotes the complex conjugate.

[2] Dirac delta for orthonormality constraint: $\delta_{m=n} = 1$ and $\delta_{m\neq n} = 0$.

$$\begin{aligned}
\mathcal{E}_e[\Psi] &= \frac{\langle\Psi|\,\hat{H}_e\,|\Psi\rangle}{\langle\Psi|\Psi\rangle} \\
&= \frac{\left\langle \Psi_0 + \sum\limits_{n=1}^{\infty} c_n\Psi_n \right| \hat{H}_e \left| \Psi_0 + \sum\limits_{n=1}^{\infty} c_n\Psi_n \right\rangle}{\left\langle \Psi_0 + \sum\limits_{n=1}^{\infty} c_n\Psi_n \right| \left. \Psi_0 + \sum\limits_{n=1}^{\infty} c_n\Psi_n \right\rangle} \\
&= \frac{\mathcal{E}_0 \left\langle \Psi_0 + \sum\limits_{n=1}^{\infty} c_n\Psi_n \right| \left. \Psi_0 + \sum\limits_{n=1}^{\infty} c_n\mathcal{E}_n\Psi_n \right\rangle}{\left\langle \Psi_0 + \sum\limits_{n=1}^{\infty} c_n\Psi_n \right| \left. \Psi_0 + \sum\limits_{n=1}^{\infty} c_n\Psi_n \right\rangle} \\
&= \frac{\mathcal{E}_0 + \sum\limits_{n=1}^{\infty} |c_n|^2\mathcal{E}_n}{1 + \sum\limits_{n=1}^{\infty} |c_n|^2} \\
&= \mathcal{E}_0 + \sum_{n=1}^{\infty} |c_n|^2(\mathcal{E}_n - \mathcal{E}_0) + \mathcal{O}\left(|c_n|^4\right). \qquad (3.8)
\end{aligned}$$

From the definition of $\mathcal{E}_0$, $\mathcal{E}_n > \mathcal{E}_0$ for $n \geq 1$, two conclusions are drawn. Firstly, $\mathcal{E}_e[\Psi] \geq \mathcal{E}_0$ with equality only when $|\Psi\rangle = |\Psi_0\rangle$ (i.e. $c_n = 0$ for $n \geq 1$). Secondly, the error in the estimate of $\mathcal{E}_0$ is second-order in the error in the wave function (i.e. c_n). The importance of the variational method is that the calculated value of the functional $\mathcal{E}[\Psi]$ provides an *upper bound* to the exact ground-state energy $\mathcal{E}_0$. Additionally, even a poor estimate of the ground-state wave function gives a relatively good estimate of $\mathcal{E}_0$. Evaluation of $\mathcal{E}[\Psi]$ proceeds by using *trial functions* (under the constraint that all states $|\Psi\rangle$ are antisymmetric under exchange of particles) which depend on a certain amount of variational parameters. The functional $\mathcal{E}[\Psi]$ then becomes a function of these variational parameters, which is minimised in order to obtain the best approximation of $\mathcal{E}_0$.

3.2 Density Functional Theory

3.2.1 Hohenberg-Kohn theorems

As a result of the Born-Oppenheimer approximation, we previously showed (see Equation 3.6) that the Coulomb potential of the nuclei is treated as a static external potential $V_{\text{ext}}(\vec{r})$:

$$V_{ext}(\vec{r}) = \sum_{k=1}^{M} \frac{Z_k}{|\vec{R}_k - \vec{r}|} \qquad (3.9)$$

where k are summed over nuclear variables respectively. The electron to nuclear interaction operator can thus be defined:

$$\hat{V}_{ext} = \sum_{i=1}^{N}\sum_{k=1}^{M} \frac{Z_k}{|\vec{R}_k - \vec{r}_i|}. \tag{3.10}$$

The remainder of $\hat{H}_\mathrm{e}$ is defined as $\hat{F}$,

$$\hat{F} = -\frac{1}{2}\sum_{i=1}^{N} \nabla^2_{\vec{r}_i} + \frac{1}{2}\sum_{i}^{N}\sum_{j\neq i}^{N} \frac{1}{|\vec{r}_i - \vec{r}_j|}, \tag{3.11}$$

so that $\hat{H}_e = \hat{F} + \hat{V}_{ext}$. $\hat{F}$ is the same for all N-electron systems, so that the Hamiltonian and hence the ground state $|\Psi_0\rangle$, are completely determined by N and $V_{ext}(\vec{r})$. The ground-state $|\Psi_0\rangle$ for this Hamiltonian gives rise to the ground-state electronic density $n_0(\vec{r})$,

$$n_0(\vec{r}) = \langle\Psi_0|\,\hat{n}\,|\Psi_0\rangle = \int \prod_{i=2}^{N} \mathrm{d}\vec{r}_i |\Psi_0(\vec{r}, \vec{r}_2, \vec{r}_3, ..., \vec{r}_N)|^2. \tag{3.12}$$

Thus the ground state $|\Psi_0\rangle$ and density $n_0(\vec{r})$ are both functionals of the number of electrons N and the external potential $V_{ext}(\vec{r})$.

3.2.1.1 Theorem 1

For any system of interacting particles in an external potential $V_{ext}(\vec{r})$, the potential $V_{ext}(\vec{r})$ is determined uniquely, except for a constant, by the ground-state particle density $n_0(\vec{r})$.

Proof by *reductio ad absurdum*: assume that a second different external potential $V'_{ext}(\vec{r})$ with ground-state $|\Psi'_0\rangle$ gives rise to the same density $n_0(\vec{r})$. The ground-state energies are $\mathcal{E}_0 = \langle\Psi_0|\,\hat{H}_e\,|\Psi_0\rangle$ and $\mathcal{E}'_0 = \langle\Psi'_0|\,\hat{H}'_e\,|\Psi'_0\rangle$ where $\hat{H}_e = \hat{F} + \hat{V}_{ext}$ and $\hat{H}'_e = \hat{F} + \hat{V}'_{ext}$. Taking $|\Psi'_0\rangle$ as a trial wave-function for $\hat{H}_e$, we obtain the strict inequality,

$$\begin{aligned}\mathcal{E}_0 < \langle\Psi'_0|\,\hat{H}_e\,|\Psi'_0\rangle &= \langle\Psi'_0|\,\hat{H}'_e\,|\Psi'_0\rangle + \langle\Psi'_0|\,(\hat{H}_e - \hat{H}'_e)\,|\Psi'_0\rangle \\ &= \mathcal{E}'_0 + \int \mathrm{d}\vec{r}\, n_0(\vec{r})[V_{ext}(\vec{r}) - V'_{ext}(\vec{r})],\end{aligned} \tag{3.13}$$

whereas taking $|\Psi_0\rangle$ as a trial wave-function for $\hat{H}'$ gives

$$\begin{aligned}\mathcal{E}_0' &< \langle\Psi_0|\,\hat{H}_e'\,|\Psi_0\rangle = \langle\Psi_0|\,\hat{H}_e\,|\Psi_0\rangle + \langle\Psi_0|\,(\hat{H}_e' - \hat{H}_e)\,|\Psi_0\rangle \\ &= \mathcal{E}_0 + \int \mathrm{d}\vec{r}\, n_0(\vec{r})[V_{ext}(\vec{r}) - V_{ext}'(\vec{r})].\end{aligned} \tag{3.14}$$

Adding equations 3.13 and 3.14 results in the contradiction

$$\mathcal{E}_0 + \mathcal{E}_0' < \mathcal{E}_0 + \mathcal{E}_0'. \tag{3.15}$$

This establishes the desired result: there cannot be two different external potentials $V_{ext}(\vec{r})$, differing by more than a constant, which give rise to the same non-degenerate ground-state electronic density $n_0(\vec{r})$. $n_0(\vec{r})$ uniquely determines $V_{ext}(\vec{r})$ of the Schrödinger equation (of which it is a solution), to within a constant. The corollary follows that, since $\hat{H}_e$ is uniquely determined by $n_0(\vec{r})$, the many-body wave-function for any state is determined by solving the Schrödinger equation with this Hamiltonian. Thus, $V_{ext}(\vec{r})$ and the number of electrons $N = \int \mathrm{d}\vec{r}\, n_0(\vec{r})$, and more generally $n_0(\vec{r})$, determines all ground-state properties of the system. This proof is restricted to all "V-representable" densities $n(\vec{r})$ that are ground-state densities of $\hat{H}_e$ with *some* external potential. This defines a space of possible densities, within which we can construct *functionals* of the density. Since all properties are uniquely determined if $n(\vec{r})$ is specified, then each property can be viewed as a functional of $n(\vec{r})$. An electronic energy functional for an arbitrary external potential $V(\vec{r})$, unrelated to $V_{ext}(\vec{r})$ and determined by $n(\vec{r})$ can be defined as:

$$\mathcal{E}_V[n] = F[n] + \int \mathrm{d}\vec{r}\, V(\vec{r})\, n(\vec{r}). \tag{3.16}$$

3.2.1.2 Theorem 2

A universal functional for the energy $\mathcal{E}_V[n]$, in terms of the V-representable density $n(\vec{r})$ can be defined, valid for any external potential $V_{ext}(\vec{r})$. For any particular $V_{ext}(\vec{r})$, the exact ground-state energy of the system is the global minimum value of this functional and the density $n(\vec{r})$, that minimizes the functional, is the exact ground-state density $n_0(\vec{r})$.

Proof of this energy variational principle: by the first theorem, a given $n(\vec{r})$ determines its own external potential $V_{ext}(\vec{r})$ and ground-state $|\Psi\rangle$. If this state is used as a trial state for $\hat{H}_e$, with external potential $V(\vec{r})$, we have

$$\begin{aligned}\langle\Psi|\,\hat{H}_e\,|\Psi\rangle &= \langle\Psi|\,\hat{F}\,|\Psi\rangle + \langle\Psi|\,\hat{V}\,|\Psi\rangle \\ &= F[n] + \int \mathrm{d}\vec{r}\,V(\vec{r})\,n(\vec{r}) \\ &= \mathcal{E}_V[n] \geq \mathcal{E}_0, \end{aligned} \tag{3.17}$$

by the variational principle. For non-degenerate ground-states, equality only holds if $|\Psi\rangle$ is the ground-state for potential $V(\vec{r})$. It follows that if the functional $F[n]$ was known, then by minimizing the electronic energy of the system (see Equation 3.17), with respect to variations in the density function $n(\vec{r})$, one could find the exact ground state density and energy. Thus, the problem of solving the Schrödinger equation for non-degenerate ground-states can be recast into a variational problem of minimizing the functional $\mathcal{E}_V[n]$, with respect to the V-representable densities.

The constrained search formulation takes into account that during a search we will encounter densities that do not correspond to the ground-state of any external potential. This problem is overcome by extending the definition of $F[n]$ to include such densities, so long as $\mathcal{E}_V$is still minimised by the correct ground-state density. Following Levy[82] we define a functional of the density $n(\vec{r})$ for the operator $\hat{F}$ as:

$$F[n] = \min_{|\Psi\rangle\rightarrow n} = \langle\Psi|\,\hat{F}\,|\Psi\rangle \tag{3.18}$$

i.e. the functional takes the minimum value of the expectation value with respect to all states $|\Psi\rangle$, which give the density $n(\vec{r})$. Essentially all densities, $n(\vec{r})$, that integrate to N, correspond to some N-electron wave-function; this property is described as “N-representability”. The requirements of N-representability are much weaker and satisfied by any well-behaved density. Furthermore, the constrained search formulation overcomes the non-degeneracy requirement.

The results of these two theorems are the existence of the universal functional $F[n]$, which is independent of the external potential and that, instead of dealing with a function of $3N$

variables (the many-electron wave-function), we can instead deal with a function of only three variables ($n(\vec{r})$). Thus, the complexity scales linearly with system size N. Although these two theorems prove the existence of the universal functional $F[n]$, they do not give the exact form, or a method to calculate the ground-state density.

3.2.2 The Kohn-Sham method

The Kohn-Sham method[83] is a formulation of DFT that lends itself to finding good approximations to $F[n]$. Central to the Kohn-Sham method is the introduction of a fictitious auxillary system, which is intended in some way to mimic the true many-electron system that we are dealing with. The fictitious system is a set of particles, whose properties are identical to those of electrons, except that the electron-electron repulsive interaction is switched off. The variational problem for the Hohenberg-Kohn density functional is rewritten, introducing a Lagrange multiplier, μ, to constrain the number of electrons to be N:

$$\delta\left[F[n] + \int \mathrm{d}\vec{r}\, V_{ext}(\vec{r})n(\vec{r}) - \mu\left(\int \mathrm{d}\vec{r}\, n(\vec{r}) - N\right)\right] = 0. \tag{3.19}$$

The Euler-Lagrange equation associated with minimisation of this functional is then

$$\mu = \frac{\delta F[n]}{\delta n(\vec{r})} + V_{ext}(\vec{r}). \tag{3.20}$$

Kohn and Sham separated $F[n]$ into three parts,

$$F[n] = T_s[n] + \mathcal{E}_h[n] + \mathcal{E}_{xc}[n], \tag{3.21}$$

where $T_s[n]$ is defined as the kinetic energy of a non-interacting gas with density $n(\vec{r})$ and may be written in terms of the non-interacting single-particle orbitals (*Kohn-Sham orbitals*) as:

$$T_s[n] = -\frac{1}{2}\sum_{i=1}^{N}\int \mathrm{d}\vec{r}\, \psi_i^*(\vec{r})\nabla^2\psi_i(\vec{r}). \tag{3.22}$$

It is important to note that this is the kinetic energy of the auxillary non-interacting systems and not the kinetic energy of the actual physical system under consideration. $\mathcal{E}_h[n]$ is the classical electrostatic (Hartree) energy:

$$\mathcal{E}_h[n] = \frac{1}{2}\int\int \mathrm{d}\vec{r}\mathrm{d}\vec{r}\,'\frac{n(\vec{r})n(\vec{r}\,')}{|\vec{r}-\vec{r}\,'|}, \tag{3.23}$$

which includes a self-interaction term. The final term, $\mathcal{E}_{xc}[n]$, is an implicit definition of the exchange-correlation energy, which contains the non-classical electrostatic interaction energy and the difference between the kinetic energies of the interacting and non-interacting systems. $T_s[n]$ and $\mathcal{E}_h[n]$ can be dealt with simply and $\mathcal{E}_{xc}[n]$, which contains the effects of the complex behaviour, is a small fraction of the total energy and can be approximated surprisingly well. Subsequently, equation 3.19 can be rewritten:

$$\mu = \frac{\delta T_s[n]}{\delta n(\vec{r})} + V_{ks}(\vec{r}), \tag{3.24}$$

where $V_{ks}(\vec{r})$ is the effective Kohn-Sham potential given by,

$$V_{ks}(\vec{r}) = V_{ext}(\vec{r}) + V_h(\vec{r}) + V_{xc}(\vec{r}). \tag{3.25}$$

The Hartree potential $V_h(\vec{r})$ is given by

$$V_h(\vec{r}) = \frac{\delta\mathcal{E}_h[n]}{\delta n(\vec{r})} = \int \mathrm{d}\vec{r}\,'\frac{n(\vec{r}\,')}{|\vec{r}-\vec{r}\,'|} \tag{3.26}$$

and the exchange-correlation potential, $V_{xc}(\vec{r})$, by

$$V_{xc}(\vec{r}) = \frac{\delta\mathcal{E}_{xc}[n]}{\delta n(\vec{r})}. \tag{3.27}$$

Equation 3.24 is the same equation that would be obtained for a non-interacting system of particles moving in an external potential $V_{ks}(\vec{r})$. We proceed by solving the Schrödinger-type equations

$$\left[-\frac{1}{2}\nabla^2 + V_{ks}(\vec{r})\right]\psi_i(\vec{r}) = \epsilon_i\psi_i(\vec{r}) \tag{3.28}$$

for $\frac{1}{2}N$ single-particle states[3] $|\psi_i\rangle$, where ϵ_i correspond to the eigenvalues of the single-particle states and the charge density $n(\vec{r})$ is constructed from the *Kohn-Sham orbitals* as

---

[3] Our restriction to non-spin-polarised systems requires that N be even.

$$n(\vec{r}) = 2\sum_{i=1}^{N/2} |\psi(\vec{r})|^2 = 2\sum_{i=1}^{N/2} \psi_i^*(\vec{r})\psi_i(\vec{r}). \tag{3.29}$$

The factor of 2 in the above equation is for spin degeneracy - we assume the orbitals are singly occupied. It should be noted that the *Kohn-Sham orbitals*, $\psi_i(\vec{r})$, are the lowest N eigenstates that satisfy equation 3.28 and the full non-interacting ground-state wave-function, Ψ_s, can be written in terms of the *Kohn-Sham orbitals*, such that its satisfies anti-symmetry in a Slater determinant[84] as follows:

$$\Psi_s(\vec{r}_1, \vec{r}_2, ..., \vec{r}_N) = \frac{1}{\sqrt{N!}} \begin{vmatrix} \psi_1(\vec{r}_1) & \psi_1(\vec{r}_2) & \cdots & \psi_1(\vec{r}_N) \\ \psi_2(\vec{r}_1) & \psi_2(\vec{r}_2) & \cdots & \psi_2(\vec{r}_N) \\ \vdots & \vdots & \ddots & \vdots \\ \psi_N(\vec{r}_1) & \psi_N(\vec{r}_2) & \cdots & \psi_N(\vec{r}_N) \end{vmatrix}. \tag{3.30}$$

Since $V_{ks}(\vec{r})$ depends upon the density $n(\vec{r})$, it is necessary to solve these equations self-consistently. Having made a guess of the form of the density, the Schrödinger equation is solved to obtain a set of orbitals $\{\psi(\vec{r})\}$, from which a new density is constructed and the process is repeated until the input and output densities are the same. Converging to the ground-state minimum is no problem due to the convex nature of the density functional.

The energy of the non-interacting system is the sum of one-electron eigenvalues,

$$\begin{aligned} 2\sum_{i=1}^{N/2} \epsilon_i &= T_s[n] + \int \mathrm{d}\vec{r}\, n(\vec{r}) V_{ks}(\vec{r}) \\ &= T_s[n] + \int \mathrm{d}\vec{r}\, n(\vec{r}) \left(V_{ext}(\vec{r}) + V_h(\vec{r}) + V_{xc}(\vec{r})\right) \\ &= T_s[n] + \int \mathrm{d}\vec{r}\, n(\vec{r}) V_{ext}(\vec{r}) + \int\int \mathrm{d}\vec{r}\mathrm{d}\vec{r}\,' \frac{n(\vec{r})n(\vec{r}\,')}{|\vec{r} - \vec{r}\,'|} + \int \mathrm{d}\vec{r}\, n(\vec{r}) V_{xc}(\vec{r}) \end{aligned} \tag{3.31}$$

which, compared to the interacting system, double-counts the Hartree energy and over-counts the exchange-correlation energy. The energy of the interacting system in the Kohn-Sham approach, $\mathcal{E}_{ks}[n]$, using Equation 3.16 and the expression for $F[n]$ (see Equation 3.21), in the presence of the external potential of the nuclei V_{ext}, is rewritten as:

$$\mathcal{E}_{ks}[n] = T_s[n] + \mathcal{E}_h[n] + \mathcal{E}_{xc}[n] + \int \mathrm{d}\vec{r}\, n(\vec{r}) V_{ext}(\vec{r}). \tag{3.32}$$

Substituting for $T_s[n]$ from Equation 3.31 into Equation 3.32 gives:

$$\mathcal{E}_{ks}[n] = 2\sum_{i=1}^{N/2}\epsilon_i - \frac{1}{2}\int\int \mathrm{d}\vec{r}\mathrm{d}\vec{r}'\frac{n(\vec{r})n(\vec{r}')}{|\vec{r}-\vec{r}'|} - \int \mathrm{d}\vec{r}\, n(\vec{r})V_{xc}(\vec{r}) + \mathcal{E}_{xc}[n]. \tag{3.33}$$

The Kohn-Sham formulation thus succeeds in transforming the N-body problem into N single-body problems, each coupled via the Kohn-Sham effective potential. Formally there is no physical interpretation of the single-particle Kohn-Sham eigenvalues and orbitals, which are merely mathematical artefacts that facilitate the determination of the true ground-state density.

3.2.3 Exchange-Correlation

The results thus far would be exact if the exact form of the functional $\mathcal{E}_{xc}[n]$ were known. The Kohn-Sham kinetic energy is not the *true* kinetic energy and we may use this fact to formally define the exchange-correlation energy as

$$\mathcal{E}_{xc}[n] = T[n] - T_s[n] + \mathcal{E}_{ee}[n] - \mathcal{E}_h[n], \tag{3.34}$$

where $T[n]$ and $\mathcal{E}_{ee}$ are the exact kinetic and electron-electron interaction energies respectively. Mathematically, antisymmetrizing a Hartree product to obtain a Slater determinant introduces exchange effects, so-called because they arise from the requirement that $|\Psi|^2$ be invariant to the exchange of space and spin coordinates of any two electrons. In particular, a Slater determinant incorporates exchange-correlation, which means that the motion of two electrons with parallel spins is correlated.

The actual form of of $\mathcal{E}_{xc}$ is not known but several approximate functionals, based upon the electron density, exist to describe this term.

3.2.3.1 Local density approximation

The simplest approximation is the local density approximation (LDA), in which the contribution to the exchange-correlation energy from each infinitesimal volume in space, $\mathrm{d}\vec{r}$, is taken to be the value it would have if the whole space were filled with a homogeneous electron gas, with the same density as found in $\mathrm{d}\vec{r}$. This assumes that there are no spatial variations in n. For a spin unpolarized system, the exchange-correlation energy looks like:

$$\mathcal{E}_{xc}^{LDA}[n] = \int \mathrm{d}\vec{r}\, n(\vec{r})\, \epsilon_{xc}^{hom}(n) = \int \mathrm{d}\vec{r}\, n(\vec{r}) \left(\epsilon_{x}^{hom}(n) + \epsilon_{c}^{hom}(n) \right), \tag{3.35}$$

where $\epsilon_{xc}^{hom}(n)$ is the exchange-correlation energy per electron in a homogeneous electron gas of density $n(\vec{r})$. The exchange term, $\epsilon_{x}^{hom}(n)$, can be expressed in simple analytic form, whilst the correlation, $\epsilon_{c}^{hom}(n)$, has been accurately tabulated for several densities using Monte Carlo methods,[85] so that a fit can be made. The LDA ignores corrections to the exchange-correlation energy due to inhomogeneities in the electron density about $\vec{r}$. Despite the severe nature of the approximation, its success appears to be due to the fact that the LDA respects the sum rule,[86] that is that exactly one electron is excluded from the immediate vicinity of a given electron at point $\vec{r}$. In finite systems, this decays asymptotically with an exponential form, whereas in reality the exchange-correlation decays more slowly in a Coulombic manner. Consequently the LDA overestimates the binding energies and cohesive energies of molecules and solids, respectively and therefore underestimates lattice parameters. Elastic constants and phonon frequencies are also slightly underestimated.

3.2.3.2 Generalized gradient approximation

The generalized gradient approximation (GGA) attempts to incorporate the effects of inhomogeneities by including the gradient of the electron density and, as such, it is a semi-local method. The GGA exchange-correlation functional can be written as:

$$\mathcal{E}_{xc}^{GGA}[n] = \int \mathrm{d}\vec{r}\, n(\vec{r})\, \epsilon_{xc}^{hom}(n) F_{xc}[n, \nabla n], \tag{3.36}$$

where $F_{xc}[n, \nabla n]$ is known as the enhancement factor. Unlike the LDA, there is no unique form for the GGA and indeed, many variations are possible,[87–91] each corresponding to a different enhancement factor. The GGA approach improves binding and atomic energies but can overestimate lattice constants, which can be simulated better with LDA in some instances, due to a fortuitous error cancellation. Both LDA and GGA are parametrized approximations, but the parameters are not adjusted to describe physical observables. Thus, they are parameter free, although approximate, techniques.

3.3 The Plane Wave Pseudopotential approach

3.3.1 Periodic systems

In periodic bulk solids, such as crystals, the system is infinite and so it is necessary to reduce the problem to the study of a finite system. The calculation of system properties, using a unit cell and periodic boundary conditions, lends itself to the study of naturally periodic crystalline systems and can also be applied to aperiodic systems, such as glasses, by imposing some false periodicity. A unit cell or simulation box is constructed, which is then replicated periodically throughout space.

3.3.2 Bloch's theorem

Bloch's theorem states that in a periodic solid each electronic wave-function (single-particle Kohn-Sham orbital, $\psi_i(\vec{r})$), can be written as the product of a cell-periodic part and a wavelike part,

$$\psi_i(\vec{r}) \quad = f_i(\vec{r})\, e^{i\vec{k}.\vec{r}}. \tag{3.37}$$

The cell-periodic part of the wave-function can be expanded using a basis set, consisting of a discrete set of plane waves, whose wave vectors are reciprocal lattice vectors of the crystal,

$$f_i(\vec{r}) = \sum_{\vec{G}} c_{i,\vec{G}}\, e^{i\vec{G}.\vec{r}}, \tag{3.38}$$

where the reciprocal lattice vectors $\vec{G}$ are defined by,

$$\vec{G} = l\vec{a}^* + m\vec{b}^* + n\vec{c}^*. \tag{3.39}$$

The primitive lattice vectors $\vec{a}^*$, $\vec{b}^*$ and $\vec{c}^*$ are related to the real space primitive lattice vectors $\vec{a}$, $\vec{b}$ and $\vec{c}$, from the definition of any real space lattice vector $\vec{R} = l\vec{a} + m\vec{b} + n\vec{c}$, via the cyclic permutations,

$$\vec{a}^* = 2\pi\frac{\vec{b}\times\vec{c}}{\Omega}, \;\; \vec{b}^* = 2\pi\frac{\vec{c}\times\vec{a}}{\Omega} \;\text{ and }\; \vec{c}^* = 2\pi\frac{\vec{a}\times\vec{b}}{\Omega}. \tag{3.40}$$

Ω is the volume of the cell, given by

$$\Omega_{cell} = |\vec{a} \cdot (\vec{b} \times \vec{c})|. \tag{3.41}$$

Therefore, each electronic wave-function can be written as a sum of plane waves,[4]

$$\psi_i(\vec{r}) = \sum_{\vec{G}} c_{i,\vec{k}+\vec{G}}\, e^{i(\vec{k}+\vec{G})\cdot\vec{r}}. \tag{3.42}$$

3.3.3 k-point sampling

Electronic states are only allowed at a set of $\vec{k}$ points, determined by the boundary conditions that apply to the bulk solid. The infinite number of electrons in the solid are accounted for by an infinite number of $\vec{k}$ points, and only a finite number of electronic states are occupied at each $\vec{k}$ point. The Bloch theorem changes the problem of calculating an infinite number of electronic wave-functions to one of calculating a finite number of electronic wave-functions at an infinite number of $\vec{k}$ points. In order to simplify the problem to manageable proportions, it is necessary to impose boundary conditions, which restrict the allowed values of $\vec{k}$.

We therefore start by choosing to model the infinitely periodic system by a large number of primitive cells $N_{cells} = N_1N_2N_3$ stacked together, with N_i cells along the $\vec{a}_i$ direction and apply periodic or generalised Born-von Karman boundary conditions to the wave-functions:

$$\psi(\vec{r} + N_i\vec{a}_i) = \psi(\vec{r}), \qquad i = 1, 2, 3. \tag{3.43}$$

The subsequent application of Bloch's theorem gives:

$$\psi(\vec{r} + N_i\vec{a}_i) = e^{iN_i\vec{k}\cdot\vec{a}_i}\psi(\vec{r}), \tag{3.44}$$

thus restricting the values of $\vec{k}$, such that the following condition is satisfied:

$$e^{iN_i\vec{k}\cdot\vec{a}_i} = e^{2\pi i N_i k_i} = 1, \qquad i = 1, 2, 3. \tag{3.45}$$

---

[4] The proof of Bloch's theorem is further expounded in Appendix subsection A.1.1, showing that $\vec{q} = \vec{k} + \vec{G}$, where the wave-function is expanded in the basis of orthornormal plane waves $|\phi\rangle = e^{i\vec{q}\cdot\vec{r}}$.

Therefore, the values of k_1, k_2 and k_3 ($\{k_i\}$) are required to be real and equal to

$$k_1 = \frac{l_1}{N_1}, \;\; k_2 = \frac{l_2}{N_2} \;\text{ and }\; k_3 = \frac{l_3}{N_3}, \tag{3.46}$$

where the $\{l_i\}$ are integers, so that the general form allowed for the Bloch wave-vectors $\vec{k}$ is

$$\vec{k} = k_i\vec{a}^{\,*} + k_i\vec{b}^{\,*} + k_i\vec{c}^{\,*}, \qquad i = 1, 2, 3. \tag{3.47}$$

As $N_i \to \infty$, there are still an infinite number of allowed $\vec{k}$-vectors but they are now members of a countably infinite set. Further to this, $\vec{k}$-vectors which differ only by a reciprocal lattice vector $\vec{G}$, are equivalent. For $\vec{k}\,' = \vec{k} + \vec{G}$, the corresponding Bloch states are related by:

$$\begin{aligned}\psi_{n\vec{k}'}(\vec{r}) &= e^{i\vec{k}'\cdot\vec{r}} f_{n\vec{k}'}(\vec{r}) \\ &= e^{i\vec{k}\cdot\vec{r}}[f_{n\vec{k}'}(\vec{r})e^{i\vec{G}\cdot\vec{r}}] \\ &= e^{i\vec{k}\cdot\vec{r}}\tilde{f}(\vec{r}) \\ &= \psi_{n'\vec{k}}(\vec{r}).\end{aligned} \tag{3.48}$$

We now only deal with $\vec{k}$-vectors within the first Brillouin zone (BZ: Wigner-Seitz primitive cell in the reciprocal lattice). For each allowed $\vec{k}$-vector, we must calculate the occupied Hamiltonian eigenstates, in order to construct the density. Since the wave-functions vary smoothly within the first BZ, only a finite set of points need to be chosen. Methods have been devised for obtaining very accurate approximations to the electronic potential and the contribution to the total energy from a filled electronic band, by calculating electronic states at special sets of $\vec{k}$-points in the first BZ. A Monkhorst-Pack grid[92] is an unbiased method of choosing a set of $\vec{k}$-points for sampling, based on a rectangular grid of points spaced evenly throughout the BZ. The larger the dimensions of the grid, the finer and more accurate will be the sampling. The volume of the BZ, Ω_{BZ}, is related to the volume of the supercell, Ω_{cell}, by $\Omega_{BZ} = (2\pi)^3/\Omega_{cell}$, so that for large systems, the BZ volume is very small and only a few $\vec{k}$-points need to be considered. Furthermore, accurate approximations for the electronic potential and the total energy of an insulator or a semi-conductor can be obtained at a very small number of $\vec{k}$-points whereas for metallic systems require a more dense set to define the Fermi surface precisely. For all of the work presented in Chapters 7 and 8 for example, wave-functions are only calculated at the centre of the BZ, $\vec{k} = 0$, known as the Γ-point.

3.3.4 Basis sets

The single-particle orbitals, ψ_i, are expanded into a convenient set of basis functions. The two commonly used methods, and the ones used in the work presented here, are plane waves and Gaussian basis sets.

3.3.4.1 Plane waves

As we have seen in sub-section 3.3.2, the orbitals can be written as the product of a plane wave and a function, which has the periodicity of the lattice. The latter can be expanded as a discrete set of plane waves, so that we arrive at the expression given in equation 3.42. In principle, an infinite plane wave basis set is required, although the coefficients $c_{i,\vec{k}+\vec{G}}$ with small kinetic energy $(\hbar^2/2m)|\vec{k}+\vec{G}|^2$, are typically more important than those with larger kinetic energy. Thus, the plane wave basis set can be truncated to a finite number of plane waves, with kinetic energies less than some particular cut-off. This truncation leads to an error in the computed total energy, the magnitude of which is reduced by increasing the value of the cut-off until a desired convergence is achieved. Plane waves are the eigenfunctions of free electrons, thereby making them a good choice of basis set for solid-state physics problems. They are delocalised and orthogonal and treat all points in space with the same accuracy. Furthermore, Pulay forces vanish because the basis does not depend on the nuclear positions.

3.3.4.2 Gaussian plane wave representation

Atomic orbitals are a set of basis functions that are centered on the atom sites, usually split into a radial part $\chi_{nl}(r)$ and a spherical harmonic $Y_{lm}(\theta, \phi)$,

$$\psi_{nlm}(\vec{r}) = \chi_{nl}(r) Y_{lm}(\theta, \phi), \tag{3.49}$$

where the sub-scripts, n, l, m, refer to the principal quantum number, orbital angular momentum and its z-component, respectively. Due to their similarity with the atomic orbitals of hydrogen, Slater-Type Orbitals (STOs) can be used as basis functions. These are described as:

$$S_{nlm}(\vec{r}) = Ar^{n-1}e^{-\zeta r}Y_{lm}(\theta, \phi), \tag{3.50}$$

where A is a normalisation factor, ζ is a constant related to the effective charge of the nucleus (spread of the function) and r is the distance of the electron from the nucleus. Integrals involving STOs are difficult to calculate when the atomic orbitals in question are centered on different nuclei. Such integrals can be made analytic by expanding the atomic orbitals as linear combinations of Gaussian functions. Gaussian-Type Orbitals (GTOs) allow the matrix elements to be calculated much faster and are expressed as:

$$G^{\zeta}_{ijk}(\vec{r}) = Ae^{-\zeta r^2}x^i y^j z^k, \tag{3.51}$$

where, $l = i + j + k$, giving the angular momentum of the GTO. The product of two Gaussians is another Gaussian with an intermediate centre, which offers the advantage of allowing two-electron integrals to be reduced to the integral of a single Gaussian. The minimum basis set is given by the number of electrons in the system. Increasing the number of basis functions generally (but not invariably) improves accuracy and by adding a second radial function, with different ζ, to each orbital, we obtain a double-ζ (DZ) basis set. The quality of the basis set can be further improved by polarising the orbitals with the addition of functions of higher angular momentum. A standard basis set is double-zeta valence polarized (DZVP), where each strongly occupied valence orbital has two radial functions and each weakly occupied orbital only one. The advantages of atomic orbitals over plane waves, for the representation of the wave-functions, are that a much smaller basis set is required to obtain solutions of comparable accuracy. However, the necessity to use incomplete basis sets results in basis set superposition error (BSSE). BSSE is based on the fact that, when interacting species approach each other, their basis functions overlap, effectively increasing the size of their basis sets and resulting in a difference in energy between the composite species and its individual parts beyond the cohesive energy. BSSE becomes less significant when larger basis sets are used and disappears in the limit of a complete basis set. Further to this, using atomic orbitals means that it is not straightforward to improve the basis set systematically, but more parameters must be optimised. Finally, unlike plane waves, a Pulay correction to the forces must be computed.

The Gaussian plane wave (GPW) representation uses plane waves to represent the electron density, thereby simplifying the calculation of $\mathcal{E}_{xc}$, whilst using Gaussians to represent the wave-function. GPW explicitly describes valence electrons only with pseudopotentials, accounting for the effect of core electrons. In this formulation the electronic energy functional becomes:

$$\begin{aligned}\mathcal{E}_{GPW}[n] = &\sum_i f_i \langle\psi_i(\vec{r})| - \frac{\nabla}{2} + V_{loc}^{pp}(\vec{r})\,|\psi_i(\vec{r})\rangle + \sum_i f_i \langle\psi_i(\vec{r})|\, V_{nl}^{pp}(\vec{r}-\vec{r}')\,|\psi_i(\vec{r}')\rangle \\ &+ 4\pi\Omega_{cell} \sum_{|\vec{G}|<\vec{G}_c} \frac{\bar{n}^*(\vec{G})\bar{n}(\vec{G})}{\vec{G}^2} + \int \mathrm{d}\vec{r}\,\bar{n}(\vec{r})\mathcal{E}_{xc}[n]. \end{aligned} \tag{3.52}$$

In the above equation, the pseudopotential is split into local (V_{loc}^{pp}) and non-local (V_{nl}^{pp}) parts, f_i is the occupancy or orbital ψ_i, defined by

$$n = \sum_i f_i |\psi_i|^2, \tag{3.53}$$

Ω_{cell} is the volume of the supercell and $\vec{G}_c$ is the wave-vector corresponding to the cut-off energy. n is the density evaluated in the primary Gaussian basis and $\bar{n}$ is the density evaluated in the auxillary plane wave basis, the two being equal if both basis sets are complete. The pseudopotentials of Goedecker, Teter and Hutter (GTH)[93–95] are appropriate for this method, since they are constructed, such that all matrix elements can be calculated analytically in a Gaussian basis. The numerical accuracy in the GPW scheme, as prescribed by Lippert *et al.*,[96] is dependent on two parameters, namely the plane wave cut-off, G_c, and the screening parameter.

3.3.5 The pseudopotential approximation

In practice, a plane wave basis set is usually very poorly suited to expanding electronic wave-functions because a very large number of plane waves are needed to expand the tightly bound core orbitals and to follow the rapid oscillations of the wave-functions of the valence electrons in the core region. These rapid oscillations arise due to the fact that valence electrons must maintain orthogonality (required by the Paul Exclusion Principle), with the core electrons localised in the vicinity of the nucleus. This results in a large kinetic energy for the valence electrons in the core region, which roughly cancels large potential energy, due to the strong Coulomb potential. Thus, the valence electrons are much more weakly bound than the core electrons.

It is known that most physical and chemical properties of solids are dependent on the valence electrons to a much greater extent than on the core electrons. It is therefore convenient to attempt to replace the strong Coulomb potential and core electrons by an effective pseudopotential which is much weaker and replace the valence electron wave-functions by pseudo wave-functions, which vary smoothly in the core region. An ionic potential, valence wave-function, corresponding pseudopotential and pseudo wave-function are illustrated schematically in Figure 3.1.

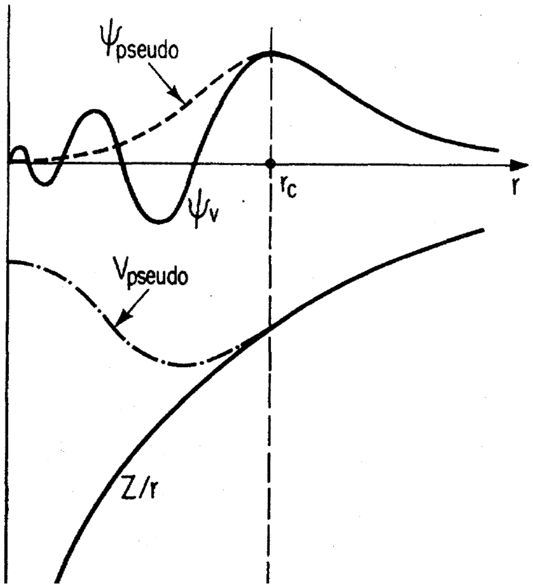

Figure 3.1: Schematic illustration of all-electron (solid lines) and pseudoelectron (dashed lines) potentials and their corresponding wave-functions. The radius at which all-electron and pseudoelectron values match is designated r_c.[86]

The pseudopotential is constructed in such a way that the pseudo wave-function has no radial nodes within the core region and that the pseudo wave-functions and potential agree with the true wave-function and potential outside some cut-off radius, r_c. The pseudopotential is constructed so that its scattering properties, or phase shifts for the pseudo wave-functions, are identical to the scattering properties of the ion and the core electrons for the valence wave-functions, but in such a way that the pseudo wave-functions have no radial nodes in the core region. As the phase shifts will, in general, be dependent upon the angular momentum state, generally a pseudopotential must be non-local, i.e. it must have projectors for the different angular momentum states. The most general form for a pseudopotential is thus,

$$V_{nl}^{pp} = \sum_{lm} |lm\rangle \, V_l^{pp} \, \langle lm| \, , \tag{3.54}$$

where $|lm\rangle$ are the spherical harmonics and V_l^{pp} is the pseudopotential for the angular momentum l. A pseudopotential that uses the same potential for all the angular momentum components of the wave-function is called a local pseudopotential and is a function only of the distance from the nucleus. In general V^{pp} is non-local, in that there is a separate local potential acting on each angular momentum component, l, of a given orbital.

Norm conserving pseudopotentials require that outside the core region, the real and pseudo wave-functions generate the same charge density, i.e.

$$\int_0^{r_c} \mathrm{d}\vec{r}\, \psi_{ae}^*(\vec{r})\psi_{ae}(\vec{r}) = \int_0^{r_c} \mathrm{d}\vec{r}\, \psi_{ps}^*(\vec{r})\psi_{ps}(\vec{r}) \tag{3.55}$$

where $\psi_{ae}(\vec{r})$ is the all electron wave-function (i.e. the Kohn-Sham orbital that would be obtained from a calculation involving all electrons) and $\psi_{ps}(\vec{r})$ is the pseudo wave-function. Relaxation of the norm conservation condition leads to ultrasoft pseudopotentials (USPP), such as the Vanderbilt USPP, allowing for smoother wave-functions and hence lower cut-off energies. This is advantageous in reducing the size of the plane wave basis set used.

3.3.6 Kohn-Sham equations in plane wave form

When plane waves are used as a basis set, expansion of the electronic wave-functions, ψ_i, in terms of plane waves (equation 3.42), allows the Kohn-Sham equations (equation 3.28) to assume a particulary simple form. Substitution of equation 3.42 into equation 3.28 and integration over $\vec{r}$ gives the secular equation

$$\sum_{\vec{G}'}\left[\frac{\hbar^2}{2m}|\vec{k}+\vec{G}|^2\delta_{\vec{G}\vec{G}'}+V_{ext}(\vec{G}-\vec{G}')+V_h(\vec{G}-\vec{G}')+V_{xc}(\vec{G}-\vec{G}')\right]c_{i,\vec{k}+\vec{G}'}$$

$$=\epsilon_i c_{i,\vec{k}+\vec{G}}. \qquad (3.56)$$

These terms are derived explicitly in Appendices A.1, A.2, A.3 and A.4. It can be seen that the reciprocal space representation of the kinetic energy is diagonal and the various potentials can be described in terms of their Fourier components. In principle this secular equation could be solved by diagonalising the Hamiltonian matrix $\hat{H}_{\vec{k}+\vec{G}_n,\vec{k}+\vec{G}'_n}$ as given in Appendix A.5. However, the size of this matrix is governed by the choice of plane wave kinetic energy cut-off,

$$E_{cut}=\frac{\hbar^2}{2m}|\vec{k}+\vec{G}_c|^2. \qquad (3.57)$$

Thus, for systems containing valence and core electrons the matrix will be intractably large.

3.3.7 Solving the Kohn-Sham equations with conventional matrix diagonalization

The Kohn-Sham equations must be solved self-consistently because the effective Kohn-Sham potential V_{ks} and the electron density $n(\vec{r})$ are closely related. This can be done numerically through self-consistent iterations, with conventional matrix diagonalization, as shown in Figure 3.2. The procedure requires an initial guess for the electronic charge density, from which the Hartree potential, $V_h(\vec{r})$, and the exchange correlation potential, $V_{xc}(\vec{r})$, can be calculated. The Hamiltonian matrices for each of the $\vec{k}$ points included in the calculation must be constructed, as in equation 3.56 and diagonalized to obtain the Kohn-Sham eigenstates. These eigenstates will normally generate a different charge density from the one originally used to construct the electronic potentials and hence, a new set of Hamiltonian matrices must be constructed, using the new electronic potentials. The eigenstates of the new Hamiltonian are obtained and the process is repeated until the solutions are self-consistent. In practice, the new electronic potential is taken to be a combination of the electronic potentials generated by the old and the new eigenstates, since this speeds the convergence to self-consistency. To complete the total-energy calculation, tests should be performed to ensure that the total energy is converged both as a function of $\vec{k}$ points and as a function of the cut-off energy for the plane wave basis set.[86]

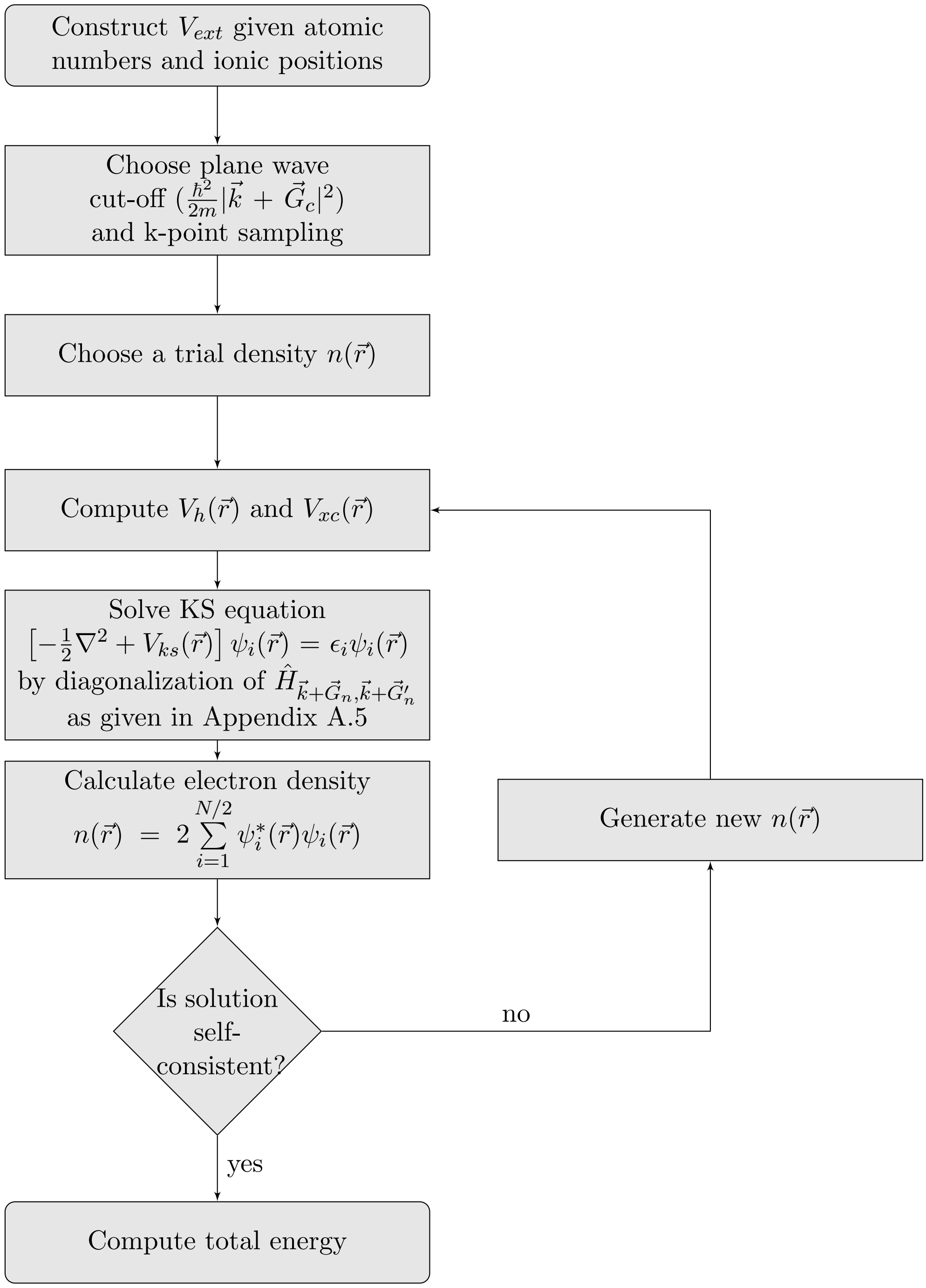

Figure 3.2: Flowchart describing the computational procedure for the calculation of the total energy of a solid, using conventional matrix diagonalization.

3.3.8 Energy Minimization

Conventional matrix diagonalization procedures (subsection 3.3.7) are ill-suited to plane wave pseudopotential calculations. In a typical calculation, there are of the order of one hundred plane wave basis states for each atom in the system. The cost of matrix diagonalization increases as the third power of the number of plane wave basis states and the memory required to store the Hamiltonian matrix increases as the square of the number of basis states. As a result, conventional matrix diagonalization techniques are restricted to the order of one thousand plane wave basis states, in turn restricting the number of atoms in the unit cell to the order of 10. An alternative technique is to directly minimize the Kohn-Sham functional, with respect to the Kohn-Sham orbitals themselves. To do this efficiently requires us to be able to calculate the gradient of the energy, with respect to the orbitals, i.e.

$$\begin{aligned}
\frac{\partial \mathcal{E}}{\partial \psi^*_{ik}(\vec{r})} &= \frac{\partial(\mathcal{E}-T_s)}{\partial \psi^*_{ik}(\vec{r})} + \frac{\partial T_s}{\partial \psi^*_{ik}(\vec{r})} \\
&= \int \mathrm{d}\vec{r}\,' \frac{\partial(\mathcal{E}-T_s)}{\partial n(\vec{r}\,')} \frac{\partial n(\vec{r}\,')}{\partial \psi^*_{ik}(\vec{r})} + \frac{\partial T_s}{\partial \psi^*_{ik}(\vec{r})} \\
&= \int \mathrm{d}\vec{r}\,' V_{ks}(\vec{r}\,') \frac{\partial n(\vec{r}\,')}{\partial \psi^*_{ik}(\vec{r})} + \frac{\partial T_s}{\partial \psi^*_{ik}(\vec{r})} \\
&= \int \mathrm{d}\vec{r}\,' V_{ks}(\vec{r}\,') \frac{\partial}{\partial \psi^*_{ik}(\vec{r})} \sum_{i'k'} \psi^*_{i'k'}(\vec{r}\,') \psi_{i'k'}(\vec{r}\,') \\
&\quad + \frac{\partial}{\partial \psi^*_{ik}(\vec{r})} \sum_{i'k'} \int \mathrm{d}\vec{r}\,' \psi^*_{i'k'}(\vec{r}\,') \left(\frac{\nabla^2}{2}\right) \psi_{i'k'}(\vec{r}\,') \\
&= 2V_{ks}(\vec{r})\psi_{ik}(\vec{r}) + \nabla^2 \psi_{ik}(\vec{r}), \qquad (3.58)
\end{aligned}$$

where V_{ks} is the Kohn-Sham potential (the local potential which causes the non-interacting system to adopt a ground state density $n(\vec{r})$), defined in equation 3.25, which can be re-written as functional derivatives of the various contributions to the total energy i.e.

$$V_{ks}(\vec{r}) = V_{ext}(\vec{r}) + \frac{\partial \mathcal{E}_h}{\partial n(\vec{r})} + \frac{\partial \mathcal{E}_{xc}}{\partial n(\vec{r})}. \qquad (3.59)$$

In reciprocal space, equation 3.58 becomes

$$\frac{\partial \mathcal{E}}{\partial c^*_{ik}(\vec{G})} = 2\sum_{\vec{G}'}\left[\frac{\hbar^2}{2m}|\vec{k}+\vec{G}|^2\delta_{\vec{G}\vec{G}'} + V_{ext}(\vec{G}-\vec{G}') + V_h(\vec{G}-\vec{G}') + V_{xc}(\vec{G}-\vec{G}')\right]c_{i,\vec{k}+\vec{G}'}. \quad (3.60)$$

The basic idea is to take the single particle trial wave-function and to minimise the contribution of this state to the total energy, whilst maintaining orthogonality to all other states. The minimization is achieved by varying the plane wave coefficients. There are various methods available to perform the minimisation procedure.

3.3.8.1 Steepest descents

The simplest method to use is that of steepest descents, as illustrated in Figure 3.3. For a function $F(x)$ the steepest descent direction $\vec{g}$ may be obtained as

$$\vec{g} = -\nabla_{x^1}F, \quad (3.61)$$

where x^1 is the point at which the function is evaluated. Once this path of steepest descent has been determined, one may carry out a line minimization, in order to determine the location of the minimum, x^2, along that line. From this point, one repeats the procedure until the minimum of the function has been found. Although this technique is beneficially simple, it does not guarantee convergence to a minimum in a finite number of steps. Furthermore, it only uses information about the current sampling point and fails to make use of previous iterations to guide the minimization more efficiently.

As illustrated in Figure 3.3 steepest descents will perform many small steps in going down a long, narrow valley, even if the valley is a perfect quadratic form. We might have hoped that, in two dimensions, the first step would take you to the valley floor and the second step directly down the long axis. However, the new gradient at the minimum point of any line minimization is perpendicular to the direction just traversed. Therefore, one must take a right angle turn, which does not, in general, take one to the minimum. A solution would be to not proceed down the new gradient but in a direction that is conjugate to the old gradient, and, insofar as possible, to all previous directions traversed.

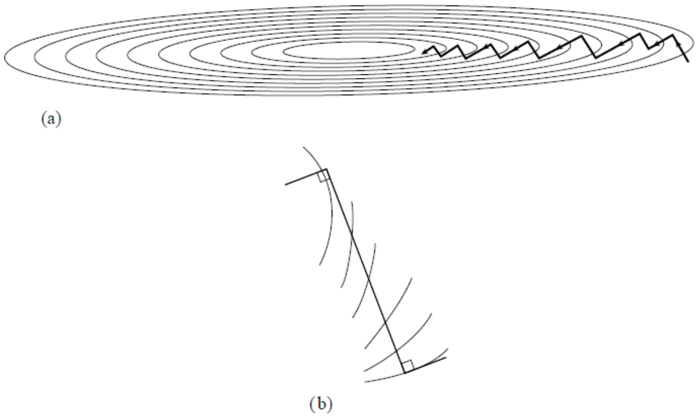

Figure 3.3: (a) Steepest descents method in a long, narrow “valley”. Shown to be an inefficient strategy, taking many steps to reach the valley floor. (b) Magnified view of one step: A step starts off in the local gradient direction, perpendicular to the contour lines, and traverses a straight line until a local minimum is reached, where the traverse is parallel to the local contour lines.[97]

3.3.8.2 Conjugate gradients

The conjugate gradients method is a more efficient method that combines the information from all previous search directions, such that a subsequent search direction is independent from all previous search directions. That is, the set of search directions forms a linearly independent set. For all n-dimensional vector space, this guarantees convergence in n iterations, as each minimisation step reduces the dimensionality of the problem by 1; hence after n iterations, the dimensionality of the problem will be zero and thus, the minimum will be reached. If $\vec{g}^m$ is the steepest descents vector associated with iteration m, then the conjugate gradients direction $\vec{\mathrm{d}}^m$ is given by

$$\vec{\mathrm{d}}^m = \vec{g}^{\,m} + \gamma^m \vec{\mathrm{d}}^{m-1}, \tag{3.62}$$

where

$$\gamma = \frac{\vec{g}^{\,m} \cdot \vec{g}^{\,m}}{\vec{g}^{\,m-1} \cdot \vec{g}^{\,m-1}}, \tag{3.63}$$

and

$$\gamma^1 = 0. \tag{3.64}$$

3.4 Geometry Optimization - Hellmann-Feynman forces

Thus far, only total energy calculations for fixed atomic coordinates have been described. The next step is to calculate the forces acting on the atoms and propagate them accordingly. The force of an ion, k, at position $\vec{R}_k$, can be obtained from the full derivative of the total energy E, by:

$$\vec{F}_k = -\frac{\mathrm{d}E}{\mathrm{d}\vec{R}_k}. \tag{3.65}$$

As the atoms move to a new position, the electronic wave-functions must also change, contributing to the force on the atom. Therefore, the full derivative from equation 3.65 has to be expressed in terms of the changes in the wave-function:

$$\vec{F}_k = -\frac{\mathrm{d}E}{\mathrm{d}\vec{R}_k} - \sum_i \frac{\partial E}{\partial \psi_i}\frac{\partial \psi_i}{\partial \vec{R}_k} - \sum_i \frac{\partial E}{\partial \psi_i^*}\frac{\partial \psi_i^*}{\partial \vec{R}_k}. \tag{3.66}$$

Since,

$$E = \langle \Psi | \hat{H} | \Psi \rangle , \tag{3.67}$$

it follows that $\partial E/\partial \psi_i$ is just $\hat{H}\psi_i$. But ψ_i are electronic eigenstates with eigenvalues ϵ_i. Therefore, after some algebraic manipulation, the final two terms of equation 3.66 can be written:

$$\sum_i \epsilon_i \frac{\partial}{\partial \vec{R}_k} \langle \psi_i | \psi_i \rangle , \tag{3.68}$$

which is trivially zero. This shows that when each orbital is an eigenstate of the Hamiltonian, then the partial derivative of the total energy, with respect to the ionic positions, is the force felt by the ions and is the statement of the Hellmann-Feynman theorem.[98, 99]

In practice, the wave-functions are only calculated to a given tolerance and they are therefore never exact eigenstates of the Kohn-Sham Hamiltonian. As a result the forces calculated using the Hellmann-Feynman theorem incur error. The so-called variational force vanishes when the wave-functions are completely converged, so that the conditions of the Hellmann-Feynman theorem are satisfied. The error on the force is first order, with respect to the error in the wave-functions. It follows that the Hellmann-Feynman theorem can only be implemented when the wave-functions are very close to self-consistency. Only then can the ionic equations of motion be integrated and the ionic positions updated in Born-Oppenheimer molecular dynamics simulations (as discussed in subsection 4.1.2).

3.5 Dispersive correction (DFT-D)

One of the shortcomings of DFT is the treatment of non-local correlations. Van der Waals interactions between two atoms or molecules arise from the interaction of instantaneously induced dipole moments, due to the fluctuation of the electron densities. The correct accounting for these forces is crucial for an accurate theoretical description of complex systems. Van der Waals forces are non-classical and non-local interactions that need proper treatment of electronic dynamic correlation. They cannot be accounted for under the local density approximation (subsubsection 3.2.3.1) or the semi-local generalized gradient approximation (subsubsection 3.2.3.2). Post-Hartree Fock methods, such as many-body perturbation theory and coupled cluster, achieve this description, but at massive computational cost.

Grimme proposed[100] the solution of limiting the density functional to short-range and describing medium- to long-range interactions with damped empirical terms. So called DFT-D techniques allow for an effective description of dispersive forces within the framework of DFT. A semi-empirical correction term can be added to the Kohn-Sham equation. Following the London formula, the correction models the long range attractive potential of dispersive forces, in terms of a pairwise atomic potential proportional to $\frac{C_6}{R^{-6}}$. Further improvement is made by the introduction of a scaling parameter, in order to fit the contribution of dispersion with the exchange repulsion behaviour of the Kohn-Sham term. A damping function is also applied to shut off the correction at short distances, where atoms may be covalently bonded.

Therefore the energy of the system is now described with,

$$\mathcal{E}_{DFT-D} = \mathcal{E}_{DFT} + \mathcal{E}_{disp}, \tag{3.69}$$

where

$$\mathcal{E}_{disp} = -\frac{1}{2}\sum_{i,j} C_{6ij}\left[\sum_{\vec{R}} |\vec{r}_{ij} + \vec{R}|^{-6} f_{damp}(|\vec{r}_{ij} + \vec{R}|)\right], \tag{3.70}$$

and

$$f_{damp}(|\vec{r}_{ij} + \vec{R}|) = s_6 . \left(1 + exp\left[-d . \left(\frac{|\vec{r}_{ij} + \vec{R}|}{r_0} - 1\right)\right]\right)^{-1} . \tag{3.71}$$

$\vec{r}_{ij} = (\vec{r}_j - \vec{r}_i)$ is the atom-atom distance vector, $\vec{R} = l\vec{a} + m\vec{b} + n\vec{c}$ are lattice vectors, s_6 is a function dependent scaling parameter and d is a parameter that tunes the steepness of the damping function. C_6 is a semi-empirical parameter, which is proportional to atomic polarizabilities and first ionization energies.

Chapter 4

The Molecular Dynamics Method

At a finite temperature, the average kinetic energy is directly related to the temperature and atoms explore a part of the potential energy hypersurface, with energies lower than the typical kinetic energy. One way to simulate the behaviour at a finite temperature is to use molecular dynamics (MD). MD is a computer simulation technique where the time evolution of a set of interacting particles is followed by integrating their equations of motion. If we consider a system of N particles contained in a cell of volume V, then, in a particular instant t, the collection of $3N$ coordinates $\{\vec{r}_i(t)\}$ and $3N$ momenta $\{\vec{p}_i(t)\}$ of all particles is a point in the $6N-$dimensional phase space, formed by all the mircostates $\Gamma = \{\vec{r}_i, \vec{p}_i; i = 1, 2, ..., N\}$ accessible to the system. The object of MD is to determine this trajectory by numerically integrating the classical equations of motion over successive time intervals (time steps).

4.1 Equations of motion

The classical equations of motion expressed in Newtonian form are:

$$m_i \frac{\mathrm{d}^2\vec{r}_i}{\mathrm{d}t^2} = \vec{f}_i = -\nabla_{\vec{r}_i} V(\vec{r}_1, \vec{r}_2, ..., \vec{r}_N) \qquad i = 1, 2, ..., N, \tag{4.1}$$

where m_i, $\vec{r}_i$ and f_i are the mass, position and force acting on atom i respectively. V is the potential energy of the system when the atoms are arranged in the specific configuration $\{\vec{r}_1, \vec{r}_2, ..., \vec{N}\}$. In the set of N interacting particles, the force acting on each particle will change whenever the particle changes its position and momentum or whenever any other particles, with which it interacts, changes position. Therefore the set of N equations 4.1 are coupled and cannot be solved analytically. The $3N$ second-order differential equations can be approximately solved by finite difference numerical methods (based on a Taylor expansion). Given a set of atomic positions at time t, we calculate the positions and velocities at a later $t + \Delta t$ and at a series of consecutive times, $t + 2\Delta t$, $t + 3\Delta t$ etc., thus generating a discrete trajectory in the phase space by successive iterations. The time interval Δt is known as the time step and typically ranges from $1 \times 10^{-15}\mathrm{s} < \Delta t < 1 \times 10^{-16}\mathrm{s}$.

4.1.1 Classical

In classical molecular dynamics, the forces on each atom ($\vec{f_i}$ in equation 4.1) are derived from the interaction potentials (equation 4.14), with the associated electrostatic potential becoming our V term in equation 4.1. Details of the specific Born-Mayer potential used in this work can be found in section 6.2. Thus, for classical techniques the electronic degrees of freedom are replaced by the interatomic potentials and are not featured as explicit degrees of freedom in the equations of motion. This amounts to a dramatic simplification, as the effective potential due to the electrons is constructed from a manageable sum of additive few-body contributions.

4.1.2 Born-Oppenheimer

As introduced in subsection 3.1.1, the Born-Oppenheimer (BO) approximation allows for the separation of nuclear and electronic motion, and to subsequently solve for the static electronic problem at each MD time step, with fixed nuclear coordinates. Thus, the electronic structure part is reduced to solving the time-independent Schrödinger equation (TISE) concurrently to propagating the nuclei via classical dynamics. The BOMD method is defined by:

$$m_k \ddot{\vec{R}}_k(t) = \nabla_k \min_{\Psi_0} \{ \langle \Psi_0 | \hat{H}_e | \Psi_0 \rangle \} \tag{4.2}$$

for the electronic ground state. For any $\{\vec{R}_1, \vec{R}_2, ..., \vec{R}_k\}$, one has to solve the TISE to obtain Ψ_0, from which the forces acting on the atoms are computed. The forces acting on the atoms are defined,

$$\vec{F}_k = -\nabla_k \langle \Psi_0 | \hat{H}_e | \Psi_0 \rangle + F_{ion-ion} \tag{4.3}$$

where $F_{ion-ion}$ is the force due to direct core-core repulsion and the first term is evaluated using Hellmann-Feynman theorem (see section 3.4). The forces calculated can then be made use of in an integration algorithm to update the ionic positions and the process can be repeated until a sufficiently long MD trajectory is generated. Therefore the steps for a BOMD simulation using PW-DFT, follow the flow diagram 3.2, at the end of which, the forces on the atoms are calculated, using Hellmann-Feynman theorem. The system is propagated via integration of the equations of motion to obtain the configuration at $t + \Delta t$, the process is then repeated.

4.2 Finite Difference Methods

4.2.1 The Verlet algorithm

For our set of N particles with positions $\vec{r_i}$, the positions, a small time step Δt later, are given by a Taylor expansion about $\vec{r}(t)$:

$$\begin{aligned} \vec{r}_{i+1} &= \vec{r_i} + \frac{\partial \vec{r}}{\partial t}(\Delta t) + \frac{1}{2}\frac{\partial^2 \vec{r}}{\partial \vec{r}^2}(\Delta t)^2 + \frac{1}{6}\frac{\partial^3 \vec{r}}{\partial \vec{r}^3}(\Delta t)^3 + ... \\ &= \vec{r_i} + \vec{v_i}(\Delta t) + \frac{1}{2}\vec{a_i}(\Delta t)^2 + \frac{1}{6}\vec{b_i}(\Delta t)^3 + ... \end{aligned} \tag{4.4}$$

The velocities $\vec{v_i}$ are the first derivatives of the positions with respect to time at time t_i, the accelerations $\vec{a_i}$ are the second derivatives at time t_i and the hyperaccelerations $\vec{b_i}$ are the third derivatives etc. The positions, a small time step Δt earlier, are,

$$\vec{r}_{i-1} = \vec{r_i} - \vec{v_i}(\Delta t) + \frac{1}{2}\vec{a_i}(\Delta t)^2 - \frac{1}{6}\vec{b_i}(\Delta t)^3 + ... \tag{4.5}$$

Thus, by adding equations 4.4 and 4.5, we obtain

$$\vec{r}_{i+1} = (2\vec{r} - \vec{r}_{i-1}) + \vec{a_i}(\Delta t)^2 + ... \tag{4.6}$$

where,

$$\vec{a_i} = \frac{\vec{f_i}}{m_i} = -\frac{1}{m_i}\frac{\mathrm{d}V}{\mathrm{d}\vec{r_i}}. \tag{4.7}$$

Hence with only the knowledge of the particles current position, last position and current acceleration, we can solve for the position of the particle a time step Δt into the future. Equation 4.6 is known as the Verlet algorithm[101] and it allows us to solve Newton's equation numerically. It is noted that the velocities are not needed for updating the positions but they are useful for estimating the kinetic energy and other dynamical information. Via the subtraction of equations 4.4 and 4.5, we obtain

$$\vec{v}(t) = \frac{\vec{r}_{i+1} - \vec{r}_{i-1}}{2\Delta t}. \tag{4.8}$$

Equation 4.6 is correct for errors of order Δt^4, whereas equation 4.8 is subject to errors of order Δt^2, so that the Verlet algorithm does not handle velocities with the same accuracy as positions. Furthermore, the algorithm suffers from the numerical disadvantage that the new positions are obtained by adding a term proportional to Δt^2 to a difference in positions $(2\vec{r}_i - \vec{r}_{i-1})$. Since Δt is a small number and $(2\vec{r}_i - \vec{r}_{i-1})$ is a difference between two large numbers, this may often lead to truncation errors due to finite precision.

4.2.2 The Verlet Leapfrog algorithm

The numerical aspect and the lack of explicit velocities in the Verlet algorithm can be remedied by the Leapfrog algorithm.[102] Performing Taylor expansions analogous to equations 4.4 and 4.5 with half a time step followed by subtraction gives:

$$\vec{r}_{i+1} = \vec{r}_i + \vec{v}_{i+\frac{1}{2}}\Delta t. \tag{4.9}$$

The velocity is obtained by analogous expansion to give,

$$\vec{v}_{i+\frac{1}{2}} = \vec{v}_{i-\frac{1}{2}} + \vec{a}_i\Delta t. \tag{4.10}$$

Equations 4.9 and 4.10 define the Verlet leapfrog algorithm and it is noted that the position and velocity updates are out of phase by half a time step. Despite a theoretical accuracy that is equivalent to the standard Verlet algorithm, the Verlet leapfrog algorithm has better numerical accuracy. Furthermore, the velocities appear directly, which facilitates a coupling to an external heat bath. The disadvantage is that the positions and velocities are not known at the same time. It should be noted that for all molecular dynamics calculations presented in this thesis, using DL_POLY code[103] (version 2.20), the Verlet leapfrog integration algorithm was used.

4.2.3 The Velocity Verlet algorithm

The velocity Verlet algorithm uses the following equations to propagate the particles,

$$\vec{r}_{i+1} = \vec{r}_i + \vec{v}_i \Delta t + \frac{1}{2}\vec{a}_i \Delta t^2 \tag{4.11}$$

$$\vec{v}_{i+1} = \vec{v}_i + \frac{1}{2}\{\vec{a}_i + \vec{a}_{i+1}\}\Delta t \tag{4.12}$$

removing the abnormalities of phase shift of the leapfrog. The velocity Verlet scheme[104] computes positions, velocities and accelerations at the time $t + \Delta t$ from the same quantities at time t. This version of the Verlet algorithm is one of the most widely used both because of its easy implementation and numerical accuracy. For all Born-Oppenheimer molecular dynamics calculations presented in this thesis, using the QUICKSTEP module[105, 106] in the CP2K code (development version 2.3.16), this scheme was used for numerical integration.

4.3 Born model of solids

Classical simulations based on the Born model[107] of solids, assume that the ions in a crystal lattice interact solely through long- and short-range electrostatic forces:

$$\mathcal{E}(\vec{r}_{ij}) = \frac{1}{4\Pi\epsilon_0}\sum_{ij}\frac{q_i q_j}{\vec{r}_{ij} + 1} + \sum_{ij}\Phi_{ij}(\vec{r}_{ij}), \tag{4.13}$$

where q_i and q_j are the charges on atoms i and j respectively and Φ_{ij} are the short-range van der Waals forces acting between neighbouring electron clouds. Thus the first term represents the long-range electrostatic interactions and the second represents all short-range forces, which are described using the Ewald methods and interatomic potential functions respectively.

4.3.1 Ewald method

The electrostatic term from equation 4.13 converges very slowly in real space. This is overcome by the use of the Ewald method,[108] which calculates the long-range interactions between particles and their infinite periodic images. The method is based on splitting the conditionally convergent series into two convergent series, one in real space and the other in reciprocal space, each of which converges rapidly.

4.3.2 Interatomic potential functions

The total short-range energy can be expressed as,

$$U(\vec{r}_1, \vec{r}_2, ..., \vec{r}_N) = \sum_{i,j} U_{ij}(\vec{r}_i, \vec{r}_j) + \sum_{i,j,k} U_{ijk}(\vec{r}_i, \vec{r}_j, \vec{r}_k), \tag{4.14}$$

where U_{ij} refers to the two-body interactions and U_{ijk} to three-body interactions. This expression combines a number of components, including non-bonded interactions (repulsion and van der Waals attraction), electronic polarisability and covalent interactions modelled by “bond-bending” and “bond-stretching” terms. For the force fields used in this thesis two interatomic potential functions are considered.

For ionic or semi-ionic solids, the most frequently used functional form for the short-range two-body interactions is the Buckingham potential which takes the form,

$$U_{ij}(\vec{r}_{ij}) = A_{ij} \exp\left(\frac{-\vec{r}_{ij}}{\rho_{ij}}\right) - \frac{C_{ij}}{\vec{r}_{ij}^{\,6}} \tag{4.15}$$

in which the first terms describes the repulsive force originating from the Pauli Exclusion Principle and the second represents the van der Waals interactions. The second interatomic potential function relevant to the current work is the simple harmonic three-body potential of the form,

$$U_{ijk}(\theta_{ijk}) = \frac{1}{2} k_{ijk} (\theta_{ijk} - \theta_0)^2, \tag{4.16}$$

where θ_{ijk} is the angle between the atomic species $i - j - k$, θ_0 is the equilibrium angle for the system and k_{ijk} is the three-body force constant. Further details of the specific Born-Mayer ionic model[109] used in this work are given in section 6.2.

4.4 Electronic Polarisability

In our description thus far, it is assumed that every atom is modelled by a point charge, without any dipole moment. Although this may be an acceptable approximation in some cases, there are many situations where polarisability plays a crucial role. A dipole moment develops when an atom is placed in an electric field and we define the electronic polarisability α as follows,

$$\vec{\mu} = \alpha \vec{E}, \tag{4.17}$$

where $\vec{\mu}$ is the induced dipole moment of the atom and $\vec{E}$ is the electric field. The shell model of Dick and Overhauser,[110] splits the polarisable atom (which in our simulations is the oxygen atom) into a core and massless shell[1] connected by a harmonic spring, such that

$$E_{cs}(\vec{r_{cs}}) = \frac{1}{2} k_{cs} \vec{r_{cs}}^{\,2}. \tag{4.18}$$

In the above equation, k_{cs} is the spring constant. The total charge of the ion is split between a core (of charge Z+Y) and a shell (of charge -Y), the latter of which, along with k_{cs}, determine the polarizability:

$$\alpha = \frac{Y^2}{k_{cs}}. \tag{4.19}$$

Both parameters are empirically fitted to experimental properties, such as dielectric and elastic constants.

4.5 Statistical Mechanics

MD simulations provide a great amount of data at the microscopic level, such as positions and velocities of all the particles. Statistical mechanics gives the mathematical rules for the conversion of this, detailed and complex information into macroscopic equilibrium properties

---

[1] In classical MD using the adiabatic shell model, a small mass is assigned from the core to the shell, such that it can be dynamically described. The fraction of the mass is chosen to ensure that the natural frequency of vibration of the harmonic spring is well above the frequency vibration of the whole atom in the bulk system. This high vibrational frequency prevents an effective exchange of kinetic energy between the core-shell unit and remaining system.

of the system under study. As stated in the introduction to this chapter, a given point in phase space or microstate Γ, in uniquely defined by the atomic positions and momenta of the N particles in the system, $\Gamma = \{\vec{r}_i, \vec{p}_i; i = 1, 2, ..., N\}$.

The thermodynamic state, or macrostate of a system, is defined by a small set of parameters such as temperature (T), pressure (P) and N. The macrostate is characterised by a probability distribution of possible states across a certain statistical ensemble of all microstates. There exist a number of different ensembles, with different characteristics:

- *Microcanonical* ensemble (NVE): an isolated equilibrium thermodynamic system. In such a system, the macrostate has a fixed energy (E), a fixed number of atoms (N) and a fixed volume (V). The probability for every accessible microstate is equal.
- *Canonical* ensemble (NVT): an ensemble to represent the possible states of a system in thermal equilibrium with an external heat bath. The system is closed and can exchange energy with the heat bath so that various possible states of the system can differ in E. In such a system, the macrostate has a fixed number of atoms (N), a fixed volume (V) and a fixed temperature (T).
- Isothermal-isobaric ensemble (NPT): in such a system, the macrostate has a fixed number of atoms (N), a fixed pressure (P) and a fixed temperature (T).
- Grand-*canonical* ensemble (μVT): an ensemble to represent the possible states of a system in thermodynamic equilibrium (thermal and chemical) with a reservoir. The system is open, as energy and particles can be exchanged with the reservoir, therby not conserving E and N. The macrostate has a fixed chemical potential (μ), a fixed volume (V) and a fixed temperature (T).

MD simulations usually describe a system where N, V and E are always constant. This being the case, the region of phase space (hypersurface) accessible to the system is also defined. The enormous number of points in this region corresponds to the ensemble of microstates associated with that equilibrium state. The fundamental postulate of statistical mechanics is that, for an isolated system with fixed energy and dimensions (specified by the parameters N, V and E), all microstates are likely at equilibrium. Therefore, during a measurement, averaged over an observation time, the system will explore all the phase space points that are compatible with the selected parameters: this is the "quasi-ergodic" hypothesis.

4.5.1 Time & ensemble averages

If we consider the determination of a system property A and suppose that $A(\Gamma)$ is the value of A when the system is in the microstate Γ, then the system evolves in time, so that Γ and hence $A(\Gamma)$ will change. If we assume that the experimentally observable "macroscopic" property A_{obs} is really the time average of $A(\Gamma)$ taken over a long time interval, then we obtain:

$$A_{obs} = \langle A(\Gamma(t)) \rangle = \min_{t_{obs}\to\infty} \frac{1}{t_{obs}} \int\limits_{0}^{t_{obs}} A(\Gamma(t))\mathrm{d}t. \tag{4.20}$$

In MD simulations the equations of motion are solved on a step-by-step basis, so that the integral becomes a finite sum over the total number of time steps, $\tau_{obs} = t_{obs}/\Delta t$:

$$A_{obs} = \langle A(\Gamma(t)) \rangle = \frac{1}{\tau_{obs}} \sum_{\tau=1}^{\tau_{obs}} A(\Gamma(t)). \tag{4.21}$$

According to the equipartition principle, the temperature of an N-particle system is proportional to its kinetic energy,

$$\langle K \rangle = \left\langle \sum_{i=1}^{N} \frac{\vec{p_i}^{\,2}}{2m_i} \right\rangle = \frac{3}{2} N k_B T \tag{4.22}$$

where $\vec{p_i}$ and m_i are the momentum vector and the mass of particle i. Hence, through equation 4.21, we obtain,

$$T = \frac{2}{3Nk_B} \frac{1}{\tau_{obs}} \sum_{j=1}^{\tau_{obs}} \sum_{i=1}^{N} \frac{\vec{p_i}^{\,2}(j)}{2m_i}. \tag{4.23}$$

In statistical mechanics, the MD time average is replaced by an ensemble average. The statistical ensemble may be considered as a set of Γ points in phase space. Each microstate has an associated probability, $\rho(\Gamma)$, dependent on the macroscopic parameters which identify the ensemble. In practice the average properties are obtained from a snapshot of the ensemble of microstates and not from the time evolution of a single element of the ensemble. This corresponds to replacing the time average in equation 4.20 by an average over all the members of the ensemble, frozen at a particular time,

$$A_{obs} = \langle A(\Gamma) \rangle_{ens} = \sum_{\Gamma} \rho_{ens}(\Gamma) A(\Gamma), \tag{4.24}$$

where ρ_{ens} is the ensemble-dependent probability function. Under the hypothesis of ergodicity, we therefore assume that the temporal average along an MD trajectory is equal to the ensemble average. However, for typical systems, the phase space is immense and a truly ergodic trajectory is not achievable.

4.5.2 Structural properties

A wide variety of properties can be calculated from MD simulations. The radial distribution function $g(r)$ (also referred to as a partial pair-correlation function) gives the number of atoms separated by the distance r, compared with the number at the same distance expected for a completely uniform distribution (as that of an ideal gas) at the same density. The maximum value of $g(r)$ represents the most likely distance between two atoms. Each time step in an MD simulation corresponds to a specific configuration that has a unique distribution of interatomic distances. At each configuration, the number of pairs of atoms $n_p(r)$ with an interatomic distance in the interval $(r, r+\delta r)$ is calculated and repeated for all microstates in the trajectory, leading to the average number of distances $\bar{n}_p(r)$ in the specific interval according to equation 4.21. This procedure is repeated over a range of intervals in r leading to the formation of a histogram of bin width δr. Since $\bar{n}_p(r)$ is also the number of atoms found on average within a spherical shell of width δr, positioned at distance r from another another at the centre, the normalisation factor is the corresponding number of atoms that would be situated in the same volume for a uniform distribution,

$$g(r) = \frac{\bar{n}_p(r)}{V_{shell}\rho}, \tag{4.25}$$

where

$$V_{shell} = \frac{4}{3}\pi \left[(r + \delta r)^3 - r^3 \right]. \tag{4.26}$$

In the above expression, V_{shell} is the volume of the spherical shell and $p = N/V$, from equation 4.25, is the particle number density.

4.5.3 Thermodynamic properties

Under our hypothesis of ergodicity, we are using the fact that the temporal average along a trajectory generated by an MD simulation is equal to the microcanonical ensemble average. As well as structural properties such as the radial distribution function, thermodynamic properties may also be extracted from a trajectory. As we have shown, the temperature T can be obtained (see equation 4.23) where the instantaneous temperature T_{inst}, is directly related to the kinetic energy K by the equipartition formula,

$$K(t) = \frac{1}{2}\sum_{i=1}^{N} m_i|\vec{v}_i(t)|^2 = \frac{3}{2}Nk_BT_{inst}(t), \tag{4.27}$$

where k_B is the Boltzmann constant, N is the number of particles, m_i and $\vec{v}_i$ are the mass and velocity of particle i. Further to this, it should be noted that a way to alter the temperature of a system is by rescaling the velocities of the constituent particles. In the velocity Verlet algorithm (see subsection 4.2.3), this rescaling may be achieved by replacing the equation for the velocities half a time step into the future,

$$\vec{v}_{i+\frac{1}{2}} = \vec{v}_i + \frac{1}{2}\vec{a}_i\Delta t, \tag{4.28}$$

with

$$\vec{v}_{i+\frac{1}{2}} = \sqrt{\frac{T_0}{T_{inst}}}\vec{v}_i + \frac{1}{2}\vec{a}_i\Delta t, \tag{4.29}$$

where T_0 is the desired temperature. It should be noted that under such a modification, the dynamics no longer following Newton's equations and the total energy is not conserved.

The measurement of pressure in an MD simulation is based on the Clausius virial function,

$$W(\vec{r}_1, \vec{r}_2, ..., \vec{r}_N) = \sum_{i=1}^{N} \vec{r}_i \cdot \frac{\mathrm{d}\vec{p}_i}{\mathrm{d}t}. \tag{4.30}$$

The virial theorem states that the virial is equal to $3Nk_BT$. For an ideal gas, the only forces are due to interactions between the gas and the container and it can be shown that the virial is,

$$W_{ideal} = -3PV. \tag{4.31}$$

Forces between the particles in an interacting system affect the virial. The total virial for a real system equates to the sum of an ideal part and a contribution between the particles,

$$W_{real} = -3PV + \sum_{i=1}^{N} \sum_{j=i+1}^{N} \vec{r}_{ij} \frac{\mathrm{d}V(r_{ij})}{\mathrm{d}r_{ij}} = -3Nk_BT. \tag{4.32}$$

Since the force between atoms i and j is defined as,

$$-f_{ij} = \frac{\mathrm{d}V(r_{ij})}{\mathrm{d}r_{ij}}, \tag{4.33}$$

we have,

$$P = \frac{1}{V} \left[Nk_BT - \frac{1}{3} \sum_{i=1}^{N} \sum_{j=i+1}^{N} \vec{r}_{ij} f_{ij} \right]. \tag{4.34}$$

Since the forces are calculated as part of the MD simulation, little additional effort is required to compute the pressure.

Chapter 5

Crystalline phosphorus pentoxide

5.1 Overview

Crystalline phosphorus pentoxide (P_2O_5) exhibits the tetrahedral bonding coordination common to the network-forming components in phosphate-based glasses and is the simplest model of the phosphorus-oxygen network. To date, only a few first-principles and experimental studies have been carried out on a single phase of P_2O_5 [111–113] and a high pressure theoretical study of the polymorphs of P_2O_5. However, still little is known, either from experiment or theoretical calculations, of the elastic properties and how these may relate to the complex chemical bonding within the different phases. These are of importance since they relate to fundamental solid-state properties and are also linked thermodynamically to specific heat and thermal expansion. Moreover, the structural and elastic properties derived from an *ab initio* study would aid the derivation of an interatomic potential model for large-scale simulations of phosphate-based glasses.

P_2O_5 crystallizes in three known phases. The thermodynamically most stable form is $o'(P_2O_5)_\infty$, which exhibits orthorhombic symmetry with dispersively bound layering orientated parallel to the lattice **bc** plane. Six-membered rings of three corner-linked PO_4 tetrahedra make up the layers. The crystallographic symmetry is *Pnma* and the conventional unit cell contains four P_2O_5 units. The second, less thermodynamically stable orthorhombic phase, $o(P_2O_5)$ is made up from six-fold helices of PO_4 tetrahedra running parallel to the lattice **c** axis. Each of the tetrahedra share three corners with adjacent helices, thus forming a three-dimensional network. The space group is *Fdd2* and the conventional unit cell contains 56 atoms. The third known polymorph is the metastable hexagonal form $h(P_2O_5)$ made up from discrete P_4O_{10} adamantoid molecules. The molecules contain four phosphorus atoms at each vertex of a tetrahedral form. The lattice is rhombohedral with space group *R3c* and the conventional unit cell contains 84 atoms.

5.2 Theoretical Method

5.2.1 Total energy and structural calculations

The calculations were carried out using a plane-wave-pseudopotential method based on the Density Functional Theory (DFT).[83, 114] Test calculations were carried out on the $o'(P_2O_5)_\infty$ phase using the Vienna Ab-Initio Simulation Package[115–118] (version 4.6.36) with projected augmented wavefunctions[119, 120] (PAW) within the generalized gradient approximation (GGA). A kinetic energy cut-off of 900 eV was used. Further tests were performed with the Quantum ESPRESSO package[121] (version 4.1.2). Within the GGA, the exchange correlation parameterized by Perdew *et al.*[91] (PBE) was used, which is commonly implemented for electronic structure calculations in solids since it represents an accurate scheme. In the current work the introduction of the gradient correction was compared to the local density approximation (LDA) parameterized by Perdew and Zunger[122] with (DFT-D) and without (DFT) dispersive correction. DFT-D techniques[123] allow for an effective description of dispersive forces within the framework of DFT. Following the London formula, the correction models the long range attractive potential of dispersive forces in terms of a pairwise atomic potential proportional to $C_6.R^{-6}$, where R is the interatomic distance and C_6 is a semi-empirical parameter which is proportional to atomic polarizabilities and first ionization energies. The core-valence electron interactions for phosphorus and oxygen species were represented using Vanderbilt ultrasoft pseudopotentials[124] (US-PP) which have been parameterized to accurately reproduce the structure and dynamics of phosphosilicate glasses.[125] For phosphorus only the 3s3p states have been explicitly considered and for oxygen the 2s2p states. All final calculations were carried out with DFT-D and US-PP within the GGA approximation using Quantum ESPRESSO (version 4.1.2).

At a plane wave kinetic energy cut-off of 952 eV, the $o'(P_2O_5)_\infty$ lattice parameters **a**, **b** and **c** are converged to within ± 0.02 Å (0.2%), ± 0.002 Å (0.04%) and ± 0.008 Å (0.1%)

respectively. A sample elastic constant displays convergence to within 0.8 GPa when comparing the second-order elastic constant (SOEC) c_{11} calculated at 952 eV and 1088 eV. The internal energy is also fully converged at this cut-off. All calculations for the $o'(P_2O_5)_\infty$ phase are therefore carried out at a plane wave kinetic energy cut-off of 952 eV for wavefunctions and a kinetic energy cut-off of 5714 eV for charge density. The Brillouin zone is sampled using 4×4×4 grids of k points (internal energy converged to 3×10^{-4} eV) following the Monkhorst-Pack scheme.[92] Following similar lines of argument, the $o(P_2O_5)$ phase calculations are carried out at a cut-off of 1088 eV for wavefunctions and 6531 eV for charge density. Here a Monkhorst-Pack grid of 2×2×2 is used since the internal energy is converged to 5×10^{-3} eV at this level of sampling. The dispersive correction used to model each phase was parameterized with a global scaling parameter of 0.75 and a cut-off radius for dispersion interactions set at 200 a.u. as in the original implementation of the DFT-D scheme[123] (parameterized for use with the PBE-GGA functional). This parametrization was also used for test calculations within the LDA.

The static (0K) theoretical crystal structures were determined for the $o'(P_2O_5)_\infty$ phase by conducting variable cell relaxation. Experimental parameters obtained from x-ray diffraction experiments[126] were adopted as starting values for the calculations. The Hellmann-Feynman force on the atoms was minimized to within 10^{-3} a.u. and convergence achieved to within 10^{-5} a.u. for the tolerance in the total-energy difference between consecutive self-consistent field (SCF) cylces. Each SCF cycle was run until the electronic energy was converged to within 10^{-7} a.u.. The known space group was maintained during the optimization for this, the thermodynamically most stable phase. However, the structure of $o(P_2O_5)$[127] markedly lost symmetry under variable cell relaxation, hence a different optimization procedure was applied in order to establish the equilibrium geometry. The experimental **a** lattice parameter was varied keeping the **b** and **c** lattice parameters fixed. For each variation, the atoms were allowed to relax in the new fixed crystallographic unit cell. A second order polynomial was fitted to the data of internal energy versus lattice parameter **a**. The form of this polynomial was differentiated with respect to **a** and set to zero in order to solve for the value of **a** that gave the lowest internal energy. Using this new value for **a** the process was repeated for the lattice parameters **b** and **c**. Iteratively cycling this process until convergence gave an initial equilibrium geometry for this phase. This initial geometry was then used as a starting point to run a variable cell relaxation. All convergence criteria used were common for the simulation of both phases. It was noted that the $o(P_2O_5)$ phase again lost orthorhombic symmetry under full variable cell relaxation but this reduced dramatically following the stepwise optimization. γ reduced by $3.6° \times 10^{-3}$ leading to an angle reduction between lattice parameters **a** and **b**, from 90° to 89.996°. This marginal loss of symmetry was restricted to deviation in the xy plane and hence α and β remained at 90°.

5.2.2 Elastic constants calculation

Ravindran *et al.*[128] first described a theoretical formalism for the calculation of single crystal SOEC using first principle calculations for crystals of orthorhombic symmetry. SOEC describe the linear elastic strain response of a material as opposed to higher order elastic constants, which reflect nonlinear elasticity, including changes in acoustic velocities due to elastic strain. An expression for the internal energy of a crystal under strain, δ, is arrived at by a Taylor expansion of the strained crystal's internal energy, in powers of the strain tensor, with respect to the internal energy of the unstrained system as follows:

$$E(V,\delta) = E(V_0,0) + V_0 \left(\sum_i \tau_i \xi_i \delta_i + \frac{1}{2} \sum_{ij} c_{ij} \delta_i \xi_i \delta_j \xi_j \right) + O(\delta^3), \tag{5.1}$$

where the volume of the unstrained system is denoted V_0 and $E(V_0,0)$ is the unstrained internal energy. To account for the use of Voigt[129] notation the factor ξ_i has been introduced, which takes the value of 1 if the Voigt index is 1, 2 or 3 and the value of 2 if the Voigt number is 4, 5 or 6. τ_i are elements in the stress tensor.

As can be seen from the above equation, the SOEC, c_{ij}, are identified as the second order coefficients. Second order polynomial expressions (in terms of the SOEC) for the energies associated with the nine independent distortions are obtained by substituting the values of the strain matrices into the previous Taylor expansion for the internal energy. Small strains can be applied to the lattice such that the limit of elasticity is not reached. *Ab initio* calculations may be conducted to establish the ground state 0K energies for each distorted geometry and the results can be numerically fitted to polynomial equations to obtain values for the SOEC.

In order to strain the lattice, deformations were imposed according to the previously reported[128] deformation matrices for orthorhombic crystals. For each of the nine independent deformations, the limit of the maximum positive and negative strain, $\pm\delta_{\mathrm{max}}$, was increased in increments of 0.005. Polynomial fits up to 6^{th} order were conducted in order to assess the deviation in SOEC and the validity of the harmonic approximation for describing the internal energy response to the strain imposed. The sensitivity of the SOEC given by each polynomial function was assessed against the increasing maximum range of applied strain. Once the SOEC was converged to within 1 GPa, the Pearson's χ^2 test statistic was compared for each value. This test function is designed to test whether an observed frequency distribution differs from a theoretical distribution and is defined as:

$$\chi^2 = \sum_{i=1}^{N} \frac{(o_i - e_i)^2}{e_i}, \tag{5.2}$$

where o_i and e_i represent observed and expected values respectively. N is the size of the data set. The value with the lowest χ^2 value was taken as the final SOEC. For all nine SOEC of each phase it was found that a second order fit provided an accurate description for the data, with a relatively low sensitivity to $\pm\delta_{\mathrm{max}}$.

Single-point self-consistent-field (SCF) electronic calculations were carried out, in which the atomic coordinates of the deformed unit cell strictly followed the linear elastic deformations imposed. However, these unrelaxed calculations do not necessarily correspond to the equilibrium state of the deformed unit cell since the phosphorus to oxygen bond distances are not allowed to equilibrate. It is physically more realistic to allow the atoms to adjust their positions such that a lower energy minimum is found post deformation. These relaxed calculations are especially important for the shear deformations when atomic relaxation involves coordinate adjustment in all directions whilst keeping the deformed unit cell shape fixed. Orthorhombic symmetry is preserved in all deformations except for the shear deformations. For the distortions leading to SOEC c_{11}, c_{22} and c_{33} the unit cell volume is changed. For the monoclinic shear distortions leading to SOEC c_{44}, c_{55} and c_{66} as well as the orthorhombic distortions leading to SOEC c_{12}, c_{13} and c_{23}, the factors $\frac{1}{(1-\delta^2)^{1/3}}$ are introduced to the non-zero elements of the deformation matrices,[128] such that the unit cell volume is conserved.

5.3 Results and discussion

5.3.1 Total energies and structure

The total internal energy differences per P_2O_5 formula unit, for the both orthorhombic phases and differing methodologies are given in Table 5.1. The energy differences are referenced from the internal energy of $o'(P_2O_5)_\infty$, for each methodology. It is shown that, with the exception of calculations performed within the GGA without the empirical dispersive correction, all methodologies result in a more negative internal energy for the $o'(P_2O_5)_\infty$ phase. Salvado *et al.*[130] state that both orthorhombic phases are very close in terms of phase stability, ordered as $o'(P_2O_5)_\infty < o(P_2O_5)$ within the LDA, with a difference of 0.281 eV per P_4O_{10} unit (0.141 eV per P_2O_5 formula unit) from their LDA calculations. Our LDA results show the same phase stability ordering at 0K (with and without dispersive correction), with a difference of 0.177 eV per P_2O_5 formula unit for DFT-D/LDA/US-PP. The calculations of Salvado *et al.*[130] further order the phase stability as $o(P_2O_5) < o'(P_2O_5)_\infty$ within the GGA, with a difference of 0.103 eV per P_4O_{10} unit (0.052 eV per P_2O_5 formula unit). Our calculations reveal the same ordering for DFT/GGA/US-PP with an energy difference of 0.093 eV per P_2O_5 formula unit. The inclusion of the dispersive correction within the GGA leads to a reduction in the energy difference between the two phases to 0.008 eV per P_2O_5 formula unit with the $o'(P_2O_5)_\infty$ phase being the slightly more stable. The increased stability of $o'(P_2O_5)_\infty$

Table 5.1: Internal energy differences ($\Delta\mathcal{E}$) per P_2O_5 formula unit, for optimised $o'(P_2O_5)_\infty$ and $o(P_2O_5)$. Values referenced as energy differences from the internal energy of $o'(P_2O_5)_\infty$, for each methodology.

phase	$\Delta\mathcal{E}$ / P_2O_5 formula unit (eV)
	DFT/GGA/US-PP
$o'(P_2O_5)_\infty$	0
$o(P_2O_5)$	-0.093
	DFT-D/GGA/US-PP
$o'(P_2O_5)_\infty$	0
$o(P_2O_5)$	+0.008
	DFT/LDA/US-PP
$o'(P_2O_5)_\infty$	0
$o(P_2O_5)$	+0.058
	DFT-D/LDA/US-PP
$o'(P_2O_5)_\infty$	0
$o(P_2O_5)$	+0.177

Table 5.2: Simulated lattice parameters (Å) and conventional unit cell volumes (Å^3) for $o'(P_2O_5)_\infty$ and $o(P_2O_5)$ phases with comparison to x-ray diffraction data. Δ values given as percentage deviations from experiment.

				$o'(\mathrm{P_2O_5})_\infty$					
method	**a**	**Δa**	**b**	**Δb**	**c**	**Δc**	cell vol.	Δ vol.
DFT/GGA/PAW	9.692	+5.44	4.943	+1.08	7.362	+2.79	352.697	+9.55
DFT/GGA/US-PP	9.625	+4.70	4.958	+1.39	7.383	+3.08	352.319	+9.43
DFT-D/GGA/US-PP	9.245	+0.57	4.950	+1.24	7.244	+1.15	331.557	+2.98
x-ray diffraction[126]	9.193		4.890		7.162		321.959	
DFT/LDA/US-PP	8.984	-2.28	4.881	-0.17	7.072	-1.25	310.156	-3.67
DFT-D/LDA/US-PP	8.704	-5.32	4.881	-0.19	6.838	-4.52	290.500	-9.77
				$o(\mathrm{P_2O_5})$				
method	**a**	**Δa**	**b**	**Δb**	**c**	**Δc**	cell vol.	Δ vol.
DFT/GGA/US-PP	16.650	+2.06	8.179	+0.79	5.592	+6.21	761.448	+9.24
DFT-D/GGA/US-PP	16.512	+1.21	8.215	+1.23	5.320	+1.04	721.614	+3.53
x-ray diffraction[127]	16.314		8.115		5.265		697.023	
DFT/LDA/US-PP	16.193	-0.74	8.077	-0.47	5.075	-3.62	663.676	-4.78
DFT-D/GGA/US-PP	16.085	-1.41	8.044	-0.87	4.938	-6.21	638.900	-8.34

at room temperature compared to that of $o(\mathrm{P_2O_5})$ is likely dictated by entropy (as previously suggested[130]).

Optimised lattice parameters and conventional unit cell volumes are given in Table 5.2. Figures 5.1 and 5.2 show the optimised crystallographic supercells for each phase. The use of standard DFT and PAW within the GGA approximation implemented in the Vienna Ab-Initio Simulation Package is shown to overestimate the lattice parameters and unit cell volume for the $o'(P_2O_5)_\infty$ phase. Standard DFT with GGA using US-PP also overestimates the lattice parameters and gives a value for the unit cell volume that deviates from the experimental value by +9.43%.

Conversely the LDA results underestimate the lattice parameters with and without dispersive correction. We note poorer structural agreement with DFT-D within the LDA compared to DFT in the LDA. This may be explained by the fact that the dispersive term is parametrized for use with PBE-GGA. Within the GGA approximation the introduction of a dispersive correction greatly improves the agreement with experimental parameters, reducing the overestimation in the lattice parameter **a** from +4.70% to +0.57% over standard DFT techniques. Lattice parameters **b** and **c** are also in better agreement with experiment, overestimating by +1.24% and +1.15% respectively.

A feature which may account for the structural improvement with DFT-D is the presence

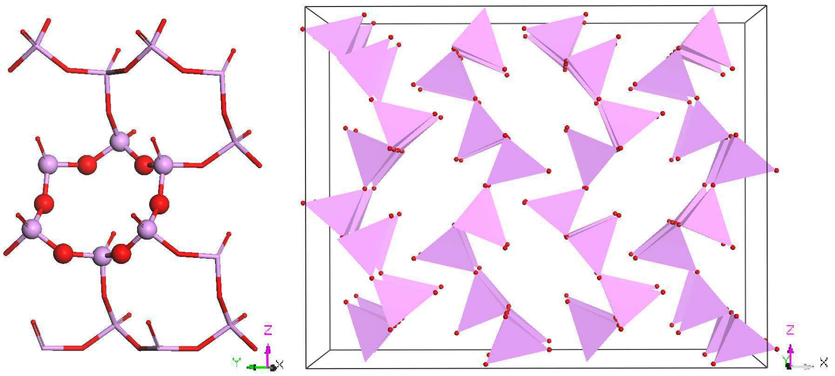

Figure 5.1: Right hand panel shows optimised (DFT-D/GGA/US-PP) 2 × 2 × 2 crystallographic supercell $o'(P_2O_5)_\infty$. Left hand panel shows single layer of supercell with six-membered phosphorus ring highlighted. Phosphorus atoms in purple and oxygen atoms in red.

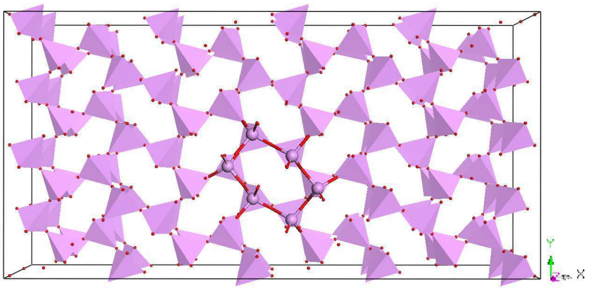

Figure 5.2: Optimised (DFT-D/GGA/US-PP) 2 × 2 × 2 crystallographic supercell $o(P_2O_5)$.

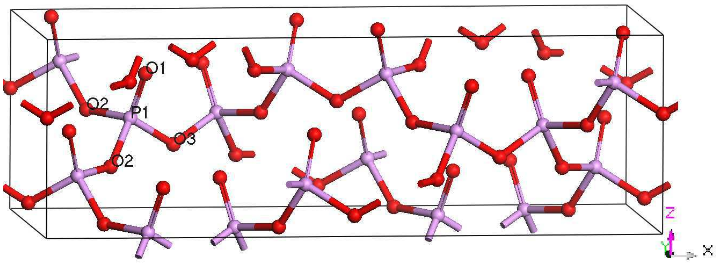

Figure 5.3: Optimised crystallographic unit cell $o(\mathrm{P_2O_5})$.

of dispersively bound layers in the most stable phase. $o'(\mathrm{P_2O_5})_\infty$ presents "hard" coordinates along the **b** lattice vector related to covalent bonding and "soft" coordinates along the lattice vector **a** ruled by non-bonding interactions. This anisotropy in bonding highlights one possible reason why the standard DFT modelling overestimates (in the case of GGA) the lattice parameter **a**, since DFT does not properly account for Van der Waals dynamical forces. The extra attractive contribution in DFT-D is likely the reason that the distance between the dispersively bound planes is reduced.

Results for the $o(\mathrm{P_2O_5})$ phase show good agreement in the lattice parameters compared

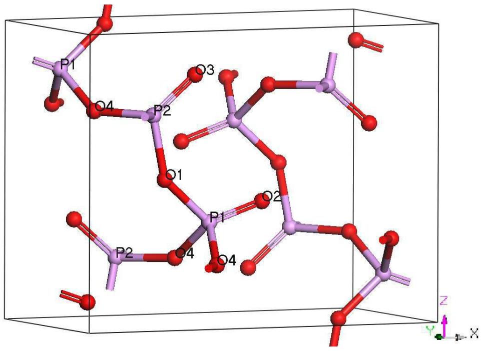

Figure 5.4: Optimised crystallographic unit cell $o'(P_2O_5)_\infty$.

Table 5.3: Simulated and experimental bond lengths (Å) for $o'(P_2O_5)_\infty$ and $o(P_2O_5)$. Δ values given as percentage deviations from experimental.

	$o'(P_2O_5)_\infty$		
Bond Length	DFT-D	Expt.[126]	Δ %
P(1)=O(2)	1.472	1.451	+1.38
P(1)-O(1)	1.591	1.566	+1.60
P(1)-O(4)	1.590	1.568	+1.40
P(2)=O(3)	1.461	1.437	+1.67
P(2)-O(4)	1.599	1.573	+1.65
P(2)-O(1)	1.599	1.574	+1.59
	$o(P_2O_5)$		
Bond Length	DFT-D	Expt.[127]	Δ %
P(1)=O(1)	1.466	1.444	+1.50
P(1)-O(2)	1.592	1.562	+1.88
P(1)-O(3)	1.611	1.582	+1.80

to experiment, with errors of +1.21%, +1.22% and +1.04% for lattice parameters **a**, **b** and **c** respectively. The conventional unit cell volume displays a discrepancy of +3.53% from the experimental value. Optimised crystallographic unit cells for each phase are shown in Figures 5.3 and 5.4. GGA characteristically underbinds and hence overestimates bond lengths. The short terminal oxygen bond and longer bridging oxygen bonds of the tetrahedral coordination are well reproduced with errors $< +2\%$ with respect to experimental results for each phase (see Table 5.3).

5.3.2 Single crystal elastic properties

The plots of internal energy deviation (from the unstrained system) versus applied strain for the nine independent SOEC of phases $o'(P_2O_5)_\infty$ and $o(P_2O_5)$ are given in figures 5.12 and 5.13. Simulated data and second order polynomial fits to data in the range $-0.03 \leq \delta \leq +0.03$ are

Table 5.4: SOEC (GPa) for $o'(P_2O_5)_\infty$ and $o(P_2O_5)$. Results from relaxed and unrelaxed calculations shown. Δ values given as percentage deviation of relaxed value from unrelaxed value. Experimental SOEC for $\alpha(SiO_2)$.

				$o'(P_2O_5)_\infty$					
method	c_{11}	c_{22}	c_{33}	c_{44}	c_{55}	c_{66}	c_{12}	c_{13}	c_{23}
relaxed	64.30	237.11	69.40	51.45	22.40	38.10	27.44	3.13	26.72
unrelaxed	453.74	359.97	346.83	117.05	194.29	136.32	76.64	142.70	65.74
Δ	-85.83	-34.13	-79.99	-56.04	-88.47	-72.05	-64.20	-97.80	-59.36
				$o(P_2O_5)$					
method	c_{11}	c_{22}	c_{33}	c_{44}	c_{55}	c_{66}	c_{12}	c_{13}	c_{23}
relaxed	147.94	107.31	38.48	34.66	8.52	41.33	42.35	12.18	33.33
unrelaxed	253.24	230.49	410.55	184.05	108.03	163.17	120.82	67.35	136.92
Δ	-40.79	-53.44	-90.63	-81.17	-92.11	-74.67	-64.94	-81.91	-75.66
				$\alpha(SiO_2)$					
method	c_{11}		c_{33}	c_{44}		c_{66}	c_{12}	c_{13}	c_{14}
Expt.[131]	87.7		106.3	59.0		40.5	6.8	12.3	18.7

shown. Both unrelaxed and relaxed results are plotted for each deformation showing significant differences. For $o'(P_2O_5)_\infty$, figures 5.12a, 5.12b and 5.12c correspond to deformations that strain the lattice along the x, y and z axis respectively. Figures 5.12d, 5.12e and 5.12f relate to volume conserving monoclinic shear distortions and Figures 5.12g, 5.12h and 5.12i to volume-conserving orthorhombic distortions. Similar sub-plots are shown in Figure 5.13 for $o(P_2O_5)$.

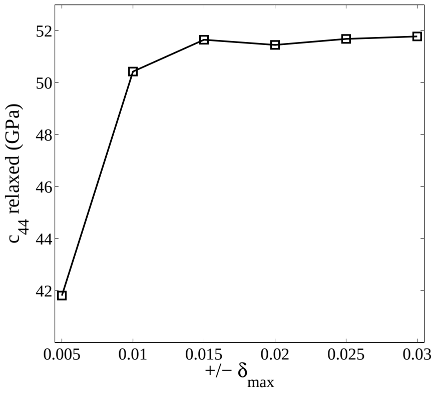

Figure 5.5: SOEC c_{44} from relaxed calculations as a function of maximum strain $\pm\ \delta_{\max}$ $o'(P_2O_5)_\infty$.

Figure 5.5 shows the sensitivity of a sample SOEC, c_{44}, to the maximum strain range imposed on the lattice. Convergence of the numeric SOEC value can be noted as the range of strain is increased. The final values of the simulated SOEC for each phase are presented in Table 5.4. It can be seen that there are substantial changes in the values of the SOEC between unrelaxed and relaxed calculations.

5.3.2.1 $o'(\mathbf{P_2O_5})_\infty$

Considering the $o'(P_2O_5)_\infty$ phase, relaxation of the atoms causes least percentage change to the value of c_{22} when comparing all SOEC. Significant reductions to c_{11} and c_{33} occur, 86% and 80% respectively. When comparing the SOEC relating to the non-volume conserving distortions along the x, y and z axes, c_{11} is the lowest and has the greatest percentage decrease under relaxation. As previously mentioned, the dispersively bound layers orientated parallel to the lattice **bc** plane lead to a "softer" response when an external force is applied parallel to the lattice **a** direction. The pure shear strains which relate to c_{44}, c_{55} and c_{66} result in a symmetry change to new space groups in the monoclinic system. Equation (5.3) shows the D_5 deformation matrix straining the lattice vectors $\vec{R}$ and introducing a z-component to the lattice parameter **a** and an x-component to the lattice parameter **c** in a volume-conserving operation.

$$\begin{aligned}\vec{R}D_5 &= \begin{bmatrix}\mathbf{a} & 0 & 0\\ 0 & \mathbf{b} & 0\\ 0 & 0 & \mathbf{c}\end{bmatrix}\begin{bmatrix}\frac{1}{(1-\delta^2)^{1/3}} & 0 & \frac{\delta}{(1-\delta^2)^{1/3}}\\ 0 & \frac{1}{(1-\delta^2)^{1/3}} & 0\\ \frac{\delta}{(1-\delta^2)^{1/3}} & 0 & \frac{1}{(1-\delta^2)^{1/3}}\end{bmatrix}\\ &= \begin{bmatrix}\frac{\mathbf{a}}{(1-\delta^2)^{1/3}} & 0 & \frac{\mathbf{a}\delta}{(1-\delta^2)^{1/3}}\\ 0 & \frac{\mathbf{b}}{(1-\delta^2)^{1/3}} & 0\\ \frac{\mathbf{c}\delta}{(1-\delta^2)^{1/3}} & 0 & \frac{\mathbf{c}}{(1-\delta^2)^{1/3}}\end{bmatrix}\end{aligned} \tag{5.3}$$

From the results it can be noted that c_{55} undergoes the largest percentage reduction upon relaxation for the shear deformations. The distortion induces a compressive force, for positive

Table 5.5: Force components ($a.u. = E_h a_0^{-1}$) on atoms involved in "double" covalent bonds pre- (un) and post-relaxation (re) for deformations $D5$ (upper section) and $D4$ (lower section) with a strain $\delta = +0.03$. $o'(P_2O_5)_\infty$ phase.

atom	F_x (un)	F_y (un)	F_z (un)	F_x (re)	F_y (re)	F_z (re)
P(1)	+0.0820	0	−0.0472	−0.0001	0	+0.0003
O(2)	−0.0548	0	−0.0297	+0.0001	0	−0.0002
P(2)	−0.0644	0	−0.0825	+0.0003	0	0
O(3)	+0.0787	0	+0.0695	0	0	+0.0003
P(1)	+0.0040	−0.0639	+0.0084	+0.0001	+0.0002	+0.0002
O(2)	−0.0012	−0.0059	−0.0005	−0.0001	+0.0001	+0.0003
P(2)	−0.0007	−0.0258	+0.0001	+0.0003	−0.0001	0
O(3)	+0.0015	+0.0094	+0.0010	+0.0002	−0.0002	0

deformations, about the terminal phosphorus to oxygen bonds. The resolved force components pre- and post-relaxation acting on the four exclusive atoms that are involved in this bonding are shown in Table 5.5. The $D5$ distortion induces a relatively “strong” resultant strain in the xz plane about the bonds in question, compared to the forces pre-relaxation for the $D4$ distortion. Each atom experiences a compressive force towards the centre of the bond as shown in Figure 5.6. Since these atoms are more tightly bound than the bridging atoms, the distortion introduced via the D_5 deformation leads to increasingly strong forces and larger changes in SOEC when moving from the strained (unrelaxed) to the unstrained (relaxed) system. Worthy of note for the final three SOEC c_{12}, c_{13} and c_{23} is that c_{13} has the highest Δ reduction of all of the nine independent SOEC (see Table 5.4). The associated strain compresses the unit cell in z and stretches in x for positive strains and vice versa for negative strains. This deformation action perpendicular to the dispersively bound planes present in this phase and along the lattice **c** direction (note relatively low values of SOEC c_{11} and c_{33} respectively) leads to the largest decrease in internal energy upon relaxation.

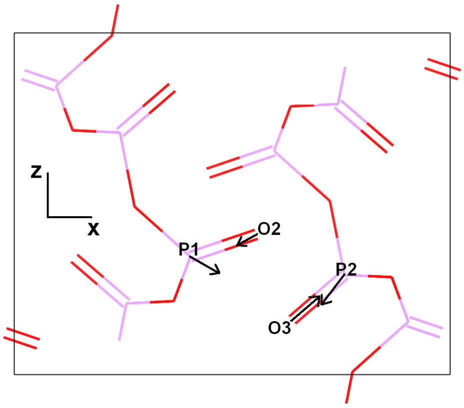

Figure 5.6: Crystallographic unit cell projected down the y axis showing the xz plane for $o'(P_2O_5)_\infty$. Resultant force vectors shown as arrows for four atoms. Lengths proportionate to relative magnitudes. Data from D5 at δ=+0.03.

5.3.2.2 $o(\mathbf{P_2O_5})$

Of the non-volume conserving distortions that lead to SOEC c_{11}, c_{22} and c_{33} the greatest percentage reduction upon atomic relaxation and lowest absolute value for relaxed calculations is that of c_{33}. The $o(P_2O_5)$ phase presents a continuous covalently bound network. The network’s six-fold helices of PO_4 tetrahedra that run parallel to the lattice **c** vector are the key structural feature that account for this relatively “soft” response to applied strain. The strain induced when expanding and contracting parallel to the z axis can be accommodated across the continuous helical structure with atomic adjustment and change to three-body angles about the bridging oxygens.

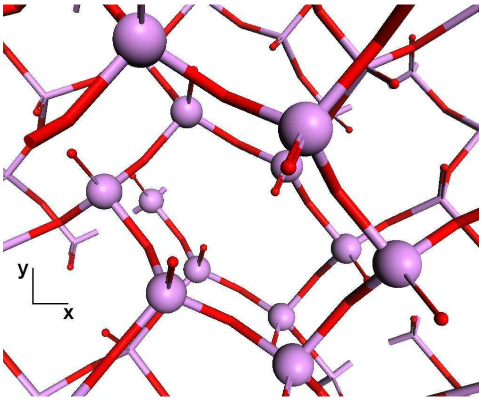

Figure 5.7: Segment of 2×2×2 supercell $o(\mathrm{P_2O_5})$ projected down the z axis.

Figure 5.7 shows a segment of the 2×2×2 supercell projected down the z axis. Twelve phosphorus atoms constituting two periods of the continuous helix are highlighted. Further analysis of the pure shear strains resulting in SOEC c_{44}, c_{55} and c_{66} shows the greatest reduction, -92.11%, upon relaxation for c_{55}. Analysis of the resolved force components for the atoms post-deformation after the first iterative SCF cycle for the $D5$ deformation shows the largest force magnitudes for the atoms involved in terminal oxygen bonding. Again, the implied higher dissociation energy of these bonds (based on bond length comparison) relative to those of phosphorus to briding oxygen atoms leads to the largest relative decrease in SOEC upon relaxation for c_{55}, as found for the $o'(\mathrm{P_2O_5})_\infty$ phase.

Of the volume conserving orthorhombic distortions D7, D8 and D9 leading to SOEC c_{12}, c_{13} and c_{23}, c_{12} is the largest value at 42.35 GPa post relaxation. The relative rigidity is due to the induced strain running perpendicular to the axis of the six-fold $\mathrm{PO_4}$ helices. When compared to c_{13} and c_{23} values, which derive from strains with compressive/tensile components parallel to the z axis, SOEC c_{12} is highest. The sum, over all 56 atoms in the unit cell, of the moduli of the z-components of the force after one SCF electronic relaxation for the $D9$ deformation at $\delta = +\ 0.03$ is 47.7 $\mathrm{eVa_0^{-1}}$. For the $D7$ deformation the same value is 19.4 $\mathrm{eVa_0^{-1}}$ showing that the magnitude of the absolute force on the atoms in this direction is a factor of 2.46 greater for the $D9$ deformation. Since the atoms experience this force in an orientation that allows relaxation across the three body angles that make up a continuous network of $\mathrm{PO_4}$ tetrahedra down the axis of the helices, there is a greater degree of freedom to relax into an even lower internal energy state. This is apparent from the greater decrease of c_{23} compared to c_{13} upon relaxation and the lower absolute value post-relaxation.

5.3.3 Polycrystalline aggregates

In samples which consist of randomly orientated polycrystals it is not possible to measure individual SOEC but aggregate average elastic properties under external load can be evaluated. By equating either the uniform strain in the aggregate to the external strain (isostrain) in the Voigt[129] (V) approximation, or the uniform stress in the aggregate to the external stress (isostress) in the Reuss[132] (R) approximation, one can calculate the polycrystalline bulk modulus (B) and shear modulus (G). For crystals with orthorhombic symmetry, B and G in each approximation are given by the following equations:

$$B_V = \frac{1}{9}(c_{11} + c_{22} + c_{33} + 2c_{12} + 2c_{13} + 2c_{23}), \tag{5.4}$$

$$\frac{1}{B_R} = (s_{11} + s_{22} + s_{33}) + 2(s_{12} + s_{13} + s_{23}), \tag{5.5}$$

$$G_V = \frac{1}{15}(c_{11} + c_{22} + c_{33} - c_{12} - c_{13} - c_{23}) + \frac{1}{5}(c_{44} + c_{55} + c_{66}), \tag{5.6}$$

$$\frac{1}{G_R} = \frac{1}{15}[4(s_{11} + s_{22} + s_{33}) + 3(s_{44} + s_{55} + s_{66}) - 4(s_{12} + s_{13} + s_{23})], \tag{5.7}$$

where c_{ij} are elements of the SOEC tensor, C and s_{ij} are elements of the compliance tensor S related by $S = C^{-1}$. The C (GPa) and S (GPa^{-1}) tensors from relaxed calculations are given in equations 5.8, 5.9, 5.10 and 5.11.

$$C_{o'(P_2O_5)_\infty} = \begin{bmatrix} +64.3002 & +27.4354 & +3.13228 & 0 & 0 & 0 \\ +27.4353 & +237.114 & +26.7236 & 0 & 0 & 0 \\ +3.13228 & +26.7236 & +69.4025 & 0 & 0 & 0 \\ 0 & 0 & 0 & +51.4537 & 0 & 0 \\ 0 & 0 & 0 & 0 & +22.4029 & 0 \\ 0 & 0 & 0 & 0 & 0 & +38.0973 \end{bmatrix} \tag{5.8}$$

$$S_{o'(P_2O_5)_\infty} = \begin{bmatrix} +0.01636 & -0.00189 & -0.00001 & 0 & 0 & 0 \\ -0.00189 & +0.00463 & -0.00170 & 0 & 0 & 0 \\ -0.00001 & -0.00170 & +0.01506 & 0 & 0 & 0 \\ 0 & 0 & 0 & +0.01943 & 0 & 0 \\ 0 & 0 & 0 & 0 & +0.04464 & 0 \\ 0 & 0 & 0 & 0 & 0 & +0.02625 \end{bmatrix} \tag{5.9}$$

$$C_{o(P_2O_5)} = \begin{bmatrix} +147.936 & +42.3532 & +12.1815 & 0 & 0 & 0 \\ +42.3532 & +107.310 & +33.3309 & 0 & 0 & 0 \\ +12.1815 & +33.3309 & +38.4781 & 0 & 0 & 0 \\ 0 & 0 & 0 & +34.6609 & 0 & 0 \\ 0 & 0 & 0 & 0 & +8.51609 & 0 \\ 0 & 0 & 0 & 0 & 0 & +41.3298 \end{bmatrix} \tag{5.10}$$

$$S_{o(P_2O_5)} = \begin{bmatrix} +0.00762 & -0.00309 & +0.00026 & 0 & 0 & 0 \\ -0.00309 & +0.01400 & -0.01115 & 0 & 0 & 0 \\ +0.00026 & -0.01115 & +0.03556 & 0 & 0 & 0 \\ 0 & 0 & 0 & +0.02885 & 0 & 0 \\ 0 & 0 & 0 & 0 & +0.11742 & 0 \\ 0 & 0 & 0 & 0 & 0 & +0.02420 \end{bmatrix} \tag{5.11}$$

Hill[133] introduced the notion that a practical estimate of the bulk and shear moduli of a polycrystalline material is obtained via calculation of the arithmetic mean of the Voigt and Reuss equations, which represent the upper and lower limits of the polycrystalline constants respectively. The moduli in Hill's approximation, B_H and G_H, are given by Equations 5.12 and 5.13.

$$B_H = \frac{1}{2}(B_V + B_R) \tag{5.12}$$

$$G_H = \frac{1}{2}(G_V + G_R) \tag{5.13}$$

Table 5.6: Isotropic bulk and shear moduli (GPa) obtained from single crystal SOEC using Voigt, Reuss and Hill's approximations (data for α(SiO$_2$) given as comparison). The Young's modulus (GPa) and the Poisson's ratio are estimated from Hill's approximation. Bulk modulus (GPa) along crystallographic axes **a**, **b** and **c**.

	B_V	B_R	B_H	G_V	G_R	G_H	E	ν	B_a	B_b	B_c
$o'(P_2O_5)_\infty$	54	35	44	43	35	39	91	0.16	69	962	75
$o(P_2O_5)$	52	34	43	31	19	25	62	0.26	208	-4183	41
$\alpha(SiO_2)$[131]			38			45		0.07			

Finally, further physical elastic properties are the Young's modulus, E, and Poisson's ratio, ν, given by Equations 5.14 and 5.15.

$$E = \frac{9B_H G_H}{3B_H + G_H} \tag{5.14}$$

$$\nu = \frac{3B_H - 2G_H}{2(3B_H + G_H)} \tag{5.15}$$

Using these equations the calculated bulk modulus, B, shear modulus, G, Young's modulus, E, and Poisson's ratio ν for each phase are summarized in Table 5.6. It can be seen that the bulk modulus for each phase in the Hill approximation is of comparable magnitude, 44 GPa for o'(P$_2$O$_5$)$_\infty$ and 43 GPa for o(P$_2$O$_5$). These values compare to the experimental bulk modulus for polycrystalline aggregrate α-quartz in the Hill approximation of 38 GPa obtained by frequency measurements of synthetic single crystal α(SiO$_2$) using the parallelepiped resonance method.[131] The larger value of G_H for o'(P$_2$O$_5$)$_\infty$, 39 GPa, compared with that of 25 GPa for o(P$_2$O$_5$) is an indication of more pronounced directional bonding between atoms in the o'(P$_2$O$_5$)$_\infty$ phase. Poisson's ratio measures the stability of a crystal against shear; $\nu \simeq$0.25 for most silicate minerals (α(SiO$_2$) is much lower due to specific structural factors)[134] since the pure-shear elastic moduli roughly equate to the sum of the off-diagonal shear moduli. Both values of ν for phosphorus pentoxide are comparable to this value and relatively small, with the o'(P$_2$O$_5$)$_\infty$ phase being even more stable to shear. Low ν values also indicate that large volume change occurs during uniaxial deformation. A final point is that for o'(P$_2$O$_5$)$_\infty$, ν=0.16, which is less than the lower limit (ν=0.25) for central-force solids and indicates that the interatomic forces in this phase are noncentral.

The bulk moduli along crystallographic directions **a**, **b** and **c** are given in Table 5.6 and calculated using the equations given in the appendix of Ravindran *et al.*[128] The values $B_a \ll$

$B_b \gg B_c$ for $o'(\mathrm{P_2O_5})_\infty$ support the analysis of the SOEC in terms of the anisotropy in chemical bonding. It is found that the unit cell volume is more resistant to change along the crystallographic direction **b** and changes more along **a** and **c** for a given external loading. The phase $o(\mathrm{P_2O_5})$ has a very low B_c value of 41 GPa which again supports the fact that loading parallel to the six-fold helices of PO_4 tetrahedra results in relatively large volume changes in the unit cell.

Using the ratio introduced by Pugh,[135] B/G, which gives the resistance to fracture (B) relative to plastic deformation resistance (G), one can analyze the ductility of a material. It is commonly accepted that a value of $B/G = 1.75$ separates brittle materials ($B/G < 1.75$) from ductile materials ($B/G > 1.75$). Interestingly $o'(P_2O_5)_\infty$ yields a value of 1.13 and $o(\mathrm{P_2O_5})$ a value of 1.72 suggesting that $o'(\mathrm{P_2O_5})_\infty$ is more brittle than the much more ductile $o(\mathrm{P_2O_5})$. Structurally this may be explained by the continuous network of bonded PO_4 tetrahedra making up the more ductile $o(P_2O_5)$ whereas the variety of chemical bonding and dispersively bound planes present in $o'(\mathrm{P_2O_5})_\infty$ make this phase more prone to irreversible structural deformation under an external load.

5.3.4 Elastic anisotropy

The elastic anisotropy of a crystal is the orientation dependence of the elastic moduli. Shear anisotropic factors describe the level of anisotropy in the bonding between atoms in different planes. The shear anisotropic factor for the (100) shear planes between the $< 011 >$ and $< 010 >$ directions is:

$$A_1 = \frac{4c_{44}}{c_{11} + c_{33} - 2c_{13}}. \tag{5.16}$$

For the (001) shear planes between the $< 101 >$ and $< 001 >$ directions it is:

$$A_2 = \frac{4c_{55}}{c_{22} + c_{33} - 2c_{23}}, \tag{5.17}$$

and for the (001) shear planes between the $< 110 >$ and $< 010 >$ directions it is:

$$A_3 = \frac{4c_{66}}{c_{11} + c_{22} - 2c_{12}}. \tag{5.18}$$

Table 5.7: Shear anisotropic factors A_1, A_2, A_3 and A_G. Compressibility anisotropic factors A_{B_a}, A_{B_c} and A_B.

	A_1	A_2	A_3	A_B	A_G	A_{B_a}	A_{B_c}
$o'(P_2O_5)_\infty$	1.62	0.35	0.62	0.22	0.11	0.07	0.08
$o(P_2O_5)$	0.85	0.43	0.97	0.21	0.24	-0.05	-0.01

For an isotropic crystal, the factors A_1, A_2 and A_3 are unity. Positive or negative deviations from this number are a measure of the degree of crystal anisotropy. In addition to the shear anisotropy, elastic anisotropy in orthorhombic systems arises from anisotropy of the linear bulk modulus. The anisotropies of the bulk modulus along the **a** lattice vector and **c** lattice vector with respect to the **b** lattice vector can be written as:

$$A_{B_a} = \frac{B_a}{B_b} \tag{5.19}$$

and

$$A_{B_c} = \frac{B_c}{B_b}, \tag{5.20}$$

respectively. As before, deviation of A_{B_a} and A_{B_c} from unity indicates a degree of elastic anisotropy. A further scheme by Chung and Buessem[136] describes the percentage anisotropy in compressibility and shear, defined as:

$$A_B = \frac{B_V - B_R}{B_v + B_R} \tag{5.21}$$

and

$$A_G = \frac{G_V - G_R}{G_V + G_R}, \tag{5.22}$$

respectively. For values of zero the material is completely isotropic whereas values of one represent the largest possible anisotropy. Table 5.7 summarizes these values for each phase, showing that both phases display a significant degree of shear and elastic anisotropy.

5.3.5 Valence charge density and Löwdin charges

Analysis of the distribution of valence charges is necessitated by the complex chemical bonding within this material which leads to the elastic anisotropy in the lattice. Figure 5.8 shows contours for the valence electron charge density in the (040) plane for $o'(P_2O_5)_\infty$. This directly bisects the centres of a sequence of bonded atoms from terminal oxygen to phosphorus to bridging oxygen to phosphorus to terminal oxygen. The valence charge topology shows a relatively localised density about the phosphorus atoms and charge density propagating further from the oxygens atoms, which suggests that a certain degree of covalency is present in the material.

As can be seen from the iso-contours the oxygen atoms display increased polarization and charge density is smeared towards the phosphorus atoms for both bonding and terminal oxygens. Table 5.8 gives the Löwdin atomic charges for each phase. The values for oxygen lie in the range $-0.78 \leq Q_L \leq -0.67$ for P_2O_5. This compares to a value of $Q_L=-1.43$ for oxygen in crystalline MgO, computed at the PBE-D level with US-PP at a plane wave kinetic energy cut-off of 30 eV using a Monkhorst-Pack grid of 5×5×5. The atomic charges for $o'(P_2O_5)_\infty$ and $o(P_2O_5)$ thus illustrate that the crystals have iono-covalent bonding character.

5.3.6 Electronic band structure and density of states

The total energy of the material is determined primarily from the densities of states below the Fermi level. The energy versus k in the first Brillouin zone for $o'(P_2O_5)_\infty$ is plotted in Figure 5.9 along the special lines between the points $\Gamma \rightarrow Z \rightarrow T \rightarrow Y \rightarrow \Gamma \rightarrow X \rightarrow S$. The top four valence and lowest four conduction bands are displayed. For $o'(P_2O_5)_\infty$ the valence band and conduction band edges occur at different k-values (Γ and Z for conduction and valence respectively) from which the indirect band gap of 4.97 eV is measured. The direct

Table 5.8: Löwdin atomic charges for $o'(P_2O_5)_\infty$ and $o(P_2O_5)$.

			$o'(P_2O_5)_\infty$			
Atom	P(1)	P(2)	O(1)	O(2)	O(3)	O(4)
Q_L	+2.16	+2.13	-0.71	-0.78	-0.74	-0.69
			$o(P_2O_5)$			
Atom	P(1)		O(1)	O(2)	O(3)	
Q_L	+2.12		-0.75	-0.69	-0.67	

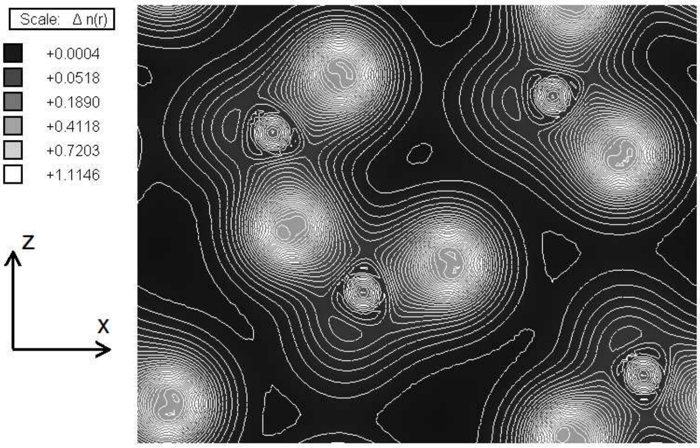

Figure 5.8: Valence electron charge density ($\frac{1}{V}$) in (040) plane for $o'(P_2O_5)_\infty$. Square root scaling function applied.

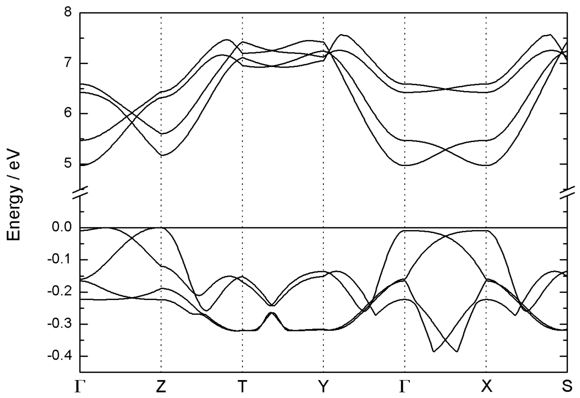

Figure 5.9: Electronic band structure for $o'(P_2O_5)_\infty$. Band energies calculated at 1×10^{-2} intervals between special points. No interpolation applied. 4 highest valence bands and 4 lowest conduction bands displayed. Zero energy set as top of valence band.

band gap from the total electronic density of states (EDOS) (see Figure 5.10) is ~4.8 eV. This compares favourably with previous calculations of the band gap performed with DFT in the LDA approximation by Abarenkov *et al*[112] which yielded a value of 5 eV. However, due to approximations assumed in the construction of DFT functionals, this band gap is much smaller than experimental data. Figure 5.11 shows the band structure for $o(P_2O_5)$ giving a direct band gap at special point Γ of 5.19 eV. Both phases are therefore insulators. Overall the EDOS for each phase are very similar, implying that there are common structural properties defining the systems. The components of the *s* and *p* states (for each atomic species) of the EDOS are plotted in Figure 5.10. For the $o'(P_2O_5)_\infty$ phase the upper valence bands are formed almost

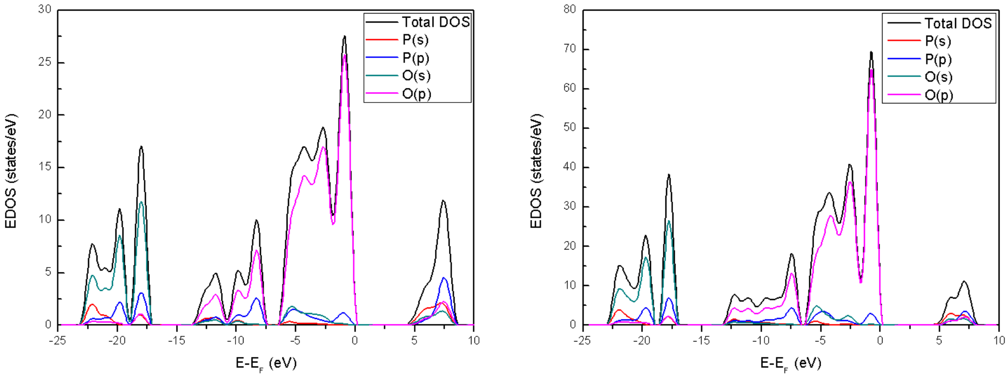

Figure 5.10: Total and partial Kohn-Sham electronic density of states for $o'(P_2O_5)_\infty$ (left hand panel) and $o(P_2O_5)$ (right hand panel). The Fermi level has been put at the zero energy. Methfessel-Paxton (order 1) 0.68 eV gaussian broadening applied.

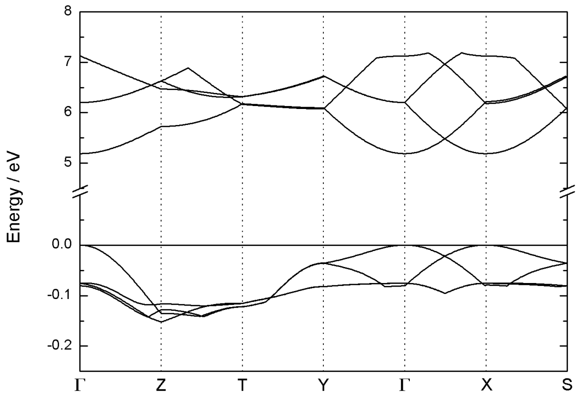

Figure 5.11: Electronic band structure for $o(P_2O_5)$. Band energies calculated at $1{\times}10^{-2}$ intervals between special points. No interpolation applied. 4 highest valence bands and 4 lowest conduction bands displayed. Zero energy set as top of valence band.

entirely from oxygen *p* states with an admixture of phosphorus *p* and oxygen *s* states. The lower valence band (-23 eV$\leq$ E-E$_F$$\leq$-17 eV) is composed dominantly of oxygen *s* states with an admixture of phosphorus *p* and *s* states. The conduction band has a dominant contribution from the phosphorus p states. For the $o(P_2O_5)$ phase the upper and lower valence bands are dominated by the same orbitals with admixtures in similar proportions to $o'(P_2O_5)_\infty$. The conduction band is formed from phosphorus and oxygen *s* and *p* states.

5.4 Summary

No previous theoretical or experimental work is reported on the mechanical properties of crystalline P_2O_5. We have performed a comprehensive set of electronic structure calculations to determine the mechanical properties of this material. We have studied the total internal energies and equilibrium lattice parameters for the two most thermodynamically stable phases $o'(\mathrm{P_2O_5})_\infty$ and $o(\mathrm{P_2O_5})$. Comparing DFT and DFT-D we have found that the addition of the dispersive correction is essential for the accurate structural description of $o'(\mathrm{P_2O_5})_\infty$. A full suite of nine independent SOEC are reported for each single crystal phase and the elastic anisotropy has been analysed in terms of resolved force components. Polycrystalline aggregate properties have been calculated with comparison made to $\alpha(SiO_2)$, showing similar bulk properties. Electronic band structures and densities of states have been calculated and show both phases to be insulators with band gaps $\sim$ 5 eV. Löwdin charges and valence charge density analysis have shown both phases to have mixed ionic and covalent bonding.

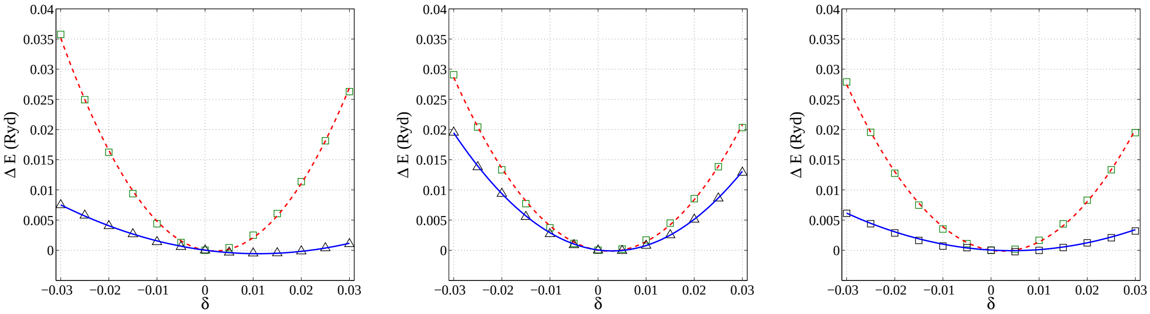

(a) $E(V,\delta) - E(V_0,0) = V_0(\tau_1\delta + (\frac{c_{11}}{2})\delta^2)$

(b) $E(V,\delta) - E(V_0,0) = V_0(\tau_2\delta + (\frac{c_{22}}{2})\delta^2)$

(c) $E(V,\delta) - E(V_0,0) = V_0(\tau_3\delta + (\frac{c_{33}}{2})\delta^2)$

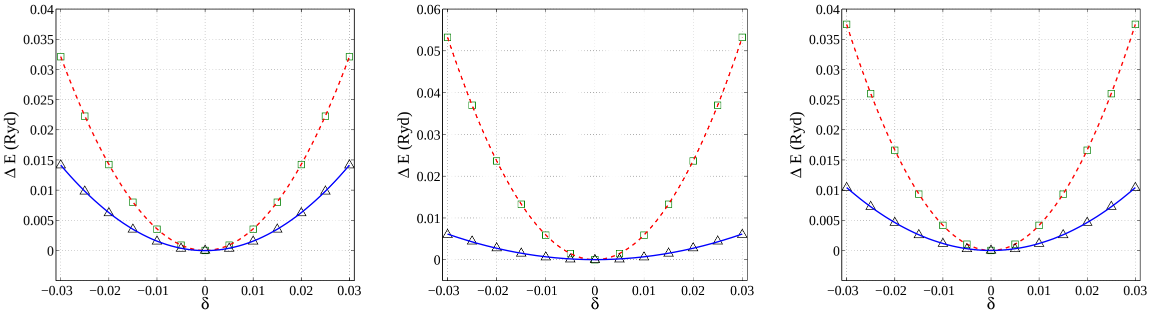

(d) $E(V,\delta) - E(V_0,0) = V_0(2\tau_4\delta + (2c_{44})\delta^2)$

(e) $E(V,\delta) - E(V_0,0) = V_0(2\tau_5\delta + (2c_{55})\delta^2)$

(f) $E(V,\delta) - E(V_0,0) = V_0(2\tau_6\delta + (2c_{66})\delta^2)$

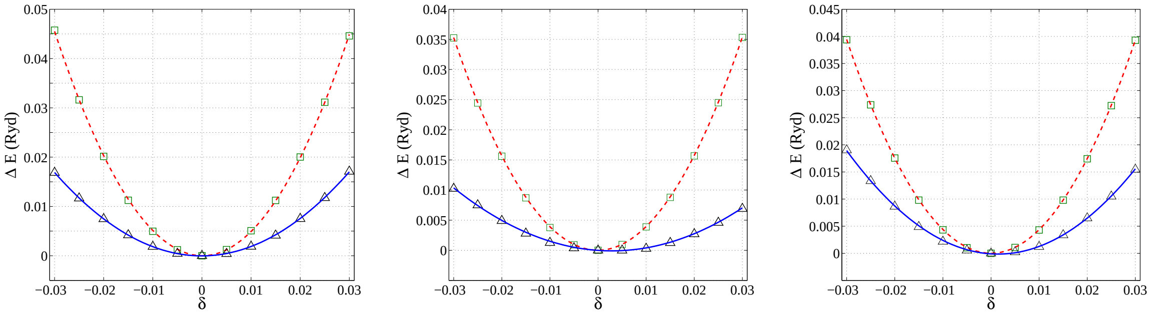

(g) $E(V,\delta) - E(V_0,0) = V_0((\tau_1 - \tau_2)\delta + \frac{1}{2}(c_{11} + c_{22} - 2c_{12})\delta^2)$

(h) $E(V,\delta) - E(V_0,0) = V_0((\tau_1 - \tau_3)\delta + \frac{1}{2}(c_{11} + c_{33} - 2c_{13})\delta^2)$

(i) $E(V,\delta) - E(V_0,0) = V_0((\tau_2 - \tau_3)\delta + \frac{1}{2}(c_{22} + c_{33} - 2c_{23})\delta^2)$

Figure 5.12: Deviation in internal energy from unstrained system versus applied strain for $o'(P_2O_5)_\infty$.

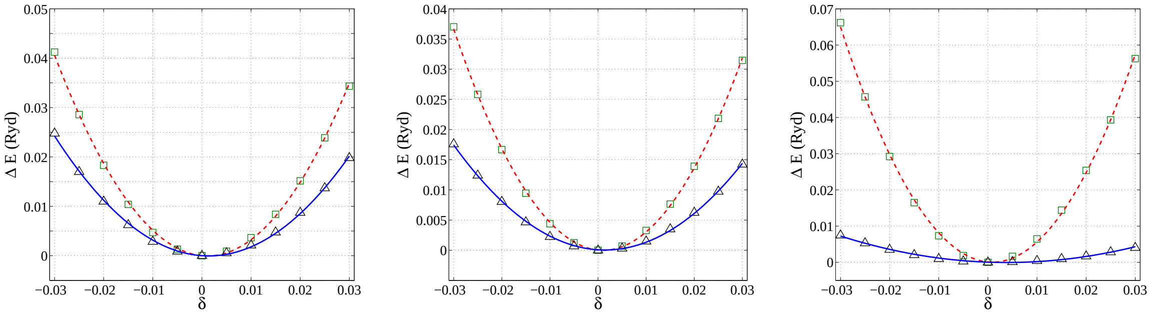

(a) $E(V,\delta) - E(V_0,0) = V_0(\tau_1\delta + (\frac{c_{11}}{2})\delta^2)$ **(b)** $E(V,\delta) - E(V_0,0) = V_0(\tau_2\delta + (\frac{c_{22}}{2})\delta^2)$ **(c)** $E(V,\delta) - E(V_0,0) = V_0(\tau_3\delta + (\frac{c_{33}}{2})\delta^2)$

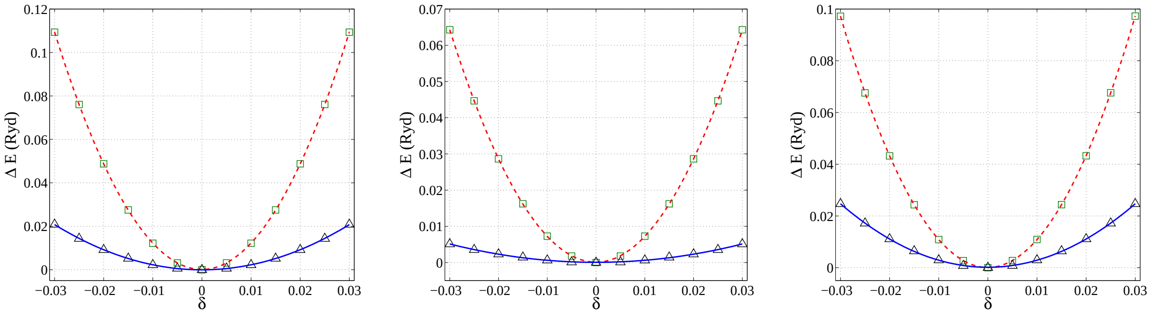

(d) $E(V,\delta) - E(V_0,0) = V_0(2\tau_4\delta + (2c_{44})\delta^2)$ **(e)** $E(V,\delta) - E(V_0,0) = V_0(2\tau_5\delta + (2c_{55})\delta^2)$ **(f)** $E(V,\delta) - E(V_0,0) = V_0(2\tau_6\delta + (2c_{66})\delta^2)$

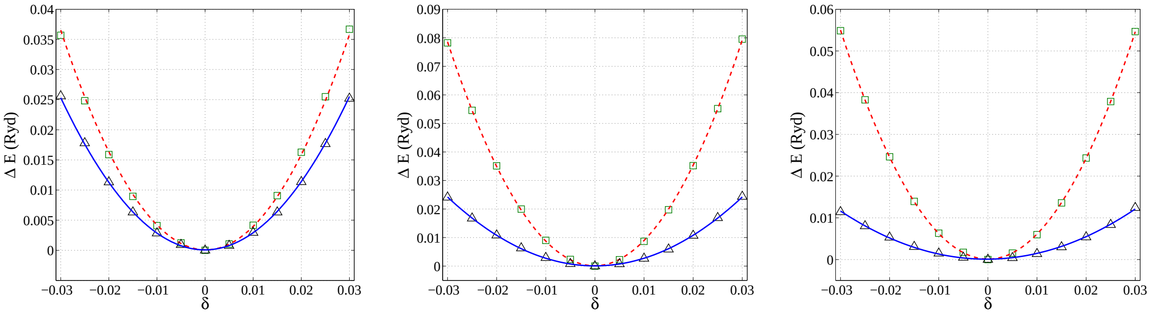

(g) $E(V,\delta) - E(V_0,0) = V_0((\tau_1 - \tau_2)\delta + \frac{1}{2}(c_{11} + c_{22} - 2c_{12})\delta^2)$ **(h)** $E(V,\delta) - E(V_0,0) = V_0((\tau_1 - \tau_3)\delta + \frac{1}{2}(c_{11} + c_{33} - 2c_{13})\delta^2)$ **(i)** $E(V,\delta) - E(V_0,0) = V_0((\tau_2 - \tau_3)\delta + \frac{1}{2}(c_{22} + c_{33} - 2c_{23})\delta^2)$

Figure 5.13: Deviation in internal energy from unstrained system versus applied strain for $o(P_2O_5)$.

Chapter 6

Amorphous P_2O_5-CaO-Na_2O systems

6.1 Overview

Despite the limited biomedical use of “undoped” phosphate-based glasses in the system, P_2O_5-CaO-Na_2O, they have been extensively studied experimentally and a sound knowledge, of how the atomic structure influences biocompatablity, is of importance. Since this undoped system forms the backbone of many compositions, that can be tailored with other dopants to better fulfil specific clinical needs, knowledge of the structural drivers behind composition dependent materials properties trends, are of transferrable importance. However, it must be noted that contradictory *in vitro* and *in vivo* biocompatability studies (see subsection 2.2.1), do not exclude PBG (with the absence of a dopant to modify dissolution characteristics) from potential biomedical applications.

6.1.1 Experimental probing techniques

The structural properties of undoped PBG systems have been investigated extensively using experimental probing techniques. X-ray diffraction produces broad features from the disordered structures and the presence of sharp diffraction peaks evidences the presence of crystalline components. High-energy diffraction can be used to probe the local structure through the Fourier Transform of the diffraction pattern to give the radial distribution function. Decomposition of the latter into partial distribution functions provides information about the short-range order of the atoms. Spectroscopic techniques are local probes which can provide information about the structure on the order of nearest neighbour and next nearest neighbours. Vibrational methods such as Fourier transform infrared (FTIR) and Raman spectroscopies are based on the absorption and scattering of electromagnetic radiation at different wave-numbers owing to different chemical groups of a molecule. They can confirm the presence of specific structural units in glasses and can be used to provide information towards explaining variations in thermophysical properties of phosphate glasses as a function of composition. X-ray spectroscopic (XAS) techniques are element specific and allow the characterization of the local environment and electronic structure of particular atoms in a wide range of materials. XAS are typically considered in two parts, firstly the X-ray absorption near-edge structure (XANES) region, which can provide information on local symmetry around the excited element and its speciation. Further to this the extended X-ray absorption fine structure (EXAFS) region, at threshold energies greater than those required for electron release, provides information on local chemical environments (the chemical nature of neighbouring atoms, together with coordination shell distance and numbers). Finally, solid state magic angle spinning nuclear magnetic resonance (MAS NMR) is an element-specific local probe that is extensively used to probe phosphate-based systems, in particular ^{31}P MAS NMR. ^{31}P has a large magnetic moment and hence one of highest receptivities of any nucleus. The nuclear properties coupled with 100% natural abundance makes ^{31}P a very sensitive nucleus. It is a spin $-\frac{1}{2}$ nucleus and therefore strongly affected by the chemical shielding interaction, resulting from the electronic density around the nucleus modifying the magnetic field experienced by the nucleus. This modification of the resonant frequency of the nucleus is termed the “chemical shift”. When there are multiple phosphorus sites, as is the case in many modified phosphate systems such as PBG and d-PBG, the broadening caused by the anisotropy produces severe overlap between different environments, which often prevents unambiguous resolution of the different sites. In order to remove the anisotropy and improve resolution, the powder sample can be rotated at a frequency of kHz at an angle of 54.7° to the main static magnetic field, a technique referred to as magic angle spinning (MAS). In such spectra, the Q^n distribution, where n represents the number of “bonded” oxygens associated with each phosphorus atom (that is oxygens which in turn bond to another phosphorus atom), can be distinguished on the basis of their differing isotropic chemical shifts. These are of structural significance and correlate with the physiochemical properties of the glass.

6.1.2 Structural & thermodynamic properties from experiment

Owing to the wealth of different metal ions and associated dopants that can be incorporated,[12] many experimental synthesis and structural characterisation studies exist for PBG, that assess the influence of such dopants as compared to an undoped ternary reference system. As a result, there is a great amount of data pertaining to undoped ternary PBG and this introduction presents experimental results from the two main studies for the melt-quench derived compositions simulated in this chapter.

Ahmed *et al.*[18] synthesised $(P_2O_5)_{0.55-x}(CaO)_{0.40-y}(Na_2O)_{1-((0.55-x)+(0.40-y))}$ ($x = 0.00$, 0.05 and 0.10 and $y = 0.00$, 0.05 and 0.10 with all combinatorial permutations) via the melt-quench procedure. ^{31}P NMR analysis was performed on all final glass structures to obtain the phosphorus Q^n distributions along with complementary X-ray powder diffraction (XRPD) to identify the main crystalline phases in glass samples annealed above the glass transition temperature. Their results identified solely Q^1 and Q^2 species for all 9 compositions, with a significant composition dependent trend for $(P_2O_5)_{0.45}$ systems. It was found that Q^2 increased from 78.29% in P45C30N25 to 79.87% in P45C35N20 and finally 82.96% in P45C40N15 with a concomitant decrease in Q^1. This increase in network connectivity (NC - defined as the mean n number of the Q^n distribution) is corroborated in other studies of the same compositions[76] and thought to evidence a key structural property governing the dissolution rate trends (outlined in Chapter 2.2.1). $(P_2O_5)_{0.50}$ and $(P_2O_5)_{0.55}$ compositions were found to comprise 96%+ Q^2 with the remainder being Q^1 phosphorus with no significant CaO/Na_2O ratio dependent Q^n trends. XRPD analysis of the $(P_2O_5)_{0.45}$ systems identified the phases $Na_4Ca(PO_3)_6$, $NaCa(PO)_3$ and $Ca_2P_2O_7$ attributed to Q^2, Q^2 and Q^1 respectively. Analysis of $(P_2O_5)_{0.50}$ and $(P_2O_5)_{0.55}$ systems showed the presence of three crystalline phases all attributed to Q^2, consistent with the NMR derived Q^n distributions. The authors further state, that the Q^1 species identified in $(P_2O_5)_{0.45}$ compositions are phosphate dimers which would increase the packing density relative to the other systems and link they this to thermal data. Thermal analysis was carried out using a differential thermal analyser (DTA), which showed that the glass transition temperatures (T_g - the temperature at which an equilibrium liquid passes through the metastable supercooled liquid state to become a non-equilibrium glass) increased with increasing CaO/Na_2O ratio. T_g was also observed to increase with increasing P_2O_5 content between the $(P_2O_5)_{0.45}$ and $(P_2O_5)_{0.50}$ compositions and subsequently decrease for like $(P_2O_5)_{0.55}$ compositions.

Carta *et al.*[76] have further investigated the compositions $(P_2O_5)_{0.45}(CaO)_x(Na_2O)_{0.55-x}$ (x = 0.30, 0.35 and 0.40) from melt-quench synthesis using FTIR. The spectra are given in Figure 6.1 and it is stated that vibrations in the range 1400-500 cm^{-1} are mainly due to the phosphate network. All the symmetric and asymmetric stretching vibrations of the phosphate network observed are characteristic of Q^1 and Q^2 groups. Absorption bands ν_{as}(P-O-P) and ν_s(P-O-P) occurring at 900 and 750 cm^{-1} are assigned, respectively, to the asymmetric and symmetric stretching of the bridging oxygen atoms bonded to a phosphorus atom in a Q^2 phosphate tetrahedron. The band at 1300-1250 cm^{-1} is assigned to asymmetric stretching modes, $\nu_{as}(PO_2)$, of the two non-bridging oxygen atoms bonded to a Q^2 phosphorus. It is stated that the vibrations of terminal groups P-O^- caused by the action of modifier oxides on the network, can be observed at 1000 cm^{-1}. Finally, the bands at around 550 cm^{-1} are ascribed to deformation modes of P-O^-, δ(P-O^-).

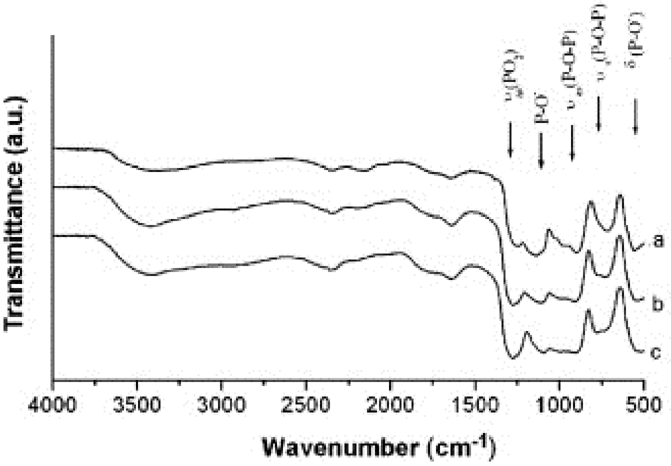

Figure 6.1: Infra-red spectra in the range 500-4000 cm^{-1} for melt-quench derived PBG (a) P45C30N25, (b) P45C35N20 and (c) P45C40N15.[76]

The results from FTIR are consistent with the deconvolution of ^{31}P MAS NMR spectra, from the same work, given in Figure 6.2. The two primary peaks centered on the isotropic chemical shifts, $\delta_{shift} = -6.3$ ppm and $\delta_{shift} = -22.2$ ppm for P45C30N25 correspond to resonances for Q^1 and Q^2 groups respectively. Both these values undergo a downfield shift to lower frequencies with increasing CaO/Na_2O ratio. The Q^n speciation and ratios were obtained using Gaussian functions with the Dmfit2002 NMR software and range from 78% to 79% and 90% Q^2 for P45C30N25, P45C35N20 and P45C40N15 respectively.

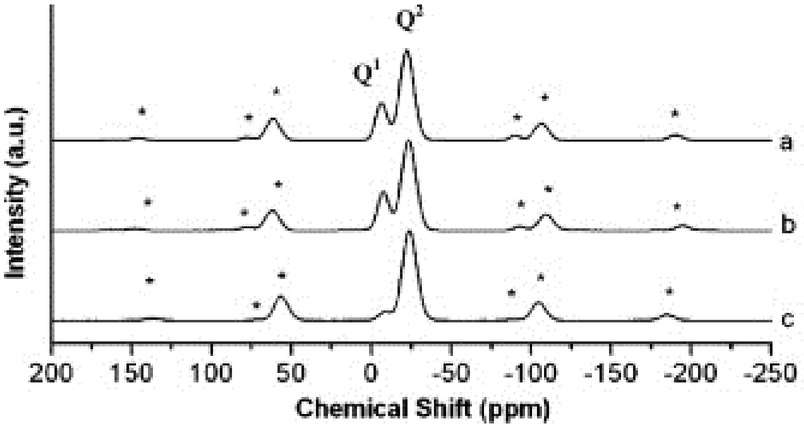

Figure 6.2: ^{31}P MAS NMR spectra for melt-quench derived PBG (a) P45C30N25, (b) P45C35N20 and (c) P45C40N15 (* denotes a spinning side band).[76]

6.1.3 Modelling PBG, PSBG & binary phosphate glasses

At the start of this PhD, published theoretical simulations of PBG and d-PBG were limited to a single paper,[15] although a substantial body of theoretical work existed on silicate-based bioglasses.[13, 14] There had also been a limited number of classical simulations of phosphate glasses mainly focusing on binary systems.[137–139]

$(P_2O_5)_{0.45}(CaO)_x(Na_2O)_{0.55-x}$ (x = 0.30, 0.35 and 0.40) PBGs have been simulated using *ab initio* molecular dynamics techniques by Tang *et al.*[15]. CPMD simulations were carried out using the Quantum Espresso code[121] (version 4.0.1) and periodic cell sizes of $\sim 10\text{Å}^3$ containing 88-90 atoms. The structures were generated using a melt-quench procedure in 10 consecutive NVT runs from 3000K to 300K reproducing a nominal cooling rate of 20 $K.ps^{-1}$. A short- and medium-range structural characterisation of the 300K trajectory was carried out showing good agreement with available experimental data. The Q^n distribution showed a prevalence of Q^2 ($\sim$ 61% – 78% across all three compositions) and Q^1 ($\sim$ 22% – 28% across all three compositions) speciation. Small quantities of othophosphate Q^0 and chain-bridging Q^3 phosphorus were noted in P45C30N25 and 5.6% Q^3 in P45C40N15. It should be noted that uncertainty is likely high due to the limited statistical sampling. FWHM values for the P-O-P angular distribution functions were shown to decrease from 24° in P45C30N25 to

16° in P45C40N15 (with increasing CaO/Na_2O ratio) with significant P-P variation. It is stated that an effect of increased CaO/Na_2O ratio is an increase in the "rigidity" of the P-O-P connectivity despite no clear linear dependency in the three mean P-P distances or O-P-O ADF peak centered positions.[1] Finally, it was found that Na^+ and Ca^{2+} coordinate to ~ 6 and 7 oxygen atoms respectively, decomposition of which, showed preferential bonding to NBO's over BO's for both ions.

Extensive theoretical simulations of bulk,[125, 142, 143] surface,[144] hydrated surface[145–147] and clustered[148] amorphous phosphosilicate systems have been undertaken. Two significant bulk simulation studies using classical techniques are directly linked to, and referenced in, the original work presented in this chapter and will be briefly summarised. The first of which is a molecular dynamics study of pure silica, sodium silicate and soda-lime silicate glasses.[149] The authors developed a formal-charge, polarizable force field based on the interatomic potential derived by Sanders *et al.*[150] for quartz. Two-body Buckingham potentials for Ca-O and Na-O were parameterized by fitting to the structures of $Na_2Ca(SiO_3)_2$ and $Na_2Ca_2(SiO_3)_3$. The rigid ion (RI) force field of Teter (potential parameters reported in [149]) was used to generate the glasses from a melt held at 6000K for 100 ps and subsequently quenched to 300K at a rate of 10 $K.ps^{-1}$. The 300K structure was then used as a starting structure for a 100 ps shell-model simulation at the same T (the last 80 ps of which were considered for structural analysis). In conjunction to these ~1500 atom RI and SM simulations, CPMD calculations were also performed for the soda-lime silicate composition, $(SiO_2)_{0.75}(CaO)_{0.15}(Na_2O)_{0.10}$, using a system containing 114 atoms. As was done for SM calculations, an initial glass was generated using the RI model in the NVT ensemble and then run for 11.8 ps using CPMD. Structural and vibrational properties were then analysed for each generated glass. It was shown that both RI and SM methodologies accurately reproduced the experimental density of the modified glasses and that significant improvements in the description of the local environment

---

[1] A similar conclusion is reached by Carta and co workers[76] based on the downfield shift in ^{31}P NMR Q^1 and Q^2 resonances with increasing CaO/Na_2O ratio (incorrectly said to increase covalency in P-BO and P-NBO bonds) and the physically implausible "charge balancing" argument. It is stated that Na^+ can interact with one bridging oxygen while Ca^{2+} can interact with two non-bridging oxygens on two different chains acting as a cross link and increasing "rigidity". This does not taking into account the complex three-dimensional distorted octahedral geometry occupied by the modifier ions Ca^{2+} and Na^+ which, as shown by Tang *et al.*[15] and the current reported simulations, coordinate to both NBO and BO (see Section 6.4.3.1 and Table6.8). Further structural analysis is discussed by Christie *et al.*.[140] Finally, the postulated increase in covalency (i.e. a shortening of P-BO and P-NBO bond lengths) with increasing CaO/Na_2O ratio is in contrast to experimental results for P50C40N10, P50C50 and P50N50 glasses[141] and also possibly in contradiction with the current simulated data (see Table 6.7) specifically for $r_{(P-NBO)}$, which may lengthen with increased CaO/Na_2O ratio.

surrounding Na^+ and Ca^{2+} were obtained by the use of the SM (using the CPMD glass as a high quality reference system). A significant result of the methodological comparisons was that the Q^n distribution for the network forming silicon of the sodium silicate glass generated by the SM, was found to be in much better agreement with experiment, than that of the RI model. A second directly relevant study was carried out by Tilocca *et al.*[151] and constituted the simulation of three compositions of phosphosilcate glasses, using an extended version of the aforementioned SM force field. In order to describe the P-O interaction, a two-body Buckingham potential was fitted to the structures of α-Na_3-PO_4, β-$Ca_3(PO_4)_2$ and $NaCaPO_4$. A screened harmonic three-body potential for the O-P-O system was parameterized as per Sastre *et al.*[152] for silicon aluminophosphates. The melt-quenched glasses were structurally analysed at the short- and medium-range as well as analysis of ion aggregation and modifier clustering. The results showed that phosphate groups are predominantly isolated as Q^0 orthophosphate units (all three compositions contained 6 wt% P_2O_5) in agreement with experimental data and that the silicate network is dominated by Q^2 and Q^3 sites. It was also shown that phosphate cross-links the silicate network with increased silica content. Regions containing a high density of phosphate groups which attract modifier cations were identified , leading to the formation of cation-rich orthosphosphate domains somewhat separated from the cation-poor silicate chains. Such simulations show that it is possible to model complex multicomponent phosphosilicate glasses using empirical interatomic potentials and derive structures in reasonable agreement with experimental data.

Binary lithium phosphate glasses in the system $(P_2O_5)_{1-x}(Li_2O)_x$ $(0 \leq x \leq 0.5)$ have been studied by molecular dynamics simulations using an RI partial-charge force field.[137] A Lennard-Jones-type two-body potential was employed to describe the short-range P-O interaction and simple three-body harmonic terms were used to model the O-P-O and P-O-P interactions. All potentials were fitted to the three known structures of crystalline P_2O_5. Analysis of the melt-quench derived glasses shows that there is a general trend of decreasing mean $\bar{r}_{(P-O)}$ from 1.57 Å for $x = 0.0$ to 1.53 Å for $x = 0.5$. The corresponding P-O stretching frequencies are expected to increase as the P-O bond shortens and this is consistent with the experimentally observed trend of the major Raman stretching band at $\sim 655 cm^{-1}$ of the phosphate series.[153] T_g was calculated, by analysis of the change in slope in the linearly-regressed V-T data, to be 628K compared to the experimentally observed 653K. Lithium was found to have a depolymerizing effect on glass network from an analysis of the Q^n distribution for phosphorus as a function of the compositional value of x. Of methodological consideration, it was shown that as the quench rate was varied from 7.1×10^{11} K.s^{-1} to 4.0×10^{11} K.s^{-1} and then to 2.0×10^{10} K.s^{-1}, for v-P_2O_5 (i.e. x = 0), the simulated proportion of Q^3 in the final glass improved from 47% to 55% and finally 60% respectively. However, v-P_2O_5 is known to be a fully connected continuous network of phosphate tetrahedra in which the proportion of Q^3 = 100%. The RI potential derived glass is still shown to poorly reproduce the medium-range structure for x = 0.0 even using the slowest quench rate and the same is true for other compositions at higher quench rates.

Tischendorf *et al.*[138] have used the same force field, incorporating a newly parameterized Zn-O potential, to model binary zinc phosphate glasses in the system $(P_2O_5)_{1-x}(ZnO)_x$ ($0.4 \leq x \leq 0.7$). Relevant structural (CN, G(r) and g(r)) and thermal (ρ and T_g) properties were analysed as a function of x. Simulated glass densities were found to be in good agreement with experimental values, deviating slightly for higher values of x, postulated to be due to poor Zn-O two-body parameterisation or the choice of simulation cell size and quench rate. As with experiment, T_g is minimized for the composition x = 0.6 and the compositional dependence is linked to network depolymerisation and zinc CN. Finally, it was shown that long-range order in the form of rings and chains exists for compositions close to x = 0.5. These structures become isolated non-bridging phosphate tetrahedra as compositions approach x = 0.7.

6.2 Force field development

The force field developed in this work is based on the Born-Mayer ionic model[109] (including short-range repulsive, dispersive attractive and long-range Coulombic interactions) employing full ionic charges. Interactions between ions i and j are expressed through the Buckingham potential combined with the electrostatic energy as given in Equation 6.1 (in atomic units),

$$E_{ij}(r_{ij}) = A_{ij} \exp\left(\frac{-r_{ij}}{\rho_{ij}}\right) - \frac{C_{ij}}{r_{ij}^6} + \frac{q_i q_j}{r_{ij}} \tag{6.1}$$

where A_{ij}, ρ_{ij} and C_{ij} are the Buckingham potential parameters of the i-j interaction, r_{ij} is the distance between ions i and j and q_i is the charge of ion i. Cubic periodic boundary conditions are used with the Buckingham terms evaluated in real space with a cut-off of 8 Å.

The oxygen-oxygen potential derived by Sanders *et al.*[150] is employed, where the polarization of the oxide ions is incorporated through the shell model potential of Dick and Overhauser,[110] in which the total charge of the ion is split between a core (of charge Z+Y) and a shell (of charge -Y), which are coupled by a harmonic spring with spring constant k_{cs}, $E_{cs}(r_{cs}) = \frac{1}{2}k_{cs}r_{cs}^2$.

In this model, all short-range and Coulombic forces act on the shell, whereas only Coulombic forces act on the cores. For each ion, the shell is Coulombically screened from the core; thus the shells are polarized by the surrounding ions. The environment-dependent polarizability therefore explicitly depends on k_{cs}, the charge of the shell (-Y) and the forces acting on the shell due to other ions.

The Coulomb energy is ill-defined for periodic three-dimensional materials and the energy density of interaction increases rather than decays with distance. Conditions of charge neutrality and zero dipole moment are imposed to yield a convergent series with a well-defined limit as per the method of Ewald.[108] The accuracy of electrostatic summations is defined as the number of converged significant figures in the electrostatic energy and is set to 10^{-8} for these calculations. Three-body forces are included through a harmonic potential,

$$E(\theta) = \frac{1}{2}k_{3b}(\theta - \theta_0)^2, \tag{6.2}$$

where θ_0 is the reference bond angle and k_{3b} is the three-body force constant.

6.2.1 Fitting strategy

The phosphorus-oxygen (P-O_s) two-body, oxygen-phosphorus-oxygen (O_s-P-O_s) and phosphorus-oxygen-phosphorus (P-O_s-P) three-body potentials, are derived by empirical fitting, via a "brute force" methodology, to experimental structural[126] and first-principles mechanical data[154] for the $o'(P_2O_5)_\infty$ crystalline phase. The scan over parameter space for the two-body interaction focuses on parameters close to those reported by Tilocca *et al.*[151] to model phosphosilicate bioglass. The three-body parameters are scanned around those by Liang *et al.*,[137] (used to model phosphate materials), which have been fitted to the three known phases of crystalline phosphorus pentoxide.

Static constant-pressure structural optimizations are carried out, using the General Utility Lattice Program (GULP) code[155] with a Broyden-Fletcher-Goldfarb-Shanno (BFGS) algorithm (recognised as an efficient optimizer), to minimise the internal energy of the system and relax the structure to zero strain. Starting with the experimental lattice parameters and fractional atomic coordinates[126] for orthorhombic $o'(P_2O_5)_\infty$ (see Figure 6.3), optimizations have been carried out for each parameterization of the P-O_s, O_s-P-O_s and P-O_s-P potentials using the "brute force" fitting code given in Appendix B.1. Differing functional forms were constructed, such as the summation over all lattice parameters of percentage errors between the lattice parameters of classically optimized and experimental unit cells, $\text{F.Q.}_{(\text{lattice})}=\Delta\mathbf{a}+\Delta\mathbf{b}+\Delta\mathbf{c}$, as shown in Figure 6.4 upper panel. Figure 6.4 lower panel shows a surface plot of the summation of sample bond length errors, defined as $\text{F.Q.}_{(\text{bonds})}$=Δ(P1-O1)+Δ(P1-O2)+Δ(P1-O4)+Δ(P2-O1)+Δ(P2-O3)+Δ(P2-O4).

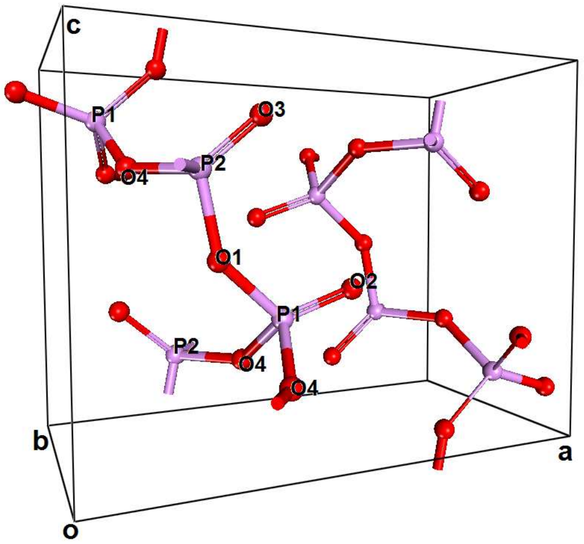

Figure 6.3: $o'(P_2O_5)_\infty$ unit cell from X-ray diffraction at 288K. Phosphorus atoms in purple and oxygen atoms in red.

Minimization of F.Q. is carried out in order to find the optimal parameterization that correctly reproduces the experimental and theoretical reference data. In order to reflect the structural and mechanical sensitivities to potential parameterizations and the relative uncertainties in the reference data, a combined error function was defined. With respect to the P-O_s potential, each unit cell bond length, lattice parameter and second order elastic constant (SOEC) was linearly weighted in proportion to the range of percentage error deviation between 1000 eV $\leq A \leq$ 1200 eV and 0.32 Å $\leq \rho \leq$ 0.36 Å. The structural observable weighting coefficients for $\text{F.Q.}_{(\text{lattice})}$ and $\text{F.Q.}_{(\text{bonds})}$ were normalised to unity. Mechanical observable coefficients for $\text{F.Q.}_{(\text{SOEC})}=\Delta(c_{11})+\Delta(c_{22})+\Delta(c_{33})+\Delta(c_{44})+\Delta(c_{55})+\Delta(c_{66})+\Delta(c_{12})+\Delta(c_{13})+\Delta(c_{23})$, were normalized to 0.1 to reflect the increased uncertainty in SOEC,[154] calculated via the numerical method of polynomial fitting to the energy strain relation. These weighting coefficients were then used to define combined error functions and subsequently minimized. An analogous procedure was subsequently followed in order to parameterize O_s-P-O_s and P-O_s-P potentials whilst keeping all other parameterization fixed.

Further validation of the final force field was carried out via the incorporation of two-body potentials describing Na-O_s and Ca-O_s interactions previously parameterized by Tilocca *et al.*[149] (used to model phosphosilicate bioglass in conjunction with the Sanders *et al.*[150] O_s-O_s two-body potential). Subsequently, static optimizations of tetragonal sodium orthophosphate, $\alpha(Na_3PO_4)$[156] and orthorhombic calcium sodium orthophosphate, $NaCaPO_4$[157] were carried out to validate the force field.

6.2.2 Force field & implementation

The final parameterization of the force field is given in Table 6.1. Due to the divergence of the r^{-6} term in the Buckingham potential ($V(r)$) as $r \rightarrow 0$, the O_s-O_s turns over at $r = 0.867$ Å. In our simulations the O_s-O_s interaction is extrapolated to positively infinite values for very low r, deviating from the quoted parameterization at interatomic distances less than $r_d = 0.952$ Å, which arbitrarily represents the numerically larger solution at 70% of the value of $V(r)$ at the maximum. The modified form at $r < r_d$, $V_{mod} = \frac{A}{r^B}$, is parameterized such that $V|_{r_d} = V_{mod}|_{r_d}$ and $(\frac{dV}{dr})|_{r_d} = (\frac{dV_{mod}}{dr})|_{r_d}$. This prevents non-physical forces at small interatomic distances which is of particular importance in high temperature dynamics trajectories.

In the adiabatic shell method,[158] a small fraction of the core mass is ascribed to the corresponding shell, in order to permit a dynamical description of both. In our simulations, the mass is split as $O_c = 15.8$ a.u. and $O_s = 0.2$ a.u., such that the frequency of the core-shell motion is high enough not to couple with the ionic frequency and therefore avoid exchange of energy. In test simulations at 2500 K, shell temperature spikes to over 4000 K were observed, possibly due to the use of three-body potentials. The use of cut-offs can create discontinuities in the forces acting on the shells, which can be solved by frictional damping. The amplitude of shell oscillation is constrained via a frictional damping term linear in velocity.

Equation 6.3 shows the frictionally damped equation of motion for O_s (including only force contributions from the core-shell interaction),

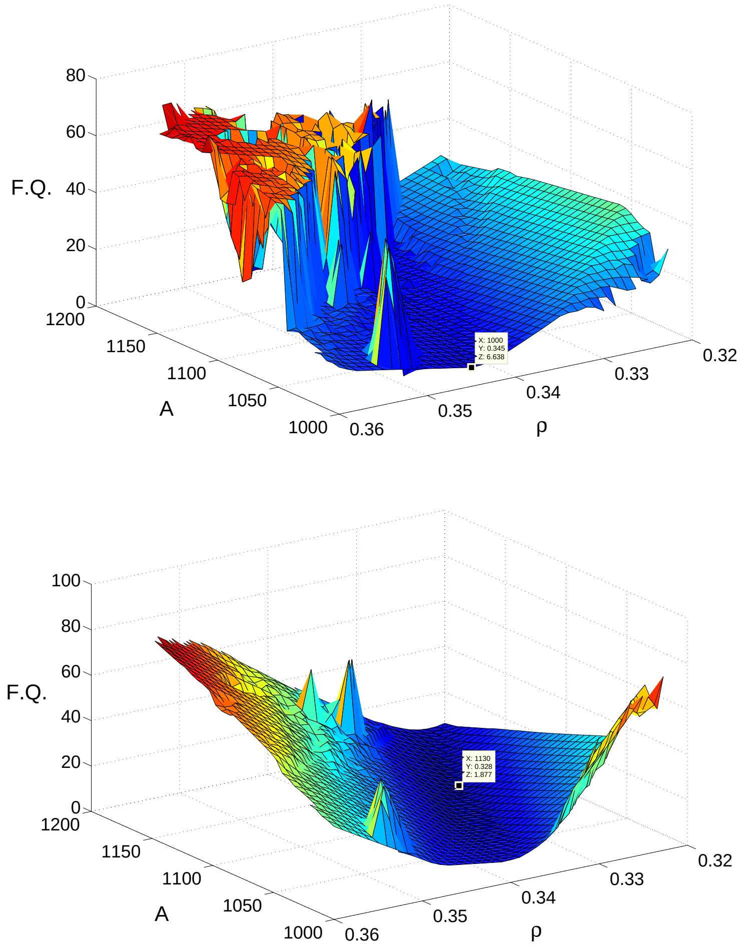

Figure 6.4: Surface plot of error functions $\mathrm{F.Q.}_{\mathrm{(lattice)}}$ (upper panel) and $\mathrm{F.Q.}_{\mathrm{(bonds)}}$ (lower panel) against A and ρ two-body parameters for P-O_s interaction (C = 0.03 eV.Å^6). Static optimization of $o'(P_2O_5)_\infty$ with all other interactions as stated in Table 6.1. Data cursors show location of minima. Generated with code given in Appendix B.

$$m_s \frac{d^2x}{dt^2} + c\frac{dx}{dt} + k_{cs}x = 0, \tag{6.3}$$

where m_s is the mass of the shell (0.2 a.u.), x is the shell displacement from the core along the core-shell axis, c is the damping coefficient and k_{cs} is the core-shell spring constant (74.92 eV.Å^{-2}). The shell frequency dependence on the parameterization of c was investigated at 2500 K via the fast Fourier transform (FFT) algorithm in MATLAB. The core-shell distance for a single core-shell unit, in the $(P_2O_5)_{0.45}(CaO)_{0.30}(Na_2O)_{0.25}$ composition, was extracted at every timestep (0.2 fs) for 2 ps at 2500 K. The signal was then recentered about the mean O_c-O_s distance and subsequently filtered for low amplitude noise via the inverse fast Fourier

Table 6.1: Formal charge shell-model force field used in this work. Buckingham two-body, harmonic three-body and core-shell potentials.

	$Ae^{-\frac{r}{\rho}} - Cr^{-6}$		
	A(eV)	ρ (Å)	C (eV.Å^6)
P-O$_s$	1020.0000	0.34322	0.0300
O$_s$-O$_s$[150]	22764.30	0.14900	27.88
Na-O$_s$[149]	56465.3453	0.193931	0.0
Ca-O$_s$[149]	2152.3566	0.309227	0.099440
	$\frac{1}{2}k_{3b}(\theta - \theta_0)^2$		
	k_{3b}(eV.rad^{-2})	θ_0(°)	
O$_s$-P-O$_s$	3.3588	109.470000	
P-O$_s$-P	7.6346	141.179333	
	$\frac{1}{2}k_{cs}r^2$		
	k_{cs}(eV.Å^{-2})	O$_c$ (e)	O$_s$ (e)
O$_c$-O$_s$[150]	74.92	+0.8482	-2.8482

transform (IFFT) algorithm. An FFT was subsequently carried out on the corrected signals at different values of c^2. The results of this analysis are presented in Table 6.2.

Table 6.2: Dominant shell frequencies and corresponding amplitudes for different damping coefficient parameterization. Sample core-shell unit at 2500 K.

c^2	Frequencies(THz)	Amplitudes(Å)
0	1.0, 3.0	0.0165, 0.0120
5	1.0, 1.5	0.0120, 0.0080
10	1.0, 4.0	0.0145, 0.0055
15	0.4, 1.5	0.0180, 0.0127
20	0.4, 1.5	0.0090, 0.0080
25	1.0, 3.0	0.0180, 0.0080
30	1.0, 2.0	0.0112, 0.0090
35	1.0, 3.5	0.0090, 0.0055
40	1.0, 2.0	0.0120, 0.0090
45	0.5, 2.5	0.0205, 0.0040
50	1.0, 3.0	0.0165, 0.0145
55	1.0, 5.0	0.0056, 0.0056
60(critical)	1.0, 2.3	0.0090, 0.0090

It is noted that increased damping leads to lower summed amplitudes. For damping $c^2 < 20$, unphysical shell temperature spikes were noted at 2500 K, hence all calculations were run with frictional damping parameterized at $20 \leq c^2 \leq 23$ ($\frac{1}{3}$ critical).

6.3 Computational details

6.3.1 Static and dynamical simulations of crystals

$o'(P_2O_5)_\infty$, $\alpha(Na_3PO_4)$ and $NaCaPO_4$ structures were optimized at 0 K using the GULP code[155] (version 3.1). The optimized lattice parameters and atomic coordinates for $o'(P_2O_5)_\infty$ were then used to generate a $4\times4\times4$ supercell for a molecular dynamics (MD) simulation. The MD run was performed in the constant volume and temperature (NVT) canonical ensemble at 300K using the DL_POLY code[103] (version 2.20). An Evans[159] thermostat was used and the timestep between successive integrations of the Newtonian equation of motion set to 0.2 fs. The system was equilibrated for 50 ps followed by a production run of 150 ps, during which time structural information was sampled.

6.3.2 Glass preparation

The compositions studied in this work are given in Table 6.3. For the P45C30N25 composition, a periodic cubic simulation box with a total of 3001 atoms (600 phosphorus, 1867 oxygen, 334 sodium and 200 calcium atoms) was generated. The experimentally observed density of 2.560 g.cm^{-3}[76] was used, such that the cubic simulation box was fixed to side 34.65 Å. For all compositions the atoms were randomly inserted into the box under the constraint that all P-O distances were no less than 90% of the phosphorus to terminal oxygen bond length previously reported by Tang *et al.*[15] for P45C30N25. All other initial atom-atom distances were constrained analogously to prevent non-physical forces between the atom pairs during initial phases of the simulation. Oxygen shells were inserted at the same initial coordinates as the corresponding cores. The systems were minimized for 10 ps at 0 K using the modified version[149] of the DL_POLY code (version 2.20) and were then heated to 2500 K and held in an NVT trajectory for 50 ps using the Evans thermostat so as to ensure a suitable sample melting. The melting was verified by checking the absolute and mean-square displacements of the ions. The systems were subsequently continuously cooled to 300 K in 11 NVT trajectories to reproduce a cooling rate of 5.50 K.ps^{-1}. In order to mimic thermal expansion, a density correction of factor 0.95 was applied to the configurations run at 2500 K and 2300 K and a factor of 0.975 applied to the configurations run at 2100 K and 1900 K. The configurations at 1700 K, 1500 K, 1300 K, 1100 K, 900 K, 700 K, 500 K and 300 K were run at the experimental

Table 6.3: Compositions simulated. $(P_2O_5)_{0.45}(CaO)_x(Na_2O)_{0.55-x}$.

x	Atoms	Cell size (Å)	Density ($g.cm^{-3}$)
0.30	3001	34.65	2.56
0.35	2998	34.69	2.57
0.40	3001	34.71	2.59

density. At 300 K, the systems were equilibrated for 50 ps, followed by a production run of 150 ps, during which time data were sampled.

6.3.3 Gas-phase complexes

Density functional theory (DFT) calculations were performed with the DMol^3 code[160–162] for various calcium and sodium phosphates complexes in gas-phase. DMol^3 implements DFT using localised atom-centered numerical orbitals. The electronic structure was described using the Perdew-Burke-Ernzerhof (PBE)[91] approximation and all-electron double-numeric-polarised (DNP) basis sets on all atoms. This basis set is variationally comparable to the 6-31G(d.p) basis set, but the numerical functions are far more complete than the traditional Gaussian functions. Owing to the quality of these orbitals, basis set superposition effects are minimized,[160, 162] and it is possible to obtain an excellent description, even of weak bonds. Each basis function was restricted to a large cut-off radius of 6.5 Å in order to properly describe the diffuse nature of the wave-function of the phosphate anions. The electron density was approximated using a multi-polar expansion up to octopole.

6.4 Results and discussion

6.4.1 Static simulations of $o'(P_2O_5)_\infty$, $\alpha(Na_3PO_4)$ and $NaCaPO_4$

The results of the constant-pressure 0 K optimizations are shown in Table 6.4. The $o'(P_2O_5)_\infty$ phase shows an absolute unit cell volume error of approximately 4%, an improvement on previous non-polarizable force fields. Inclusion of the potentials for Na-O and Ca-O and the subsequent optimization of $\alpha(Na_3PO_4)$ and $NaCaPO_4$ validate the complete force field's ability to describe accurately the structure of phosphate-based materials that include Na and Ca atoms. The 0 K optimized short-range structural properties, including bond lengths and three-body angles, along with mechanical properties (SOEC and bulk modulus), are presented

Table 6.4: Lattice parameters (Å), unit cell volume (Å^3) and associated percentage errors (compared with experiment), of various structures simulated with our force field.

	a	**b**	**c**	V
$o'(P_2O_5)_\infty$				
XRD[126]	9.193	4.890	7.162	322
this work	8.693	4.945	7.184	309
Δ	-5.44	+1.12	+0.31	-4.07
Teter[163]	8.623	5.073	6.921	302
Δ	-6.20	+3.74	-3.36	-6.21
$\alpha(Na_3PO_4)$				
XRD[156]	10.811	10.811	6.818	797
this work	10.772	10.772	6.793	788
Δ	-0.36	-0.36	-0.37	-1.09
$NaCaPO_4$				
XRD[157]	20.397	5.412	9.161	1011
this work	21.218	5.399	9.159	1049
Δ	+4.03	+0.24	-0.02	+3.74

in Table 6.5. All phosphorus to oxygen bond distances are described to within 2.7% absolute accuracy when compared with experimental data. The force field (employing a single P-O two-body potential) successfully distinguishes between the shorter, P=O phosphorus to non-bonded oxygen (NBO) and longer, P-O phosphorus to bonded oxygen (BO) bonds, with errors of -0.48% and -0.90% for the P=O bonds.

A reproduction of the relations between the nine independent SOEC is achieved. The bulk modulus in the Hill approximation (B_{Hill}) is 39 GPa compared to a value of 44 GPa from first-principles data,[154] which is in good agreement.

6.4.2 Molecular dynamics simulations of $o'(P_2O_5)_\infty$ at 300 K

Selected average distances and three-body angles for $o'(P_2O_5)_\infty$ simulated at 300 K are given in Table 6.6. Data are taken from the MD production trajectories at 300 K. Experimental data for $o'(P_2O_5)_\infty$, obtained at 233 K using XRD[126] are given for comparison.

The simulated first coordination peak for the phosphorus to oxygen radial distribution function (RDF), not presented here, represents $r_{(P=O)}$ and is located at 1.440 Å. This equates to an error of -0.56% when compared to experimental data. $r_{(P-O)}$ is located at 1.602 Å (+2.04%). The simulated $r_{(P-P)}$ value is 2.965 Å (+0.10%) and $r_{(O-O)}$ is 2.558 Å (+1.47%). These results are in good agreement with the experimental data obtained at 233 K.[126]

Table 6.5: 0 K optimization. $o'(P_2O_5)_\infty$ bond lengths (Å), three-body angles (°) and second order elastic constants (GPa) with associated percentage errors (compared with experiment).

	XRD[126]	this work	Δ
P1-O1	1.566	1.604	+2.42
P1=O2	1.452	1.445	-0.48
P1-O4	1.568	1.592	+1.53
P2-O1	1.574	1.616	+2.67
P2=O3	1.437	1.424	-0.90
P2-O4	1.573	1.613	+2.54
O1-P1=O2	119.032	118.743	-0.24
O1-P2=O3	119.144	118.855	-0.24
O1-P2-O4	99.060	97.623	-1.45
O4-P1=O2	113.527	112.758	-0.68
O4-P1-O4	101.641	100.631	-0.99
O4-P1-O1	103.357	105.036	+1.62
O4-P2=O3	116.779	118.591	+1.55
P1-O1-P2	143.744	134.909	-6.15
P1-O4-P2	139.897	134.623	-3.77
	DFT-D[154]	this work	
c_{11}	64.30	36.67	
c_{22}	237.11	223.25	
c_{33}	69.40	54.56	
c_{44}	51.45	33.63	
c_{55}	22.40	12.74	
c_{66}	38.10	5.38	
c_{12}	27.44	20.91	
c_{13}	3.13	11.07	
c_{23}	26.72	43.36	
B_{Hill}	44	39	

As shown in Chapter 5, $o'(P_2O_5)_\infty$ displays mixed ionic and covalent characteristics with Löwdin atomic charges in the range -0.78 $\leq q_L \leq$ -0.69 for oxygen and +2.13 $\leq q_L \leq$ +2.16 for phosphorus.[154] However, the current potential parameterizations used in conjunction with formal charges does not adversely affect the short-range order, specifically regarding $r_{(P=O)}$, $r_{(P-P)}$ and $r_{(O-O)}$, which are very well reproduced with absolute errors below 1.50%. Short-range order uncertainty for periodic crystalline materials obtained by XRD techniques are typically of the order of ± 0.02 Å. $\theta_{(O-P-O)}$ and $\theta_{(O-P=O)}$ three-body angles are also in good agreement with experiment, whereas $\Delta(\theta_{(P-O-P)})$ = -5.25%.

Table 6.6: 300 K dynamics. Selected average distances, r (Å) and angles, θ (°). $o'(P_2O_5)_\infty$ Experimental x-ray diffraction (XRD) results given as comparison.

	XRD[126]	this work	Δ
$r_{(P=O)}$	1.440	1.432	-0.56
$r_{(P-O)}$	1.570	1.602	+2.04
$r_{(P-P)}$	2.962	2.965	+0.10
$r_{(O-O)}$	2.521	2.558	+1.47
$\theta_{(O-P-O)}$	101	101.53	+0.52
$\theta_{(O-P=O)}$	117	117.61	+0.52
$\theta_{(P-O-P)}$	142	134.54	-5.25

Table 6.7: 300 K dynamics. Selected average distances (Å) and angles (°). $(P_2O_5)_{0.45}(CaO)_x(Na_2O)_{0.55-x}$ (x = 0.30, 0.35 and 0.40). Experimental data, obtained via neutron (ND) and x-ray (XRD) diffraction along with nuclear magnetic resonance (NMR), for a range of vitreous phosphate systems are given for comparison.

	P45C30N25	P45C35N20	P45C40N15	P50N50[164]	P45C30N25[76]	P50C40N10[141]
	this work	this work	this work	XRD	XRD	ND & NMR
$r_{(P=O)}$	1.485	1.486	1.487	1.50 ±0.025	1.52 ± 0.02	1.49 ± 0.02
$r_{(P-O)}$	1.623	1.622	1.613	1.64 ±0.025	1.60 ± 0.02	1.60 ± 0.02
$r_{(O-O)}$	2.543	2.543	2.543		2.54 ± 0.02	2.52 ± 0.02
$r_{(P-P)}$	3.040	3.041	3.039		2.95 ± 0.02	2.93 ± 0.02
$r_{(Na-O)}$	2.353	2.371	2.363		2.41 ± 0.02	2.33 ± 0.02
$r_{(Ca-O)}$	2.334	2.333	2.329		2.40 ± 0.02	2.34 ± 0.02
$\theta_{(O-P-O)}$	108.65	108.67	108.99			
$\theta_{(P-O-P)}$	134.50	134.56	134.52	130		

6.4.3 Molecular dynamics simulations of $(P_2O_5)_{0.45}(CaO)_x(Na_2O)_{0.55-x}$ $(x = 0.30, 0.35$ and $0.40)$ systems at 300 K

6.4.3.1 Short-range structure

For each simulated glass, the starting configuration is randomized and melted at 2500 K. The large volume of configurational space that can be explored at these energies while allowing energy barriers between potential-energy basins to be crossed, makes the high temperature melt-quench protocol a sound test for any new force field. Table 6.7 shows selected average distances at 300K for all three compositions of PBG studied in this work (P45C30N25, P45C35N20 and P45C40N15) and summarizes the peak positions of all RDFs and angular distribution functions (ADFs). Hoppe *et al.*[165] have reviewed experimental data relating to phosphate glass and shown P-O distances to be sensitive to the molar ratio $(n(Me_{2/v}O)/n(P_2O_5))$ composition in a range of binary metaphosphate systems (including CaO-P_2O_5 and Na_2O-P_2O_5), where Me is the modifier cation. At a molar ratio of 1.22 their linearly extrapolated $r_{(P=O)}$ and $r_{(P-O)}$ values are 1.475 Å and 1.617 Å, respectively. For the three pyrophosphate compositions simulated in this work, a molar ratio of 1.22, taken as $[n(CaO)+n(Na_2O)]/n(P_2O_5)$, yields mean values, across all three compositions, of $\mu(r_{(P=O)}) = 1.486$ Å and $\mu(r_{(P=O)}) = 1.619$ Å. Carta *et al.*[76] have studied these compositions using high energy X-ray diffraction (XRD) and found for P45C30N25 that, $r_{(P=O)} = 1.52$ Å ± 0.02 Å and $r_{(P-O)} = 1.60$ Å ± 0.02 Å. However, the authors note that the analysis of short-range structure in complex glass systems using XRD is complicated, due to the overlap in correlations and they have subsequently fitted their data to other experiments.

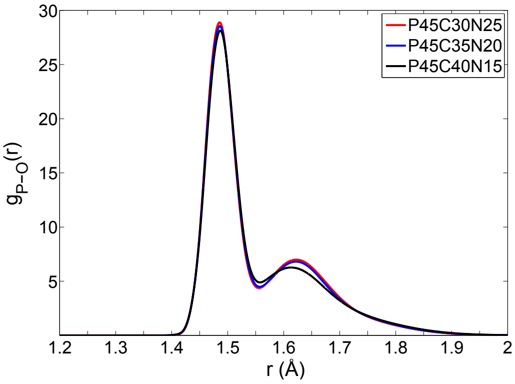

Figure 6.5: P-O radial distribution function averaged over 300K trajectory.

Figure 6.5 shows the RDF for the phosphorus to oxygen separation. The force field describes the split between $r_{(P=O)}$ at 1.485 Å and $r_{(P-O)}$ at 1.623 Å for P45C30N25 and a small linear increase in $r_{(P=O)}$ is noted with increasing Ca^{2+}/Na^+ compositional ratio. $r_{(P-O)}$ displays a maximum value of 1.623 Å for the P45C30N25 composition, which decreases with increasing Ca^{2+}/Na^+ (see Table 6.7). Pickup *et al.*[141] have studied PBG compositions P50C50, P50C40N10 and P50N50 via neutron diffraction and ^{31}P nuclear magnetic resonance. They have shown that for an increasing Ca^{2+}/Na^+ ratio, a lengthening of $r_{(P=O)}$ and shortening in $r_{(P-O)}$ occurs. These features are thought to be due to the increased field strength of Ca^{2+} compared to Na^+, drawing electron density into the bond between Me and NBO, leading to increased covalency in this bond. Our data reflect these experimental features. Figures 6.6a and 6.6b display the RDFs for O-O and P-P along with the ADFs for O-P-O and P-O-P,

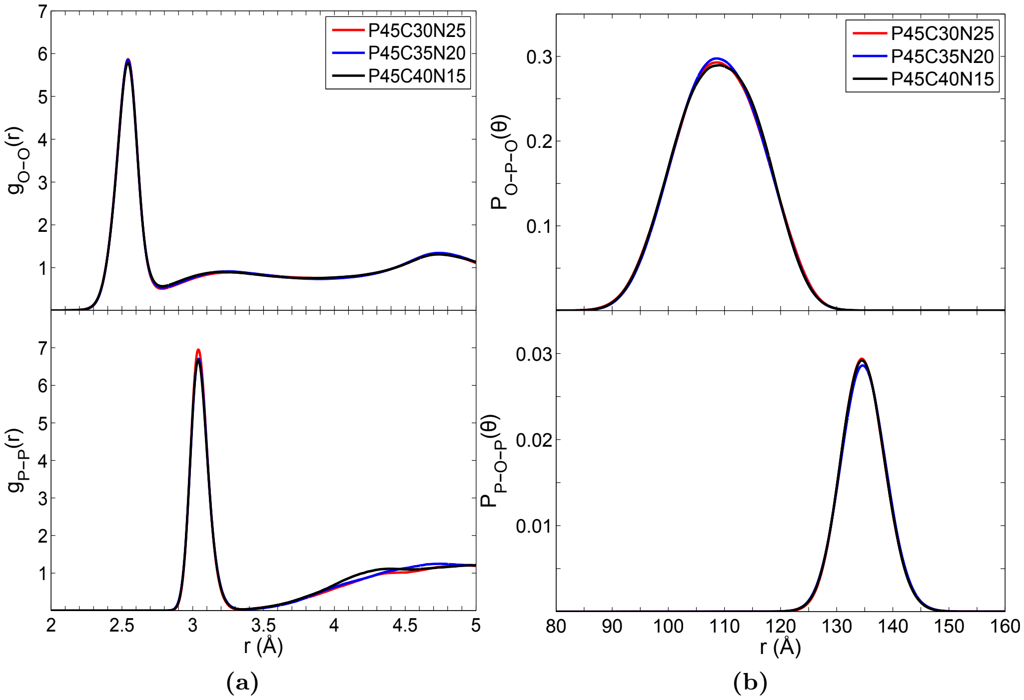

Figure 6.6: (a) O-O and P-P radial distribution functions averaged over 300K trajectory. (b) O-P-O and P-O-P angular distribution functions averaged over 300K trajectory.

respectively.

$r_{(O-O)} = 2.543$ Å and shows no variation for the three compositions studied. $r_{(P-P)} = 3.040$ Å for P45C30N25 and is distributed over a range of ±0.001 Å across all three compositions. The overestimation relative to experimental data, is thought to reflect the increased electrostatic repulsion due to the use of formal charges. The full-width-half-maximum (FWHM) value for the P45C35N20 composition is 0.146 Å for g_{P-P} and 0.176 Å for g_{O-O}. This, in part, reflects the increased value of k_{3b} for the P-O_s-P interaction compared to O_s-P-O_s. The mean O-P-O angle across all three compositions ($\mu(\theta_{(O-P-O)})$) is 108.77° ranging from 108.65° in P45C30N25 to 108.99° in P45C40N15. $\mu(\theta_{(P-O-P)}) = 134.53°$ with the three peaks distributed across a range of 0.06°. FWHM values for the O-P-O ADF (19.6°) and P-O-P ADF (9.4°), for the sample intermediate composition P45C35N20, differ by 10.2°. This again is a reflection of a relatively stiffer P-O_s-P potential.

Figure 6.7a displays the RDFs for Na-O and Ca-O, showing characteristically broader first peaks with FWHM values of 0.412 Å and 0.339 Å respectively, for P45C35N20. $r_{(Na-O)}$ and $r_{(Ca-O)}$ are distributed over 0.018 Å and 0.005 Å respectively. Interestingly, a non-linear relation exists between $r_{(Na-O)}$ and Ca^{2+}/Na^{+} molar ratio. A maximum value of $r_{(Na-O)} =$

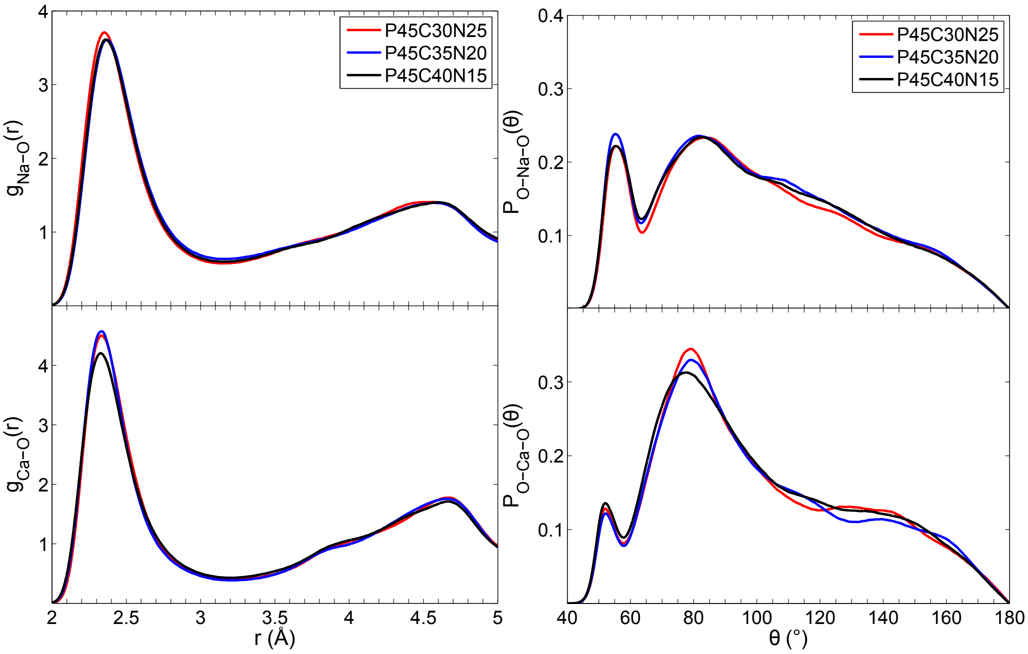

(a) **(b)**

Figure 6.7: (a) Na-O and Ca-O radial distribution functions averaged over 300K trajectory. (b) O-Na-O and O-Ca-O angular distribution functions averaged over 300K trajectory.

2.371 Å is obtained for the intermediate composition P45C35N20 ($Ca^{2+}/Na^{+} = 0.875$), with 0.76% and 0.34% decreases for compositional ratios of 0.600 and 1.333, respectively (see Table 6.7).

Figure 6.7b displays the ADFs for O-Na-O and O-Ca-O, normalized for the first coordina-

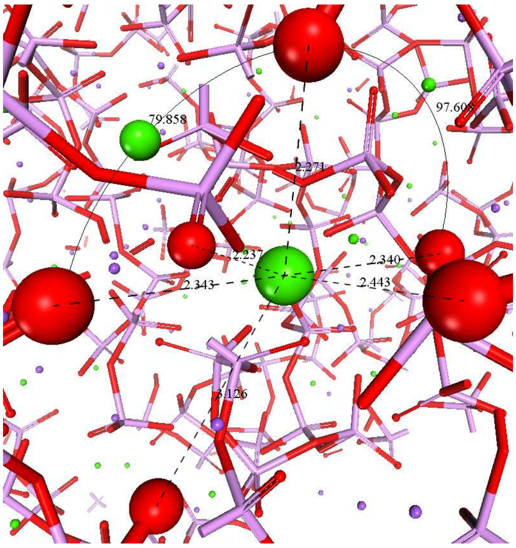

Figure 6.8: Ca^{2+} pseudo-octahedral bonding environment. Snapshot from P45C35N20 trajectory at 300K. Calcium atoms in green, sodium atoms in deep purple, phosphorus atoms in light purple and oxygen atoms in red.

tion sphere. Both ADFs show strong peaks at approximately 77° $\leq \theta \leq$ 84° associated with a pseudo-octahedral coordination shell, as shown for Ca^{2+} in Figure 6.8. Considering O-Na-O, a 2.5° shift in the second peak from 81.5° in the P45C35N20 composition to 84.0° in P45C30N25 is noted. P45C40N15 (the highest Ca^{2+}/Na^{+} ratio) has a peak centered around an angle intermediate to the other two compositions at 83.0°. The second peak in the ADF for O-Ca-O is centered around 79.0° for P45C30N25 and P45C35N20 compositions and displays a decrease for the P45C40N15 composition to 77.5°. The first peaks in the ADFs, centered at approximately 56° for O-Na-O and 52° for O-Ca-O, relate to Me coordination with two oxygens bonded to the same PO_4 tetrahedron. A decrease in first peak intensity and corresponding increase in second peak intensity (O-Me-O bonds involving oxygens from differing tetrahedra) is noted as Me field strength increases. The same feature has been observed in yttrium phosphosilicate glasses.[166]

Table 6.8 gives the modifier coordination numbers (CN) decomposed into BO and NBO contributions. The average undecomposed CN across all three compositions for Ca-O is 6.85 and 6.55 for Na-O. It has been shown that an increased Ca^{2+}/Na^{+} ratio leads to a slower dissolution rate.[18] It is assumed[19] that the cross-linking of different phosphate chains via Ca-NBO bonds improves the network strength and contributes to slower degradation in solution. Our results show $[CN^{Ca-NBO}/CN^{Ca-BO}]>[CN^{Na-NBO}/CN^{Na-BO}]$ and that $r_{(Ca-NBO)}$= 2.3 Å compared to $r_{(Ca-BO)}$= 3.8-4.5 Å (taken from decomposition of g_{Ca-O} for P45C30N25). From this we infer Ca^{2+} has the ability to bond to more oxygens (within its first coordination shell) more strongly via increased coordination to NBO, when compared to Na^{+}. These results explicitly point to a possible structural mechanism contributing to the composition-dependent trends in dissolution rates.

6.4.3.2 Medium-range structure

The Q^n distributions, where n represents the number of BO in the first coordination shell of phosphorus, for all three compositions are given in Table 6.9. Network connectivity (NC) (mean number of BO per tetrahedron) and the mean phosphorus coordination (P_c) are also presented. In a vitreous P_2O_5 composition, the network is completely bound with 100% Q^3. The introduction of modifiers, Ca^{2+} and Na^{+}, breaks up the phosphate network and leads to a predominance of Q^2 and Q^1 species. Two trends of increasing Q^1 (25.9% in P45C30N25

Table 6.8: Modifier coordination environments. Na-O and Ca-O cut-offs set at 3.15 Å and 3.22 Å respectively.

	P45C30N25	P45C35N20	P45C40N15
Atomic Pair	CN	CN	CN
Na-O	6.49	6.59	6.57
Na-BO	1.26	1.30	1.32
Na-NBO	5.23	5.29	5.25
CN^{Na-NBO}/CN^{Na-BO}	4.15	4.07	3.98
Ca-O	6.86	6.82	6.87
Ca-BO	0.59	0.55	0.62
Ca-NBO	6.27	6.27	6.25
CN^{Ca-NBO}/CN^{Ca-BO}	10.63	11.40	10.08

Table 6.9: Q^n species distribution (%) for phosphorus with respect to oxygen. Network connectivity (NC) and mean phosphorus coordination (P_c). Experimental data derived from ^{31}P MAS NMR spectra[76] given for comparison.

	Q^0	Q^1	Q^2	Q^3	Q^4	NC	P_c	Q^1[76]	Q^2[76]
P45C30N25	0.0	25.9	70.1	4.0	0.0	1.78	4.0	22 ±2	78 ±2
P45C35N20	0.0	27.7	67.0	5.1	0.2	1.78	4.0	21 ±2	79 ±2
P45C40N15	0.0	28.7	64.6	6.7	0.0	1.78	4.0	10 ±2	90 ±2

to 28.7% in P45C40N15) and decreasing Q^2 (70.1% in P45C30N25 to 64.6% in P45C40N15) are noted with increasing Ca^{2+}/Na^+ ratio. In contrast to our results, Carta *et al.*[76] have shown opposing Q^1 and Q^2 trends (see Table 6.9), albeit with an overlap of associated error bars for two of the three data points. Tang *et al.*[15] have shown there to be an increase in Q^1 with increasing Ca^{2+}/Na^+ ratio but no clear trend in Q^2. However, the system sizes used (ranging from 88 to 90 atoms) prevent any conclusive derivation of trends due to poor statistical sampling. Furthermore, small percentage contributions (4.0%-6.7%) of Q^3 are noted in this work, as found in *ab initio*[15] simulations but not experiment.[76] These factors provide an inconclusive picture and investigation of further compositions with differing Ca^{2+}/Na^+ ratios would be beneficial. The presence of a very small percentage (0.2%) of over-coordinated Q^4 defects is seen in the P45C35N20 composition and may relate to transient diffusive effects. Network fragments, across all three glass compositions studied, are solely chain-like (with small proportions of branching Q^3) and no ring structures are found, in agreement with theory[167] for doped vitreous phosphate compositions containing $P \leq 50$.

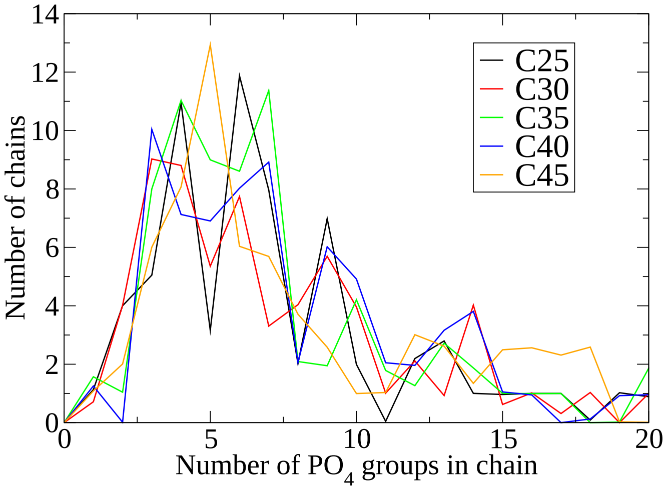

Figure 6.9: The distributions of the phosphate chain lengths in the different compositions. The mean chain lengths are 8.5 (composition C25), 8.6 (C30), 8.0 (C35), 8.4 (C40) and 8.7 (C45) phosphate units.[140]

6.4.3.3 Phosphate chains

Further medium-range analysis of P45C30N25, P45C35N20 and P45C40N15 (named C30, C35 and C40 for the remainder of the chapter) was conducted along with two further "end" compositions, namely P45C25N30 (C25) and P45C45N10 (C45). These further compositions were classically simulated using the same protocol as C30-C40, using linearly extrapolated densities of 2.55 g.cm^{-3} and 2.60 g.cm^{-3} for C25 and C45 respectively. As the glass structures primarily comprise of chains as indicated by the prevalence of Q^2 species along with chain terminating Q^1 species, an interesting structural metric to analyse is that of phosphate chain length and distribution. It is known that the average chain length solely depends on the ratio of the number of oxygens and phosphorus atoms,[168, 169] a value that is approximately constant for C25-C45 and this is reflected in the simulations. The distributions of phosphate chain lengths are given for all five compositions in Figure 6.9 and show a mean chain length in the range 8.0-8.7 with no discernable compositional trends. Further analysis was conducted to assess how the phosphate chains are bound to the rest of the glass structure.

Table 6.10 gives the distribution of the number of phosphate chains bound to the network modifiers calcium and sodium. From the results no significant compositional trends are noted, however there is a clear difference between the two modifiers. On average Ca bonds to 3.90-3.96

Table 6.10: The percentage distribution of number of phosphate chains bonded to Na and Ca.[140]

				Na (%)				
	0	1	2	3	4	5	6	AVERAGE
C25	0.0	1.2	15.4	46.3	32.0	4.4	0.6	3.25
C30	0.0	1.8	9.9	52.7	32.3	3.3	0.0	3.25
C35	0.0	0.4	14.9	46.6	32.3	5.6	0.2	3.28
C40	0.0	1.0	14.1	48.8	32.2	3.7	0.3	3.24
C45	0.0	1.3	17.9	44.8	29.9	6.1	0.0	3.22
				Ca (%)				
	0	1	2	3	4	5	6	AVERAGE
C25	0.0	0.0	3.1	23.9	47.7	21.9	2.7	3.95
C30	0.0	0.0	5.0	31.2	40.9	20.0	2.9	3.85
C35	0.0	0.0	5.7	22.2	45.3	24.4	2.5	3.96
C40	0.0	0.0	3.7	24.7	50.6	17.6	3.3	3.92
C45	0.0	0.0	4.5	24.9	48.5	20.0	2.1	3.90

distinct phosphate chains, whereas Na bonds to 3.22-3.28. Thus upon substitution of Na_2O for CaO, moving from C25-C45, more chains are bound by a modifier, thereby strengthening the network. A representative Na atom bound to three phosphate fragments is given in Figure 6.10. The field strength of an ion, as defined by Dietzel[170], is $F = Z/a^2$ where Z is the charge of the ion and a is the modifier-oxygens bond length in an octahedral environment. Since a is roughly equal for Na and Ca then the higher charge of Ca means that it has a higher field strength. It's increased preference to bond to NBO in the first coordination shell compared to Na (see Table 6.8) is an indicator of this difference in Z. Since, by definition, BO are linked to two further phosphorus atoms in the same phosphate chain, the fact that Na has a higher proportion of BO within its coordination shell, sterically restricts the space available for multiple chains to coordinate to Na.

A further structural metric that has been computed, is the number of PO_4 tetrahedra bonded to the modifier ions, via the number of distinct phosphorus atoms bonded to oxygen atoms within the first coordination shell of the modifier. The results of this analysis show Na is bound to 5.8-6.0 PO_4 tetrahedra whereas Ca is bound to 6.3-6.4 PO_4 tetrahedra. The prevalence of different (O-P-)$_n$-O chain lengths, where the terminal oxygens are bound to the same modifier, is presented in Table 6.11. Shorter chains are more numerous for both Ca and Na and the average number of (O-P-)$_2$-O and (O-P-)$_3$-O chains increases with increasing Ca/Na ratio.

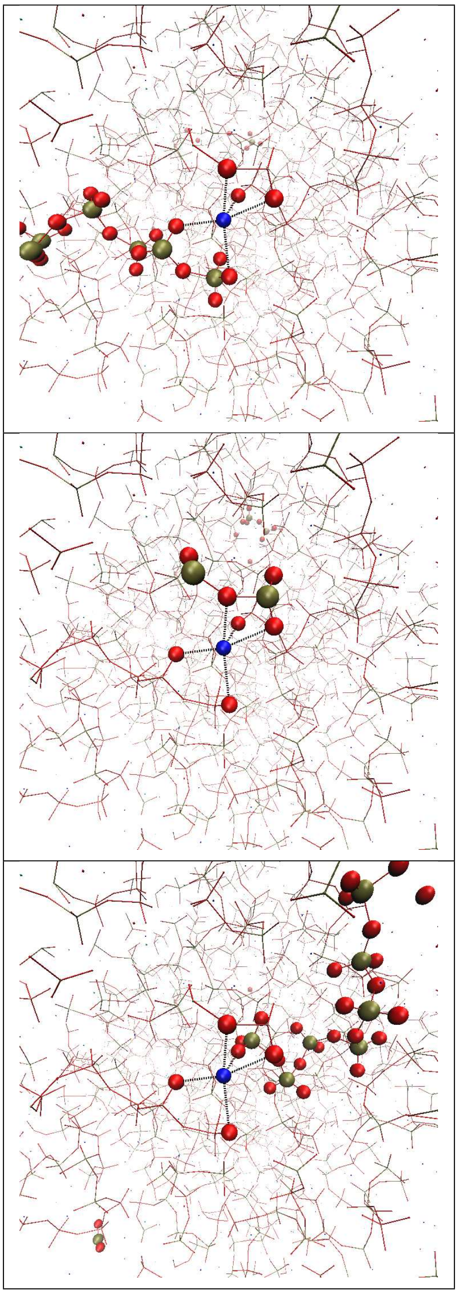

Figure 6.10: A Na atom bound to three phosphate fragments. The central Na atom (blue) and its first coordination shell are highlighted in all pictures; each picture highlights a different phosphate fragment anchored to the Na. The remainder of the glass structure has been shrunk for clarity.[140]

Table 6.11: The average number of M...(O-P-)$_n$-O...M chains of length n around a single M atom, where M = Na or Ca.[140]

	n	C25	C30	C35	C40	C45
Na	1	1.21	1.20	1.25	1.22	1.26
	2	0.77	0.78	0.88	0.91	0.88
	3	0.44	0.47	0.54	0.56	0.67
Ca	1	0.91	1.10	0.97	0.89	0.91
	2	0.88	0.89	0.80	0.83	0.90
	3	0.51	0.52	0.60	0.66	0.53

6.4.4 Gas-phase simulations of calcium/sodium phosphate complexes

The distribution and populations of various chain lengths can be characterized and understood through the use of accurate DFT gas-phase simulations. The energies of formation (ΔE_{form}) give information about the relative conformational stabilities of each complex in the gas phase, in terms of the total electronic energy change at 0K. Table 6.12 shows that the complexes containing a phosphorus chain with two phosphate groups ($Na(H_2PO_4)(H_2P_2O_7)^{2-}$ and $Ca(H_2PO_4)(H_2P_2O_7)^{-}$) have more negative ΔE_{form} values (ΔE_e for $Na(H_2PO_4)_2{}^{-}+H_2P_2O_7{}^{2-} \rightarrow Na(H_2PO_4)(H_2P_2O_7)^{2-}+H_2PO_4{}^{-}$ = -32.54 kcal mol^{-1}, and -103.57 kcal mol^{-1} for the equivalent Ca reaction) than the corresponding three-membered phosphate chains for like cations (-12.47 kcal mol^{-1} and -93.18 kcal mol^{-1} respectively).[2] This increased stability partly explains the increased number of two-membered ($n = 2$) chains compared with three-membered ($n = 3$) chains for both sodium and calcium across all three compositions studied (Table 6.11). Furthermore the difference between ΔE_{form} for two-membered and three-membered chains is more pronounced for the sodium complexes (20.07 kcal mol^{-1}) than for that of the calcium complexes (10.39 kcal mol^{-1}), in agreement with the larger difference between the number of two-membered chains around sodium and calcium, than the difference in the number of three-membered chains. Figure 6.11 shows an example optimized $Na(H_2PO_4)(H_3P_3O_{10})^{2-}$ complex.

---

[2] The hydrogen atoms are included to charge balance the oxygen atoms not bonded to the modifier.

Table 6.12: Energies of formation ($\Delta E_{form} = \sum_{products} E_{form} - \sum_{reactants} E_{form}$) for the sodium and calcium complexes investigated.

Reactants → Products	ΔE_{form} (kcal mol^{-1})
$Na(H_2PO_4)_2{}^{-}$+$H_2P_2O_7{}^{2-}$ →	
$Na(H_2PO_4)(H_2P_2O_7)^{2-}$+$H_2PO_4{}^{-}$	-32.54
$Na(H_2PO_4)_2{}^{-}$+$H_3P_3O_{10}{}^{2-}$ →	
$Na(H_2PO_4)(H_3P_3O_{10})^{2-}$+$H_2PO_4{}^{-}$	-12.47
$Ca(H_2PO_4)_2$+$H_2P_2O_7{}^{2-}$ →	
$Ca(H_2PO_4)(H_2P_2O_7)^{-}$+$H_2PO_4{}^{-}$	-103.57
$Ca(H_2PO_4)_2$+$H_3P_3O_{10}{}^{2-}$ →	
$Ca(H_2PO_4)(H_3P_3O_{10})^{-}$+$H_2PO_4{}^{-}$	-93.18

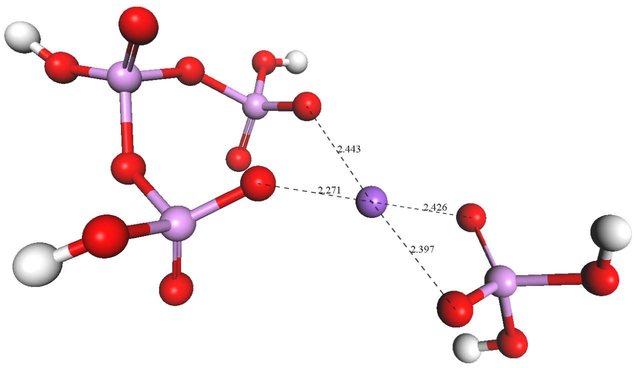

Figure 6.11: DFT-PBE optimized $Na(H_2PO_4)(H_3P_3O_{10})^{2-}$ gas-phase complex. Sodium, phosphorus, hydrogen and oxygen displayed in deep purple, light purple, white and red resepctively.

6.4.5 Structural evolution of $(P_2O_5)_{0.45}(CaO)_x(Na_2O)_{0.55-x}$ ($x = 0.30, 0.35$ and 0.40) systems from melt to solid

Further to the results presented, smaller 90 atoms systems, of the same three PBG compositions, were simulated using, a full *ab initio* molecular dynamics (AIMD) melt-quench, as reported by Tang *et al.*,[15] and also using the reported force field. The same initial configurations and analogous simulation protocols were used for each methodology.[171] Of particular consideration for high-temperature, melt-quench computer simulations of amorphous systems, is that a correct description of the liquid-like character of the melt gives way to an accurate model for the final glass at 300 K, as the system is quenched. A detailed analysis of the total fraction of under- and over-coordinated phosphorus atoms (see Figure 6.12) shows that, between 3000 K and 1800 K, there are a significant percentage ($3 - 11\%$) of 3-coordinated phosphorus species. The oxygen atoms are mostly 2-coordinated, with less than 2% of O_{0c} species and no 3-coordinated oxygen atoms at 3000 K. These results show that the structural

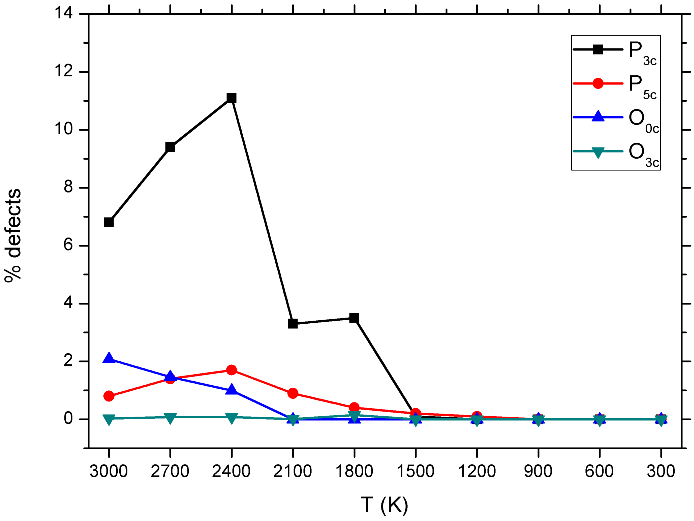

Figure 6.12: Average total fraction of threefold- and fivefold-coordinated phosphorus, threefold coordinated oxygen and under-coordinated oxygen from *ab initio* molecular dynamics, as a function of temperature for P45C40N15.[171]

defects rapidly decrease during the cooling phase and that, at temperatures below 1800 K, the system is free of under- and over-coordinated species.

Figure 6.13 reports the change in the Q^n distribution as the 3000 K melt, of the P45C40N15 systems, is quenched to 300 K. The results show a decrease in Q^0, Q^1 and Q^3 with a corresponding increase in Q^2. Results for both the AIMD and classical methodologies show good agreement. The Q^2 proportion from AIMD results increases from 40.1%, in the 3000 K melt, to 66.7% at 300 K. These results are compared to a Q^2 change from 46.3% to 66.7% respectively for classical MD. Similarly good agreement is shown for the temperature trends and absolute values of all other Q^n species. For simulations of bioactive phosphosilicate glasses and melts, Tilocca[172] has shown that shell-model potentials perform better than RI models in theses systems. The correct description of the dynamical balance between the interconversion of Q^n species during the cooling of a melt is of importance for an accurate accounting of medium-range structure in the final glass. Our results are a further validation of the developed force field.

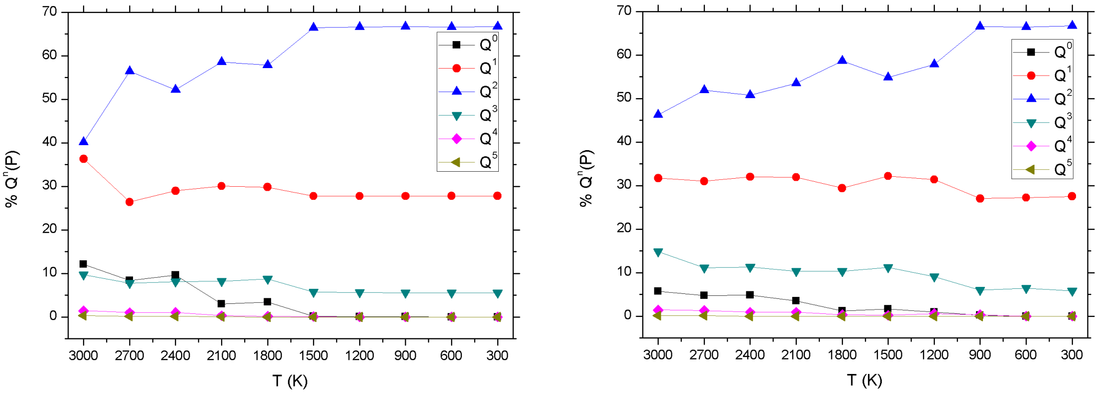

Figure 6.13: P45C40N15 Q^n distribution vs. temperature from AIMD (left) and classical MD (right) simulations.[171]

6.5 Summary

This work presents the first classical MD simulation of phosphate-based glasses in the system P_2O_5-CaO-Na_2O. A novel empirical force field has been developed with full ionic charges and a shell-model formalism for polarization effects, which enables the simulation of different glass compositions. A linear frictional damping of the core-shell spring force has been parameterized, via a FFT analysis of the shell vibrational dynamics at 2500 K, at $\frac{1}{3}$ critical in order to prevent core-shell heating. The use of a single P-O_s potential is shown to reproduce $r_{(P=O)}$ and $r_{(P-O)}$ accurately and all other short-range order is in good agreement with available experimental data. An analysis of the medium-range structure shows the phosphate network to be connected as NC = 1.78 for all three PBG compositions studied. Each composition shows a dominant Q^2 contribution with significant Q^1, as seen in experimental data. An increased Ca^{2+}/Na^+ ratio leads to an increase in Q^1 and decrease in Q^2 across all compositions. We have shown Na^+ and Ca^{2+} to occupy pseudo-octahedral bonding coordination with mean coordination numbers of 6.55 and 6.85 respectively. A decomposition of the coordination into BO and NBO contributions shows that Ca^{2+} has a higher CN^{Me-NBO}/CN^{Me-BO} ratio for all three compositions with a mean value of 10.70 compared to 4.07 for Na^+. One possible inference is that Me field strength and CN^{Me-NBO}/CN^{Me-BO} ratios are of structural significance in the dissolution mechanism and solubility rate trends. Furthermore, it is noted that Ca binds together more phosphate fragments and more PO_4 tetrahedra than Na.

Chapter 7

Amorphous P_2O_5-CaO-Na_2O-Ag_2O systems

7.1 Overview

The biocidal effects of silver ions against a wide range of microbes lend Ag-PBG to several of biomedical applications as outlined in subsection 2.2.2. The bulk structural characterisation of Ag-PBG is of importance to help better understand and optimize the antibacterial action of such materials. Knowledge of the composition to structural relationships also aids the interpretation of dissolution rate data and *in vitro* information. The interplay of composition and dissolution rates for example, leads to non-intuitive materials properties, such as diminished antimicrobial effects for higher Ag mol%.

7.1.1 Structural information from experimental probes

Ahmed *et al.*[173] have used thermal analysis, X-ray diffraction (XRD), nuclear magnetic resonance (NMR) and X-ray absorption Near Edge Structure (XANES) techniques to elucidate the structures of $(P_2O_5)_{0.50}(CaO)_{0.30}(Na_2O)_{0.20-x}(Ag)_x$ (x = 0.00, 0.03 and 0.05) glasses. Thermal analysis showed that T_g rose from ∼653 K for the x = 0.00 composition to ∼672 K for both Ag-PBG compositions. The only phase identified from XRD analysis was that of sodium metaphosphate, $NaCa(PO_3)_3$. ^{31}P MAS NMR spectra revealed a single peak at -26 ppm for the 0 and 5 mol% Ag compositions, corresponding to a 100% Q^2 distribution for the network forming phosphate species. The Ag K-edge XANES spectra for the reference compounds AgO, Ag_2O, Ag_3PO_4 and Ag_2SO_4 are shown from this work in Figure 7.1, with comparison to the spectra for 5 mol% Ag. Information on the oxidation state of the silver ions is obtained from the position of the X-ray absorption edge in each spectrum. Since AgO has a mixture of Ag^{I} and Ag^{III} ions, the edge position for this material appears at the highest energy, since more energy is required to remove electrons from the higher valence ions. The Ag K-edge becomes sharper as the number of oxygen atoms surrounding the silver (i.e. the coordination number, $\eta_{(Ag-O)}$) increases. In Ag_2O, $\eta_{(Ag-O)} = 2$ whereas for Ag_2SO_4 and Ag_3PO_4 the coordination numbers are $\eta_{(Ag-O)} = 6$ and $\eta_{(Ag-O)} = 8$ respectively. Figure 7.1 illustrates the similarity between the XANES spectra of 5 mol% Ag-PBG and Ag_2SO_4, suggesting that the Ag ions in the glass reside in a six-coordinated local environment, as in silver sulphate. The authors also note that the silver ions are shown to be in the oxidation state Ag^{I}.

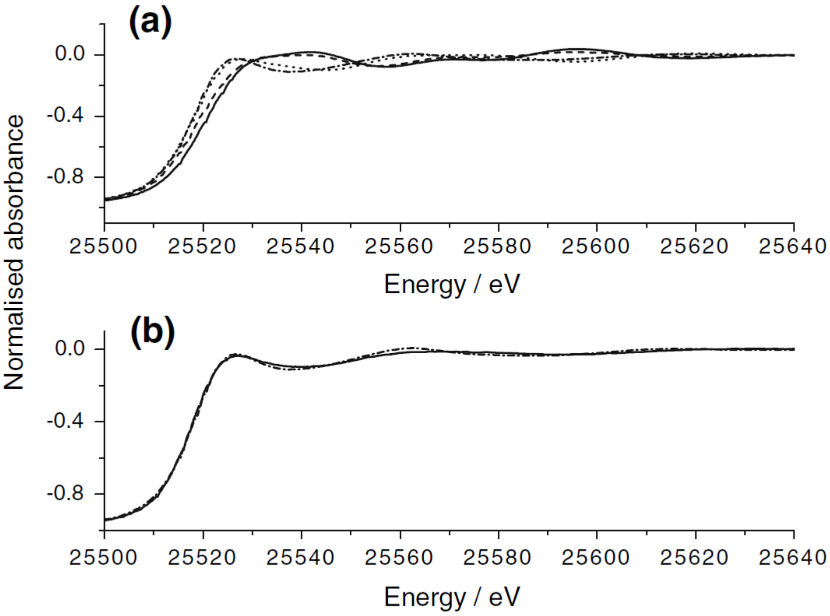

Figure 7.1: Ag K-edge XANES spectra. (a) Reference compounds: AgO (—), Ag_2O (- - -), Ag_3PO_4 (· · ·) and Ag_2SO_4 (- · · -). (b) P50C30N15A5 PBG (—) compared with Ag_2SO_4 (- · · -).[173]

The glass compositions $(P_2O_5)_{0.50}(CaO)_{0.30}(Na_2O)_{0.20-x}(Ag)_x$ (x = 0.00, 0.10, 0.15 and 0.20) have been synthesised via the standard melt-quench approach.[31] Structural analysis was carried out using ^{31}P MAS NMR, high energy X-ray diffraction (HEXRD) and Ag k-edge XANES. Figure 7.2 shows the ^{31}P MAS NMR for all compositions studied with a single most prominent peak at a chemical shift of -27 ppm, assigned to Q^2 groups. For compositions of $\geq$10 mol% Ag two weaker resonances are observed at -6 and -37 ppm assigned to the presence of Q^1 and Q^3 environments. This change in the Q^n distribution is indicative of a disproportionation of Q^2, upon the substitution of sodium for silver and is discussed further, in the analysis of the original computational results, presented later in this chapter.

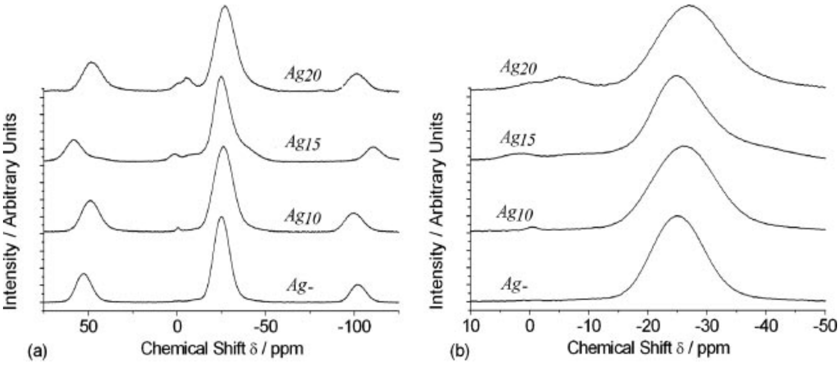

Figure 7.2: (a)^{31}P MAS NMR for $(P_2O_5)_{0.50}(CaO)_{0.30}(Na_2O)_{0.20-x}(Ag)_x$ (x = 0.00, 0.10, 0.15 and 0.20) glasses, (b) highlights of the prominent peaks.[31]

Valappil *et al.*[31] also present the HEXRD pair-distribution functions for all Ag-PBG compositions studied, as shown in Figure 7.3. The peaks centered at ~1.55 Å are composed of the two P-O components, namely the shorter distance P-NBO (~1.49 Å) and the longer P-BO (~1.60 Å). The shape of the peak in the samples changes as mol% Ag is increased, consistent with Q^2 disproportionating into Q^1 and Q^3 groups.

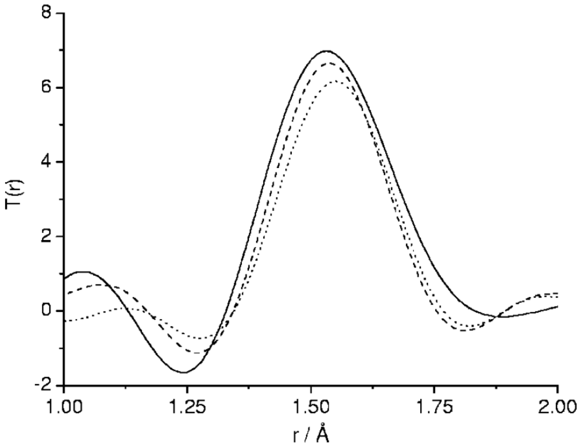

Figure 7.3: HEXRD pair-distribution for 10 mol% Ag (—), 15 mol% Ag (- - -) and 20 mol% Ag (· · ·) PBG, showing the peak due to P-O bonding.[31]

As with the study by Ahmed *et al.* (P50C30N15A5[173]), the Ag K-edge XANES spectra for P50C30N10A10, P50C30N5A15 and P50C30A20 from the work of Valappil *et al.*,[31] display similarities to that of Ag_2SO_4, confirming silver to be in the Ag^I oxidation state.

Due to overlap of real space correlations in the region 2.2 − 2.6 Å, standard diffraction methods such as ND and X-rays do not reveal information about Ag-O bonding. Further to this, XANES measurements reveal variations in coordination numbers and local symmetry but cannot yield definitive structural parameters. Neutron diffraction with isotopic substitution (NDIS) utilizes the variation in scatttering length between isotopes of the same element. Thus, by using two samples with identical compositions and structures, but differing silver isotopes, it is possible to isolate the silver contributions to the glass network. Moss *et al.*[174] conducted NDIS for P50C30N10A10 PBG compositions, using samples enriched with ^{107}Ag and ^{109}Ag isotopes. The associated ND Q-space interference functions are presented in Figure 7.4.

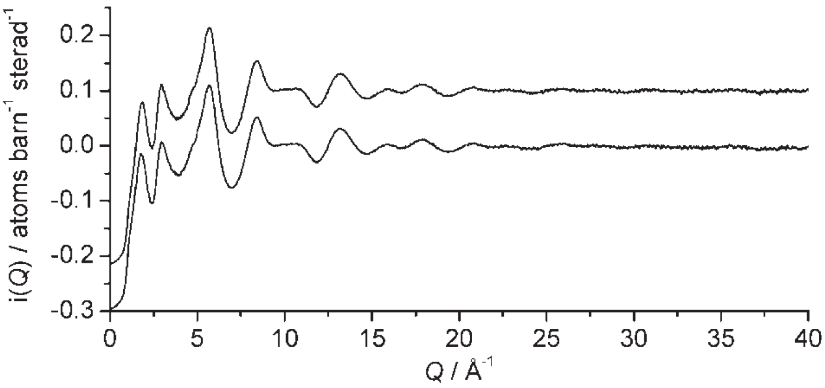

Figure 7.4: Neutron diffraction Q-space interference functions, i(Q), measured for the ^{107}Ag (upper) and ^{109}Ag (lower) doped P50C30N10A10. The ^{107}Ag i(Q) is off-set by +0.1 atoms barn^{-1} sterad^{-1} for clarity.[174]

Fourier transformation of the i(Q) curves yields the real-space correlation functions. By taking the first-order difference of these functions, the authors obtained the difference correlation function $T_{Ag-j}(r)$. The structural parameters obtained by fitting $T_{Ag-j}(r)$ are given in Table 7.1. The Ag-O bond distances and coordination numbers obtained, are consistent with the silver ions occupying a site surrounded by a distorted octahedron of oxygen atoms. Further discussion of the decomposition of the Ag-O bonding environment is given later in the chapter, with comparison made to the theoretical results presented in this work.

7.2 Computational Methods

7.2.1 *Ab initio* molecular dynamics

Born-Oppenheimer molecular dynamics (BOMD) simulations were performed with the QUICKSTEP module[105, 106] in the CP2K code (development version 2.3.16). A dual basis set was used, in which the Kohn-Sham orbitals are expanded in an atom-centered Gaussian basis

Table 7.1: Ag-j correlations determined by fitting the difference $T_{Ag-j}(r)$. Correlations shown with $\cdots$ separators represent nearest neighbours which are not directly bonded; i.e. the Ag $\cdots$ O correlation is considered to be in the second coordination sphere. The values of R (bond length), N (coordination number) and σ (disorder parameter) given with uncertainties.[174]

Correlation	R [Å] (±0.03)	N (±0.5)	σ [Å] (±0.03)
Ag-O	2.28	2.1	0.08
Ag-O	2.51	2.7	0.09
Ag-O	2.73	1.1	0.10
Ag $\cdots$ O	2.99	2.5	0.12
Ag $\cdots$ P	3.31	6.0	0.11

set while the electronic charge density was described using an auxiliary plane-wave basis set.[96] Core electrons were described with the pseudopotential of Goedeker, Teter and Hutter (GTH)[93–95] incorporating scalar-relativistic core corrections. Valence electrons were treated with the Perdew, Burke and Ernzerhof (PBE)[90] gradient-corrected exchange-correlation functional in the double-ζ valence polarized (DZVP) basis set. The orbital transformation method[175] was employed for an efficient wavefunction optimization.

The compositional nomenclature used henceforth for amorphous systems is, P = P_2O_5, C = CaO, N = Na_2O and A = Ag_2O, followed by the percentage molar composition for each component. The internal energy of a structurally randomised P50C30N10A10 composition is converged to $\pm 3.81 \times 10^{-5}$ Ry per atom at a plane-wave kinetic-energy cutoff of 700 Ry for charge density, which was therefore used in the calculations. For every SCF loop, the electronic gradient was converged to 1×10^{-5} Hartree. The timestep for each dynamics step was set to 1 fs with the positions, velocities and Mulliken charges[176] of all the atoms recorded for each step.

The glass generation followed a standard melt-quench protocol in which atoms were initially quasi-randomly inserted into cubic simulation boxes (periodic in three-dimensions) to reproduce the experimental densities given in Table 7.2. For P50C30N10A10, a linear extrapolation of the experimental densities for ^{107}Ag and ^{109}Ag[174] was used, to reflect 50:50 isomeric abundancies.

The configurations were then evolved for 3 ps in the NVE ensemble. Subsequently the systems were heated to 2500 K in the NVT ensemble and equilibrated for 30 ps. Equilibration was checked by examining the ions actual and mean-square displacements. The systems were then cooled to 300 K at a rate of $\sim$24 K.ps^{-1} in the NVT ensemble. The protocol followed 15

Table 7.2: $(P_2O_5)_{0.50}(CaO)_{0.40-x}(Na_2O)_{0.10}(Ag_2O)_x$ compositions simulated. First-principles and classical methodologies labelled as (f.p.) and (c.) respectively.

Glass code	x	Atoms	Cell (Å)	Density (g.cm^{-3})
P50C40N10 (f.p.)	0.00	294	15.9862	2.590[141]
P50C30N10A10 (f.p.)	0.10	298	16.2615	2.846[174]
P50C40N10 (c.)	0.00	6008	43.6907	2.590[141]
P50C30N10A10 (c.)	0.10	6007	44.3763	2.846[174]

ps NVT trajectories run consecutively at 2200 K, 1900 K, 1600 K, 1300 K, 1000 K and 700 K. At 300 K the trajectory was evolved for 40 ps during which time structural and electronic data was sampled. The results in this paper are averaged over this time using every timestep and all first principles results are named f.p..

7.2.2 Classical molecular dynamics

The classical simulations followed a similar protocol, at a reduced quench rate of ~2 K.ps^{-1}, using the formal-charge force field shown in Table 7.3 to describe inter-atomic forces. This has previously been shown to accurately reproduce the structure of glasses in the system P_2O_5-CaO-Na_2O[140, 171, 177] and also includes an Ag-O_s two-body potential taken from Woodley *et al.*.[178] Molecular dynamics were run using the DL_POLY code[103] (version 2.20) using an Evans[159] thermostat in the NVT ensemble. The dynamics timestep was set at 0.2 fs for an accurate description of the O_s motion. The ~6000-atom systems were heated to 2400 K and melted for 50 ps, after which the temperature was reduced in steps of 100 K, running each trajectory for 50 ps. Core-shell frictional damping was parameterized as $20 \leq c^2 \leq 25$ (where c is the core-shell damping coefficient which is linear in velocity) for all temperatures in the range 2400 K − 1500 K, $c^2 = 15$ at 1400 K, $c^2 = 10$ at 1300 K and $c^2 = 5$ for all temperatures in the range 1200 K − 300 K. A density correction factor of 0.950 was applied to the trajectories run at 2400 K, 2300 K and 2200 K. Likewise, a factor of 0.975 was applied at 2100 K, 2000 K and 1900 K in order to mimic thermal expansion. Since $C_{(O_s-O_s)}$ is non-zero, the simple power law expression for the dispersive energy means that $V_{(O_s-O_s)} \rightarrow -\infty$ for low r. To avoid this unphysical possibility (there is a finite probability that the system will gain sufficient kinetic energy to overcome the repulsive barrier) during the high temperature trajectories 2400K − 1500K, the potential was substituted for one of the form $V_{(O_s-O_s)} = \frac{A}{r^B}$,[149, 179] below a cut-off distance of $r_{(O_s-O_s)} = 0.952$Å. As for f.p., all classical data (labelled c.) is averaged from the 300 K trajectory with output printed every 1 fs (to match f.p. despite the smaller timestep of 0.2 fs).

Table 7.3: Formal charge shell-model force field used in this work, including Buckingham-type two-body, harmonic three-body and core-shell potentials.

	$V_{ij} = Ae^{-\frac{r}{\rho}} - Cr^{-6}$		
i-j	A(eV)	ρ (Å)	C (eV.Å^6)
P-O_s[177]	1020.0000	0.343220	0.0300
O_s-O_s[150]	22764.30	0.149000	27.88
Na-O_s[149]	56465.3453	0.193931	0.00
Ca-O_s[149]	2152.3566	0.309227	0.099440
Ag-O_s[178]	962.197	0.300000	0.00
	$V_{ijk} = \frac{1}{2}k_{3b}(\theta - \theta_0)^2$		
i-j-k	k_{3b}(eV.rad^{-2})	θ_0(°)	
O_s-P-O_s[177]	3.3588	109.470000	
P-O_s-P[177]	7.6346	141.179333	
	$V_{ij} = \frac{1}{2}k_{cs}r^2$		
i-j	k_{cs}(eV.Å^{-2})	O_c (e)	O_s (e)
O_c-O_s[150]	74.92	+0.8482	-2.8482

7.3 Results and discussion

7.3.1 Short-range order: network formers

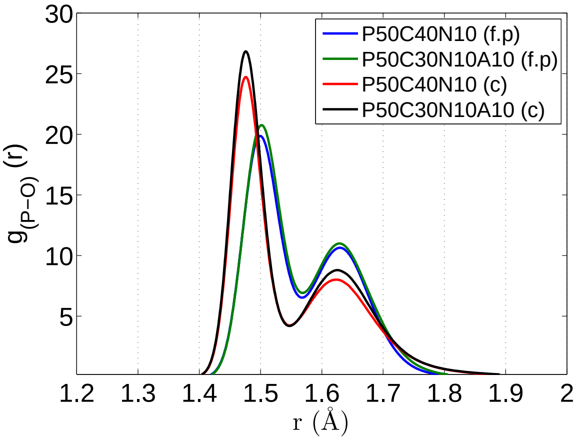

Figure 7.5: P-O partial pair-correlation functions.

The glass network for each composition is made up from inter-linked PO_4 tetrahedra. Figure 7.5 displays the partial pair-correlation functions $g_{(P-O)}$ (r) between 1.2 – 2.0 Å (within the first coordination shell). Both methodologies distinguish between the longer phosphorus to "bridging" oxygen bonds (P-BO), with $g_{(P-O)}$ (r) peaks centered between $1.62-1.63$ Å and the shorter phosphorus to "non-bridging" oxygen bonds (P-NBO), centered between $1.48-1.50$ Å. The slight overestimation from DFT-MD results are likely due to GGA underbinding and hence overestimating bond lengths. Pickup *et al.*[141] used neutron diffraction (ND) and ^{31}P magic angle spinning nuclear magnetic resonance (MAS NMR) spectroscopy to probe the structure of P50C40N10. The structural parameters were obtained via simulation of the reciprocal-space data and conversion of the results to real-space via Fourier transform (to make comparison to the correlation function from ND). Their results give $r_{(P-BO)} = 1.60$ Å ± 0.02 Å and $r_{(P-NBO)} = 1.49$ Å ± 0.02 Å. The classical simulations reproduce these bond lengths within the experimental error ranges (see Table 7.4), as does the glass simulated by first-principles techniques, with the exception of $r_{(P-BO)} = 1.63$ Å. For the Ag-PBG composition (P50C30N10A10) comparison is made to data from ND experiments,[174] using samples enriched with both ^{107}Ag and ^{109}Ag. Experimentally, it was shown that for both silver isotopes, $r_{(P-BO)} = 1.60$ Å ± 0.01 Å and $r_{(P-NBO)} = 1.48$ Å ± 0.01 Å. From the current work, $r_{(P-BO)}$ is slightly overestimated by both methodologies, with an accurate representation of $r_{(P-NBO)}$ in P50C30N10A10 (c.). It can be seen from these results that the addition of Ag to the glass has no effect on $r_{(P-BO)}$ and $r_{(P-NBO)}$.

The disorder parameters σ_{ij}, measuring static and thermal disorder, from the pair functions for P-BO and P-NBO are a measure of the width of the relevant pair-correlation peak. In experimental work, σ_{ij} are derived from Q-space simulation using Equation 7.1:

$$p(Q)_{ij} = \frac{N_{ij} w_{ij}}{c_j} \frac{\sin QR_{ij}}{QR_{ij}} \exp\left[\frac{-Q^2 \sigma_{ij}^2}{2}\right], \tag{7.1}$$

where $p(Q)_{ij}$ is the pair function in reciprocal space, N_{ij}, R_{ij} and σ_{ij} are the coordination number, atomic separation and disorder parameter (referred to as σ_{ij}^{ND} from this point onwards), respectively, of atom i with respect to j. c_j is the concentration of atom j and w_{ij} is the weighting factor, given by $w_{ij} = 2c_i c_j b_i b_j$ if $i \neq j$ and $w_{ij} = c_i^2 b_i^2$ if $i = j$ (where b represents the coherent scattering length). From the current work the full-width-half-maximum (FWHM) values of the decomposed partial-pair correlation functions $g_{(P-O)}$ (f.p.) have been calculated. Making the assumption that $g_{(P-NBO)}$ (r) and $g_{(P-BO)}$ (r) are normally distributed (for the first coordination sphere) gives, $\mathrm{FWHM}_{\mathrm{ij}}^{\mathrm{f.p.}} = 2\sqrt{2\ln 2}\sigma_{\mathrm{ij}}^{\mathrm{f.p.}}$, from which $\sigma_{\mathrm{ij}}^{\mathrm{f.p.}}$ are derived.

Comparison of the compositional trends in simulated $\sigma_{(\mathrm{P-BO})}^{\mathrm{ND}}$ and $\sigma_{(\mathrm{P-NBO})}^{\mathrm{ND}}$ from ND experimental work, with trends in $\sigma_{\mathrm{ij}}^{\mathrm{f.p.}}$ values of $\mathrm{g}_{(\mathrm{P-BO})}$ and $\mathrm{g}_{(\mathrm{P-NBO})}$ from this work, are presented in Table 7.5. Experimentally, it is noted that P-BO disorder increases upon Ag-doping from $\sigma_{(\mathrm{P-BO})}^{\mathrm{ND}} = 0.048$Å to $\sigma_{(\mathrm{P-BO})}^{\mathrm{ND}} = 0.060$Å. From the current work, $\sigma_{(\mathrm{P-BO})}^{\mathrm{f.p.}}$ increases from 0.048 Å in P50C40N10 (f.p.) to 0.052 Å in P50C30N10A10 (f.p.) in good agreement with ND. $\sigma_{(\mathrm{P-NBO})}^{\mathrm{ND}}$ increases from 0.036 Å to 0.060 Å with the inclusion of silver. No significance can be attributed to the 0.001 Å increase upon doping, for the associated $\mathrm{g}_{(\mathrm{P-NBO})}$ FWHM values from this work, however, ND and f.p. $\sigma_{(\mathrm{P-NBO})}$ are in reasonable agreement for P50C40N10. Increases in disorder parameters are linked to changes in local bonding environments and, in turn, linked to a disproportionation in the medium-range structure[174] (see sub-section 7.3.4).

Figure 7.6a displays the partial pair-correlation functions for O-O and P-P. It can be seen that there are no significant compositional or methodological dependencies on the O-O distributions. However, the second coordination shell at ∼3.2 Å, is stronger for first-principles results in conjunction with stronger O-P-O (f.p.) angular distribution function (ADF) peaks (see Figure 7.6b), when compared to classical results. These differences are most likely a feature of the parameterization of the force field used in this work. The first peak in $\mathrm{g}_{(\mathrm{P-P})}$ (r) shifts from a peak-centered position of 2.93 Å in P50C40N10 (f.p.) to 2.95 Å in P50C30N10A10 (f.p.) and sharpens considerably. This is accompanied by an increase of approximately 4% in the peak-centered positions of $\mathrm{P}_{(\mathrm{P-O-P})}(\theta)$ from 125° in P50C40N10 (f.p.) to 129° in P50C30N10A10 (f.p.), thus indicating a possibly significant structural change upon doping the glass via substitution of CaO for $\mathrm{Ag_2O}$. This is further discussed in Section 7.3.3, in relation to the coordination environment of Ag. The classical results do not corroborate these features due to the inclusion of a P-$\mathrm{O_s}$-P three-body potential, as previously discussed.[177]

7.3.2 Short-range order: network modifiers

The partial pair-correlation functions for the network modifiers (Me) Ca, Na and Ag, with respect to oxygen, are given in Figure 7.7a. The classical and first-principles distributions are in good agreement. For both methodologies, the normalised peak intensities for Ca-O and Na-O increase upon Ag-doping, with the consequence of decreasing the FWHM in all cases. The ill-defined first minimum for $\mathrm{g}_{(\mathrm{Ag-O})}$ (r) from P50C30N10A10 (f.p.) (2.7 Å − 3.2 Å), suggests

Table 7.4: $(P_2O_5)_{0.50}(CaO)_{0.40-x}(Na_2O)_{0.10}(Ag_2O)_x$ (x = 0 and 0.10) selected partial pair-correlation peak distances ($r_{(X-X)}$ (Å)). Experimental data obtained via neutron (ND) and X-ray (XRD) diffraction, are given for comparison. $^{(*)}$ Further analysis of Ag-O average distances ($\bar{r}_{(Ag-O)}$) given in Table 7.8.

	P50C40N10 first prin.	P50C40N10 classical	P50C40N10 ND[141]
$r_{(P-NBO)}$	1.50	1.48	1.49 ±0.02
$r_{(P-BO)}$	1.63	1.62	1.60 ±0.02
$r_{(O-O)}$	2.56	2.54	2.52 ±0.02
$r_{(P-P)}$	2.94	3.02	2.93 ±0.02
$r_{(Ca-O)}$	2.35	2.33	2.34 ±0.02
$r_{(Na-O)}$	2.38	2.36	2.33 ±0.02
	P50C30N10A10 first prin.	P50C30N10A10 classical	P50C30N10A10 ND & XRD[174]
$r_{(P-NBO)}$	1.50	1.48	1.48 ±0.01
$r_{(P-BO)}$	1.63	1.62	1.60 ±0.01
$r_{(O-O)}$	2.57	2.55	2.51 ±0.01
$r_{(P-P)}$	2.96	3.03	2.93 ±0.01
$r_{(Ca-O)}$	2.34	2.31	2.38 ±0.01
$r_{(Na-O)}$	2.37	2.34	2.33 ±0.01
$r_{(Ag-O)}^{(*)}$	2.37	2.29	2.28,2.51,2.73 ±0.03

Table 7.5: Full-width-half-maximum (FWHM) values from the decomposed partial-pair correlation functions $g_{(P-O)}$ (f.p.) and disorder parameters $\sigma_{ij}^{f.p.}$ (standard deviation under the assumption that $g_{(P-BO)}$ and $g_{(P-NBO)}$ are normally distributed). Disorder parameters σ_{ij}^{ND} from Q-space simulation (see Equation 7.1) of experimental ND diffraction data.[141, 174]

i-j	Model	$FWHM_{ij}^{f.p.}$ (Å)	$\sigma_{ij}^{f.p.}$(Å)	σ_{ij}^{ND} (Å)
P-BO	P50C40N10 (f.p.)	0.114	0.048	0.048 ±0.01[141]
P-BO	P50C30N10A10 (f.p.)	0.123	0.052	0.060 ±0.01[174]
P-NBO	P50C40N10 (f.p.)	0.075	0.032	0.036 ±0.01[141]
P-NBO	P50C30N10A10 (f.p.)	0.076	0.032	0.060 ±0.01[174]

a distorted first coordination shell (however the 298 atom model also leads to poorer statistical sampling and increased signal noise). This in turn narrows the bond length distributions for the other modifiers Ca and Na due to geometrical constraints.

The peaks of the distributions $g_{(Me-O)}$ (r) from classical simulations are centered on bond lengths $0.05 - 0.15$ Å below the peaks of respective compositions from first-principles results, consistent with comparison of a structure derived from a well-parameterized force field and an underbinding GGA calculation. As with the short-range structure of the network forming species, the network-modifier bond lengths are in good agreement with available experimental

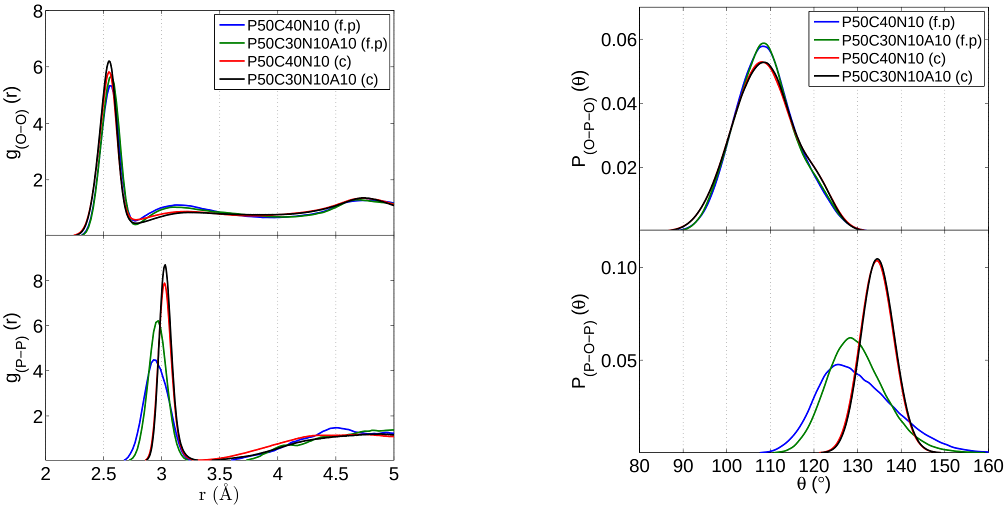

(a) **(b)**

Figure 7.6: (a) O-O and P-P partial pair-correlation functions. (b) O-P-O and P-O-P angular distribution functions.

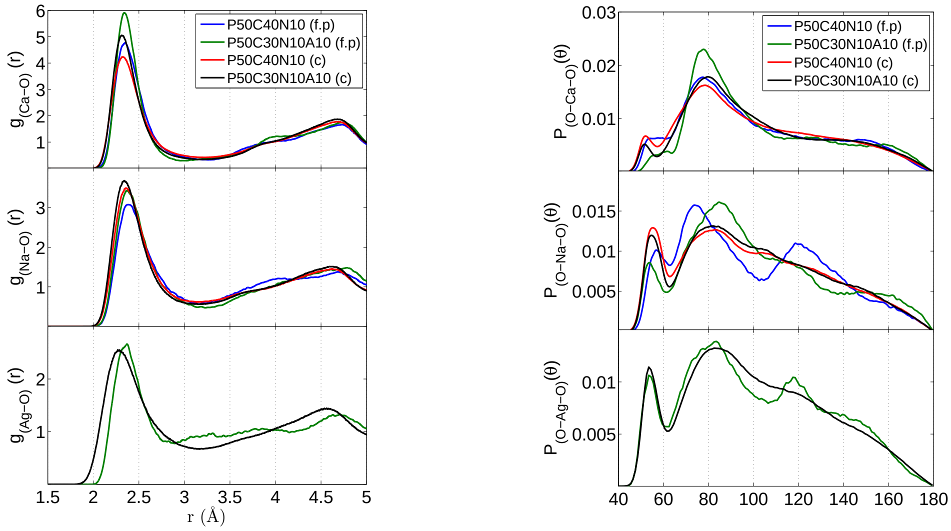

(a) **(b)**

Figure 7.7: (a) Ca-O, Na-O and Ag-O partial pair-correlation functions. (b) O-Ca-O, O-Na-O and O-Ag-O angular distribution functions. Me-O cut-offs taken as first minimum of respective radial distribution functions.

data (see Table 7.4).

Figure 7.7b displays the ADFs for the three-body systems O-Me-O. For the O-Ca-O system there is a strong localisation of bond angles at ~80° and a significant contribution of angles up to 150°, consistent with a distorted octahedral coordination, as found in other Ag-free PBG.[177] As also indicated, by a large normalised peak intensity in $g_{(\mathrm{Ca-O})}$ (r) and first minimum located at 3 Å, the O-Ca-O distribution for P50C30N10A10 (f.p.) displays increased intensity at ~80° when compared to P50C40N10 (f.p.) (a dopant dependent feature also seen in classical results). This indicates that, the Ca ions in this model, bond in a more symmetric octahedron and is likely linked to the presence of two further modifier species in the composition. A secondary set of peaks of lower intensity in the range $50-65°$ are attributed to intra-tetrahedral environments, for which both oxygens are bonded to a common phosphorus atom.[166, 177] The ADFs for O-Na-O show significant compositional dependence for f.p. models. P50C40N10 (f.p.) has peaks at 57°, 75° and 120° compared to the stronger octahedral coordination of P50C30N10A10 (f.p.) with peaks at 52°, 84° and ~ 160°. Results from the classical simulations show no significant compositional dependence although there is increased intra-tetrahedral contribution. The O-Ag-O distribution for P50C30N10A10 (f.p.) has three dominant peaks centered at 54°, 84°, 118° with a shoulder feature at ~140°, suggesting a distorted bonding environment (representative Ag environment shown in Figure 7.8). The classical results show very good agreement, with a slightly smoother distribution of O-Ag-O bond-angles (likely a statistical effect coupled with a differing description of inter-atomic forces). Peaks from the latter are centered on 54° and 84° with a shoulder at ~120° (see Figure 7.7b).

7.3.3 Modifier coordination

Both compositions studied contain a variety of local environments. f.p. results commonly show more highly resolved angular contributions, which may be a product of poor statistical sampling, or may reflect the highly accurate description of inter-atomic forces. As previously shown from ADFs, Ca displays a distorted octahedral coordination environment and this is confirmed with coordination numbers ($\eta_{(\mathrm{Ca-O})}$) of 6.91 and 6.57 for P50C40N10 (f.p.) and P50C30N10A10 (f.p.) respectively (see Table7.6). This 0.34 decrease in $\eta_{(\mathrm{Ca-O})}$ further indicates increased octahedral symmetry upon Ag-doping. f.p. results show $\eta_{(\mathrm{Na-O})} = 6.07$ reducing to $\eta_{(\mathrm{Na-O})} = 5.85$ when the glass is doped. These results are similar to previous MD simulations of ultra-phosphate PBG compositions.[177] For f.p. results, $\eta_{\mathrm{Ag-O}} = 5.42$ at a cut-off of 3.20 Å. As previously stated, there is an ill-defined minimum in $\mathrm{g}_{(\mathrm{Ag-O})}$ (r) and the dependence of $\eta_{(\mathrm{Ag-O})}$ on Ag-O cut-off (Ag-O$_{(\mathrm{cut})}$) is given in Table 7.7, ranging from $\eta_{(\mathrm{Ag-O})} = 3.71$ at Ag-O$_{(\mathrm{cut})}$ = 2.80 Å to $\eta_{(\mathrm{Ag-O})} = 6.55$ at Ag-O$_{(\mathrm{cut})}$ = 3.40 Å.

Table 7.6: Modifier & dopant coordination environments for f.p. and c. simulations. Coordination numbers (η) with Ca-O, Na-O and Ag-O cut-offs set at 3.22 (f.p.)/ 3.25 (c.) Å, 3.15 (f.p.)/ 3.15 (c.) Å and 3.20 (f.p.) / 3.15 (c.) Å respectively. η decomposed into BO and NBO contributions.

	P50C40N10 (f.p.)	P50C30N10A10 (f.p.)
Atomic Pair	η	η
Ca-O	6.91	6.57
Ca-BO	0.52	0.48
Ca-NBO	6.39	6.09
Na-O	6.07	5.85
Na-BO	0.99	0.85
Na-NBO	5.08	5.00
Ag-O	–	5.42
Ag-BO	–	0.82
Ag-NBO	–	4.60
	P50C40N10 (c.)	P50C30N10A10 (c.)
Atomic Pair	η	η
Ca-O	6.79	6.44
Ca-BO	0.65	0.49
Ca-NBO	6.14	5.95
Na-O	6.48	6.02
Na-BO	1.43	1.18
Na-NBO	5.05	4.84
Ag-O	–	5.54
Ag-BO	–	0.98
Ag-NBO	–	4.56

Several X-ray absorption Near Edge Structure studies (XANES) of 0 – 20 mol% Ag PBG, have shown the shape and position of the Ag K-edge spectra, to be identical to the reference material Ag_2SO_4.[31, 173, 174] From these studies, the authors have concluded that, the Ag ion in Ag-PBG, has a structural environment very similar to that of Ag_2SO_4. Figure 7.8 shows an example Ag ion coordination environment from the P50C30N10A10 (f.p.) model along with the local coordination environment of Ag^{I} in Ag_2SO_4 in the upper and lower panels respectively.[180] Both structures show a distorted octahedral symmetry, providing further evidence of the similarities in Ag local ordering.

Moss *et al.*[174] have previously conducted neutron diffraction with isotopic substitution (NDIS) using P50C30N10A10 samples enriched with ^{107}Ag and ^{109}Ag isotopes. This allows for the simplification of complex correlations[181] (assuming each sample has identical composition and structure) by the application of difference function methods.[182, 183] They showed[174] that the Ag-O correlation has three components in the first coordination shell at 2.28 Å, 2.51

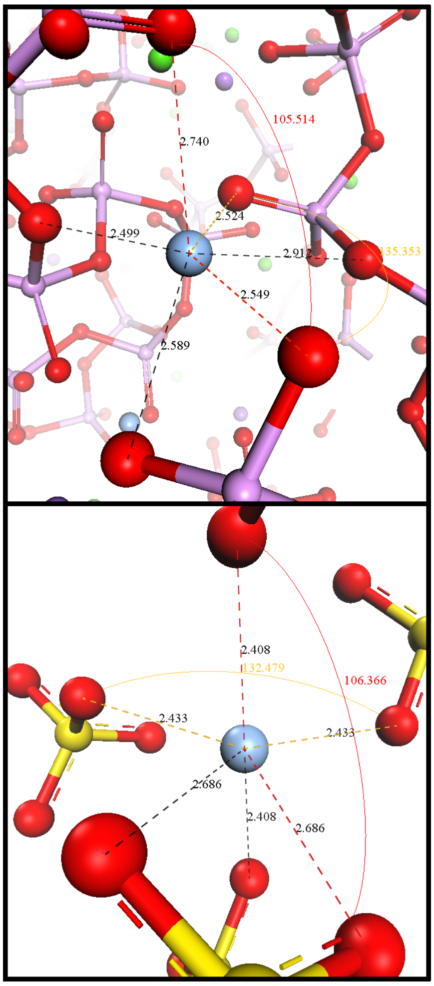

Figure 7.8: Example Ag coordination environment in P50C30N10A10 (f.p.) (upper panel) and crystalline Ag_2SO_4 - space group *Fddd*, No. 70[180] (lower panel). Common distorted octahedral geometry and in-plane intra-tetrahedral coordination.

Table 7.7: Silver to oxygen coordination numbers (η) as a function of Ag-O cut-off for P50C30N10A10 (f.p.).

	2.80 Å	2.90 Å	3.00 Å	3.10 Å	3.20 Å	3.30 Å	3.40 Å
Atomic Pair	η	η	η	η	η	η	η
Ag-O	3.71	4.07	4.47	4.92	5.42	5.98	6.55
Ag-BO	0.22	0.33	0.47	0.63	0.82	1.05	1.29
Ag-NBO	3.49	3.74	4.00	4.29	4.60	4.93	5.26

Å and 2.73 Å with coordination numbers of 2.1, 2.7 and 1.1 respectively. $g_{(\mathrm{Ag-O})}$ (r) from the current work (see Table 7.7a for peak position) displays a unimodal distribution within the first coordination sphere, for both methodologies, with no evidence for multiple resolved peaks. Table 7.8 shows the Ag-O mean bond lengths, $\bar{r}^{\mathrm{f.p.}}_{(\mathrm{Ag-O})}$ and $\bar{r}^{\mathrm{c.}}_{(\mathrm{Ag-O})}$, as a function of $\mathrm{Ag\text{-}O}_{(\mathrm{cut})}$ for the first coordination sphere. The experimental value of $\bar{r}^{\mathrm{NDIS}}_{(\mathrm{Ag-O})} = 2.47$ Å ± 0.07 Å[174] is

Table 7.8: Mean silver to oxygen bond lengths ($\bar{\mathrm{r}}_{(\mathrm{Ag-O})}$ (Å)) in first coordination sphere as a function of Ag-O cut-off for P50C30N10A10 (f.p.) and P50C30N10A10 (c.) Average bond length from experiment $\bar{\mathrm{r}}^{\mathrm{NDIS}}_{(\mathrm{Ag-O})}$ = 2.47 Å ±0.07 Å.[174]

	2.90 Å	2.95 Å	3.00 Å	3.05 Å	3.10 Å	3.15 Å	3.20 Å	3.25 Å	3.30 Å
$\bar{\mathrm{r}}^{\mathrm{f.p.}}_{(\mathrm{Ag-O})}$	2.46	2.47	2.49	2.50	2.53	2.54	2.57	2.58	2.61
$\bar{\mathrm{r}}^{\mathrm{c.}}_{(\mathrm{Ag-O})}$	2.41	2.44	2.47	2.50	2.53	2.55	2.58	2.61	2.64

derived using the published bond lengths weighted according to coordination number. $\bar{\mathrm{r}}^{\mathrm{f.p.}}_{(\mathrm{Ag-O})}$ and $\bar{\mathrm{r}}^{\mathrm{f.p.}}_{(\mathrm{Ag-O})}$ provide a more direct comparison to experiment, compared to the peak centered position of $\mathrm{g}_{(\mathrm{Ag-O})}$ (r), due to the fact the partial pair-correlation does not decay to zero at the limit of the first coordination sphere, resulting in the deviation of peak centered value from the mean bond length. $\bar{\mathrm{r}}^{\mathrm{f.p.}}_{(\mathrm{Ag-O})}$ and $\bar{\mathrm{r}}^{\mathrm{c.}}_{(\mathrm{Ag-O})}$ range from 2.46 − 2.61 Å and 2.41 − 2.64 Å respectively, across the range Ag-O$_{(\mathrm{cut})}$ = 2.90 Å − 3.30 Å, in good agreement with experiment.

Figure 7.8 facilitates a more detailed assignment of peaks in the P50C30N10A10 (f.p.) O-Ag-O ADF from Figure 7.7b. The peak at 54° corresponds to intra-tetrahedral bonding as evidenced in the example environment shown. This distorted ocatahedral geometry also shows further in plane angles at 77°, 135° and 147° contributing to the peak 84° and shoulder feature at ∼140° in the ADF. Further to this, 5-coordinated distorted trigonal bi-pyramidal Ag-O first-coordination environments were observed, constituting contributions to the ADF peaks centered on 84° and 118°.

$\eta_{(\mathrm{Me-O})}$ values from classical simulations (c.) are given in the lower half of Table 7.6 with amended cut-offs to reflect differing first minima in $\mathrm{g}_{(\mathrm{Me-O})}$ (r) (c.). Direct comparison to f.p. results shows good agreement for $\eta_{(\mathrm{Ca-O})}$ and $\eta_{(\mathrm{Na-O})}$ with similar decompositions for BO and NBO. Upon Ag-doping $\eta_{(\mathrm{Ca-O})}$ (c.) and $\eta_{(\mathrm{Na-O})}$ (c.) decrease by 0.35 and 0.46 respectively, in line with decreases of 0.34 (f.p.) and 0.22 (f.p.) respectively. $\eta_{(\mathrm{Ag-O})}$ = 5.54 (c.) at Ag-O$_{(\mathrm{cut})}$ = 3.15 Å, which compared to similar cut-off values for (f.p.) results given in Table 7.7, is in reasonable agreement.

7.3.4 Medium-range order

The larger simulation models used in classical methods facilitate a more statistically sound analysis of the medium-range structure, providing insight into compositionally dependent structural trends at these length scales. Thus, only results from the classical simulations

Table 7.9: Q^n species distribution (%) (for phosphorus with respect to oxygen) and network connectivity (NC). Experimental data (expt.) from fitting to ^{31}P MAS NMR spectra.[141]

	Q^0	Q^1	Q^2	Q^3	Q^4	NC
P50C40N10 expt.	0.0	4.0	96.0	0.0	0.0	1.96
P50C40N10 (c.)	0.6	9.9	79.7	9.7	0.1	1.99
P50C30N10A10 (c.)	0.4	10.9	78.0	10.6	0.1	1.99

are presented in this section. Moss *et al.*[174] have inferred that a disproportionation in the medium-range Q^n distribution occurs upon CaO substitution with Ag_2O for the compositions studied here. The authors, using a simple bond-order model, show that an increase in $\sigma_{(P-BO)}$ and static disorder of P-NBO implies a disproportionation in the network structure. Valappil *et al.*[31] explicitly showed, via ^{31}P MAS NMR spectral analysis, that the substitution of Na_2O with Ag_2O, for the compositions $(P_2O_5)_{0.50}(CaO)_{0.30}(Na_2O)_{0.20-x}(Ag_2O)_x$ (x = 0.00, 0.10, 0.15 and 0.20), leads to a disproportionation of Q^2 units approximating the relation $2Q^2 \rightarrow Q^1 + Q^3$, for $x \geq 0.10$.

The phosphorus Q^n distributions from classical simulations are given in Table 7.9. P50C40N10 (c.) comprises 79.7% Q^2, 9.9% Q^1 and 9.7% Q^3 from our simulations compared to 96% Q^2 and 4% Q^1 from experiment.[141] Similar levels of agreement with experiment are found for classical MD derived phosphate,[177] phosphosilicate[151] and sodium silicate[149, 184] glasses.

The potential reasons for discrepancies between theoretical and experimental Q^n distributions are wide ranging and include modal assumptions when deconvoluting experimental NMR signals. From the theory side, Stebbins[185] found that both an increase in glass transition temperature (known to be higher in theoretical simulations than experiment) and higher field strength modifiers caused the disproportionation reactions, $2Q^n \rightarrow Q^{n-1} + Q^{n+1}$ (for n = 1, 2 and 3), in silicate glasses. The discrepancies in Q^1, Q^2 and Q^3 proportions for P50C40N10 (c.) from the current work (compared to experiment) may relate to fictive temperatures that are in excess of experiment (further limitations with MD methods are discussed by Pota *et al.*[186]). For P50C30N10A10 (c), Q^2 reduces to 78% with concomitant rises in Q^1 and Q^3, approximating the relation found by Valappil and co-workers.[31]

Network connectivity (NC), defined as the mean number of BO within the first coordination shell of phosphorus summed over all P atoms, is 1.99 for both simulated compositions. This is very close to the value of 2.0 expected theoretically and found experimentally.[141]

Table 7.10: Mean Mulliken charges for all atomic species X ($Q_{(X)}$) in P50C40N10 (f.p.) and P50C30N10A10 (f.p.).

	P50C40N10 (f.p.)	P50C30N10A10 (f.p.)
$Q_{(P)}$	+0.760	+0.766
$Q_{(O)}$	−0.459	−0.453
$Q_{(BO)}$	−0.384	−0.384
$Q_{(NBO)}$	−0.497	−0.488
$Q_{(Ca)}$	+1.146	+1.130
$Q_{(Na)}$	+0.810	+0.791
$Q_{(Ag)}$	—	+0.540

7.3.5 Atomic charges

The mean atomic charges obtained by Mulliken population analysis are given in Table 7.10. These are summed over all timesteps of the 300 K trajectory from f.p. models. No significant changes are noted upon Ag-doping with net phosphorus charges of +0.760 and +0.766 for P50C40N10 (f.p.) and P50C30N10A10 (f.p.) respectively. It should be noted that Mulliken charges are calculated by determining the electron population of each atom as defined by the basis functions and absolute values are therefore dependent on the choice of basis set. For example, the electronic states and chemical bonding in phosphate glass have previously been studied by Kowada *et al.*[187] using the DV-Xα cluster method. For the charge balanced P_4O_{10} cluster the net charge on phosphorus was found to be +1.31 using Mulliken population analysis. In the context of the other atoms in this study, the phosphorus atoms have a covalent interaction with the surrounding oxygens. The mean oxygen atomic charges have been deconvoluted into BO and NBO, with the NBO displaying increased ionic character with net charges of −0.497 and −0.488 for PBG and Ag-PBG respectively. Mean BO charges are found to be +0.113 and +0.104 higher due to the presence of two phosphorus atoms in their first coordination sphere. These changes are in good agreement with the relation $Q_{(BO)} = Q_{(NBO)} + 0.12$ for the cluster P_4O_{10}.[187] All modifier ions show increased ionic character compared to the network formers, with Na showing more ionic character than that of Ag. From these results, it can be surmised that the silver resides in the Ag^{I} oxidation state, in agreement with XANES analysis.[173]

7.4 Summary

The structures of $(P_2O_5)_{0.50}(CaO)_{0.40-x}(Na_2O)_{0.10}(Ag_2O)_x$ (x = 0.00 and 0.10) biomedically relevant glasses have been investigated, using first-principles (f.p.) and classical (c.) molecular dynamics simulations. Good structural agreement is found between the results from c. simulations (using a force field that has previously developed within our group[177]) and the high level f.p. reference calculations. The c. methodology outperforms f.p. in reproducing some key structural features, such as P-O bond distances, when compared to experimental data. The Ag ion is noted to have little effect on short-range order but there is evidence for a disproportionation in the medium-range Q^n distribution for phosphorus upon doping, following the relation $2Q^2 \rightarrow Q^1 + Q^3$. An increase in P-BO bond disorder (as seen in experiment[141, 174]) from f.p. results, further supports this feature. These structural changes are of likely consequence in the observed decrease in dissolution rates with increased Ag mol%.

The Ag ion has a distorted octahedral and trigonal bi-pyramidal structure with an ill defined first-coordination shell. The Ag coordination number is 5.42 (f.p.) and 5.54 (c.).

Mulliken charge analysis shows the network modifiers (Ca, Na and Ag) to be ionic with charges that are close to formal. The network forming phosphorus show higher levels of covalency with mean Mulliken net charges of $\sim$+0.76.

Chapter 8

Amorphous P_2O_5-CaO-Na_2O-TiO_2 systems

8.1 Overview

The incorporation of TiO_2 in PBG has been shown to increase glass density and T_g, while reducing the degradation and ion release rates. As discussed in subsection 2.2.3, these changes in materials properties lend such compositions to hard tissue engineering. It is widely suggested that the increased structural stability, can be attributed to changes in the medium-range structure of the glasses, typically described by the network forming Q^n distribution. Furthermore, titanium-doped PBGs are known to have increased oseteoconductive properties.

8.1.1 Experimental structural & thermodynamic data

$(P_2O_5)_{0.445}(CaO)_{0.445}(Na_2O)_{0.110-x}(TiO_2)_x$ (x = 0.000, 0.030, 0.050 and 0.080) have been prepared by the melt-quench procedure and the structures analysed.[38] The authors used FT - Raman spectroscopy, after different periods of immersion in SBF, to detect possible changes in the glass structure produced during degradation. Radiation was supplied by an Ar^+ laser tuned to the green line at 516.5 nm and data were taken at frequencies between 300 and 1400 cm^{-1}. Figure 8.1 shows the Raman spectra for all compositions labelled G0 (x = 0.000), G3 (x = 0.030), G5 (x = 0.050) and G8 (x = 0.080). G0 displays characteristic shifts of the $(PO_2)_{asym}$ stretch at ~1260 cm^{-1}, the $(PO_2)_{sym}$ stretch at ~1170 cm^{-1} and the $(POP)_{sym}$ stretch near ~690 cm^{-1}, all corresponding to Q^2 groups. The $(PO_3)_{sym}$ stretch at ~1040 cm^{-1}

corresponds to Q^1 groups. The influence of TiO_2 doping is clearly evidenced, for compositions G3, G5 and G8, by new bands at 900 cm^{-1} and 630 cm^{-1} corresponding to the TiO_5 and TiO_6 units stretch respectively. These bands increase in intensity for increased mol% TiO_2. The left hand panel of Figure 8.2 illustrates the effects of dissolution and surface hydration on the structure of glasses G0 and G5 before and after 9 weeks in SBF at 37°C. For the undoped G0 glass, new bands appear after 9 weeks, at 960 cm^{-1} corresponding to orthophosphate PO_4 groups. Further to this, the bands at 690 cm^{-1} and 1170 cm^{-1} notably decrease in intensity. The effects of TiO_2 are clearly shown by comparison to the spectra for G5, which remains almost intact, illustrating the enhanced chemical durability of Ti-PBG. The evolution of the Raman spectra for the G5 composition, over the total study time of 12 weeks in SBF, is shown in the right hand panel of Figure 8.2. The intensity of the shifts are diminished as the dissolution time increases (linked to uniformity in the glass surface affecting the collection of data) but the identity of the main shifts remains constant.

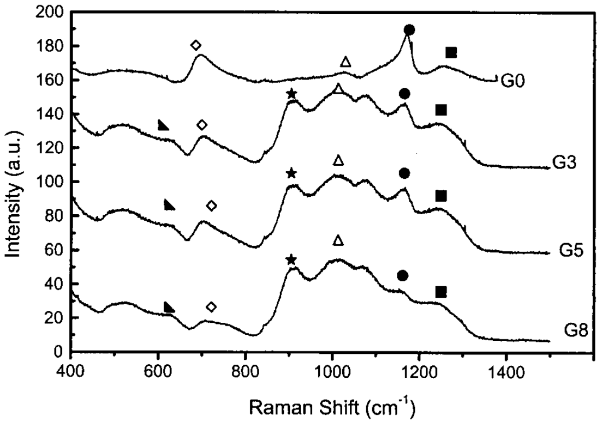

Figure 8.1: Raman spectra of glasses $(P_2O_5)_{0.445}(CaO)_{0.445}(Na_2O)_{0.110-x}(TiO_2)_x$ (G0 (x = 0.000), G3 (x = 0.030), G5 (x = 0.050) and G8 (x = 0.080)). Highlighted shifts are $(PO_2)_{asym}$(■), $(PO_2)_{sym}$(•), $(PO_2)_{sym}$ stretch (△), TiO_5 units stretch (★), $(POP)_{sym}$ stretch (◇) and TiO_6 units stretch (◄).[38]

$(P_2O_5)_{0.55}(CaO)_{0.30}(Na_2O)_{0.15-x}(TiO_2)_x$ (x = 0.00, 0.01, 0.03 and 0.05) have been synthesised and characterised by Kiani *et al.*[188] using XRD, SSNMR, Raman and FTIR spectroscopy. Melt quench derived samples were annealed above T_c and the crystalline phase $NaCa(PO_3)_3$ was subsequently identified for x = 0.00 and 0.01 compositions. For the 3 and 5 mol% TiO_2 compositions the main crystalline phase was identified as CaP_2O_6 with a secondary TiP_2O_7 phase. The Raman spectra produced for these glasses are given in Figure 8.3. The $(POP)_{sym}$ stretch at ~690 cm^{-1} is ascribed to BO linking Q^3 tetrahedra. The $(PO_2)_{sym}$ stretch peak

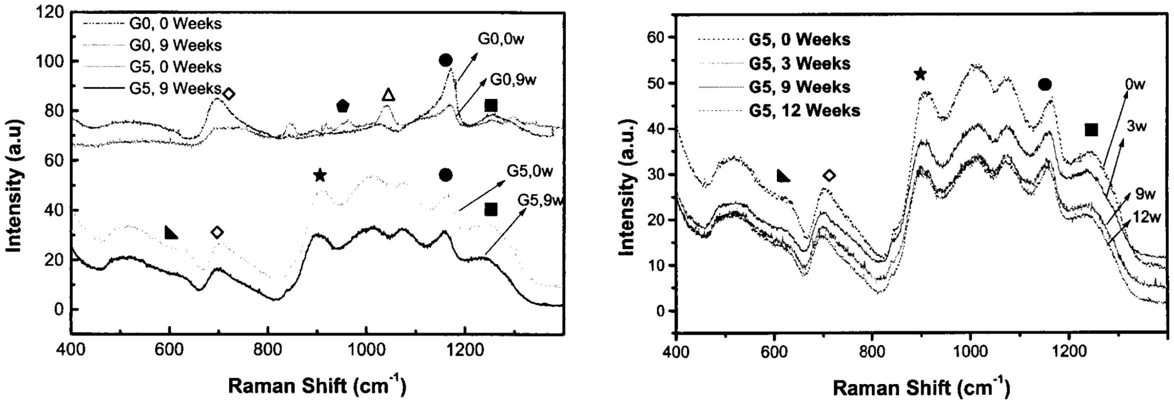

Figure 8.2: Left hand panel: Raman spectra of glasses $(P_2O_5)_{0.445}(CaO)_{0.445}(Na_2O)_{0.110-x}(TiO_2)_x$ (G0 (x = 0.000) and G5 (x = 0.050)) before degradation and after 9 weeks of dissolution. $(PO_2)_{sym}$(●), $(PO_2)_{sym}$ stretch (△), TiO_5 units stretch (★), $(POP)_{sym}$ stretch (◇), TiO_6 units stretch (◀) and (PO_4) stretch (⬠). Right hand panel: Raman spectra of G5 (x = 0.050) after 0, 3, 9 and 12 weeks of dissolution in SBF at 37°C (highlighted shifts key as for left hand panel).[38]

for NBO coordinated to Q^2 tetrahedra occurs at ~1180 cm^{-1} and the band at ~1280 cm^{-1} is attributed to $(PO_2)_{asym}$. An increase in intensity of the symmetric stretch of P-NBO near 1370 cm^{-1}, is cited as evidence of a more cross-linked structure with a further peak at ~930 cm^{-1}, corresponding to a Ti-O band, increasing in intensity with increased mol% TiO_2.

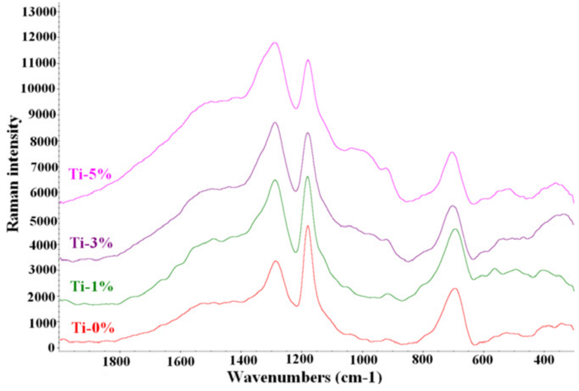

Figure 8.3: Raman spectra of glasses $(P_2O_5)_{0.55}(CaO)_{0.30}(Na_2O)_{0.15-x}(TiO_2)_x$ (x = 0.00, 0.01, 0.03 and 0.05).[188]

Results of the FTIR analysis are given in Figure 8.4 and show bands at ~1300-1250 cm^{-1} assigned to asymmetric stretching modes, ν_{as}(O-P-O), of the two NBO associated with Q^2 phosphate tetrahedron. Absorption bands near 1100 and 1000 cm^{-1} are assigned to the asymmetric and symmetric stretching of chain-terminating Q^1 groups ($\nu_{as}(PO_3)^{2-}$, $\nu_s(PO_3)^{2-}$), respectively. Interestingly, the band near to 1070 cm^{-1} is attributed to Q^0 $(PO_4)^{3-}$ end groups and it is noted that there is a reduction in both Q^0 and Q^1 species with increasing mol% TiO_2. This is cited as possible indirect evidence for the formation of Ti-O-P bonds, leading to a reduction in the number of NBO as the dopant concentration is increased.

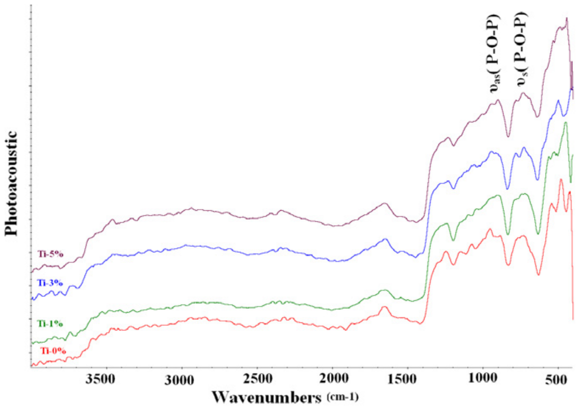

Figure 8.4: FTIR spectra of glasses $(P_2O_5)_{0.55}(CaO)_{0.30}(Na_2O)_{0.15-x}(TiO_2)_x$ (x = 0.00, 0.01, 0.03 and 0.05).[188]

Solid-state ^{31}P MAS NMR spectra were deconvoluted with a bimodal model. The ratio of the resonances was obtained by fitting with Gaussian line shapes and summing the intensities of the isotropic peaks and the full span of corresponding spinning sidebands. The results of this analysis give a Q^n distribution of 72% Q^2 / 28% Q^3 for P55C30N15 (in contrast to Ahmed *et al.*[18] who assign 0.31% Q^1 / 99.69% Q^2 from static ^{31}P NMR). As TiO_2 mol% is increased, the proportion of Q^3 increases steadily to 40% in P55C30N10T5 with a concomitant decrease in Q^2, falling to 60% for the 5 mol% TiO_2 composition. The authors state that, the changes in the medium-range structure indicate increasing polymerization of the phosphate network correlating with enhanced glass stability. The anomaly between FTIR and ^{31}P MAS NMR data, regarding the presence or lack of Q^0 and Q^1 species is postulated as possibly caused by differing sample preparations. It is also stated that the detection limit of ∼1 mol% for NMR may be the reason for the disagreement. Density measurements from the same study show an increase in density from 2.56 g.cm^{-3} in P55C30N15 to 2.58 g.cm^{-3} in P55C30N10T5 explained in terms of increased close packing of atoms by the strong P-O-Ti bonds. Finally, thermal analysis was carried out and the DTA trace is shown in Figure 8.5. T_g increases from 654 K in P55C30N15 to 710 K in P55C30N10T5. The upward peaks are exothermic and represent T_c which also increases from 863 K to 985 K moving for compositions x = 0.00 and x = 0.05 respectively.

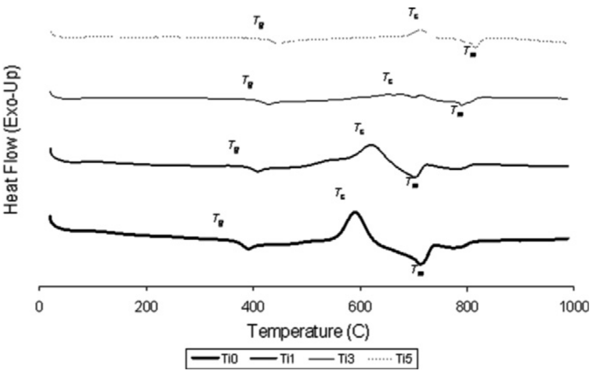

Figure 8.5: DTA trace of glasses $(P_2O_5)_{0.55}(CaO)_{0.30}(Na_2O)_{0.15-x}(TiO_2)_x$ (x = 0.00, 0.01, 0.03 and 0.05) when heated up to 1273 K.[188]

8.1.2 Theoretical ^{31}P NMR & MD-GIPAW

Solid-state nuclear magnetic resonance (NMR) detects the transition energies from the reorientation of nuclear magnetic moments when an external magnetic field is applied to a material. Since the external field induces electronic motion within the atomic orbitals generating a small magnetic field in the *opposite* direction to the external field, the nucleus is shielded. The nuclear shielding is dependent on the specific electronic environment around each nucleus and can be used, experimentally, to identify different atomic sites within a material.

Static ^{31}P NMR and dynamic ^{31}P MAS NMR are sensitive probes of medium-range structure and routinely used, in the context of phosphate-based glasses, to assign a specific Q^n distribution for P atoms.[18, 141, 188, 189] The assignment of ^{31}P NMR and ^{31}P MAS NMR peaks for P_2O_5-CaO-Na_2O systems using a binomial (Q^1 and Q^2) model[18, 76] has been shown to be in contrast with Q^n distributions from a computational study,[177] which additionally contain $4 - 6\%$ Q^3. Further to this, contrasting Q^n distributions have been found experimentally for $(P_2O_5)_{0.55}(CaO)_{0.30}(Na_2O)_{0.15}$, interpreted as 0.31% Q^1 / 99.69% Q^2 from NMR[18] and 72% Q^2 / 28% Q^3 from MAS NMR.[188] FTIR data from the same study shows the presence of both Q^0 and Q^1 species, not identified in MAS NMR. These studies illustrate the complex nature of Q^n distribution assignment due to anisotropic broadening and chemical species detection limits of ~ 1 mol% in NMR.

Chemical shifts from density-functional NMR calculations allow for the explicit atomic assignment of signals contributing to the composite NMR signal, enhancing the analysis of such data. Furthermore, theoretical data give a deeper insight into the electronic structure at given sites within a material and the effects on the chemical shift. Pickard and Mauri[190] have previously adapted Blöchl's projector augmented wave (PAW) method[191] to respect the translational invariance of a system in a magnetic field, as implemented in the gauge-including projector augmented wave (GIPAW) method. GIPAW allows for the first principles calculation of all-electron NMR chemical shifts in periodic systems, using plane-wave DFT, and has subsequently been extended for use with ultrasoft pseudopotentials.[192] The application of the highly accurate MD-GIPAW approach, has been shown to be widely successful for the generation of structural models and the interpretation of experimental NMR spectra in many chemical systems,[193, 194] and more specifically, oxide glasses.[195]

The GIPAW method allows the user to calculate the chemical shift and electric field gradient interaction for each atom in a periodic system to all-electron accuracy. As also briefly described in subsection 8.2.3, the experimentally attainable chemical shift, δ_{iso}, is obtained from the isotropic magnetic shielding, σ_{iso}:

$$\sigma_{\mathrm{iso}} = \frac{1}{3} Tr \left\{ \overset{\leftrightarrow}{\sigma} \right\} \tag{8.1}$$

through,

$$\delta_{\mathrm{iso}} = \sigma_{\mathrm{ref}} - \sigma_{\mathrm{iso}}, \tag{8.2}$$

where σ_{ref} is the isotropic chemical shielding of the same nucleus in a reference system. The anisotropy of the symmetrized tensor $\overset{\leftrightarrow}{\sigma}$ is characterised by the chemical shift anisotropy (CSA), δ_{CSA}, reflecting its magnitude and by an asymmetry parameter, η_{CSA} describing its deviation from cylindrical symmetry ($\eta_{CSA} = 0$),

$$\delta_{\mathrm{CSA}} = \delta_{\mathrm{ZZ}} - \delta_{\mathrm{iso}} \tag{8.3}$$

and

$$\eta_{\mathrm{CSA}} = \frac{\delta_{\mathrm{YY}} - \delta_{\mathrm{XX}}}{\delta_{\mathrm{CSA}}}. \tag{8.4}$$

δ_{XX}, δ_{YY} and δ_{ZZ} are the eigenvalues of the symmetric chemical shift tensor, such that $|\delta_{\mathrm{ZZ}} - \delta_{\mathrm{iso}}| \geq |\delta_{\mathrm{XX}} - \delta_{\mathrm{iso}}| \geq |\delta_{\mathrm{YY}} - \delta_{\mathrm{iso}}|$.[195] For a nucleus with spin $I > \frac{1}{2}$, the NMR response will include an interaction between the quadrupole moment of the nucleus, $e\mathrm{Q}$, and the electric field gradient tensor by the surrounding electronic structure.[194] The quadrupolar coupling constant, C_Q, and the assymetry parameter, η_Q, can be obtained from the diagonalized electric field gradient tensor whose eigenvalues are labelled V_XX, V_YY and V_ZZ, such that $|V_\mathrm{ZZ}| \geq |V_\mathrm{XX}| \geq |V_\mathrm{YY}|$:

$$C_\mathrm{Q} = \frac{eV_\mathrm{ZZ}\mathrm{Q}}{h} \tag{8.5}$$

and

$$\eta_\mathrm{Q} = \frac{V_\mathrm{XX} - V_\mathrm{YY}}{V_\mathrm{ZZ}}. \tag{8.6}$$

The MD-GIPAW method refers to the GIPAW method combined with molecular dynamics (MD), thus linking the variations in local structure of disordered solids and the experimental distributions of the NMR parameters. With the correct statistical approaches to thermal, time and configurational averaging, MD-GIPAW enables the direct comparison between experimental NMR and MD data, through the theoretical NMR spectrum.

8.2 Computational methods

8.2.1 *Ab initio* molecular dynamics

Born-Oppenheimer molecular dynamics (BOMD) simulations were performed with the QUICKSTEP module[105, 106] in the CP2K code (development version 2.3.16). A dual basis set was used, in which the Kohn-Sham orbitals are expanded in an atom centered Gaussian basis set while the electronic charge density is described using an auxiliary plane wave basis set.[96] Core electrons were described with the pseudopotential of Goedeker, Teter and Hutter (GTH).[93–95] Valence electrons were treated with the Perdew-Burke-Ernzerhof (PBE)[90] gradient corrected exchange-correlation functional in the double-ζ valence polarized, molecular optimised basis set (DZVP-MOLOPT-SR-GTH).[196] The orbital transformation method[175] was employed for an efficient wavefunction optimization. The convergence criteria for the SCF loop was set at 1×10^{-5} Hartree for each step.

The internal energy of crystalline $CaNaPO_4$ is converged to $\pm 8.52\times10^{-4}$ Ry per formula unit at a plane wave kinetic energy cutoff of 8163 eV for the charge density. For a crystalline $TiPO_4$ reference system the internal energy is converged to $\pm 5.98\times10^{-5}$ Ry per formula unit at this cutoff. All calculations (undoped and titanium-doped) were therefore run at a plane wave kinetic energy cutoffs of 8163 eV for charge density (with a model periodic in three-dimensions) in the Γ-point approximation. The timestep for each dynamics step was set to 1 fs.

The glass generation followed a standard melt-quench protocol in which atoms were initially quasi-randomly inserted into cubic simulation boxes to reproduce experimental densities, the details of which are given in Table 8.1. The configurations were then evolved for 3 ps in the NVE ensemble. Subsequently each system was equilibrated at a target temperature of 2500K, in the NVT ensemble (using a Nosé-Hoover thermostat[198–200]), for 45 ps. A full melting was assessed via analysis of the mean-square atomic displacements. Each system was then cooled to 300 K at a nominal rate of 24.4 $K.ps^{-1}$ in a series of NVT trajectories of target temperatures 2200 K, 1900 K, 1600 K, 1300 K, 1000 K and 700 K. The final 300 K trajectories were run for 40 ps, during which time average structural data were sampled. The compositional nomenclature used henceforth is, P = P_2O_5, C = CaO, N = Na_2O and T = TiO_2, followed by the percentage molar composition for each component.

Table 8.1: Compositions simulated. $(P_2O_5)_{0.45}(CaO)_{0.3}(Na_2O)_{0.25-x}(TiO_2)_x$.

x	Atoms	Cell size (Å)	Density ($g.cm^{-3}$)
0.00	199	13.8958	2.63[197]
0.15	199	13.8406	2.74[197]

8.2.2 Mechanical properties

Theodorou and Suter[201] showed that entropic contributions to the elastic response to deformation can be neglected in polymeric glasses. Further to this, the insignificance of vibrational contributions of the hard degrees of freedom, allows for the estimation of elastic constants from changes to the potential energy of static microscopic structures subjected to simple deformations. The bulk modulus (B), or inverse of compressibility (where p is the pressure imposed on the system), can be rewritten as the partial second order derivative of the internal energy with respect to volume for a given number of atoms (N) at a given temperature (T), multiplied by the volume at the minimum energy (V_0):

$$B = -V_0 \left(\frac{\partial p}{\partial V}\right)_{N,T}\Bigg|_0 = V_0 \left(\frac{\partial^2 E}{\partial V^2}\right)_{N,T}\Bigg|_0 \tag{8.7}$$

where $|_0$ indicates the value is evaluated for the minmum in energy. The final snapshot of the 300K DFT-MD trajectory, for each composition, was taken and geometry optimised at 0K using the afore-mentioned methodology implemented in the CP2K code. Using this structure, small strains in the range $-0.03 \leq \delta_{\mathrm{strain}} \leq +0.03$ were imposed to the periodic cubic unit cell sides and in each case, the system re-optimised. The subsequent change in internal energy from the unstrained system was plotted against strain and a quadratic fitted to the resulting data points.

8.2.3 Chemical shieldings

Taking snapshots from the DFT-MD trajectories for each composition at 300K, isotropic chemical shifts (σ_{iso}) were calculated using the GIPAW method implemented in the Cambridge Serial Total Energy Package (CASTEP) PW DFT code[202] using the GGA approximation functional PBE. A plane-wave basis set cut-off energy of 750 eV for wavefunctions was used (internal energy, post geometry optimisation, is converged to 0.078 eV at this cut-off) in the Γ-point approximation.

In order to incorporate the influence of motional effects, it was previously found (for organic systems) that using snapshots from DFT-MD trajectories to sample configurational space, suffered from limited sampling due to the relatively short simulation times.[203] It was shown using block sampling, that sampling every 50 fs, over a total simulation time of 3.2 ps lead to correlated chemical shifts for some sites. In the current work we use an increased sampling timestep of 2 ps over the final 20 ps of the 300K trajectory.

The isotropic chemical shift for a nucleus (δ_{iso}) is obtained using the following relation,

$$\delta_{\mathrm{iso}} = \sigma_{\mathrm{ref}} - \sigma_{\mathrm{iso}}, \tag{8.8}$$

where σ_{iso} is the isotropic chemical shielding and related to the trace of the NMR shielding tensor ($\overleftrightarrow{\sigma}$) via $\sigma_{\mathrm{iso}} = \frac{1}{3}Tr\left\{\overleftrightarrow{\sigma}\right\}$. σ_{ref} is the isotropic chemical shielding of the same nucleus in a reference system. Theoretical ^{31}P NMR spectra were constructed via the superposition of Gaussian functions of the form $f(x) = a.\exp\left(\frac{-(x-\sigma_{\mathrm{iso}})^2}{2b^2}\right)$ centered on each isotropic chemical shift and parameterized (constants a and b) to minimize the error in the definite integral compared to experiment. Trapezoidal numerical integration was performed using a δ_{iso} spacing of 1 ppm such that all computed spectra integrals were to less than ±0.4% of the experimental integrals.

8.3 Results and discussion

8.3.1 Short-range order & coordination environments

Figure 8.6 displays the partial pair-correlation functions for various atomic species. The split peak in $g_{(\mathrm{P-O})}(\mathrm{r})$ relates to the shorter P-NBO and longer P-BO distances. The P-NBO peaks are centered at 1.51 Å for both simulated compositions with a decrease from 1.63 Å to 1.61 Å for the P-BO peak centered position upon Ti-doping. The shortening in $\mathrm{r}_{(\mathrm{P-BO})}$, with increased mol% of higher field strength modifier ions, has previously been noted in theoretical[177] and experimental[141] studies of PBG. The same effect is noted as a decrease in P-P distances from $\mathrm{r}_{(\mathrm{P-P})} = 2.97$ Å to $\mathrm{r}_{(\mathrm{P-P})} = 2.88$ Å upon Ti-doping. The small peak at 2.43 Å in the $g_{(\mathrm{P-P})}(\mathrm{r})$ distribution for P45C30N25 relates to a strained P_2O_6 structure in the final glass which should be regarded as a structural relic from the high temperature melt. This feature is further evidenced in the P-O-P angular distribution (ADF), given in Figure 8.8, as a peak at ∼95°.

All partial pair-correlation first peak centered positions are summarised in Table 8.2. The first peak for $g_{(\mathrm{Ti-O})}(\mathrm{r})$ is centered on 1.87 Å with a well defined first coordination shell and broader bond distribution than $g_{(\mathrm{P-O})}(\mathrm{r})$, including Ti-$\mathrm{O}_{(\mathrm{Ti})}$ (titanium to oxygen coordination in which the oxygen in turn bonds to another titanium atom), Ti-$\mathrm{O}_{(\mathrm{P})}$ and longer Ti-$\mathrm{O}_{(\mathrm{P\&Ti})}$ (see Table 8.3 for decomposition). It was noted that Ti-$\mathrm{O}_{(\mathrm{P\&Ti})}$ were only formed with orthophosphate species (i.e. those P atoms that coordinate to solely NBO - defined to $\mathrm{exclude}_{(\mathrm{e})}$ P-O-Ti contributions). Tiwari *et al.*[205] have also found Ti-O-Ti linkages, connected with discrete PO_4 tetrahedra, in amorphous sodium alumino-phosphates for compositions containing > 10 mol% TiO_2. Comparison is made to short-range order in crystalline TiP_2O_7 obtained from ambient X-ray diffraction[204] in Table 8.2. This structure is made up from distorted TiO_6 octahedra and PO_4 tetrahedra sharing corners in a three-dimensional network with Ti-O bonds in the range 1.89−1.95 Å. The local Ti-O coordination number ($\mathrm{CN}_{(\mathrm{Ti-O})}$) is found to

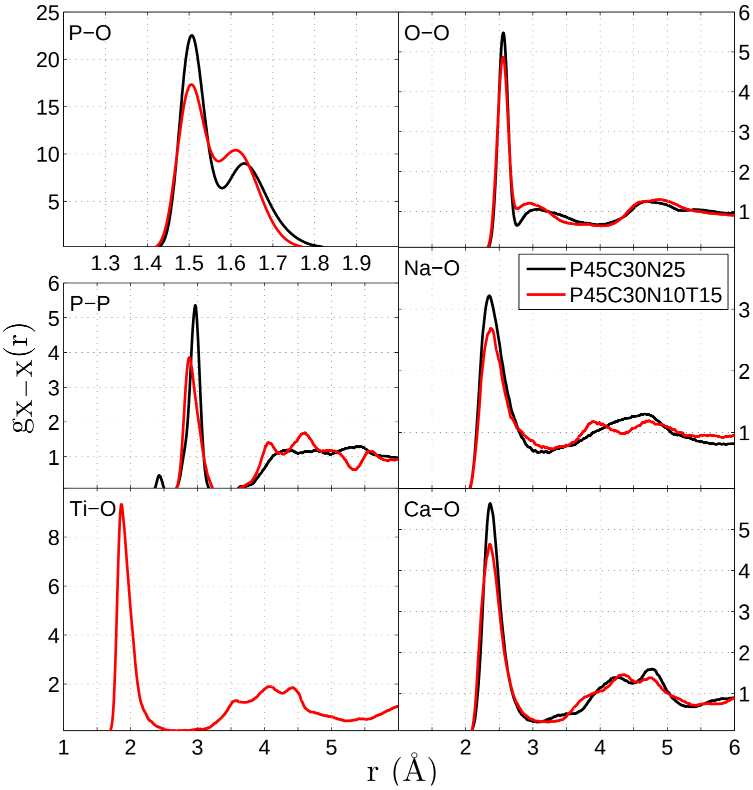

Figure 8.6: Partial pair-correlation functions for various atomic pairs (X − X) averaged over each timestep of the 40 ps 300K DFT-MD trajectories.

be 5.61 and all oxygens within the first coordination shell are NBO (see Table 8.3). The O-Ti-O ADF (see Figure 8.8) shows two distinct peaks centered on 90.5° and 171.5°, in line with a symmetric octahedral environment. Pickup *et al.*[206] have probed the coordination geometry of titanium atoms in Ti-PBG containing 0.01, 0.03 and 0.05 mol% TiO_2, using Ti K-edge X-ray absorption near edge structure (XANES) spectroscopy. Their results have demonstrated that Ti occupies a sixfold coordination with a degree of distortion that is lower than in a range of crystalline reference materials including, Na_2TiSi_5, $CaSiTiO_5$ and rutile-TiO_2. The two well resolved peaks of the O-Ti-O ADF and a value of $CN_{(Ti-O)} = 5.61$ for P45C30N10T15 in this work, corroborate these experimental findings.

The possible formation of P-O-Ti bonds in Ti-PBG has been widely proposed in experimental literature, based on ^{31}P MAS NMR and thermal analysis,[197] along with Raman and Fourier Transform infrared (FTIR) spectroscopies.[188] From Table 8.3, titanium forms strong covalent bonds, ($r_{(Ti-O)}$ = 1.87 Å) in Ti-$O_{(P)}$ sequences, to 4.60 oxygens within the first coordination shell, confirming the postulated P-O-Ti bond formation from experiment.

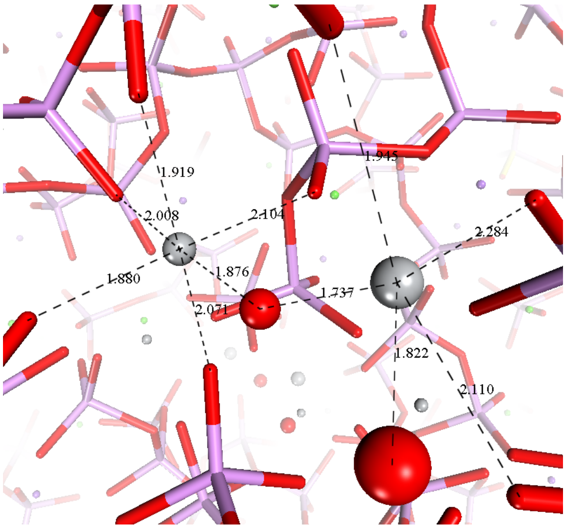

Figure 8.7: Snapshot of P45C30N10T15 300 K MD trajectory. Ti atoms fulfilling network forming roles. Ti-O$_{(\mathrm{Ti})}$-Ti-O$_{(\mathrm{Ti})}$ $\cdots$ Ti(not shown) sequence highlighted. Showing oxygens that solely coordinate to Ti atoms (O$_{(\mathrm{Ti})}$) with the first coordination shell.

Table 8.2: 300K dynamics. Selected first coordination shell average distances (Å) and angles (°). $(P_2O_5)_{0.45}(CaO)_x(Na_2O)_{0.55-x}$ (x=0.30, 0.35 and 0.40). Experimental data, obtained via neutron (ND) and x-ray (XRD) diffraction along with nuclear magnetic resonance (NMR), for a range of vitreous phosphate systems given for comparison. * Two of the six independent angles are constrained to 180°.

	P45C30N25 this work	P45C30N25[76] XRD	P45C30N10T15 this work	Crystalline TiP_2O_7[204] X-Ray
$r_{(P-NBO)}$	1.508	1.52 ±0.02	1.508	
$r_{(P-BO)}$	1.631	1.60 ±0.02	1.610	
$r_{(P-O)}$				1.5332-1.5815
$r_{(O-O)}$	2.562	2.54 ±0.02	2.557	
$r_{(P-P)}$	2.968	2.95 ±0.02	2.876	
$r_{(Na-O)}$	2.352	2.41 ±0.02	2.375	
$r_{(Ca-O)}$	2.368	2.40 ±0.02	2.363	
$r_{(Ti-O)}$			1.866	1.8884-1.9453
$\theta_{(O-P-O)}$	109.4		108.2	104.16-113.61
$\theta_{(P-O-P)}$	128.0		122.8	141.21-144.51*
$\theta_{(O-Ti-O)}$			90.5,171.5	86.75-92.81
$\theta_{(Ti-O-Ti)}$			85.4,120.2,148.2	
$\theta_{(Ti-O-P)}$			135.7	

Furthermore, $CN_{(Ti-O_{(Ti)})} = 0.57$, providing evidence that titanium forms Ti-O-Ti bonds, thus acting as a true network former, a result that hitherto had not been proposed for these compositions. Figure 8.7 shows a snapshot from the P45C30N10T15 300 K trajectory and displays this bonding behaviour.

The Ti-O-Ti ADF (Figure 8.8) has a dominant peak centered on 120.2° for P45C30N10T15,

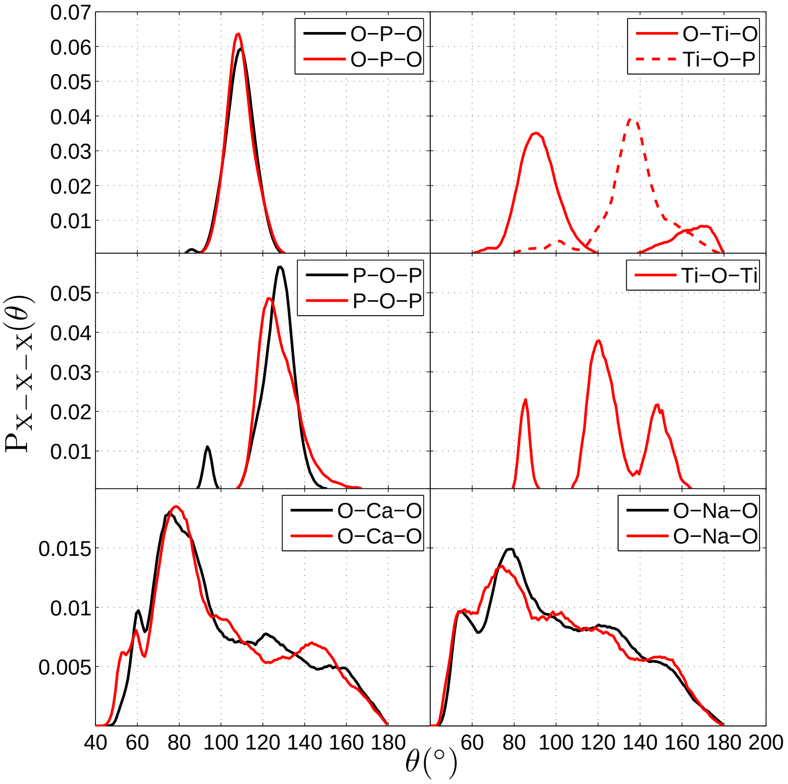

Figure 8.8: Angular distribution functions for various three-body systems (X − X − X) averaged over each timestep of the 40 ps 300K DFT-MD trajectories. P45C30N25 and P45C30N10T15 results presented in black and red respectively.

comparable with the unimodal P-O-P ADF peak at 122.8° for the same composition. Two further peaks exist at 148.2° and 85.4°, the latter relating to Ti-$O_{(P\&Ti)}$-Ti links associated with a PO_4 tetrahedron. Interestingly, the ADFs for Ca-O-Ca and Na-O-Na (not presented) show continuous distributions of $\sim$80°− $\sim$160° and $\sim$70°− $\sim$140° respectively for P45C30N10T15, suggesting that titanium coordinates in an intermediate manner, between a modifier and network former, within the second coordination shell.

Within the first coordination shell, peak intensities for $g_{(Ca-O)}(r)$ and $g_{(Na-O)}(r)$ (Figure 8.6) decrease upon Ti-doping, with no noticable change in FWHM values (albeit small shifts to longer bond lengths for the first minima are noted), indicating a similar range of bond lengths within the first coordination spheres for both compositions. Analysis of quadrupolar coupling constants (C_Q) and ΔC_Q (a quantitative measure of disorder) from ^{23}Na MAS NMR, for Ti-PBG,[188, 197] have shown the local Na environment does not change significantly with the substitution of Na_2O for TiO_2. This finding is broadly supported in this work. $CN_{(Ca-O)} = 6.90$ and $CN_{(Ca-O)} = 6.69$ for P45C30N25 in good agreement with values of

Table 8.3: Coordination environments. Na-O, Ca-O and Ti-O cutoffs (PBG/Ti-PBG) set at 3.25/3.30 Å, 3.15/3.22 Å and 2.80 Å respectively. Since Ti can be defined as a network former and all coordinating oxygens are NBO (as defined by the primary network former P), decomposition is also done in terms of oxygens which in turn coordinate to P (Ti-O_P) or Ti (Ti-O_{Ti}) or to both P and Ti (Ti-$O_{P\&Ti}$).

	P45C30N25	P45C30N10T15
Atomic Pair	CN	CN
Na-O	6.69	6.94
Na-BO	1.21	0.91
Na-NBO	5.48	6.03
Ca-O	6.90	7.13
Ca-BO	0.27	0.51
Ca-NBO	6.63	6.62
Ti-O	–	5.61
Ti-BO	–	0.00
Ti-NBO	–	5.61
Ti-$O_{(P)}$	–	4.60
Ti-$O_{(Ti)}$	–	0.57
Ti-$O_{(P\&Ti)}$	–	0.44

6.86 and 6.49 respectively, for the same composition from a previous classical simulation.[177] The decomposition into BO and NBO contributions (Table 8.3) shows $\frac{CN^{(Ca-NBO)}}{CN^{(Ca-BO)}} = 24.56$ and 12.98 for P45C30N25 and P45C30N10T15 respectively, whereas $\frac{CN^{(Na-NBO)}}{CN^{(Na-BO)}} = 4.53$ and 6.63 respectively. The increased affinity of Ca to coordinate with NBO has previously been noted.[177]

8.3.2 Medium-range order

8.3.2.1 Q^n distributions & ^{31}P isotropic chemical shieldings

The phosphorus Q^n distributions for P45C30N25 and P45C30N10T15 are given in Table 8.4. P45C30N25 comprises 70.0 % Q^2, 25.0% Q^1 and 5.0% Q^3, in reasonable agreement with experimental values of 78 % Q^2 and 22% Q^1.[197] It is noted that other simulated P45C30N25 compositions have been found to contain small Q^3 contributions,[171, 177] not deconvoluted from experimental NMR spectra.[18, 76] The Q^n distribution for P45C30N10T15 has been presented to include$_{(i)}$ and exclude$_{(e)}$ P-O-Ti contributions, i.e. defining the linking oxygen to be either BO or NBO respectively. It is noted that for P45C30N10T15$_{(e)}$, 10% of P atoms are Q^0, which are associated with Ti-O-Ti linkages as discussed in Section 8.3.1. P45C30N10T15$_{(i)}$ primarily contains Q^2 (58.2%) and Q^3 (29.3%) with small amounts of Q^1 and Q^4. Upon Ti-

Table 8.4: Q^n species distribution (%) for phosphorus with respect to oxygen and network connectivity (NC). P45C30N10T15 results for phosphorus Q^n species distribution including$_{(i)}$ and excluding$_{(e)}$ P-O-Ti contributions. Experimental NMR results[197] given for comparison. P-O and Ti-O cut-offs set at 2.0 and 2.8 Å respectively.

	Q^0	Q^1	Q^2	Q^3	Q^4	NC	Q^1[197]	Q^2[197]
P45C30N25	0.0	25.0	70.0	5.0	0.0	1.80	22 ±1	78 ±1
P45C30N10T15$_{(i)}$	0.0	5.0	58.2	29.3	7.5	2.39	5 ±1	95 ±1
P45C30N10T15$_{(e)}$	10.0	30.0	55.0	5.0	0.0	1.55		

Table 8.5: Q^n species distribution (%) for titanium with respect to oxygen and network connectivity (NC) including Ti-O-P contributions. P-O and Ti-O cut-offs set at 2.0 and 2.8 Å respectively.

	Q^0	Q^1	Q^2	Q^3	Q^4	Q^5	Q^6	NC
P45C30N10T15	0.0	0.0	0.0	0.0	0.6	38.1	61.3	5.61

doping, it is noted experimentally, that Q^1 decreases from 22% ±1% to 5% ±1%. If P-O-Ti oxygens are included as BO, we note a decrease in Q^1 from 25.0% to 5.0% in the present work, in good agreement with experiment.

Table 8.5 gives the titanium Q^n distribution, primarily comprising 38.1% Q^5 and 61.3% Q^6 for P45C30N10T15 (including Ti-O-P contributions). The fact that NC= 5.61, matching the value for CN_{Ti-O}, illustrates that all oxygens coordinating to titanium within the first coordination shell, in turn bond to either another Ti or to P. Therefore, there exist no Ti-O-Ca or Ti-O-Na linkages in P45C30N10T15. This result is also confirmed from the decomposition of Ti-O into Ti-O$_{(P)}$, Ti-O$_{(Ti)}$ and Ti-O$_{(P\&Ti)}$ contributions, which normalize to $CN_{(Ti-O)}$ (see Table 8.3).

The mean values of ^{31}P isotropic chemical shieldings for each phosphorus atom (see Equation 8.9) summed over 10 timesteps (t.s.), calculated using the GIPAW method,[190] are shown in Figure 8.9. The convergence of the mean $\bar{\sigma}_{\rm iso}^{\rm P}$ values for specific Q^n bonding environments ($\bar{\sigma}_{\rm iso}^{\rm Q^n}$ - see Equation 8.10) was assessed with increasing t.s.. $\bar{\sigma}_{\rm iso}^{\rm Q^2}$ for P45C30N25 was found to be converged to within 0.025 ppm at 10 t.s. in line with convergence values of 0.2 ppm and 0.02 ppm for carbon and hydrogen average chemical shieldings in an L-alanine molecular crystal, as reported by Robinson and Haynes.[207]

$$\bar{\sigma}_{\rm iso}^{\rm P} = \frac{1}{\rm t.s.} \sum_{\rm i=1}^{\rm t.s.} \sigma_{\rm iso}^{\rm P_i} \tag{8.9}$$

$$\bar{\sigma}_{\mathrm{iso}}^{\mathrm{Q^n}} = \frac{1}{\mathrm{Q^n}} \sum_{1}^{\mathrm{Q^n}} \bar{\sigma}_{\mathrm{iso}}^{\mathrm{P}} \tag{8.10}$$

The results for P45C30N25 and P45C30N10T15 are given in the upper and lower panels of Figure 8.9 respectively. The $\mathrm{Q^n}$ identity for each P is reported on the x axis of each plot. The values of $\bar{\sigma}_{\mathrm{iso}}^{\mathrm{Q^n}}$ are plotted as horizontal bars and also reported in Table 8.6. There is a clear linear dependency of $\bar{\sigma}_{\mathrm{iso}}^{\mathrm{Q^n}}$ with increasing $\mathrm{Q^n}$ from $\bar{\sigma}_{\mathrm{iso}}^{\mathrm{Q^1}} = 267.70$ppm to $\bar{\sigma}_{\mathrm{iso}}^{\mathrm{Q^2}} = 285.04$ppm and $\bar{\sigma}_{\mathrm{iso}}^{\mathrm{Q^3}} = 297.64$ppm for P45C30N25. The P45C30N10T15 composition shows a similar trend with the exception of $\bar{\sigma}_{\mathrm{iso}}^{\mathrm{Q^4}} = 294.25$ppm (it should be noted that the $\mathrm{P45C30N10T15_{(i)}}$ $\mathrm{Q^n}$ assignment was used). Upfield/downfield compositional trends are discussed in subsection 8.3.2.2 making comparison to the relevant experimental NMR spectra.

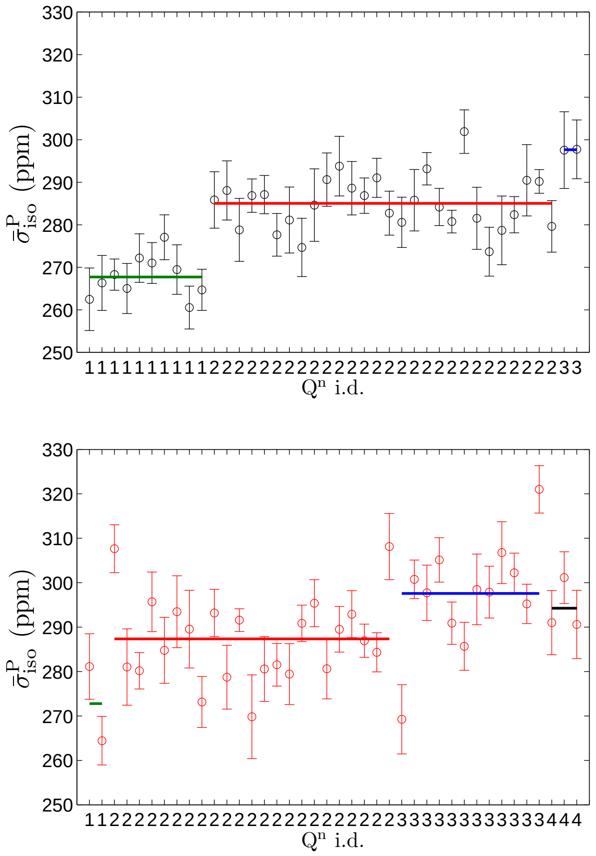

Figure 8.9: Calculated mean isotropic chemical shielding for each P atom summed over snapshots ($\bar{\sigma}_{\mathrm{iso}}^{\mathrm{P}}$). Error bars ±1 s.d.. x axis labels represent the $\mathrm{Q^n}$ identity of each P atom in each system including P-O-Ti contributions. P45C30N25 and P45C30N10T15 results given in upper and lower panels respectively.

$\bar{\sigma}_{\mathrm{iso}}^{\mathrm{Q^n}}$ were plotted as a function of the number of P-O-Ti linkages, within the first coordina-

Table 8.6: $\bar{\sigma}_{\mathrm{iso}}^{\mathrm{Q^n}}$ (ppm) for P45C30N25 and P45C30N10T15.

	$\bar{\sigma}_{\mathrm{iso}}^{\mathrm{Q^1}}$	$\bar{\sigma}_{\mathrm{iso}}^{\mathrm{Q^2}}$	$\bar{\sigma}_{\mathrm{iso}}^{\mathrm{Q^3}}$	$\bar{\sigma}_{\mathrm{iso}}^{\mathrm{Q^4}}$
P45C30N25	267.70	285.04	297.64	–
P45C30N10T15	272.78	287.35	297.59	294.25

tion shell, for the Ti-PBG as shown in Figure 8.10. For all $\mathrm{Q^n}$ P atoms, $\bar{\sigma}_{\mathrm{iso}}^{\mathrm{Q^n}}$ decreases linearly with increasing P-O-Ti contribution, indicating the shielding effect of these oxygens is less than those in P-O-P linkages. An increase in δ_{iso} for ^{31}P has been previously attributed to the replacement of P-O-P with P-O-Ti linkages, in Ti-doped sodium alumino-phosphate glasses, due to lower Z/r values for $\mathrm{Ti^{4+}}$ compared to $\mathrm{P^{5+}}$.[208] Significant overlap is exhibited between average shieldings from differing $\mathrm{Q^n}$ identities in Figure 8.10, suggesting that the deconvolution of experimental spectra may be complicated due to the inclusion of Ti in these systems.

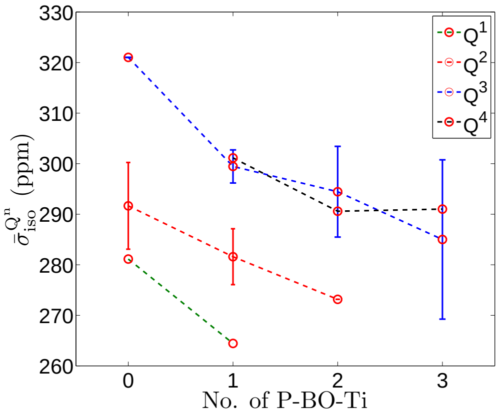

Figure 8.10: $\bar{\sigma}_{\mathrm{iso}}^{\mathrm{Q^n}}$ versus number of P-O-Ti for P45C30N10T15. Error bars ±1 s.d. (no error bar indicates only one $\mathrm{Q^n}$ P atom maintains the specific decomposition of P-O-P/P-O-Ti contribution). $\mathrm{P45C30N10T15_{(i)}}$ $\mathrm{Q^n}$ assignment used (see Table 8.4).

8.3.2.2 Chemical shifts and NMR spectra

The explicit atomistic information from first principles simulations provides a direct model (a $\mathrm{Q^n}$ distribution) from which a 1-D NMR spectra can be constructed, in contrast to the simulation of experimental NMR spectra, which depend on several assumptions about the nature of the $\mathrm{Q^n}$ distribution (i.e. bimdoal/trimodal and fitting procedures). The theoretical ^{31}P NMR spectra are given in Figure 8.11 with comparison made to experiment. The spectra using all 400 (10 snapshots × 40 P atoms in each system) chemical shieldings are reported

(Theory - 400) along with “reconstructed” spectra (Theory - R) for each composition. The latter were generated using Gaussians centered on the mean calculated chemical shifts (using $\bar{\sigma}_{\rm iso}^{\rm Q^n}$ reported in Table 8.6) and weighted according to the relative abundance of each $\rm Q^n$ P species present in the samples as given in Table 8.4 (using those proportions including P-O-Ti contributions). This technique biases the final spectra using structural information and we propose, in the light of the limited configurational averaging, allows for convergence in the final signal.

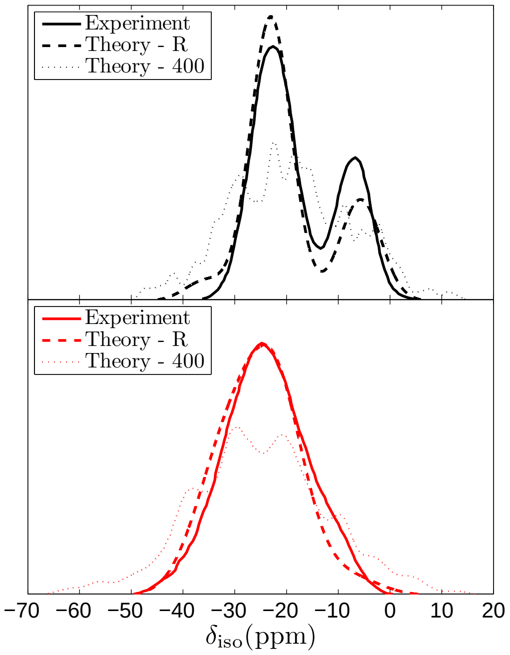

Figure 8.11: ^{31}P MAS NMR Spectra for P45C30N25 (upper panel) and P45C30N10T15 (lower panel). Theory - R is the reconstructed signal using $\bar{\sigma}_{\rm iso}^{\rm Q^n}$ values as described in the main body text. Theory - 400 uses all 400 calculated $\sigma_{\rm iso}$. $\sigma_{\rm ref}$ = 262 ppm and 265 ppm are used for the theoretical spectra for P45C30N25 and P45C30N10T15 respectively. Experimental ^{31}P MAS NMR given for comparison.

Experimentally it is noted that $\delta_{\rm iso}^{\rm Q^1}$ undergoes a downfield shift from -6.6 ppm ±0.1 to -10.2 ppm ±0.1 upon Ti-doping, for the compositions studied.[197] $\delta_{\rm iso}^{\rm Q^2} = -22.2$ ppm ±0.1 for P45C30N25 and, from the peak experimentally assigned as soley $\rm Q^2$, $\delta_{\rm iso}^{\rm Q^2} = -23.9$ ppm ±0.1 for P45C30N10T15. In order to provide good correspondance of spectral peak positioning between theory and experiment (see Figure 8.11), different values of $\sigma_{\rm ref}$ were used for each composition in this work. Accounting for this, the theoretical $\rm Q^2$ peak shift is shifted 2.3 ppm downfield upon Ti-doping compared with that of experiment at 1.7 ppm ±0.2. A caveat to this is that the single peak for P45C30N10T15 (from spectra Theory - R) cannot solely be attributed to Q^2 P atoms, as postulated from the binomial interpretation of experimental results.[197] This is evidenced by the explicit Q^n distribution and significant overlap in σ_{iso} values for P of differing Q^n speciation in P45C30N10T15 (both discussed in the previous section). In this work, $\delta_{\text{iso}}^{Q^1}$ $= -5.7$ ppm for P45C30N25. From the reconstructed P45C30N10T15 NMR spectra (Theory - R in lower panel of Figure 8.11) we cannot assign a specific $\delta_{\text{iso}}^{Q^1}$ value, however a shouldered peak centered at ~ -10 ppm is observed in the Theory - 400 spectrum for this composition.

The experimental $\delta_{\text{iso}}^{Q^3}$ values range from -31.4 ppm to -32.9 ppm for Sr-PBG[45] and between -33.3 ppm and -34.0 ppm for ultra-phosphate compositions of Ti-PBG.[188] It is noted that $\delta_{\text{iso}}^{Q^3}$ shifts further upfield with increasing TiO_2 mol% for P55 compositions with $\delta_{\text{iso}}^{Q^3} = -33.3$ ppm corresponding to P55C30N10T5. These isotropic shift values overlap with the experimental spectral range for P45C30N10T15 (see Figure 8.11) and are also close to $\delta_{\text{iso}}^{Q^3} = 32.59$ ppm from this work. This analysis in conjunction with $\delta_{\text{iso}}^{Q^4} = 29.25$ ppm and close correspondance of $\bar{\sigma}_{\text{iso}}^{Q^3}$ and $\bar{\sigma}_{\text{iso}}^{Q^4}$ values (see Figure 8.10) are suggestive that a decomposition of the experimental ^{31}P MAS NMR spectrum for P45C30N10T15 in terms of Q^{1-4} is not inconsistent.

8.3.3 Mechanical properties

Navarro *et al.*[38] have shown that the addition of TiO_2 in PBG leads to an increase in the elastic (Young's) modulus from 66.60 to 75.95 GPa for P44.5C44.5N11 and P44.5C44.5N3T8 respectively. The change in internal energy from the unstrained system vs periodic cell strain plots are presented in Figure 8.12 with second order polynomials fitted to reduce the residual sum of squares. Using Equation 8.7, making comparison to the second order coefficients from the fitted polynomial of deviation in internal energy vs. volume leads to the values for the bulk moduli (B) presented in Table 8.7. Rajendran *et al.*[39] have previously calculated various elastic moduli for Ti-PBG using measured values of density, longitudinal and shear velocities. Their calculated value for the P45C31N24 of B = 38.3 GPa ±0.05 is in good agreement with the value from this work for P45C30N25 of B = 38.96 GPa. Substitution of 15 mol% Na_2O for 15 mol% TiO_2 leads to an increase in B by 4.98 GPa to B = 43.94 GPa for P45C30N10T15. The increased resistance to uniform pressure is noted experimentally and generally attributed to a more cross-linked network.[209] In the current study we can link a change in NC from 1.80

Table 8.7: Bulk moduli (B) for P45C30N25 and P45C30N10T15. Residual sum of squares (RSS) from second order polynomial fits (see Figure 8.12). Experimental value for P45C31N24 given for comparison.[39]

	B (GPa)
P45C31N24	38.3 ±0.05[39]
P45C30N25	38.96 (RSS = 0.20)
P45C30N10T15	43.94 (RSS = 0.17)

to 2.39 (see Table 8.4) to the change in B. The depolymerisation of the phosphate network,[210] as indicated by rises in Q^0 and Q^1 for $P45C30N10T15_{(e)}$, is compensated via the formation of covalent P-O-Ti and Ti-O-Ti covalent linkages leading to the rise in NC, moving from P45C30N25 to $P45C30N10T15_{(i)}$.

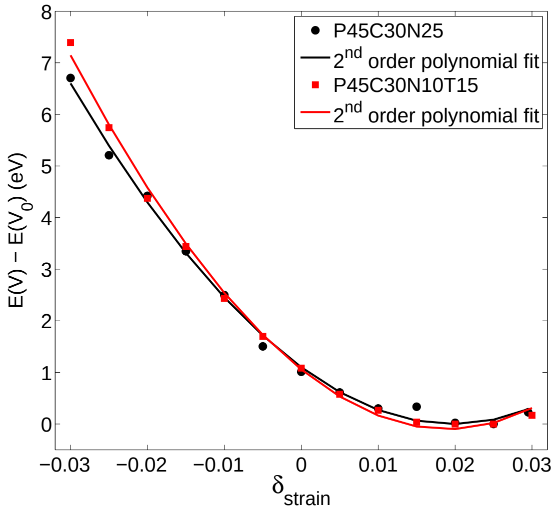

Figure 8.12: Deviation in internal energy from the unstrained system vs. strain for P45C30N25 and P45C30N10T15.

8.3.4 Electronic properties

The total and partial Kohn-Sham electronic density of states (EDOS) are given in Figure 8.13. The top of the valence band is set to the zero / Fermi energy (E_F). It is noted that the band gap decreases from ~3.3 eV in P45C30N25 to ~2.1 eV in P45C30N10T15. The latter value is of similar magnitude to optical band gaps found in a range of amorphous phosphates of composition $Ce_{1-x}Ti_xP_2O_7$ (x = 0 – 1), in which E_{opt} = 2.30 – 2.95 eV.[211] The direct band gap is measured to a small sub-band formed mainly by oxygen s states for P45C30N25. The decrease in the electrical band gap upon Ti-doping is noted alongside a dominant contribution of Ti d orbitals to the conduction band in P45C30N10T15. The valence band for each compositions is formed almost entirely from oxygen p states with small contributions from oxygen s, phosphorus p and d states. The upper and lower valence bands are dominated by the same orbitals with admixtures in similar proportions for both compositions. The substitution Na_2O for TiO_2 in P45C30N10T15, leads to the decreased contribution of sodium p orbitals to the EDOS for the lower valence band.

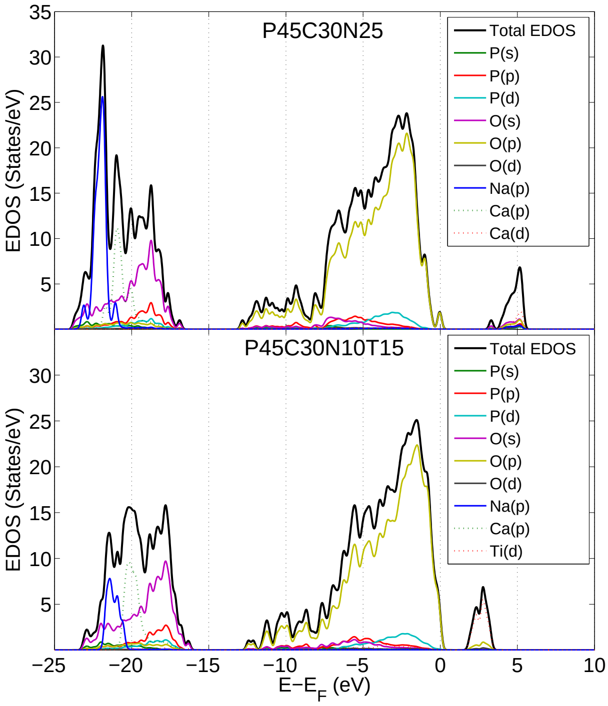

Figure 8.13: Total and partial Kohn-Sham electronic density of states (EDOS) P45C30N25 and P45C30N10T15.

8.4 Summary

BOMD simulations of amorphous $(P_2O_5)_{0.45}(CaO)_{0.30}(Na_2O)_{0.25-x}(TiO_2)_x$ ($x = 0.00$ and 0.15), have been carried out. Theoretical ^{31}P chemical shieldings have been calculated using the gauge-including projector augmented wave method and ^{31}P NMR spectra have been reconstructed. Our results demonstrate that previous binomial interpretations of medium-range structure distributions in Ti-PBG are insufficient due to significant chemical shift overlap. The effects of local Ti atoms on the chemical shifts of ^{31}P are suggestive that P-O-Ti contributions should be included as contributing to the Q^n distribution and that the unimodal spectral peak (obtained from theory and experiment) comprises Q^{1-4} P atoms.

Upon Ti-doping a depolymerisation of the phosphate network is noted, offset by the formation of P-O-Ti and Ti-O-Ti linkages, leading to a more dense and more highly connected network. Titanium is shown to occupy a non-distorted octahedral environment with $r_{(\mathrm{Ti-O})} = 1.87$ Å and a coordination number of $\mathrm{CN}_{(\mathrm{Ti-O})} = 5.61$. Good agreement is found for short-range order when compared to available experimental data.

The inclusion of Ti leads to an increase in the bulk modulus from 38.96 GPa to 43.94 GPa, due to increased network connectivity. Electronic properties show a reduction in the band gap from $\sim$3.3 eV to $\sim$2.1 eV upon Ti-doping.

Chapter 9

Concluding remarks

9.1 Our aims

As discussed in Chapter 1, an understanding of the structural drivers behind the compositionally dependent dissolution rate trends in phosphate-based glasses (PBGs) and doped phosphate-based glasses (d-PBGs), is of importance for better optimizing this class of material for use in biomedicine. It has been suspected that short- and medium-range structural features such as bonding coordination, Q^n distribution and network connectivity play central roles in governing the rate at which glass surfaces become hydrated and subsequently release modifier ions and phosphate chains into solution. The detailed review of current and prospective applications in Chapter 2 illustrates the importance of PBGs in biomedicine. Furthermore, the lack of theoretical simulations, limited to a single publication[15] before the work in this thesis was carried out, provided strong motivating reasons for the current work.

The work documented in this thesis, which is based on the application of methods rooted in the theoretical foundations outlined in Chapters 3 and 4, aims to fulfil the need for a deeper understanding, at an atomistic level, of how composition influences bulk structure in PBG/d-PBG which can in turn, be related to dissolution rate phenomena and biocompatability.

9.2 Our results

Several broad research objectives have been achieved, namely:

- A detailed structural, mechanical and electronic characterisation of crystalline $o'(P_2O_5)_\infty$

and $o(P_2O_5)$.

- Development of a robust methodology to facilitate large-scale classical bulk simulations of PBG and d-PBG, including the development of a force field and an advanced melt-quench simulation protocol.
- Development of a transferrable “brute-force” approach to fitting potentials via the scanning parametrical space.
- Detailed characterisations of the physical properties of bulk PBG, Ag-PBG and Ti-PBG.
- The simulation of several, previously unknown, composition dependent structural features, adding to the interpretation of dissolution rate trends in PBG and d-PBG.
- The corroboration and expansion of key experimental findings, shedding new light on the interpretation of some long-postulated hypotheses.

In chapter 5 we applied density functional theory (DFT) techniques to study crystalline $o'(P_2O_5)_\infty$ and $o(P_2O_5)$ at 0K. It was found that the inclusion of the empirical dispersion correction (DFT-D) was essential in reproducing some of they key structural features of $o'(P_2O_5)_\infty$. The second order elastic constants for the orthorhombic phases were obtained from a polynomial fit to the calculated energy-strain relation. Both phases are shown to be highly elastically anisotropic due to structural features. Analysis of the complex chemical bonding was carried out using Löwdin atomic charge and valence charge density data showing mixed ionic and covalent character in both phases. Calculation of the electronic band structure and partial Kohn-Sham density of states showed that the upper valence bands are formed almost entirely from oxygen p states with an admixture of phosphorus p and oxygen s states, for both phases. The $o'(P_2O_5)_\infty$ conduction bands are formed by a dominant contribution from phosphorus p states with the $o(P_2O_5)$ phase formed from phosphorus and oxygen s and p states. Direct band gaps of ~ 5 eV showed both phases to be insulators.

In chapter 6 we reported the development of a formal-charge, shell-model force field (parameterized on the mechanical data from the previous chapter) and the first classical molecular dynamics (MD) simulation of phosphate-based glasses in the system P_2O_5-CaO-Na_2O. A novel approach of ‘brute-force” scanning parametrical space was coded and used to fit two-body and three-body potentials for the network forming species. A stable melt quench-protocol was developed using linear frictional damping of the core-shell spring force, which was empirically parameterized at $\frac{1}{3}$ critical, in order to prevent core-shell heating at high temperatures. An analysis of the medium-range structure showed the phosphate network to be connected as NC = 1.78 for all three PBG compositions studied ($(\mathrm{P_2O_5})_{0.45}(\mathrm{CaO})_{\mathrm{x}}(\mathrm{Na_2O})_{0.55-\mathrm{x}}$). Each composition showed a dominant Q^2 contribution with significant Q^1, as seen in experimental data. New structural insight was obtained, most significantly that $\mathrm{CN}^{\mathrm{Me-NBO}}/\mathrm{CN}^{\mathrm{Me-BO}}$ ratios are likely of structural significance in the dissolution mechanism and solubility rate trends. Further analysis showed that Ca binds together more phosphate fragments and more PO_4 tetrahedra than Na.

In chapter 7 *ab initio* and classical molecular dynamics simulations of PBG and Ag-PBG were reported. Good structural agreement was found between the results from classical simulations and the high level *ab initio* reference calculations, providing further validation of the developed force field, in d-PBG systems. Furthermore, the classical methodology was found to outperform *ab initio* methods in reproducing some key structural features, such as phosphorus to oxygen bond distances, when compared to experimental data. The inclusion of Ag was shown to have little effect on short-range order when compared to the undoped composition. Ag was shown to occupy a distorted local-coordination with a mean bond length of 2.5 Å and an ill-defined first coordination shell. This environment was shown to be distorted octahedral / trigonal bi-pyramidal. Ag-O coordination numbers of 5.42 and 5.54 were calculated for *ab initio* and classical methodologies respectively. A disproportionation in the medium-range phosphorus Q^2 distribution was explicitly displayed upon silver-doping via CaO substitution. The accompanying increase in the full-width half-maximum of the phosphorus to bridging oxygen partial pair-correlation function were in line with experimental findings of increased disorder, and strongly evidence a bulk structural mechanism associated with decreased dissolution rates with increased silver content.

Finally, chapter 8 describes *ab initio* molecular dynamics simulations of PBG and Ti-PBG. Theoretical ^{31}P NMR parameters were calculated using the gauge-including projector augmented wave method and theoretical 1D-NMR spectra were reconstructed. The results provide deeper insight into the structural role of titanium in Ti-PBG and the interpretation of experimental ^{31}P NMR spectra. We explicitly showed that titanium not only forms Ti-O-P linkages but also acts as a network former via Ti-O-Ti bonds, a result that hitherto, had not been proposed. A depolymerisation of the phosphorus network was found to occur upon doping, offset by the afore-mentioned linkages, such that the network connectivity rises from 1.80 in PBG to 2.39 in Ti-PBG for the compositions studied. Previous binomial interpretations, of the medium-range phosphorus $\mathrm{Q^n}$ distribution, were found to be insufficient due to the influence of next-nearest neighbour titanium atoms on ^{31}P isotropic chemical shieldings. Our results suggested that an inclusion of P-O-Ti linkages in the phosphorus $\mathrm{Q^n}$ distribution is appropriate, based on the shielding effect of titanium, and that consequently a distribution of Q^{1-4} is present in Ti-PBG. The bulk modulus was found to rise from 38.96 GPa in PBG to 43.94 GPa Ti-PBG and to be linked to a more cross-linked network. Density of state calculations showed a reduction in the band gap from $\sim$3.3 eV to $\sim$2.1 eV upon Ti-doping.

9.3 Possible directions for further research

In the work presented in this thesis a sound simulation methodology has been set up and validated on a number of crystalline and amorphous systems. The formal-charge nature of the force field, along with the use of the widely cited shell-model Sanders *et al.*[150] O_s-O_s two-body potential, means that this methodology is highly transferrable and would facilitate the simulation of a host of other biomedical PBG and d-PBG compositions.[12] As illustrated in Chapter 7 the inclusion of an Ag-$\mathrm{O_s}$[178] two-body potential was straightforward and lead to a level of structural agreement with experiment (in the resulting melt-quenched derived glass) that outperformed the vastly more computationally expensive *ab initio* simulation results. Furthermore, for applied theoretical approaches in materials science, the production of accurate models usually defines the first step towards the calculation of other relevant physical properties such as atomic diffusion and transport properties. The PBG and d-PBG models reported here, have been rigorously compared with the available experimental literature and could facilitate such extended studies.

As stated in Chapter 6, extensive theoretical simulations of bulk,[125, 142, 143] surface,[144] hydrated surface[145–147] and clustered[148] amorphous phosphosilicate systems have been undertaken. Of particular interest for bioactive materials such as Bioglass and PBGs is the interface with aqueous environments. Identification of the sequence of physiochemical steps following immersion of glasses in body fluids and how the material subsequently interfaces with tissue, are long-term targets and only achievable via an integrated applied theoretical and experimental approach. The need for a clear understanding of the way in which these processes are affected by structural and chemical properties of the glass at an atomistic level, mean that this will likely be an active field of research for many years to come.

Appendices

Appendix A

Mathematical derivations

A.1 Coulombic (ee interaction) in plane wave reciprocal space representation

$$\left\langle \phi' \middle| \hat{V}_h(\vec{r}) \middle| \phi \right\rangle = \left\langle \phi' \middle| \frac{1}{2} \int d\vec{r} \int d\vec{r}\,' \frac{n(\vec{r})n(\vec{r}\,')}{|\vec{r}-\vec{r}\,'|} \middle| \phi \right\rangle$$

A.1.1 Proof that $\vec{q} = \vec{k} + \vec{G}$: Blochs theorem

Since $\hat{V}_h$ is periodic it can be expanded in a discrete Fourier series as follows (ϕ represent elements of the basis set i.e. plane waves $e^{i\vec{q}.\vec{r}}$):

$$\begin{aligned}
\left\langle \phi' \middle| \hat{V}_h(\vec{r}) \middle| \phi \right\rangle &= \left\langle \phi' \middle| \sum_m V_h(\vec{G}_m) e^{i\vec{G}_m.\vec{r}} \middle| \phi \right\rangle \\
&= \sum_m V_h(\vec{G}_m) \left\langle \phi' \middle| e^{i\vec{G}_m.\vec{r}} \middle| \phi \right\rangle \\
&= \sum_m V_h(\vec{G}_m) \int\limits_{\Omega_{\text{cell}}} e^{-i\vec{q}\,'.\vec{r}} e^{i\vec{G}_m.\vec{r}} e^{i\vec{q}.\vec{r}} d^3\vec{r} \\
&= \sum_m V_h(\vec{G}_m) \int\limits_{\Omega_{\text{cell}}} e^{-i(\vec{q}\,'-\vec{q}-\vec{G}_m).\vec{r}} d^3\vec{r} \\
&= \sum_m V_h(\vec{G}_m) \delta_{\vec{q}\,'-\vec{q},\vec{G}_m}
\end{aligned}$$

When $\vec{q}$ and $\vec{q}\,'$ differ by a vector of the reciprocal lattice ($\vec{G}$) then, $\delta_{\vec{q}\,'-\vec{q},\vec{G}_m} \neq 0$, thus giving rise to the definitions $\vec{q} = \vec{k} + \vec{G}_n$ and $\vec{q}\,' = \vec{k} + \vec{G}_n'$.

A.1.2 Main proof

$$\begin{aligned}\left\langle \phi' \left| \hat{V}_h(\vec{r}) \right| \phi \right\rangle &= \int\limits_{\Omega_{cell}} e^{-i(\vec{k}+\vec{G}'_n).\vec{r}} \hat{V}_h(\vec{r}) e^{i(\vec{k}+\vec{G}_n).\vec{r}} d^3\vec{r} \\ &= \int\limits_{\Omega_{cell}} e^{-i(\vec{G}'_n).\vec{r}} \hat{V}_h(\vec{r}) e^{i(\vec{G}_n).\vec{r}} d^3\vec{r} \\ &= \int\limits_{\Omega_{cell}} \hat{V}_h(\vec{r}) e^{i(\vec{G}_n-\vec{G}'_n).\vec{r}} d^3\vec{r} \\ &= V_h(\vec{G}_n - \vec{G}'_n)\end{aligned}$$

A.2 Electronic kinetic energy in plane wave reciprocal space representation

$$\begin{aligned}\left\langle \phi' \left| \hat{T}[n] \right| \phi \right\rangle &= \left\langle \phi' \left| -\frac{\hbar^2}{2m}\nabla^2 \right| \phi \right\rangle \\ &= \int\limits_{\Omega_{cell}} e^{-i(\vec{k}+\vec{G}'_n).\vec{r}} \left(-\frac{\hbar^2}{2m}\nabla^2 \right) e^{i(\vec{k}+\vec{G}_n).\vec{r}} d^3\vec{r} \\ &= -\frac{\hbar^2}{2m} \int\limits_{\Omega_{cell}} e^{-i(\vec{k}+\vec{G}'_n).\vec{r}} \nabla^2 e^{i(\vec{k}+\vec{G}_n).\vec{r}} d^3\vec{r} \\ &= \frac{\hbar^2}{2m} |\vec{k}+\vec{G}_n|^2 \int\limits_{\Omega_{cell}} e^{-i(\vec{k}+\vec{G}'_n).\vec{r}} e^{i(\vec{k}+\vec{G}_n).\vec{r}} d^3\vec{r} \\ &= \frac{\hbar^2}{2m} |\vec{k}+\vec{G}_n|^2 \left\langle \phi' \mid \phi \right\rangle \\ &= \frac{\hbar^2}{2m} |\vec{k}+\vec{G}_n|^2 \delta_{\vec{G}'_n \vec{G}_n}\end{aligned}$$

A.3 Ionic (ne interaction) in plane wave reciprocal space representation

$$\begin{aligned}
\left\langle \phi' \middle| \hat{V}_{ext}(\vec{r}) \middle| \phi \right\rangle &= \int\limits_{\Omega_{cell}} e^{-i(\vec{k}+\vec{G}'_n).\vec{r}} \hat{V}_{ext}(\vec{r}) e^{i(\vec{k}+\vec{G}_n).\vec{r}} d^3\vec{r} \\
&= \int\limits_{\Omega_{cell}} e^{-i(\vec{G}'_n).\vec{r}} \hat{V}_{ext}(\vec{r}) e^{i(\vec{G}_n).\vec{r}} d^3\vec{r} \\
&= \int\limits_{\Omega_{cell}} \hat{V}_{ext}(\vec{r}) e^{i(\vec{G}_n-\vec{G}'_n).\vec{r}} d^3\vec{r} \\
&= V_{ext}(\vec{G}_n - \vec{G}'_n)
\end{aligned}$$

A.4 Exchange correlation in plane wave reciprocal space representation

$$\begin{aligned}
\left\langle \phi' \middle| \hat{V}_{xc}(\vec{r}) \middle| \phi \right\rangle &= \int\limits_{\Omega_{cell}} e^{-i(\vec{k}+\vec{G}'_n).\vec{r}} \hat{V}_{xc}(\vec{r}) e^{i(\vec{k}+\vec{G}_n).\vec{r}} d^3\vec{r} \\
&= \int\limits_{\Omega_{cell}} e^{-i(\vec{G}'_n).\vec{r}} \hat{V}_{xc}(\vec{r}) e^{i(\vec{G}_n).\vec{r}} d^3\vec{r} \\
&= \int\limits_{\Omega_{cell}} \hat{V}_{xc}(\vec{r}) e^{i(\vec{G}_n-\vec{G}'_n).\vec{r}} d^3\vec{r} \\
&= V_{xc}(\vec{G}_n - \vec{G}'_n)
\end{aligned}$$

A.5 $\hat{H}_{\vec{k}+\vec{G}_n,\vec{k}+\vec{G}'_n}$

See overleaf.

$$\hat{H}_{\vec{k}+\vec{G}_n,\vec{k}+\vec{G}'_n} = \begin{bmatrix} \begin{array}{c} \Big(\hat{V}_h(\vec{G}_1-\vec{G}'_1)+\frac{\hbar^2}{2m}\left|\vec{k}+\vec{G}_1\right|^2\delta_{\vec{G}'_1\vec{G}_1} \\ +\hat{V}_{ION}(\vec{G}_1-\vec{G}'_1)+\hat{V}_{XC}(\vec{G}_1-\vec{G}'_1)\Big) \end{array} & \begin{array}{c} \Big(\hat{V}_h(\vec{G}_1-\vec{G}'_2)+\hat{V}_{ION}(\vec{G}_1-\vec{G}'_2) \\ +\hat{V}_{XC}(\vec{G}_1-\vec{G}'_2)\Big) \end{array} & \dots & \begin{array}{c} \Big(\hat{V}_h(\vec{G}_1-\vec{G}'_n)+\hat{V}_{ION}(\vec{G}_1-\vec{G}'_n) \\ +\hat{V}_{XC}(\vec{G}_1-\vec{G}'_n)\Big) \end{array} \\ \begin{array}{c} \Big(\hat{V}_h(\vec{G}_2-\vec{G}'_1)+\hat{V}_{ION}(\vec{G}_2-\vec{G}'_1) \\ +\hat{V}_{XC}(\vec{G}_2-\vec{G}'_1)\Big) \end{array} & \begin{array}{c} \Big(\hat{V}_h(\vec{G}_2-\vec{G}'_2)+\frac{\hbar^2}{2m}\left|\vec{k}+\vec{G}_2\right|^2\delta_{\vec{G}'_2\vec{G}_2} \\ +\hat{V}_{ION}(\vec{G}_2-\vec{G}'_2)+\hat{V}_{XC}(\vec{G}_2-\vec{G}'_2)\Big) \end{array} & \dots & \begin{array}{c} \Big(\hat{V}_h(\vec{G}_2-\vec{G}'_n)+\hat{V}_{ION}(\vec{G}_2-\vec{G}'_n) \\ +\hat{V}_{XC}(\vec{G}_2-\vec{G}'_n)\Big) \end{array} \\ \vdots & \vdots & \ddots & \vdots \\ \begin{array}{c} \Big(\hat{V}_h(\vec{G}_n-\vec{G}'_1)+\hat{V}_{ION}(\vec{G}_n-\vec{G}'_1) \\ +\hat{V}_{XC}(\vec{G}_n-\vec{G}'_1)\Big) \end{array} & \begin{array}{c} \Big(\hat{V}_h(\vec{G}_n-\vec{G}'_2)+\hat{V}_{ION}(\vec{G}_n-\vec{G}'_2) \\ +\hat{V}_{XC}(\vec{G}_n-\vec{G}'_2)\Big) \end{array} & \dots & \begin{array}{c} \Big(\hat{V}_h(\vec{G}_n-\vec{G}'_n)+\frac{\hbar^2}{2m}\left|\vec{k}+\vec{G}_n\right|^2\delta_{\vec{G}'_n\vec{G}_n} \\ +\hat{V}_{ION}(\vec{G}_n-\vec{G}'_n)+\hat{V}_{XC}(\vec{G}_n-\vec{G}'_n)\Big) \end{array} \end{bmatrix}_{\vec{k}+\vec{G}_n,\vec{k}+\vec{G}'_n}$$

Appendix B

Code

The following are a suite of Perl and Bash scripts, along with a master input (**gigen.pl**, **sub_gigen.pl**, **run_gigen.sh** and **MASTER.inp**), developed to automate the submission of General Utility Lattice Program (GULP)[155] static optimizations.

B.1 gigen.pl

Gulp Input GENeration (**gigen.pl**) is a Perl script that automates the submission of General Utility Lattice Program[155] static optimizations. The script loops over user-specified parametrical ranges, in order to facilitate the visualization of parametrical sensitivities to structural reference values, when seeking to fit interatomic potentials.

```
#!/usr/bin/perl -w
use strict;
use warnings;

my $start = time;

print "============================== \n";
print "\n";
print "Brute Force Fitting Method\n";
print "\n";
print "============================== \n";

# Path of Gulp executable
my $gulp = "/usr/local/gulp/gulp.3.1";

# Min and max value of A
# Number of A values

my $a_min = A_MIN;
my $a_max = A_MAX;
```

```
my $n_a = NUM_A;

# Min and max value of rho
# Number of rho values

my $rho_min = RHO_MIN;
my $rho_max = RHO_MAX;
my $n_rho = NUM_RHO;

my ($incr_a, $incr_rho);

if ($a_max == $a_min) {
   $incr_a = 1;
}
else {
   $incr_a = ($a_max - $a_min)/$n_a;
}

if ($rho_max == $rho_min) {
   $incr_rho = 1;
}
else {
   $incr_rho = ($rho_max - $rho_min)/$n_rho;
}

# Local variables

my ($vol, $cell_a, $cell_b, $cell_c, $alpha, $beta, $gamma);
my ($c11, $c22, $c33, $c44, $c55, $c66, $c12, $c13, $c23);
my ($br, $bv, $bh, $sr, $sv, $sh);
my $p1o1; my $p1o2; my $p1o4; my $p2o1; my $p2o3; my $p2o4;

my $cputime;

# Enter reference values

my %reference=(
                vol     =>    331.556618,
                a       =>    9.193,
                b       =>    4.890,
                c       =>    7.162,
                alpha   =>    90.00,
                beta    =>    90.00,
                gamma   =>    90.00,
                c11     =>    64.30,
                c22     =>    237.11,
                c33     =>    69.40,
                p1o1    =>    1.566,
                p1o2    =>    1.451,
                p1o4    =>    1.568,
                p2o1    =>    1.574,
                p2o3    =>    1.437,
                p2o4    =>    1.573,
                bh      =>    44,
                sh      =>    39
)
```

```

# Open the file ”RESULTS.txt” − A_buck and rho_buck giving structure in agreement with
# reference values within the defined threshold.

open (DATA, '>>', "RESULTS.txt") or die "Can't open RESULTS.txt: $!";
print DATA ("================================", "\n",
        "Reference cell parameters:", "\n\n",
        "Volume = ",$reference{vol}, "\n",
        "a = ",   $reference{a}, "\n",
        "b = ",   $reference{b}, "\n",
        "c = ",   $reference{c}, "\n",
        "alpha = ", $reference{alpha}, "\n",
        "beta = ", $reference{beta},  "\n",
        "gamma = ", $reference{gamma}, "\n",
        "c11 = ", $reference{c11}, "\n",
        "c22 = ", $reference{c22}, "\n",
        "c33 = ", $reference{c33}, "\n",
        "P101 = ", $reference{p1o1}, "\n",
        "P102 = ", $reference{p1o2}, "\n",
        "P104 = ", $reference{p1o4}, "\n",
        "P201 = ", $reference{p2o1}, "\n",
        "P203 = ", $reference{p2o3}, "\n",
        "P204 = ", $reference{p2o4}, "\n",
        "Bh = ", $reference{bh}, "\n",
        "Gh = ", $reference{sh}, "\n",
      "================================ \n\n"
)


my @list = ("A_buck", "rho_buck", "Volume", "a", "b", "c", "alpha", "beta", "gamma",
"C11", "C22", "C33", "P101", "P102", "P104", "P201", "P203", "P204", "Bh", "Gh");

print DATA sprintf('%-10s', "It" );
for my $elem (@list) {print DATA sprintf('%10s', $elem);};
print DATA ("\n\n");


# Open the file OUT.txt which will inform the user which A_buck and rho_buck successfully
# optimize and which do not, the % err, and the CPU time.

open (OUT, '>>', "OUT.txt") or die "Can't open OUT.txt: $!";

my $iter = 0;

my $a = $a_min;
LOOP_A: do {
   my $rho = $rho_min;
   LOOP_RHO: do {


         open (INPUT, '<', "MASTER.inp") or die "A = $a, rho = $rho: can't open
             MASTER.inp file: $!";
         open (OUTPUT, '>', "GULP.inp") or die "A = $a, rho = $rho: can't open
             input file: $!";
         while (defined ($_=<INPUT>)){
            s{A_buck}{$a}e;
```

```
            s{rho_buck}{$rho}e;

            print OUTPUT "$_";
        }

        system ("$gulp < GULP.inp > GULP.out");
        $iter=$iter+1;
        print OUT ("$iter: ");

        my $cf;
        open IN, "GULP.out";
            while (<IN>) {
                $cf.= $_ ;
            }
        close IN;

        my $optim = 0;
        my @cf = split (/\n/, $cf);
        my $row = 0;
        for (@cf) {
            if ($_ =~ /Total CPU time/) {my @list = split(' ',$_); $cputime = $list[3];};
            if ($_ =~ /Optimisation achieved/) {$optim = 1;};
            if ($optim eq 1) {
                if ($_ =~ /Primitive cell  volume/) {
                    my @list = split(' ',$_);
                    $vol  = $list [4];
                }
                if ($_ =~ /        a   /) {
                    my @list = split(' ',$_);
                    $cell_a  = $list [1];
                }
                if ($_ =~ /        b   /) {
                    my @list = split(' ',$_);
                    $cell_b  = $list [1];
                }
                if ($_ =~ /        c   /) {
                    my @list = split(' ',$_);
                    $cell_c  = $list [1];
                }
                if ($_ =~ /alpha   /) {
                    my @list = split(' ',$_);
                    $alpha = $list [1];
                }
                if ($_ =~ /beta   /) {
                    my @list = split(' ',$_);
                    $beta = $list [1];
                }
                if ($_ =~ /gamma /) {
                    my @list = split(' ',$_);
                    $gamma = $list[1];
                }
                if ($_ =~ /Elastic Constant Matrix/) {
                    my @list = split (' ', $cf[$row+5]);
                    $c11  = $list [1];
                    $c12  = $list [2];
                    $c13  = $list [3];
```

```
                    @list  = split (' ', $cf[$row+6]);
                    $c22   = $list [2];
                    $c23   = $list [3];
                    @list  = split (' ', $cf[$row+7]);
                    $c33   = $list [3];
                    @list  = split (' ', $cf[$row+8]);
                    $c44   = $list [4];
                    @list  = split (' ', $cf[$row+9]);
                    $c55   = $list [5];
                    @list  = split (' ', $cf[$row+10]);
                    $c66   = $list [6];
                }
                if ($_ =~ /Bulk Modulus/) {
                    my @list = split (' ',$_);
                    $br = $list [4];
                    $bv = $list [5];
                    $bh = $list [6];
                }
                if ($_ =~ /Shear Modulus/) {
                    my @list = split (' ',$_);
                    $sr  = $list [4];
                    $sv  = $list [5];
                    $sh  = $list [6];
                }
                if ($_ =~ /1   P1    core          O1    core/) {
                    my @list = split (' ', $_);
                    $p1o1 = $list [6];
                }
                if ($_ =~ /1   P1    core          O1    core/) {
                    my @list = split (' ', $cf[$row+1]);
                    $p1o2 = $list [3];
                }
                if ($_ =~ /1   P1    core          O1    core/) {
                    my @list = split (' ', $cf[$row+2]);
                    $p1o4 = $list [3];
                }
                if ($_ =~ /5   P2    core          O1    core/) {
                    my @list = split (' ', $_);
                    $p2o1 = $list [6];
                }
                if ($_ =~ /5   P2    core          O1    core/) {
                    my @list = split (' ', $cf[$row+1]);
                    $p2o3 = $list [3];
                }
                if ($_ =~ /5   P2    core          O1    core/) {
                    my @list = split (' ', $cf[$row+2]);
                    $p2o4 = $list [3];
                }
            }
            $row = $row + 1;
        }

        $a = sprintf('%10.5f', $a);
        $rho  = sprintf('%10.5f', $rho);

        $cputime= sprintf('%4.1f' , $cputime);
```

```
            if ($optim eq 0) {print OUT ("A($a) -- rho($rho): Optimisation not achieved *** Total CPU time $cputime sec\n")}
            if ($optim eq 1) {
                my $errvol     = abs((($vol-$reference{vol})/$reference{vol})*100); my $th_vol = $errvol   < 50;
                my $erra       = abs((($cell_a-$reference{a})/$reference{a})*100);  my $th_a = $erra  < 50;
                my $errb       = abs((($cell_b-$reference{b})/$reference{b})*100);  my $th_b = $errb  < 50;
                my $errc       = abs((($cell_c-$reference{c})/$reference{c})*100);  my $th_c = $errc  < 50;
                my $erralpha   = abs((($alpha-$reference{alpha})/$reference{alpha})*100); my $th_alpha = $erralpha    < 50;
                my $errbeta    = abs((($beta-$reference{beta})/$reference{beta})*100);   my $th_beta = $errbeta  < 50;
                my $errgamma   = abs((($gamma-$reference{gamma})/$reference{gamma})*100); my $th_gam = $errgamma  < 50;
                my $errbh      = abs((($bh-$reference{bh})/$reference{bh})*100);
                my $errsh      = abs((($sh-$reference{sh})/$reference{sh})*100);
                $errvol  = sprintf('%4.1f', $errvol);
                $erra    = sprintf('%4.1f', $erra);
                $errb    = sprintf('%4.1f', $errb);
                $errc    = sprintf('%4.1f', $errc);
                print OUT ("A($a) -- rho($rho): err_vol= $errvol, err_a= $erra, err_b = $errb, err_c= $errc *** Total CPU time $cputime sec\n");
                my $thresh = ($th_vol && $th_a && $th_b && $th_c && $th_alpha && $th_beta && $th_gam);
                if ($thresh) {
                    my @list = ($a, $rho,
                                $vol, $cell_a , $cell_b , $cell_c , $alpha, $beta, $gamma,
                                $c11, $c22, $c33, $p1o1, $p1o2, $p1o4, $p2o1, $p2o3, $p2o4,
                                                $bh, $sh);



                    print DATA sprintf('%-10s', "$iter:" );
                    for my $elem (@list) {
                        print DATA sprintf('%10.5f', $elem);
                    }
                    print DATA ("\n");
                }
            }


        $rho = $rho + $incr_rho
    } while ($rho <= $rho_max);
    $a = $a + $incr_a;
} while ($a <= $a_max);

my $duration = time - $start;

print OUT "\n Execution time: $duration s\n";
```

B.2 sub_gigen.pl

sub_gigen.pl generates the relevant subdirectories, categorized according to the user specified ranges over which parametrical scans are conducted. Each directory is populated with the relevant scripts and input files and submitted for calculation.

```perl
#!/usr/bin/perl -w
use strict;
use warnings;

# This is the list of A values and the number of A values.
my @a_list = (1000.0, 1020.0, 1040.0, 1060.0, 1080.0, 1100.0, 1120.0, 1140.0, 1160.0,
      1180.0, 1200.0);
my $n_a = 300;

# This is the list of rho values and the number of rho values.
my @rho_list = (0.320, 0.360);
my $n_rho = 300;


my ($a_min, $a_max, $rho_min, $rho_max);

my $i = 0;
foreach my $a_elem (@a_list){
   $a_min = $a_list[$i]; $a_max = $a_list[$i+1];
   my $j = 0;
   foreach my $rho_elem(@rho_list){
      $rho_min = $rho_list[$j]; $rho_max = $rho_list[$j+1];
         open (INGEN, '<', "gigen.pl") or die "Can't open gigen.pl: $!";
         open (OUTGEN,'>', "gigen.$a_elem-$rho_elem.pl") or die "Can't open gigen
             .$a_elem-$rho_elem.pl: $!";;
         while (defined ($_=<INGEN>)){
            s{A_MIN}{$a_min}e;
            s{A_MAX}{$a_max}e;
            s{NUM_A}{$n_a}e;
            s{RHO_MIN}{$rho_min}e;
            s{RHO_MAX}{$rho_max}e;
            s{NUM_RHO}{$n_rho}e;
            print OUTGEN "$_";
         };
         close OUTGEN;

         system ("mkdir $a_elem-$rho_elem/");
         system ("mv gigen.$a_elem-$rho_elem.pl $a_elem-$rho_elem/");
         system ("chmod u+x $a_elem-$rho_elem/gigen.$a_elem-$rho_elem.pl");
         system ("cp MASTER.inp $a_elem-$rho_elem/");

         open (INRUN, '<', "run_gigen.sh") or die "Can't open run_gigen.sh: $!";
         open (OUTRUN, '>', "run_$a_elem-$rho_elem.sh") or die "Can't open
             run_$a_elem-$rho_elem.sh: $!";
         while (defined ($_=<INRUN>)){
            s{DIR}{"$a_elem-$rho_elem"}e;
            s{GIGEN.PL}{"gigen.$a_elem-$rho_elem.pl"}e;
            print OUTRUN "$_";
```

```
        };
        system ("mv run_$a_elem-$rho_elem.sh $a_elem-$rho_elem/");

        my $gigen = "$a_elem-$rho_elem/run_$a_elem-$rho_elem.sh";
        system ("qsub $gigen");


      $j = $j + 1;
      if (($j+1) eq scalar(@rho_list)) {last};
    };
    $i = $i + 1;
    if (($i+1) eq scalar(@a_list)) {last};
};
```

B.3 MASTER.inp

MASTER.inp is the master GULP input file for constant pressure static optimisation, containing the experimental unit cell for $o'(P_2O_5)_\infty$ and relevant force field interactions.

```
conp opti properties distance

maxcyc 100
switch rfo gnorm 0.1

 cell
   9.193  4.890  7.162    90.  90.  90.
 fractional
P1  core     0.40207  0.25   0.34571  5.0
P1  core     0.09793  0.75   0.84571  5.0
P1  core     0.90207  0.25   0.15429  5.0
P1  core     0.59793  0.75   0.65429  5.0
P2  core     0.24238  0.25   0.70848  5.0
P2  core     0.25762  0.75   0.20848  5.0
P2  core     0.74238  0.25   0.79152  5.0
P2  core     0.75762  0.75   0.29152  5.0
O1  core     0.2762   0.25   0.493   0.848200
O1  core     0.2238   0.75   0.993   0.848200
O1  core     0.7762   0.25   0.007   0.848200
O1  core     0.7238   0.75   0.507   0.848200
O2  core     0.5517   0.25   0.4104   0.848200
O2  core     0.9483   0.75   0.9104   0.848200
O2  core     0.0517   0.25   0.0896   0.848200
O2  core     0.4483   0.75   0.5896   0.848200
O3  core     0.3612   0.25   0.8389   0.848200
O3  core     0.1388   0.75   0.3389   0.848200
O3  core     0.8612   0.25   0.6611   0.848200
O3  core     0.6388   0.75   0.1611   0.848200
O4  core     0.3642   0.0014    0.2162  0.848200
O4  core     0.1358   0.9986    0.7162  0.848200
O4  core     0.8642   0.4986    0.2838  0.848200
```

```
O4  core    0.6358  0.5014  0.7838  0.848200
O4  core    0.6358  0.9986  0.7838  0.848200
O4  core    0.8642  0.0014  0.2838  0.848200
O4  core    0.1358  0.5014  0.7162  0.848200
O4  core    0.3642  0.4986  0.2162  0.848200
O1  shel    0.2762     0.25     0.493   −2.84820
O1  shel    0.2238     0.75     0.993   −2.84820
O1  shel    0.7762     0.25     0.007   −2.84820
O1  shel    0.7238     0.75     0.507   −2.84820
O2  shel    0.5517     0.25     0.4104   −2.84820
O2  shel    0.9483     0.75     0.9104   −2.84820
O2  shel    0.0517     0.25     0.0896   −2.84820
O2  shel    0.4483     0.75     0.5896   −2.84820
O3  shel    0.3612     0.25     0.8389   −2.84820
O3  shel    0.1388     0.75     0.3389   −2.84820
O3  shel    0.8612     0.25     0.6611   −2.84820
O3  shel    0.6388     0.75     0.1611   −2.84820
O4  shel    0.3642     0.0014   0.2162   −2.84820
O4  shel    0.1358     0.9986   0.7162   −2.84820
O4  shel    0.8642     0.4986   0.2838   −2.84820
O4  shel    0.6358     0.5014   0.7838   −2.84820
O4  shel    0.6358     0.9986   0.7838   −2.84820
O4  shel    0.8642     0.0014   0.2838   −2.84820
O4  shel    0.1358     0.5014   0.7162   −2.84820
O4  shel    0.3642     0.4986   0.2162   −2.84820

observables
 elastic  9
1 1   64.30
2 2   237.11
3 3   69.40
4 4   51.45
5 5   22.40
6 6   38.10
1 2   27.44
1 3   3.13
2 3   26.72
end

 origin
0 0 0
buck
P core O shel   A_buck   rho_buck     0.030000      0.0   8.0  0 0 0
buck
O shel O shel   22764.30       0.14900    27.88000       0.0   8.0  0 0 0
spring
O 74.9204 0
cuts  1.0
three
P core O shel O shel   3.3588000 109.470000 0.000 2.000 0.000 2.000 0.000 3.200
three
O shel P core P core   7.634600 141.179333 0.000 2.000 0.000 2.000 0.000 3.500

cutd 2.00
output xyz stac.xyz
```

B.4 run_gigen.sh

The following is a Bash script (**run_gigen.sh**) that submits **gigen.pl**.

```
#!/bin/bash
# setting up the environment for SGE:
#$ −l h_rt=800:00:00
#$ −cwd −V
#$ −q all.q
#$ −N jobname
#$ −e /home/richard/gigen.err
#$ −o /home/richard/gigen.out

CWD="/home/richard"

cd $CWD/DIR

$CWD/DIR/GIGEN.PL
```

References

1. Hench, L. L., Splinter, R. J., Allen, W. C. & Greenlee, T. K. *Journal of Biomedical Materials Research* **5,** 117–141 (Nov. 1971) (see p. 20)
2. Hench, L. L. *Journal of Materials Science. Materials in Medicine* **17,** 967–978 (Nov. 2006) (see p. 20)
3. Kokubo, T. *Biomaterials* **12,** 155–163 (Mar. 1991) (see p. 20)
4. LeGeros, R. Z. *Clinical Orthopaedics and Related Research,* 81–98 (Feb. 2002) (see p. 20)
5. Tadjoedin, E. S., Lange, G. L., Holzmann, P. J., Kuiper, L. & Burger, E. H. *Clinical Oral Implants Research* **11,** 334–344 (Aug. 2000) (see p. 20)
6. Tadjoedin, E. S., de Lange, G. L., Lyaruu, D. M., Kuiper, L. & Burger, E. H. *Clinical Oral Implants Research* **13,** 428–436 (Aug. 2002) (see p. 20)
7. Silver, I. A., Deas, J & Erecinska, M. *Biomaterials* **22,** 175–185 (Jan. 2001) (see p. 20)
8. Leven, R. M., Virdi, A. S. & Sumner, D. R. *Journal of Biomedical Materials Research. Part A* **70,** 391–401 (Sept. 2004) (see p. 20)
9. Knowles, J. C. *Journal of Materials Chemistry* **13,** 2395 (2003) (see pp. 21, 25, 26)
10. Abou Neel, E. A., Pickup, D. M., Valappil, S. P., Newport, R. J. & Knowles, J. C. *Journal of Materials Chemistry* **19,** 690 (2009) (see pp. 21, 46)
11. Kiani, A. *et al. Philosophical Transactions of the Royal Society A: Mathematical, Physical and Engineering Sciences* **370,** 1352–1375 (Feb. 2012) (see p. 21)
12. Lakhkar, N. J. *et al. Advanced Drug Delivery Reviews* **65,** 405–420 (Apr. 2013) (see pp. 21, 116, 187)
13. Tilocca, A. *Proceedings of the Royal Society A: Mathematical, Physical and Engineering Sciences* **465,** 1003–1027 (Jan. 2009) (see pp. 21, 118)

14. Tilocca, A. *Journal of Materials Chemistry* **20,** 6848 (2010) (see pp. 21, 118)
15. Tang, E., Di Tommaso, D. & de Leeuw, N. H. *Advanced Engineering Materials* **12,** B331–B338 (July 2010) (see pp. 21, 118, 119, 127, 136, 141, 184)
16. Hasan, M. S., Ahmed, I., Parsons, A. J., Walker, G. S. & Scotchford, C. A. *Journal of Materials Science: Materials in Medicine* **23,** 2531–2541 (July 2012) (see p. 25)
17. Franks, K, Abrahams, I & Knowles, J. C. *Journal of Materials Science. Materials in Medicine* **11,** 609–614 (Oct. 2000) (see pp. 25–27)
18. Ahmed, I., Lewis, M., Olsen, I. & Knowles, J. *Biomaterials* **25,** 491–499 (Feb. 2004) (see pp. 25, 38, 116, 135, 165, 166, 175)
19. Uo, M. *Biomaterials* **19,** 2277–2284 (Dec. 1998) (see pp. 26, 135)
20. Salih, V *et al. Journal of Materials Science. Materials in Medicine* **11.** PMID: 15348085, 615–620 (Oct. 2000) (see p. 27)
21. Haberland, A. *et al. Biochimica et Biophysica Acta (BBA) - Gene Structure and Expression* **1445,** 21–30 (Apr. 1999) (see p. 27)
22. Han, W, Li, D, Stout, A. K., Takimoto, K & Levitan, E. S. *The Journal of Neuroscience: The Official Journal of the Society for Neuroscience* **19,** 900–905 (Feb. 1999) (see p. 27)
23. Bitar, M., Salih, V., Mudera, V., Knowles, J. C. & Lewis, M. P. *Biomaterials* **25,** 2283–2292 (May 2004) (see p. 27)
24. Clover, J. & Gowen, M. *Bone* **15,** 585–591 (Nov. 1994) (see p. 27)
25. Skelton, K *et al. Acta Biomaterialia* **3,** 563–572 (July 2007) (see p. 27)
26. Navarro, M., Ginebra, M.-P. & Planell, J. A. *Journal of Biomedical Materials Research* **67A,** 1009–1015 (Dec. 2003) (see pp. 28, 32)
27. Sanzana, E. *et al. Acta Biomaterialia* **4,** 1924–1933 (Nov. 2008) (see p. 28)
28. Gilchrist, T, Healy, D. & Drake, C. *Biomaterials* **12,** 76–78 (Jan. 1991) (see p. 28)
29. Avent, A. G., Carpenter, C. N., David Smith, J., Healy, D. M. & Gilchrist, T. *Journal of Non-Crystalline Solids* **328,** 31–39 (Oct. 2003) (see p. 29)
30. Ahmed, I., Ready, D., Wilson, M. & Knowles, J. *Journal of Biomedical Materials Research Part A* **79A,** 618–626 (Dec. 2006) (see p. 29)

31. Valappil, S. P. *et al. Antimicrobial Agents and Chemotherapy* **51,** 4453–4461 (Oct. 2007) (see pp. 29, 145, 146, 156, 159)
32. Mulligan, A., Wilson, M & Knowles, J. *Biomaterials* **24,** 1797–1807 (May 2003) (see p. 30)
33. Sheridan, R., Doherty, P. J., Gilchrist, T. & Healy, D. *Journal of Materials Science: Materials in Medicine* **6,** 853–856 (Dec. 1995) (see p. 30)
34. Valappil, S. P. *et al. Advanced Functional Materials* **18,** 732–741 (Mar. 2008) (see p. 31)
35. Pickup, D. M. *et al. The Journal of Chemical Physics* **130,** 064708 (2009) (see p. 31)
36. Valappil, S. *et al. Acta Biomaterialia* **5,** 1198–1210 (May 2009) (see p. 31)
37. Navarro, M. *et al. Biomaterials* **25,** 4233–4241 (Aug. 2004) (see p. 32)
38. Navarro, M. *et al. Journal of the American Ceramic Society* **86,** 1345–1352 (Aug. 2003) (see pp. 32, 162–164, 180)
39. Rajendran, V., Gayathri Devi, A., Azooz, M. & El-Batal, F. *Journal of Non-Crystalline Solids* **353,** 77–84 (Jan. 2007) (see pp. 32, 180, 181)
40. Nan, Y., Lee, W. E. & James, P. F. *Journal of the American Ceramic Society* **75,** 1641–1647 (June 1992) (see p. 32)
41. Abou Neel, E. A. & Knowles, J. C. *Journal of Materials Science: Materials in Medicine* **19,** 377–386 (July 2007) (see p. 33)
42. Saarto, T., Janes, R., Tenhunen, M. & Kouri, M. *European Journal of Pain* **6,** 323–330 (Oct. 2002) (see p. 33)
43. Meyer, K. & Barz, A. *Physics and Chemistry of Glasses* **42,** 371–380 (Dec. 2001) (see p. 33)
44. Pires, R., Abrahams, I., Nunes, T. G. & Hawkes, G. E. *Journal of Non-Crystalline Solids* **337,** 1–8 (June 2004) (see p. 33)
45. Abou Neel, E. A *et al. Journal of The Royal Society Interface* **6,** 435–446 (Sept. 2008) (see pp. 33, 180)
46. Manupriya, Thind, K. S., Singh, K., Sharma, G. & Rajendran, V. *Physica Status Solidi (A)* **206,** 1447–1455 (July 2009) (see p. 34)

47. Smith, J. M. *et al. The Journal of Chemical Physics* **138,** 034501 (2013) (see p. 34)
48. Allen, W. M., Sansom, B. F., Mallinson, C. B., Stebbings, R. J. & Drake, C. F. *The Veterinary record* **116,** 175–177 (Feb. 1985) (see p. 35)
49. Grace, N. D. & Knowles, S. O. *Veterinary Medicine International* **2012,** 1–8 (2012) (see p. 35)
50. Telfer, S. & Zervas, G. *Animal Production* **34,** 379–380 (1982) (see p. 35)
51. Telfer, S., Zervas, G. & Carlos, G. *Canadian Journal of Animal Science* **64,** 234–235 (1984) (see p. 35)
52. Givens, D. I., Zervas, G., Simpson, V. R. & Telfer, S. B. *The Journal of Agricultural Science* **110,** 199 (Mar. 2009) (see p. 36)
53. Kendall, N. *et al. Animal Science* **73,** 163–169 (Aug. 2001) (see p. 36)
54. Hayashida, M., Orden, E., Cruz, E., Cruz, L. & Fujihara, T. *Asian-Australasian Journal of Animal Sciences* **16,** 189–197 (Feb. 2003) (see p. 36)
55. Kendall, N., Mackenzie, A. & Telfer, S. *Livestock Science* **148,** 81–86 (Sept. 2012) (see p. 36)
56. Gross, J. G., Bou-Gharios, G. & Morgan, J. E. *Cell and Tissue Research* **298,** 371–375 (Oct. 1999) (see p. 37)
57. Kapsa, R., Kornberg, A. J. & Byrne, E. *The Lancet Neurology* **2,** 299–310 (May 2003) (see p. 37)
58. Fan, Y., Maley, M., Beilharz, M. & Grounds, M. *Muscle & Nerve* **19,** 853–860 (July 1996) (see p. 37)
59. Ahmed, I., Collins, C., Lewis, M., Olsen, I. & Knowles, J. *Biomaterials* **25,** 3223–3232 (July 2004) (see pp. 37–39)
60. Ahmed, I., Lewis, M., Olsen, I. & Knowles, J. *Biomaterials* **25,** 501–507 (Feb. 2004) (see pp. 37, 38)
61. Khang, G., Lee, S., Lee, J. & Lee, H. *Korea Polymer Journal* **7,** 102–107 (Nov. 1999) (see p. 37)

62. Shah, R., Sinanan, A., Knowles, J., Hunt, N. & Lewis, M. *Biomaterials* **26,** 1497–1505 (May 2005) (see p. 38)
63. Bitar, M., C. Knowles, J., Lewis, M. P. & Salih, V. *Journal of Materials Science: Materials in Medicine* **16,** 1131–1136 (Dec. 2005) (see pp. 39, 40)
64. Nazhat, S. N. *et al. Biomacromolecules* **8,** 543–551 (Feb. 2007) (see pp. 39–41)
65. Alekseeva, T., Abou Neel, E. A., Knowles, J. C. & Brown, R. A. *Journal of Biomaterials Applications* **26,** 733–744 (Feb. 2012) (see p. 41)
66. Parsons, A. J. *et al. Journal of Bionic Engineering* **6,** 318–323 (Dec. 2009) (see p. 42)
67. Felfel, R., Ahmed, I., Parsons, A. & Rudd, C. *Journal of the Mechanical Behavior of Biomedical Materials* **17,** 76–88 (Jan. 2013) (see p. 42)
68. Joo, N.-Y. *et al. Acta Biomaterialia* **8,** 1802–1812 (May 2012) (see pp. 42, 43)
69. Vitale-Brovarone, C., Novajra, G., Milanese, D., Lousteau, J. & Knowles, J. *Materials Science and Engineering: C* **31,** 434–442 (Mar. 2011) (see p. 44)
70. Vitale-Brovarone, C. *et al. Acta Biomaterialia* **8,** 1125–1136 (Mar. 2012) (see pp. 44, 45)
71. Li, R., Clark, A. E. & Hench, L. L. *Journal of Applied Biomaterials* **2,** 231–239 (1991) (see p. 46)
72. Carta, D., Pickup, D. M., Knowles, J. C., Smith, M. E. & Newport, R. J. *Journal of Materials Chemistry* **15,** 2134 (2005) (see p. 46)
73. Pickup, D. M. *et al. Journal of Materials Chemistry* **17,** 4777 (2007) (see pp. 46, 48)
74. Pickup, D. M., Wetherall, K. M., Knowles, J. C., Smith, M. E. & Newport, R. J. *Journal of Materials Science: Materials in Medicine* **19,** 1661–1668 (Oct. 2007) (see p. 47)
75. Carta, D., Knowles, J. C., Guerry, P., Smith, M. E. & Newport, R. J. *Journal of Materials Chemistry* **19,** 150 (2009) (see p. 47)
76. Carta, D. *et al. Journal of Non-Crystalline Solids* **353,** 1759–1765 (June 2007) (see pp. 47, 116–119, 127, 131, 132, 136, 166, 173, 175)
77. Loehrer, P. J. & Einhorn, L. H. *Annals of Internal Medicine* **100,** 704–713 (May 1984) (see p. 47)

78. Pickup, D. M., Newport, R. J. & Knowles, J. C. *Journal of Biomaterials Applications* **26,** 613–622 (Sept. 2010) (see p. 47)

79. Jakupec, M. & Keppler, B. *Current Topics in Medicinal Chemistry* **4,** 1575–1583 (Nov. 2004) (see p. 48)

80. Pickup, D. M. *et al. Journal of Materials Science* **44,** 1858–1867 (Feb. 2009) (see p. 48)

81. Born, M. & Oppenheimer, R. *Annalen der Physik* **84,** 0457–0484 (1927) (see p. 51)

82. Levy, M. *Proceedings of the National Academy of Sciences* **76,** 6062–6065 (Dec. 1979) (see p. 56)

83. Kohn, W. & Sham, L. J. *Physical Review* **140,** A1133–A1138 (Nov. 1965) (see pp. 57, 91)

84. Slater, J. *Physical Review* **81,** 385–390 (Feb. 1951) (see p. 59)

85. Ceperley, D. M. *Physical Review Letters* **45,** 566–569 (Aug. 1980) (see p. 61)

86. Payne, M. C., Arias, T. A. & Joannopoulos, J. D. *Reviews of Modern Physics* **64,** 1045–1097 (Oct. 1992) (see pp. 61, 68, 70)

87. Perdew, J. *Physical Review Letters* **55,** 1665–1668 (Oct. 1985) (see p. 61)

88. Becke, A. D. *Physical Review A* **38,** 3098–3100 (Sept. 1988) (see p. 61)

89. Perdew, J. P. & Wang, Y. *Physical Review B* **45,** 13244–13249 (June 1992) (see p. 61)

90. Perdew, J., Burke, K. & Wang, Y. *Physical Review B* **54,** 16533–16539 (Dec. 1996) (see pp. 61, 148, 168)

91. Perdew, J. P., Burke, K. & Ernzerhof, M. *Physical Review Letters* **77,** 3865–3868 (Oct. 1996) (see pp. 61, 91, 128)

92. Monkhorst, H. J. & Pack, J. D. *Physical Review B* **13,** 5188–5192 (June 1976) (see pp. 64, 92)

93. Goedecker, S., Teter, M. & Hutter, J. *Physical Review B* **54,** 1703–1710 (July 1996) (see pp. 67, 148, 168)

94. Hartwigsen, C., Goedecker, S. & Hutter, J. *Physical Review B* **58,** 3641–3662 (Aug. 1998) (see pp. 67, 148, 168)

95. Krack, M. *Theoretical Chemistry Accounts* **114,** 145–152 (May 2005) (see pp. 67, 148, 168)

96. Lippert, G., Hutter, J. & Parinello, M. *Molecular Physics* **92,** 477–488 (Oct. 1997) (see pp. 67, 148, 168)

97. Press, W., Teukolsky, S., Vetterling, W. & Flannery, B. *Numerical Recipes in Fortran 77: The Art of Scientific Computing* (Cambridge University Press, 1992) (see p. 74)

98. Hellmann, H. *Einfuhrung in die Quantumchemie* (Deuticke, Leipzig, 1937) (see p. 75)

99. Feynman, R. *Physical Review* **56,** 340–343 (Aug. 1939) (see p. 75)

100. Grimme, S. *Journal of Computational Chemistry* **27,** 1787–1799 (Nov. 2006) (see p. 76)

101. Verlet, L. *Physical Review* **159,** 98–103 (July 1967) (see p. 81)

102. Allen, M. & Tildesley, D. *Computer Simulation of Liquids* (Clarendon, 1989) (see p. 81)

103. Smith, W. & Forester, T. *Journal of Molecular Graphics* **14,** 136–141 (June 1996) (see pp. 82, 127, 149)

104. Andersen, H. C. *The Journal of Chemical Physics* **72,** 2384 (1980) (see p. 82)

105. Krack, M. & Parinello, M. **25** (ed Grotendorst, J.) 29–51 (2004) (see pp. 82, 147, 168)

106. VandeVondele, J. *et al. Computer Physics Communications* **167,** 103–128 (Apr. 2005) (see pp. 82, 147, 168)

107. Born, M. & Huang, K. *Dynamical Theory of Crystal Lattices* (Clarendon Press, 1954) (see p. 82)

108. Ewald, P. P. *Annalen der Physik* **369,** 253–287 (1921) (see pp. 82, 122)

109. Born, M. & Mayer, J. E. *Zeitschrift fur Physik* **75,** 1–18 (Jan. 1932) (see pp. 83, 121)

110. Dick, B. & Overhauser, A. *Physical Review* **112,** 90–103 (Oct. 1958) (see pp. 84, 122)

111. Sferco, S. *et al. Physical Review B* **42,** 11232–11239 (Dec. 1990) (see p. 90)

112. Abarenkov, I., Tupitsyn, I., Kuznetsov, V. & Payne, M. *Physical Review B* **60,** 7881–7885 (Sept. 1999) (see pp. 90, 109)

113. Cherry, B. R., Alam, T. M., Click, C., Brow, R. K. & Gan, Z. *The Journal of Physical Chemistry B* **107,** 4894–4903 (May 2003) (see p. 90)

114. Hohenberg, P. *Physical Review* **136,** B864–B871 (Nov. 1964) (see p. 91)

115. Kresse, G. & Hafner, J. *Physical Review B* **47,** 558–561 (Jan. 1993) (see p. 91)

116. Kresse, G. & Hafner, J. *Physical Review B* **49,** 14251–14269 (May 1994) (see p. 91)

117. Kresse, G. & Furthmuller, J. *Computational Materials Science* **6,** 15–50 (July 1996) (see p. 91)

118. Kresse, G. *Physical Review B* **54,** 11169–11186 (Oct. 1996) (see p. 91)

119. Blochl, P. E. *Physical Review B* **50,** 17953–17979 (Dec. 1994) (see p. 91)

120. Kresse, G. & Joubert, D. *Physical Review B* **59,** 1758–1775 (Jan. 1999) (see p. 91)

121. Giannozzi, P. *et al. Journal of Physics: Condensed Matter* **21,** 395502 (Sept. 2009) (see pp. 91, 118)

122. Perdew, J. P. & Zunger, A. *Physical Review B* **23,** 5048–5079 (May 1981) (see p. 91)

123. Barone, V. *et al. Journal of Computational Chemistry* **30,** 934–939 (Apr. 2009) (see pp. 91, 92)

124. Vanderbilt, D. *Physical Review B* **41,** 7892–7895 (Apr. 1990) (see p. 91)

125. Tilocca, A. & de Leeuw, N. H. *The Journal of Physical Chemistry B* **110,** 25810–25816 (Dec. 2006) (see pp. 91, 119, 187)

126. Stachel, D., Svoboda, I. & Fuess, H. *Acta Crystallographica Section C Crystal Structure Communications* **51,** 1049–1050 (June 1995) (see pp. 92, 96, 98, 122, 123, 129–131)

127. Arbib, E. H., Elouadi, B., Chaminade, J. P. & Darriet, J. *Journal of Solid State Chemistry* **127,** 350–353 (Dec. 1996) (see pp. 92, 96, 98)

128. Ravindran, P. *et al. Journal of Applied Physics* **84,** 4891 (1998) (see pp. 93, 94, 105)

129. Voigt, W. *Lehrbuch der Krystallphysik* (Teubner, Leipzig, 1928) (see pp. 93, 103)

130. Salvado, M. A. & Pertierra, P. *Inorganic Chemistry* **47,** 4884–4890 (June 2008) (see pp. 95, 96)

131. Ohno, I. *Journal of Physics of the Earth* **43,** 157–169 (1995) (see pp. 99, 105)

132. Reuss, A. *Journal of Applied Mathematics and Mechanics* **9,** 49–58 (1929) (see p. 103)

133. Hill, R. *Proceedings of the Physical Society, London, Section B* **65,** 396 (1952) (see p. 104)

134. Levien, L., Prewitt, C. & Weidner, D. *American Mineralogist* **65,** 920–930 (1980) (see p. 105)

135. Pugh, S. *Philosophical Magazine Series 7* **45,** 823 (1954) (see p. 106)

136. Chung, D. H. *Journal of Applied Physics* **39,** 2777 (1968) (see p. 107)

137. Liang, J.-J, Cygan, R. & Alam, T. *Journal of Non-Crystalline Solids* **263-264,** 167–179 (Mar. 2000) (see pp. 118, 120, 122)

138. Tischendorf, B., Alam, T., Cygan, R. & Otaigbe, J. *Journal of Non-Crystalline Solids* **316,** 261–272 (Feb. 2003) (see pp. 118, 121)

139. Al-Hasni, B. & Mountjoy, G. *Journal of Non-Crystalline Solids* **357,** 2775–2779 (July 2011) (see p. 118)

140. Christie, J. K., Ainsworth, R. I., Di Tommaso, D. & de Leeuw, N. H. *The Journal of Physical Chemistry B* **117,** 10652–10657 (Aug. 2013) (see pp. 119, 137–140, 149)

141. Pickup, D. M. *et al. Journal of Physics: Condensed Matter* **19,** 415116 (Oct. 2007) (see pp. 119, 131, 132, 149, 151, 153, 159, 161, 166, 171)

142. Tilocca, A. & Cormack, A. N. *The Journal of Physical Chemistry B* **111,** 14256–14264 (Dec. 2007) (see pp. 119, 187)

143. Tilocca, A. *Physical Review B* **76** (Dec. 2007) (see pp. 119, 187)

144. Tilocca, A. & Cormack, A. N. *Journal of Physical Chemistry C* **112,** 11936–11945 (Aug. 2008) (see pp. 119, 187)

145. Tilocca, A. & Cormack, A. N. *ACS Applied Materials & Interfaces* **1,** 1324–1333 (June 2009) (see pp. 119, 187)

146. Tilocca, A. & Cormack, A. N. *Langmuir* **26,** 545–551 (Jan. 2010) (see pp. 119, 187)

147. Tilocca, A. & Cormack, A. N. *Proceedings of the Royal Society A: Mathematical, Physical and Engineering Sciences* **467,** 2102–2111 (Feb. 2011) (see pp. 119, 187)

148. Tilocca, A. *Journal of Materials Chemistry* **21,** 12660 (2011) (see pp. 119, 187)

149. Tilocca, A., de Leeuw, N. & Cormack, A. *Physical Review B* **73** (Mar. 2006) (see pp. 119, 124, 126, 127, 149, 150, 159)

150. Sanders, M. J., Leslie, M. & Catlow, C. R. A. *Journal of the Chemical Society, Chemical Communications,* 1271 (1984) (see pp. 119, 122, 124, 126, 150, 187)

151. Tilocca, A., Cormack, A. N. & de Leeuw, N. H. *Chemistry of Materials* **19,** 95–103 (Jan. 2007) (see pp. 120, 122, 159)

152. Sastre, G., Lewis, D. W. & Catlow, C. R. A. *The Journal of Physical Chemistry* **100,** 6722–6730 (Jan. 1996) (see p. 120)

153. Hudgens, J., Brow, R., Tallant, D. & Martin, S. *Journal of Non-Crystalline Solids* **223,** 21–31 (Jan. 1998) (see p. 120)

154. Ainsworth, R. I., Tommaso, D. D. & de Leeuw, N. H. *The Journal of Chemical Physics* **135,** 234513 (2011) (see pp. 122, 124, 129, 130)

155. Gale, J. D. & Rohl, A. L. *Molecular Simulation* **29,** 291–341 (May 2003) (see pp. 122, 127, 194)

156. Harrison, R. J., Putnis, A. & Kockelmann, W. *Physical Chemistry Chemical Physics* **4,** 3252–3259 (July 2002) (see pp. 124, 129)

157. Benamara, M., Vlasse, M., Le Flem, G. & Hagenmuller, P. *Acta Crystallographica Section C Crystal Structure Communications* **39,** 1483–1485 (Nov. 1983) (see pp. 124, 129)

158. Mitchell, P. J. & Fincham, D. *Journal of Physics: Condensed Matter* **5,** 1031–1038 (Feb. 1993) (see p. 124)

159. Evans, D. J. & Morriss, O. *Computer Physics Reports* **1,** 297–343 (July 1984) (see pp. 127, 149)

160. Delley, B. *The Journal of Chemical Physics* **92,** 508 (1990) (see p. 128)

161. Delley, B. *Computational Materials Science* **17,** 122–126 (June 2000) (see p. 128)

162. Delley, B. *The Journal of Chemical Physics* **113,** 7756 (2000) (see p. 128)

163. Clark, E. B., Mead, R. N. & Mountjoy, G. *Journal of Physics: Condensed Matter* **18,** 6815–6826 (July 2006) (see p. 129)

164. Suzuki, K. & Ueno, M. *Le Journal de Physique Colloques* **46,** C8–261–C8–265 (Dec. 1985) (see p. 131)

165. Hoppe, U., Walter, G., Kranold, R. & Stachel, D. *Journal of Non-Crystalline Solids* **263-264,** 29–47 (Mar. 2000) (see p. 131)

166. Christie, J. K., Malik, J. & Tilocca, A. *Physical Chemistry Chemical Physics* **13,** 17749 (2011) (see pp. 135, 155)

167. Bunker, B., Arnold, G. & Wilder, J. *Journal of Non-Crystalline Solids* **64,** 291–316 (May 1984) (see p. 136)

168. Hoppe, U. *Journal of Non-Crystalline Solids* **195,** 138–147 (Feb. 1996) (see p. 137)

169. Brow, R. K. *Journal of Non-Crystalline Solids* **263-264,** 1–28 (Mar. 2000) (see p. 137)

170. Dietzel, A. *Electrochem* **48,** 9–23 (1942) (see p. 138)

171. Di Tommaso, D., Ainsworth, R. I., Tang, E. & de Leeuw, N. H. *Journal of Materials Chemistry B* (2013) (see pp. 141–143, 149, 175)

172. Tilocca, A. *The Journal of Chemical Physics* **129,** 084504 (2008) (see p. 142)

173. Ahmed, I. *et al. Journal of Materials Science* **42,** 9827–9835 (Aug. 2007) (see pp. 144–146, 156, 160)

174. Moss, R. M. *et al. Advanced Functional Materials* **18,** 634–639 (Feb. 2008) (see pp. 147–149, 151–153, 156–159, 161)

175. VandeVondele, J. & Hutter, J. *The Journal of Chemical Physics* **118,** 4365 (2003) (see pp. 148, 168)

176. Mulliken, R. S. *The Journal of Chemical Physics* **23,** 1833 (1955) (see p. 148)

177. Ainsworth, R. I., Tommaso, D. D., Christie, J. K. & de Leeuw, N. H. *The Journal of Chemical Physics* **137,** 234502 (2012) (see pp. 149, 150, 152, 154, 155, 159, 161, 166, 171, 175)

178. Woodley, S. M., Battle, P. D., Gale, J. D. & Richard A. Catlow, C. *Physical Chemistry Chemical Physics* **1,** 2535–2542 (1999) (see pp. 149, 150, 187)

179. Bakaev, V. A. & Steele, W. A. *The Journal of Chemical Physics* **111,** 9803 (1999) (see p. 149)

180. Mehrotra, B. N., Hahn, T., Eysel, W., Ropke, H. & Illguth, A. *Neues Jahrbuch fur Mineralogie, Monatshefte,* 408–421 (1978) (see pp. 156, 157)

181. Wasse, J. C., Petri, I. & Salmon, P. S. *Journal of Physics: Condensed Matter* **13,** 6165–6176 (July 2001) (see p. 156)

182. Penfold, I. & Salmon, P. *Physical Review Letters* **64,** 2164–2167 (Apr. 1990) (see p. 156)

183. Salmon, P., Xin, S. & Fischer, H. *Physical Review B* **58,** 6115–6123 (Sept. 1998) (see p. 156)

184. Du, J. & Cormack, A. *Journal of Non-Crystalline Solids* **349,** 66–79 (Dec. 2004) (see p. 159)

185. Stebbins, J. F. *Journal of Non-Crystalline Solids* **106,** 359–369 (Dec. 1988) (see p. 159)

186. Pota, M. *et al. Computational Materials Science* **47,** 739–751 (Jan. 2010) (see p. 159)

187. Kowada, Y., Adachi, H. & Minami, T. *The Journal of Physical Chemistry* **97,** 8989–8992 (Sept. 1993) (see p. 160)

188. Kiani, A. *et al. Acta Biomaterialia* **8,** 333–340 (Jan. 2012) (see pp. 163–166, 172, 174, 180)

189. Kirkpatrick, R. & Brow, R. K. *Solid State Nuclear Magnetic Resonance* **5,** 9–21 (Oct. 1995) (see p. 166)

190. Pickard, C. & Mauri, F. *Physical Review B* **63** (May 2001) (see pp. 166, 176)

191. Van de Walle, C. & Blochl, P. *Physical Review B* **47,** 4244–4255 (Feb. 1993) (see p. 167)

192. Yates, J., Pickard, C. & Mauri, F. *Physical Review B* **76** (July 2007) (see p. 167)

193. Charpentier, T. *Solid State Nuclear Magnetic Resonance* **40,** 1–20 (July 2011) (see p. 167)

194. Bonhomme, C. *et al. Chemical Reviews* **112,** 5733–5779 (Nov. 2012) (see pp. 167, 168)

195. Charpentier, T., Menziani, M. C. & Pedone, A. *RSC Advances* **3,** 10550 (2013) (see p. 167)

196. VandeVondele, J. & Hutter, J. *The Journal of Chemical Physics* **127,** 114105 (2007) (see p. 168)

197. Kiani, A. *et al. Materials Chemistry and Physics* **120,** 68–74 (Mar. 2010) (see pp. 169, 172, 174–176, 179, 180)

198. Nose, S. *The Journal of Chemical Physics* **81,** 511 (1984) (see p. 169)

199. Hoover, W. *Physical Review A* **31,** 1695–1697 (Mar. 1985) (see p. 169)

200. Martyna, G. J., Klein, M. L. & Tuckerman, M. *The Journal of Chemical Physics* **97,** 2635 (1992) (see p. 169)

201. Theodorou, D. N. & Suter, U. W. *Macromolecules* **19,** 139–154 (Jan. 1986) (see p. 169)

202. Segall, M. D. *et al. Journal of Physics: Condensed Matter* **14,** 2717–2744 (Mar. 2002) (see p. 170)

203. Dumez, J.-N. & Pickard, C. J. *The Journal of Chemical Physics* **130,** 104701 (2009) (see p. 170)

204. Norberg, S. T., Svensson, G. & Albertsson, J. *Acta Crystallographica Section C Crystal Structure Communications* **57,** 225–227 (Mar. 2001) (see pp. 171, 173)

205. Tiwari, B., Sudarsan, V., Dixit, A. & Kothiyal, G. P. *Journal of the American Ceramic Society* **94,** 1440–1446 (May 2011) (see p. 171)

206. Pickup, D. M. *et al. Journal of Materials Science: Materials in Medicine* **19,** 1681–1685 (Dec. 2007) (see p. 172)

207. Robinson, M. & Haynes, P. D. *The Journal of Chemical Physics* **133,** 084109 (2010) (see p. 176)

208. Tiwari, B., Pandey, M., Sudarsan, V., Deb, S. & Kothiyal, G. *Physica B: Condensed Matter* **404,** 47–51 (Jan. 2009) (see p. 178)

209. Bridge, B. & Higazy, A. A. *Physics and Chemistry of Glasses* **27,** 1–14 (Feb. 1986) (see p. 180)

210. Brow, R., Tallant, D., Warren, W. & McIntyre, A. *Physics and Chemistry of Glasses* **38,** 300–306 (Dec. 1997) (see p. 181)

211. Imanaka, N., Masui, T., Hirai, H. & Adachi, G.-y. *Chemistry of Materials* **15,** 2289–2291 (June 2003) (see p. 181)